An Investigation on Interactions between Plant Physiological-Hydrological-Biogeochemical processes and Acid Mine Drainage in Coal Refuse Piles using Optimality Principle Theory

by

Héctor William Clavijo Sanabria

Civil Engineer, Universidad de Los Andes, Bogotá, Colombia, 2001

Master of Engineering, Universidad de Los Andes, Bogota, Colombia, 2002

Submitted to the Graduate Faculty of

Swanson School of Engineering in partial fulfillment

of the requirements for the degree of

Doctor of Philosophy

University of Pittsburgh

2020

UNIVERSITY OF PITTSBURGH

SWANSON SCHOOL OF ENGINEERING

This dissertation was presented

by

Hector William Clavijo Sanabria

It was defended on

November 22, 2019

and approved by

Jeen-Shang Lin, Ph.D., Associate Professor, Department of Civil and Environmental Engineering

Emily Elliot, Ph.D., Associate Professor, Department of Geology and Environmental Science

Zhi-Hong Mao, Ph.D., Professor, Department of Electrical and Computer Engineering

Dissertation Director: Xu Liang, Ph.D., Professor, Department of Civil and Environmental Engineering

An Investigation on Interactions between Plant Physiological-Hydrological-Biogeochemical Processes and Acid Mine Drainage in Coal Refuse Piles using Optimality Principle Theory

Hector William Clavijo Sanabria, PhD

University of Pittsburgh, 2020

Human civilization has changed the global biogeochemical cycles since last century. Carbon and nitrogen cycles have been affected by industrialization and by disturbance of natural vegetation distribution (i.e. deforestation, fires, agriculture and mining). As one of the pollution processes, Acid Mine Drainage (AMD) has played a special role on disturbances on water, carbon and nitrogen cycles. The study of this role is the main part of analysis in the present dissertation. More specifically, this work investigates the reciprocal action between hydrological and biogeochemical processes after coal mines disturbances by applying a comprehensive mathematical formulation to assess the effects of vegetation as passive phytoremediation on AMD in two coal refuse mines using an optimal plant physiological approach.

The development of this dissertation has resulted in the following findings:

1) The optimality formulation developed in this dissertation, based on minimum unit cost function, could be extended to integrate water-stress conditions in a more constrained manner than the majority of optimal formulations presented in literature. 2) The strategy of having as many as possible constraints to avoid parameter equifinality has been a point paramount significance in the formulation in this study. 3) The analysis and simulations show that the main interactions between the biogeochemical processes and pyrite oxidation as main AMD processes are driven primarily by the seasonally plant evapotranspiration through the soil moisture variation; the effect of mineral nitrogen processes and organic matter oxidation reducing the pH; and the solute plant uptake

reducing the amount of concentrations. 4) The long-term simulation of passive bioremediation with grass vegetation has shown to be environmentally efficient only in the amended layer. On the other hand, using tree vegetation suggests better performance to reduce solute concentrations and increase the pH. 5) The solute transport simulations make possible to establish an estimation of the autonomous time of pollution recovery at watershed scales. 6) Finally, the use of vegetation as passive bioremediation, such as grass or tree vegetation, is worth in terms of surface water quality.

Table of Contents

Acknowledgements xxx

1.0 Introduction 1

  1.1 Background and Motivation 1

  1.2 Research Problem and Scope 4

    1.2.1 Research Questions 5

  1.3 Research Design 5

    1.3.1 General Method 6

    1.3.2 Sites of Study 9

      1.3.2.1 Mather Site 9

      1.3.2.2 Ernest Site 10

      1.3.2.3 Oensingen Site 11

    1.3.3 Data Sets 12

    1.3.4 Dissertation Organization 13

2.0 Extending Unit Cost Function Optimal Theory to Include Interactions in Soil-Plant-Atmosphere under Water-Limited Conditions 14

  2.1 Introduction 14

  2.2 Mathematical Model Formulation 20

    2.2.1 Processes Modeled 21

    2.2.2 Empirical Approach for Stomatal Conductance 23

    2.2.3 Optimal Approach Using Unit Cost Function 24

    2.2.4 Strategy for Constraining Model Parameters 26

2.3 Computational Implementations 31

2.3.1 Empirical Approach Algorithm 33

2.3.2 Optimal Unit Cost Function Algorithm 34

2.3.3 Constrained Optimal Algorithm 36

2.3.4 Coding Adjustments in DHSVM-HTGCM for the Evapotranspiration Module 37

2.4 Geometrical and Conceptual Analysis of the Models 38

2.4.1 Constraining and Linking Evapotranspiration Models 39

2.4.2 The Equilibrium Equation – Constraining Carbon Assimilation Models ... 44

2.4.3 Empirical Approach Integrated Model 50

2.4.4 Optimal Prentice Approach Integrated Model 55

2.4.5 Empirical and Optimal Approaches Correspondences as Modeling Strategy 60

2.5 Model Calibrations 63

2.5.1 Model Parameters 64

2.5.2 Calibration at the Mather Site using DHSVM 67

2.5.3 Calibration at Oensingen-Switzerland Site using DHSVM 69

2.6 Simulations and Analyses 71

2.6.1 Empirical and Optimal Unit Cost Functions 72

2.6.2 Strategy for *a/b* Optimal Parameter to Constrain Optimal 75

2.6.3 Comparison of Empirical and Optimal Approaches Results 78

2.6.4 Strategy for *a'* Empirical Parameter Constraining g_s and *a'* in Optimal Approach 82

2.6.5 Exploring Hypotheses about the Implications of Optimal Approaches....... 84

2.6.6 Review of c_i/c_a Relationships under Optimal Theory 92

2.6.6.1 Hyperbola Curve in Unit Cost Trade-off 92

2.6.6.2 Time variation of c_i/c_a.. 94

2.6.6.3 Relationships Between c_i/c_a and Temperature 95

2.6.6.4 Relationships Between c_i/c_a with Vapor Pressure Deficit and Carboxylation Capacity 96

2.7 Conclusions 98

3.0 Development of a Pyrox+Hydro-Biogeochemical Model linked to AMD Processes Modeling 100

3.1 Introduction 100

3.2 Mathematical Model Formulation.. 105

3.2.1 Plant Physiology Processes and Soil Moisture Dynamics............................ 107

3.2.2 Carbon and Nitrogen Biochemical Cycles Processes................................... 110

3.2.3 Soil Inorganic Biogeochemical Dynamics and Chemical Equilibrium of pH 114

3.2.4 Pyrite Oxidation and Transport Metals Processes 118

3.3 Computational Implementations 122

3.3.1 Carbon Assimilation-Evapotranspiration Module in DHSVM-HTGCM. 123

3.3.2 CASA-CN Model implementation within DHSVM-HTGCM 124

3.3.3 Biogeochemical Transport-Reaction Module 125

3.3.4 Pyrox Module and Phreeqc Model (iPhreeqc version)................................ 128

3.3.5 Complete Model Framework Workflow.. 129

3.4 Qualitative Mathematical Analysis of the Dynamics of the Model 130

3.4.1 Dynamics of Plant Growth 131

3.4.2 Dynamics of Organic Matter and Dissolved Oxygen 133

3.4.3 Dynamics of Pyrite Oxidation and Interactions with Biogeochemical Processes 136

3.5 Model Calibrations 143

3.5.1 Calibration of Biogeochemical-Pyrox Processes using Experimental Column Lab Data 145

3.5.2 Calibration Biogeochemical-Pyrite Oxidation Processes at Mather Site... 148

3.6 Simulation Analysis of Interactions 150

3.6.1 Interactions Between Soil Hydrology and Pyrite Oxidation 150

3.6.2 Effect of pyrite oxidation induced pH on Nitrogen Pools 154

3.6.3 Effect of Organic Matter Oxidation on Pyrite Oxidation Process 156

3.6.4 Effect of Nitrification on Pyrite Oxidation Process 158

3.6.5 Effect of Metal Plant Uptake on Pyrite Oxidation Process 159

3.7 Simulation Scenarios of Bioremediation 163

3.7.1 Remediation Scenario with Grass, Alkaline Clay and Coal Refuse 163

3.7.2 Remediation Scenario with Tree Vegetation Types and AC-CR 171

3.8 Conclusions 178

4.0 Acid Mine Drainage Pollutant Storage Capacity and Transport on the Watershed Scale 180

4.1 Introduction 180

4.2 Model Implementation 182

4.2.1 From Column Process to Watershed Scale Modeling 183

4.2.2 Subsurface Acid Mine Drainage Solute Transport on the Watershed Scale 187

4.2.3 Surface Acid Mine Drainage Solute Transport on the Watershed Scale... 188

4.2.4 Conceptual Acid Mine Drainage Capacity and Resilience on the Watershed Scale 189

4.3 Application Simulations and Analyses 190

4.3.1 Capacity and Resilience of AMD Pollutants on the Watershed Scale 190

4.3.2 Transport Scenario with Grass, Alkaline Clay and Coal Refuse 200

4.3.3 Transport Scenario with Tree Vegetation and AC-CR.............................. 203

4.4 Conclusions 206

5.0 Contributions and Future Work 207

5.1 Contributions 207

5.1.1 From the Hydro-Biological Model Study... 207

5.1.2 From the Hydro-Biogeochemical-Pyrox Model Study 208

5.1.3 From the Hydro-Transport Model Application.. 209

5.2 Future Work 209

Appendix A Derivation of Equations for the Optimization Problem for Plant Physiology using Prentice Optimality Theory and Complete water-controlled conditions 211

A.1 Penman-Monteith Equation 212

A.2 Water storage and transport model (capacitance model)...................................... 213

A.3 Carbon assimilation (Biochemical Farquhar model).. 214

A.4 Carbon diffusion 216

A.5 General Mathematical Formulation for the Optimization Problem-Prentice and Luo et al (2013) Equations 216

A.6 Compact Mathematical Formulation of the Optimization Problem- Prentice and Luo et al (2013) Equations. 217

A.7 Optimality Condition for the Optimization Problem 218

A.8 Components of the Optimality Condition Equation 219

A.9 System of Equations for Optimality Approach 221

Appendix B Vegetation species and Empirical Parameter Adjustment and Estimation 222

Appendix C Solution of Biogeochemical Transport-Reactive Partial Differential Equations 226

Appendix D Solution of The Multiple System of Ordinary and Partial Differential Equations 230

Bibliography 235

List of Tables

Table 1 Parameters used in validation for Empirical and Optimal Constrained Approaches 66

Table 2 Modeling setup for calibration of lab experiments and Mather site observations 144

Table 3 Parameters for lab experiments and Mather site calibration 144

Table 4 Empirical Values Reported by Literature for different species 223

Table 5 Final Averaging of Empirical Values according to Literature and species 225

List of Figures

Figure 1 Representation of Acid Mine Drainage AMD and pyrite oxidation processes linked to hydrological processes on coal refuse piles which is the main aim of this study. ... 4

Figure 2 General scheme of the research method used in this study based on the three stages of model computational development: a) Hydro-biological modeling, b) Hydro-biogeochemical model and c) Hydro-solute-transport modeling. 8

Figure 3. Location of Mather Site Mine [google maps]... 10

Figure 4 Location of Ernest Site Mine [google maps]. 11

Figure 5 Location of Oensingen Site flux tower owned by ETH-Zurich [google maps]. 12

Figure 6 Geometrical representation of an ideal case of the general formulation of the modeling strategy of constraining parameters. a) Plane of X_i,Y_j variables with two model curves approaches: Model A in red dashed and continuous line and shaded blue area of feasible values, *Model B* in continuous blue. The green curve is the constraining equation for variables X_i and Y_j. b) Plane of Π_k, Π_p parameters of *Model A* and *Model B*, respectively. The red brown curve is the equifinality curve among the parameters and the green curve is the constraint equation in the parameters plane. 29

Figure 7 Scheme of optimal approach algorithm for the solution of the system of equations of section 2.2.3. The algorithm stars with initial values for c_i and Ψ_L in the upper portion of the scheme. The workflow moves downward solving for *E*, g_s, carbon assimilation and carbon diffusion as the equilibrium equation (Equation 2.4) and

finally solving the optimality equation (Equation 2.2 or Equation 2.3) in the outer iteration loop on c_i. 35

Figure 8 Scheme of the algorithm of the modeling strategy for constraining parameters applied to the optimality and empirical approaches. The workflow begins in the phase I with the optimality algorithm, moves with phase II of computing *a'* and finally phase III with use of the empirical algorithm. 37

Figure 9 Penman-Monteith Model Curve and its variations under changing parameters. Left side: linear relationship between vapor pressure deficit *D* and potential evapotranspiration E_{pot}. Right side: the different evapotranspiration curves. 40

Figure 10 Plant Hydraulics or capacitance-resistance water transport model curves. Right plane [Ψ_L x E] shows the numerical model and its feasible area in shaded blue. Left planes [C_p x B] and [C_p x M] are the curve of the parameters of the numerical model in the right side plane. 41

Figure 11 Integration of Plant Hydraulics and Penman-Monteith models curves. Plane [E x g_s] shows the Penman-Monteith curve. Plane [E x Ψ_L] shows the capacitance-resistance water transport or plant hydraulic model. Plane [Ψ_L x g_s] shows the resulting relationship between Ψ_L and g_s. 43

Figure 12 Carbon Assimilation Farquhar (Rubisco-Limited) Model Curve constrained by water limited condition factor. 45

Figure 13 Carbon Diffusion Model curve constrained by atmospheric-boundary-layer conductance g_{ab}. The shaded area shows the feasible area of values where it is possible to have equilibrium conditions points. 46

Figure 14 Equilibrium condition with constraining carbon diffusion as supply and carbon assimilation as demand for carbon by plants. Blue shaded area represents the set of points where the equilibrium points are possible for a range of temperature and radiation conditions. 47

Figure 15 Equilibrium condition curve in plane [c_i *x* Ψ_L] in green and the corresponding points in the evapotranspiration-water transport curves. Plane [*E x* g_s] shows the Penman-Monteith curve. Plane [*E x* Ψ_L] shows the water transport-plant hydraulics line. Plane [c_i *x* A_n] shows the equilibrium condition from the intersection between carbon assimilation and carbon diffusion curves. Stomatal conductance g_s and carbon assimilation A_n are actually on different axes though sharing one here for graphical purposes. 49

Figure 16 Integrated curves of evapotranspiration, plant hydraulics, carbon assimilation, carbon diffusion and equilibrium curve to empirical approach curve. The point *P* represents the solution of the two variable c_i, Ψ_L system of equations described in Section 2.2. The curve in the c_i – g_s plane is a BBL equation (Equation 2.1) representation where carbon assimilation A_n changes. 51

Figure 17 Variation of the empirical approach solutions under cold and hot climate conditions. Planes [c_i *x* Ψ_L] , [*E x* g_s] , [*E x* Ψ_L] and [c_i *x* A_n] are similar to those in Figure 15. Plane [c_i *x* g_s] right bottom is similar to that in Figure 16. 53

Figure 18 Empirical approach simulation data for carbon assimilation, evapotranspiration, stomatal conductance, CO_2 in-leaf concentration and water leaf potential at the Mather site, following the same axis arrangement as the graphical analysis in Figure 17.. 54

Figure 19 Total unit cost function with the two components: transpiration unit cost and the carboxylation unit cost. The Plane [c_i x $dCost/dc_i$] shows the derivatives for the unit cost components and the condition for minimum cost at intersection point *P*. The corresponding stomatal conductance is shown on external axis. 56

Figure 20 Integrated curves of evapotranspiration, plant hydraulics, carbon assimilation, carbon diffusion and equilibrium curve to the optimal approach curve. The point *P* represents the solution of the two variable c_i, Ψ_L system of equations described in Section 2.2. 57

Figure 21 Variation in the empirical approach solutions under cold and hot climate conditions. Planes [c_i x Ψ_L], [E x g_s], [E x Ψ_L] and [c_i x A_n] are similar to those in Figure 15. Plane [c_i x $dCost/dc_i$] right bottom is similar to the one in Figure 20. 58

Figure 22 Optimal approach simulation data for carbon assimilation, evapotranspiration, stomatal conductance, CO_2 in-leaf concentration and water leaf potential a the Mather site, following the same axis arrangement the graphical analysis in Figure 21. 59

Figure 23 Correspondence between the optimal and empirical approach solutions under different climate conditions. Plane [c_i x g_s] shows the empirical approach curve. Plane [c_i x $dCost/dc_i$] shows the derivative conditions for the optimal approach. 61

Figure 24 Geometrical and conceptual explanation of the three possibilities for optimal coupled with empirical approach: a) optimal by minimum cost point; b) constrained by g_s and a'; c) constrained by condition limit carbon diffusion = carbon assimilation. Plane [E x g_s] shows the Penman-Monteith curve. Plane [E x Ψ_L] shows the water transport-plant hydraulics line. Plane [c_i x A_n] show the equilibrium condition from

the intersection between carbon assimilation and carbon diffusion curves. Plane [c_i x *Cost*] corresponds to unit cost function. 62

Figure 25 Comparison of modeled results with the observations at Mather site for the year 2010 using the empirical and optimal constrained approaches. a) Gross primary productivity (GPP) using the empirical approach; b) Evapotranspiration using the empirical approach; c) Gross primary productivity (GPP) using the optimal constrained approach; d) Evapotranspiration using the optimal constrained approach. e) Comparison of gross primary productivity of the empirical and optimal constrained approaches. f) Comparison of evapotranspiration of the empirical and optimal constrained approaches. 68

Figure 26 Comparison of modeled results with the observations at the Oensingen site for the year 2010 using the empirical and optimal constrained approaches. a) Gross primary productivity (GPP) using the empirical approach; b) Evapotranspiration using the empirical approach; c) Gross primary productivity (GPP) using the optimal constrained approach; d) Evapotranspiration using the optimal constrained approach. e) Comparison of gross primary productivity of the empirical and optimal constrained approaches. f) Comparison of evapotranspiration of the empirical and optimal constrained approaches. 70

Figure 27 Stomatal conductance and a/b behavior in time using the modeling strategy on a/b optimal parameter. 76

Figure 28 Comparisons of empirical (red points) and unconstrained optimal (blue points) approach simulations over the course of a year. a) and b) Carbon assimilation; c) and d) Evapotranspiration; e) and f) Stomatal conductance: g) and h) Equivalent

empirical parameter a’. Mather site (Left-side panels) and Oensingen site (Right-side panels). 79

Figure 29 Comparisons of unconstrained optimal (blue points) and optimal coupled with empirical (green points) approaches simulations over the course of a year. a), b) Carbon assimilation; c), d) Evapotranspiration; e), f) Stomatal conductance: g), h) Equivalent empirical parameter a’. Mather site (Left-side panels) and Oensingen site (Right-side panels). 83

Figure 30 Comparisons of constrained optimal using g_s only (yellow points) and constrained optimal using g_s and *a’* (green points) approaches simulations in a year at the Mather site. a) Carbon assimilation; b) Evapotranspiration; c) Stomatal conductance; d) Water leaf potential; e) Carbon concentration in-leaf; f) Equivalent empirical parameter *a’*. 84

Figure 31 Geometrical and conceptual explanation of stomatal conductance variation with ci under hot and cold climate conditions. Plane [c_i x A_n] shows the equilibrium condition from the intersection between carbon assimilation and carbon diffusion curves at high and low temperature conditions. Plane [c_i x g_s] corresponds to stomatal conductance curves. 85

Figure 32 Conditions that explain high Equivalent Parameters a’ values at the Mather and Oensingen sites in red and blue points. All the points shown are simulation results from optimality unconstrained without any bounding on g_s or *a’*. 87

Figure 33 Scatter Plots of forcing meteorological data showing relationships with unconstrained optimal approach (grey points), with constrained by g_s (green points) and with constrained by *a’* (red points). a) and b) temperature vs radiation; c) and d) temperature vs shortwave; e) and f) temperature vs vapor pressure deficit. Left plots a), c) and e) are for Mather site. Right plots b), d) and e) for Oensingen site. 90

Figure 34 Comparison among hyperbola curves for empirical. Optimal unconstrained and optimal constrained (optimal coupled with empirical in the figure) approaches where $V=V_{cmax}/A_n$ *and* $G= g_s/A_n$. a) Hyperbola curves for the Mather site; b) Hyperbola curves for the Oensingen site. 93

Figure 35 *Ci/Ca* Relationship with Time. a) Ratio *Ci/Ca* vs time comparing optimal unconstrained and optimal constrained (optimal coupled with empirical in the figure) approaches for the Mather site; b) Frequency distribution of ratio *Ci/Ca* over time at the Mather site; c) Ratio *Ci/Ca* vs time comparing optimal unconstrained and optimal constrained (optimal coupled with empirical in the figure) approaches for the Oensingen site; d) Frequency distribution of ratio *Ci/Ca* over time at the Oensingen site. 94

Figure 36 *Ci/Ca* Relationship with Temperature. 95

Figure 37 *Ci/Ca* relationships with carboxylation capacity V_{cmax} and Vapor Pressure Deficit *VPD*. a) Ratio *Ci/Ca* vs V_{cmax} comparing optimal unconstrained and optimal constrained approaches for the Mather site; b) Ratio *Ci/Ca* vs V_{cmax} comparing optimal unconstrained and optimal constrained approaches for the Oensingen site; c) Ratio *Ci/Ca* vs VPD comparing optimal unconstrained and optimal constrained for the Mather site; d) Ratio *Ci/Ca* vs VPD comparing optimal unconstrained and optimal constrained approaches for the Oensingen site. Optimal constrained is labeled optimal coupled with empirical in the figure. 97

Figure 38 Schematic representation of the main interactions between Acid Mine Drainage with pyrite oxidation (Xu 2013; Xu et al. 2019) and biogeochemical processes (included in this study as a contribution) using vegetation as passive bioremediation. The violet arrows represents the fluxes between pyrox processes and biogeochemical processes. Dashed violet arrows show the effect of pH chemical equilibrium over metals and biogeochemical species. The mathematical model aims to describe the above processes.. 106

Figure 39 Schematic workflow of computational implementation of carbon assimilation-evapotranspiration module using the optimal-empirical algorithm within the DHSVM-HTGCM model interacting with the unsaturated flow computation part (*unsaturatedFlow* module) and carbon biochemical cycle computation module (CASA-CN) Section 3.3.2. 124

Figure 40 Schematic workflow of computational implementation of biochemical cycles processes in the CASA-CNP model (Wang, 2010) within the DHSVM-HTGCM model interacting with the carbon assimilation-evapotranspiration module Section 3.3.1, unsaturated flow computation part (*unsaturatedFlow* module) and biogeochemical inorganic transport model, Section 3.3.3. 125

Figure 41 Schematic workflow of computational implementation of biogeochemical inorganic transport model within the DHSVM-HTGCM model interacting with carbon-nitrogen cycles processes (CASA-CN) model, Section 3.3.2, and pyrox module, Section 3.3.4. 127

Figure 42 Schematic workflow of computational implementation of pyrite oxidation and metals transport model within the DHSVM-HTGCM (Xu, 2013) model interacting with plant physiology processes module Section 3.3.1, and biogeochemical transport model, Section 3.3.3. 128

Figure 43 Complete schematic workflow of computational implementation of inclusion of vegetation as bioremediation into DHSVM-HTGCM (Xu 2013) model. The boxes show the general module structures of DHSVM-HTGCM. The blue boxes are the main modifications developed in this study. The arrows represent the flow of variables and data inside the general computational development. 129

Figure 44 Phase portrait of carbon C_{Plant} and nitrogen N_{Plant} leaf pools dynamics. The green line and red brown curve correspond their respective to steady-dynamics points. The arrows represent the direction of flows of the variables dynamics. Point $C_{p\text{-}Steady}$,$N_{p\text{-}Steady}$ is the equilibrium point, which is an attractor. 132

Figure 45 Phase portrait of Organic Matter pool OM and Dissolved Oxygen pool O_2 dynamics as a representation of Equation 3.39 and Equation 3.40. Green and blue curves correspond to their respective steady-dynamics points. Arrows represent the direction of flows of the variables' dynamics. Point $OM_{\text{-}Steady}$,$O_{2\text{-}Steady}$ is the equilibrium point, which is an attractor. 135

Figure 46 Phase portrait of Sulfate SO_4 ions production driven by the Pyrite Particle Radius r_c. The violet curve in plane [SO_4 x r_c] shows a transient trajectory of the variables. The violet curve in plane [dSO_4/dt x r_c] represents the production rate of SO_4 and H^+ ions depending on r_c. 137

Figure 47 Phase portraits of pyrite oxidation dynamics with dissolved oxygen O_2 and pyrite particle radius r_c as described by Equation 3.40 and Equation 3.47. Blue and red curves correspond to respective steady-dynamics points. Arrows represent the direction of flows of the variables' dynamics. The point at $r_c=0$ and $O_2= O_{2\ Steady}$, is the equilibrium point which is an attractor. 139

Figure 48 Phase portraits of Sulfates SO_4 with Pyrite Particle Radius r_c as dynamics using the unsaturated soil transport described by Equation 3.46 and Equation 3.47 without a) and with b) biogeochemical interactions. Violet and red curves correspond to respective steady-dynamics points. Arrows represent the direction of flows of the variables' dynamics. The point at $r_c=0$ and $SO_{4}= SO_{4\ Steady}$, is the equilibrium point, which is an attractor. 141

Figure 49 Phase portraits of Hydrogen Ions H^+ with Pyrite Particle Radius r_c as dynamics using the unsaturated soil transport described by Equation 3.47 and Equation 3.48 without a) and with b) biogeochemical interactions. Blue and red curves correspond to respective steady-dynamics points. Arrows represent the direction of flows of the variables' dynamics. The point at $r_c=0$ and $H^+ = H^+_{Steady}$, is the equilibrium point, which is also an attractor. 142

Figure 50 Comparison between observed and simulated data for SO_4 and pH at Lab Column Experiment A1 amended 90%CR+10%AC no bioremediation. Simulation time: 1400 days. 145

Figure 51 Comparison between observed and simulated data for SO_4 and pH at Lab Column Experiment A2 amended 90%CR+10%AC with grass as bioremediation. Simulation time: 800 days. 146

Figure 52 Comparison between observed and simulated data for SO_4 and pH at Lab Column Experiment B1 non-amended 100%CR no bioremediation. Simulation time: 800 days. 147

Figure 53 Comparison between observed and simulated data for SO_4, Fe and pH at amended and non-amended layers at the Mather site as validation process of the mathematical model. Dates of simulation: Jun 2009 to Dec 2014, equal to 2000 days. 149

Figure 54 Relationship between soil moisture and sulfate concentration SO_4 as product of pyrite oxidation under the effect of plant evapotranspiration. The points are a 10-year simulation at 61 cm of the amended layer with 10%AC+90%CR. 151

Figure 55 Plots of pyrite grain radius with sulfate SO_4 and H+ ions following the dynamical analysis phase portrait plots of the qualitative analysis in Section 3.4.3. The points are a 10-year simulation at 61 cm of the amended layer with 10%AC+90%CR and at 91 cm of the non-amended layer with 100%CR composition....................................... 153

Figure 56 Comparison of sulfates SO_4 and pH time series under the effect of plant evapotranspiration through the change of soil moisture levels. The simulation series represent a 10-year simulation at 61 cm of the amended layer with 10%AC+90%CR. 154

Figure 57 Comparison of annual simulated behavior of ammonia NH_3 and ammonium ions NH_4 through the effect of pH chemical equilibrium under pyrite oxidation. 155

Figure 58 Phase portraits of dynamics of interaction among organic matter, oxygen and shrinking core radius, following the dynamical system phase portrait plots of the qualitative analysis in Section 3.4.2 and Sections 3.4.3. 156

Figure 59 Comparison of dissolved oxygen, sulfates SO_4 and pH production and pyrite grain radius time series under the effect of organic matter oxidation. Simulation series represent a 10-year simulation at 61 cm of the amended layer with 10%AC+90%CR. 157

Figure 60 Hydrogen ions dynamic behavior under only nitrification effect. a) Plot of phase portrait of H^+ ions and pyrite radius dynamics, b) Comparison of H+ content between condition with nitrification and without nitrification. The points are a 10-year simulation at 61 cm of the amended layer with 10%AC+90%CR. 158

Figure 61 Comparison of pH time series between nitrification environment and without nitrification. Simulation series represent a 10-year simulation at 61 cm of the amended layer with 10%AC+90%CR. 159

Figure 62 Phase portraits of pyrite grain radius with sulfate SO_4 and H+ ions following the dynamical analysis phase plots of the qualitative analysis in Section 3.4.3 under metals plant uptake only effect. The points are a 10-year simulation at 61 cm of the amended layer with 10%AC+90%CR and at 91 cm of non-amended layer with 100%CR composition. 160

Figure 63 Comparison of sulfates SO_4 time series under the effect of only metals plant uptake before chemical equilibrium given by pH. Simulation series represent a 10-year simulation at 61 cm of the amended layer with 10%AC+90%CR. 161

Figure 64 Comparison of sulfates SO_4 and pH time series under the effect of only metals plant uptake after chemical equilibrium by pH. Simulation series represent a 10-year simulation at 61 cm of the amended layer with 10%AC+90%CR. 162

Figure 65 Comparison of sulfates SO_4 time series with and without grass bioremediation scenarios at three different amended conditions layers: a) at 61 cm of the amended layer with 10%AC+90%CR. b) at 91 cm of the non-amended layer with 100% and c) at the bottom layer of the non-amended layer with 100%CR. Also, Pyrite Particle

Radius is shown as a measure of potential pollution. Time series represent a 100-year simulation.. 165

Figure 66 Comparison of pH (as logarithm of Hydrogen ions concentration activity) time series with and without grass bioremediation scenarios at three different amended conditions layers: a) at 61 cm of the amended layer with 10%AC+90%CR. b) at 91 cm of the non-amended layer with 100% and c) at the bottom layer of the non-amended layer with 100%CR. Time series represent a 100-year simulation. 166

Figure 67 Comparison of Sulfates pH and SO_4 depth distributions with and without grass bioremediation at four different simulation times: 1st Year, 20th Year, 50th Year and 100th Year... 167

Figure 68 Comparison of Ferric Fe, Calcium Ca, Sodium Na, Magnesium Mg and Potassium K concentrations time series with and without grass bioremediation scenarios at three different amended conditions layers: a) at 61 cm of the amended layer with 10%AC+90%CR. b) at 91 cm of the non-amended layer with 100% and c) at the bottom layer of the non-amended layer with 100%CR. Time series represent a 100-year simulation.. 169

Figure 69 Comparison of Silicon Si, Phosphorus P, Aluminum Al, Chlorine Cl, and Manganese Mn concentrations time series with and without grass bioremediation scenarios at three different amended conditions layers: a) at 61 cm of the amended layer with 10%AC+90%CR. b) at 91 cm of the non-amended layer with 100% and c) at the bottom layer of the non-amended layer with 100%CR. Time series represent a 100-year simulation.. 170

Figure 70 Comparison of sulfates SO_4 time series with and without tree vegetation bioremediation scenarios at three different amended conditions layers: a) at 61 cm of the amended layer with 10%AC+90%CR. b) at 91 cm of the non-amended layer with 100% and c) at the bottom layer of the non-amended layer with 100%CR. Also, Pyrite Particle Radius is shown as a measure of potential pollution. Time series represent a 100-year simulation. 172

Figure 71 Comparison of pH (as logarithm of Hydrogen ions concentration activity) time series with and without tree vegetation bioremediation scenarios at three different amended conditions layers: a) at 61 cm of the amended layer with 10%AC+90%CR. b) at 91 cm of the non-amended layer with 100% and c) at the bottom layer of the non-amended layer with 100%CR. Time series represent a 100-year simulation.. 173

Figure 72 Comparison of Sulfates pH and SO_4 depth distributions with and without tree vegetation bioremediation at four different simulation times: 1st Year, 20th Year, 50th Year and 100th Year. 174

Figure 73 Comparison of Ferric Fe, Calcium Ca, Sodium Na, Magnesium Mg and Potassium K concentrations time series with and without tree vegetation bioremediation scenarios at three different amended conditions layers: a) at 61 cm of the amended layer with 10%AC+90%CR. b) at 91 cm of the non-amended layer with 100% and c) at the bottom layer of the non-amended layer with 100%CR. Time series represent a 100-year simulation. 175

Figure 74 Comparison of Silicon Si, Phosphorus P, Aluminum Al, Chlorine Cl, and Manganese Mn concentrations time series with and without tree vegetation bioremediation scenarios at three different amended conditions layers: a) at 61 cm of

the amended layer with 10%AC+90%CR. b) at 91 cm of the non-amended layer with 100% and c) at the bottom layer of the non-amended layer with 100%CR. Time series represent a 100-year simulation. 176

Figure 75 Scheme linking column pyrite-biogeochemical computation to watershed stream network transport computation. a) The 8-direction flow direction method is used to transport solutes through the watershed. b) The soil unsaturated-saturated column mass balance represents the pollution storage at each cell. 184

Figure 76 Schematic formulation of stream network based on 8-direction Digital Elevation Model DEM information. This system information for stream network is used to develop the connection between the soil column model in Chapter 3.0 and the subsurface and surface transport models. 185

Figure 77 Digital Elevation Models for Mather and Ernest sites watersheds used for column to watershed transport computations. 186

Figure 78 Scheme of subsurface solute balance for each cell according to Equation 4.1, extension of scheme in Figure 75. 187

Figure 79 Time series of Acid Mine Capacity as pollution mass storage and fluxes in Mather site portion of coal pile. The outlet pH and SO_4 concentrations are also shown in plot c). 192

Figure 80 Time series at first and last 10 years of Acid Mine Capacity as pollution mass storage and fluxes in Mather site portion of coal pile. The plots show the details of simulation of mass storage, import and export of SO_4 from data in Figure 79. 193

Figure 81 Time series of Acid Mine Capacity as pollution mass storage and fluxes at the Ernest site watershed with coal pile. The outlet pH and SO_4 concentrations are also shown in plot c).. 194

Figure 82 Time series at first and last 10 years of Acid Mine Capacity as pollution mass storage and fluxes at the Ernest site watershed with coal pile. The plots show the details of simulation of mass storage, import and export of SO_4 from data in Figure 81.. 195

Figure 83 Spatial distribution of SO_4 mass storage or Acid Mine Drainage Capacity at the end of 1st, 25th, 75th and 100th year at the Mather site a), b), c), d) and the Ernest site e), f), g), h)... 196

Figure 84 Time series of Total Mass of SO_4, export of SO_4 out of portion of watershed coal pile, and SO_4 concentration at outlet in Mather site coal pile as measurement of pollution recovery capacity or resilience. 198

Figure 85 Time series of Total Mass of SO_4, export of SO_4 out of watershed coal pile, and SO_4 concentration at outlet in Ernest site coal pile as measurement of pollution recovery capacity or resilience.. 199

Figure 86 General transport results for SO_4, Fe, Ca and pH with grass bioremediation at the Mather site.. 201

Figure 87 General transport results for SO_4, Fe, Ca and pH with grass bioremediation at the Ernest site. 202

Figure 88 General transport results for SO_4, Fe, Ca and pH with tree vegetation bioremediation at the Mather site. 204

Figure 89 General transport results for SO_4, Fe, Ca and pH with tree vegetation bioremediation at the Ernest site. **205**

Figure 90 Comparison empirical *a'* (BBL) and *a'*(BBL-Luo) parameters to get second transfer Function in Mather site. **224**

Figure 91 Comparison empirical *a'* (BBL) and *a'*(BBL-Luo) parameters to get second transfer Function in Ernest site. **225**

Figure 92 Scheme of the numerical discrete mass balance for the equation C1. .... **227**

Figure 93 Numerical scheme of the system of partial differential equations based on the interaction between concentration C*i* and concentration C*j* through the jointed reactions *Rij*. **229**

Acknowledgements

A great journey is full of sinusoidal and mysterious way. Each step calls us for the other ones before and for the promise to stand at the end of the miracle of the finished duty. At this stage of my short but multicolor life I can say, this was that kind of a great journey. Mostly every minute I spent these brilliant years was thanks to my Colombian people; those who wake up very early in the morning to fight with our difficulties as a society; those who dream aloud to encounter his own way in the life and those who has great dreams to have the opportunity I had. Thanks to the immense effort my country took to bring me here, I am realizing my little child dream of being, at least for a couple of years, a scientist, and inventor, a deep thinker. Thanks, definitely to my Mother Gilma, who in the middle of the journey took off to your final spiritual voyage to the heavens; but She left the most important heritage she could, her passion for work and my education. Persons like me in Colombia do not have this kind of opportunities in their lives. It was only possible to the never ending restless of my Mother every day work. But not only was the legacy of my Mother that leads to me to this dream. I acknowledge the support given by Sonia Mangones in my way. She was the light in the shadows of my visits to the hospital. And obvious to my precious daughter Ana, that with her cute hearth and love to me, gave me balsamic energy to continue even in the most difficult times. I want to thank Professor Xu Liang, the person in academia who believes me that I could finish my Ph.D. I am grateful for Professor Liang's valuable academic guidance throughout my Ph.D. study and her financial support under the grant of CBET-1236403 by the U.S. National Science Foundation as a Research Assistant in the first two years of my Ph.D. study. I want to give special thanks to Matos Family, to Efigenia who became my mother on earth in these past years, to Emiro who accompanied us in our journey; to Hortencia who were

unconditional in our critical times; to Myriam who give home this last part of this adventure; to Blas who give me intensive insights of how to write and an immense and enjoyable friendship; To Cecilia who offered us support to be established in Bogota these last years; To Mateo with his lucid and warmer brotherhood.

I want to thank my lab colleagues. Daniel Salas who was the bridge between Professor Liang and me; German Villalba who helps me and teaches me how to handle the Linux storming universe. Felipe Hernandez for his warm welcome at Pittsburgh. Daniel Luna for his immense and refreshing friendship and his invaluable help at the end of this final stages. Liuyan for her friendship and her collaboration with our first paper. Also, Fernando Plaza for his valuable friendship and co-working times in some parts of this journey.

I want to thank the committee advisors. Professor Mao for his unforgettable and enjoyable classes. Professor Emily for her advice in the early stages in my studies and Professor Lin for his valuable comprehension in difficult times.

Finally, and not least important, I want to thank my great brother Ruben Dario, for his support and strong link we have built all our lives. I want to thank CMU Professor Paulina Jaramillo and her family, for her immense support not only to me last year but also to our family and to Sonia in the darkest times. I want to thank Dr. Annabel and German Andres for giving me home these last days of intense work and for their comprehension.

And formally, I thank to COLCIENCIAS the Science Foundation Agency in Colombia, for supporting my studies the last three years. My deep hope is to give back all I got here to Colombia.

Para Gilmita y Hector, mis papás allá en el cielo

Para mi hijita, Anita

1.0 Introduction

1.1 Background and Motivation

Human civilization has changed the global biogeochemical cycles since last century. Changes include carbon and nitrogen cycle alteration. Carbon cycle has been affected mainly by industrialization (CO_2 emissions) and by disturbance of natural vegetation distribution (i.e. deforestation, fires and agriculture). Alterations in nitrogen cycle have been induced by intensive agriculture (excess of nutrients), and urbanization pollution (Vitousek et al. 1997). Pollution, which causes modifications in carbon and nitrogen cycles, have altered chemical equilibrium patterns in soil and streams at the watershed level, and in exports at ocean level (Hofmann 2009; Hofmann et al. 2008). As one of these pollution processes, Acid Mine Drainage (AMD) has played a special role in disturbances on water, carbon and nitrogen cycles, and thus, it is a main part of analysis in the present dissertation.

Scientific literature shows that acidification of soils caused by Acid Mine Drainage (AMD) is an important contemporary ecological problem, which can cause long-term impairment to water resources and biodiversity (Bahrami and Doulati Ardejani 2016; Doulati Ardejani et al. 2013). Plants play a central role in carbon and nitrogen cycles, and in hydrology. Indeed, plant's physics and physiology determine carbon assimilation, evapotranspiration and nutrient uptake at watershed level (Tague and Band 2004), which are key to explain and mitigate effects of disturbances on acidification of soils and streams. In coal refuse piles AMD is the result of pyrite oxidation when they are exposed to oxygen and moisture (Ash et al. 1951). One passive remediation technique uses plants as strategy to remove heavy metals and other hazardous substances (Johnson and Hallberg 2005). However, to the best of our knowledge, assessing the environmental impacts of plants on AMD in coal refuse piles through the passive remediation approach is still unknown (Karaca et al. 2018; Liu et al. 2018).

Majority of the AMD modeling studies have been focused on pyrite oxidation processes from an inorganic chemical perspective (Nordstrom 2011, 2019b; Plaza et al. 2018; Wunderly et al. 1996; Xu 2013). Pyrite oxidation kinetics, chemical equilibrium and transport are the processes typically considered in such type of the modeling studies (e.g. Gerke et al. 1998; Wunderly et al. 1996) but not the biogeochemical interactions involved in the processes. Recent studies use algorithmic heuristics to forecast Pyrite oxidation variables under specific conditions (Bahrami and Doulati Ardejani 2016; Doulati Ardejani et al. 2013) with little effort in deep understanding of the physical-chemical interactions. In this study, impacts of vegetation the relevant biogeochemical processes included in AMD are investigated and analyzed.

Integrating vegetation into a complete hydrology and pyrite oxidation computation as developed by Xu (2013) implies including a coupled calculation of evapotranspiration and carbon assimilation. This provides an opportunity to apply the optimality principle to this environmental engineering problem to test and understand interaction between pyrite oxidation and other biogeochemical elements such as, organic soil matter, mineral nitrogen and carbon efflux.

The optimality principle in eco-hydrology promotes a versatile modeling framework to study complex interactions between plants, water, metals, pollutants and atmosphere (Luo et al. 2013; Porporato and Rodriguez-iturbe 2013). This type of framework is known to be parsimonious and therefore requires less calibration of the parameters (Luo et al. 2013).

The inclusion of plant physiology computation in this study is based on Prentice et al. (2014) which uses the concept of Minimum Unit Cost Function. This Optimality Theory is extended to represent the interactions within the plant-soil-atmosphere continuum (Bonan et al. 2014; Clark et al. 2016; Dewar 2010), considering nutrient limitation and water-stress and atmospheric conditions.

Interactions between biogeochemical and AMD processes are part of open questions to understand the effect of vegetation as remediation on coal refuse piles (Plaza 2018; Xu 2013). The pH as a main indicator of chemical equilibrium among AMD sub-products, nitrification products and inorganic carbon species is a key point that is modeled in an integrated manner in this study. Acidification reduction and metal ions content in the soil in coal refuse piles mines has been studied through laboratory column experiments by Plaza (2018), Plaza et al. (2018), Xu (2013), Xu et al. (2020). Study conducted by Xu (2013) is used as a support for the present modeling analysis.

The mathematical modeling tool and its computational implementation developed in this dissertation can be used to model different scales of environmental fluxes from spot scale to large scale in LSM. The model can be used to study broader questions about effects of mining, soil acidification, non-point sources pollutant and ecological services assessment.

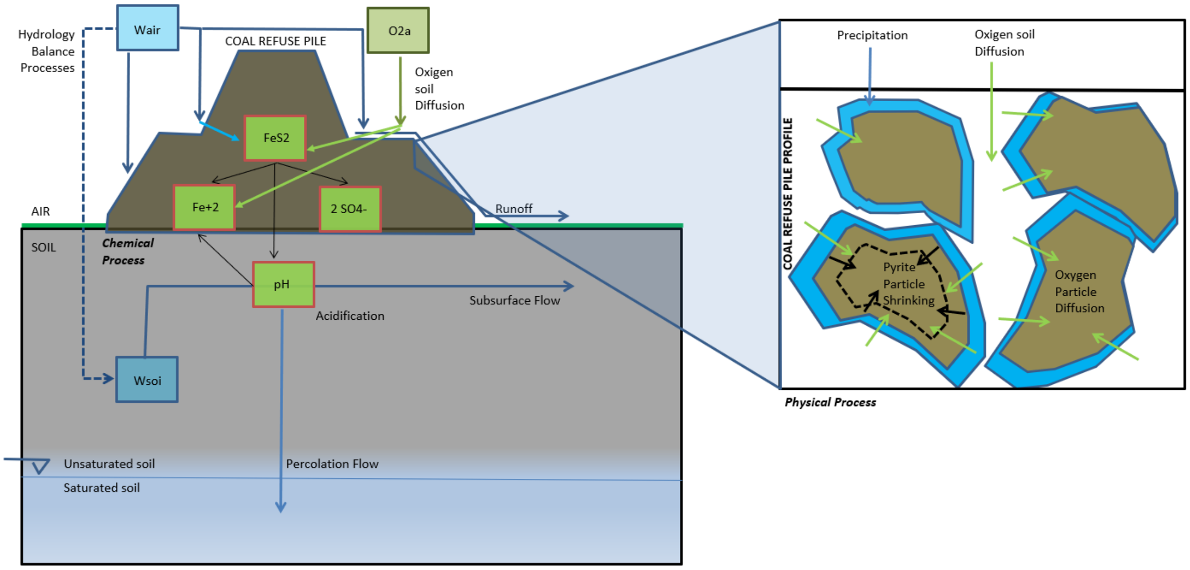

Figure 1 Representation of Acid Mine Drainage AMD and pyrite oxidation processes linked to hydrological processes on coal refuse piles which is the main aim of this study.

1.2 Research Problem and Scope

During the past decade the US-Japan research community has discussed important research themes to develop a better understanding of hydrology and biogeochemistry processes (McDonnell and Tanaka 2001; Mcguire et al. 2014). Problems identified include the integration of biogeochemical processes to other environmental issues with special relevance on water transport (Mcguire et al. 2014). Following this general advice, this dissertation explores issues related to those open research questions. More specifically, this work investigates the convolution between hydrological and biogeochemical processes after coal mines disturbances by applying a comprehensive mathematical formulation to assess the effects of vegetation on AMD in a coal refuse mine.

To fulfill this research purpose, a modeling tool is developed. This tool is able of tackling the water-stress and nutrient limitation environment with an optimality function, which has less calibration parameters and not use of empirical biological equations.

1.2.1 Research Questions

Specifically, this work will answer the following research questions, further described in the three chapters that follow:

I. How to develop a mathematical formulation that describes water-stress conditions and nutrient limitations in eco-hydrological land surface models (LSM) applied to coal refuse mine sites within an optimality principle framework?

II. What are the effects of vegetation, as a remediation solution for AMD process, on the soil and stream acidification and metal ions transport, using plant optimality principle?

III. What is the capacity of transport or retention of pollutants excess, under the concept of plant optimality at a coal refuse mine?

1.3 Research Design

The research questions above are addressed by constructing a physically-, chemically- and physiologically-based mathematical and computational model. This spatially distributed model quantifies the fluxes and the state variables of the water cycle, energy balance, carbon-nitrogen cycles, vegetation physiology, vegetation growth dynamics and solute transport. The model is developed in three stages: i) Optimality formulation in the hydro-biological model; ii) The hydro-biogeochemical model; iii) The hydro-solute transport model. The biological and biogeochemical phases are intrinsically coupled, because they share common inputs-outputs between them. The solute-transport model mainly depends on the biogeochemical phase, as its inputs are given by the biogeochemical part. The following section describes details of the three different stages.

1.3.1 General Method

The hydro-biological stage integrates vegetation leaf physiology dynamics of photosynthesis, transpiration and soil water balance into the Hydro-Thermal-Geo-Chemical Model (HTGCM-DHSVM) (Xu, 2013) based on the optimality principle computed internally as a static constraint for each time step. This change in HTGCM carries out the computation of evapotranspiration based on physiological characteristics of the plant, and it enables the computation of gross primary production (*GPP*), which is the main input of the biogeochemical model.

The hydro-biological stage implementation can be done by two modeling framework approaches: (i) Empirical modeling framework used in VIC+ (Ivanov et al. 2008; Luo 2013; Luo et al. 2016; Luo et al. 2013) which is based on similar approaches as Daly et al. (2004) and Tuzet et al. (2003). (ii) The optimality principle modeling framework based on the components of the unit cost function of Prentice et al. (2014) with an integrated formulation derived from the whole equations coupled in a constraining manner. The difference between approaches (i) and (ii) is that the latter replaces the Tuzet et al. (2003) stomatal conductance empirical equation by the optimality principle in a more comprehensive and integrative way, while the other components used in the VIC+ (Luo et al. 2013) are kept unchanged.

In this work, the optimality principle modeling framework of Prentice et al. (2014) using a unit cost function is employed and extended. The modeling framework is referred to as extension of Prentice et al. (2014). Such framework includes two equations for physical diffusion, in carbon and in water; the complete biochemical model for carbon assimilation (i.e., Biochemical Farquhar Model for photosynthesis) and physical equation for actual evapotranspiration (i.e., Penman-Monteith equation). These last four equations are from the modeling framework used in VIC+ for systems with water-limited conditions (Luo et al. 2016; Luo et al. 2013). This approach addresses the first research question described above.

The hydro-biogeochemical model introduces vegetation growth dynamics and carbon-nitrogen-phosphorus cycles into the hydro-biological model stage. This implementation is carried out in two steps: i) Integration of the Carnegie-Ames-Stanford-Approach Model CASA-CNP for carbon and nitrogen dynamics, developed by Fung et al. (1997), Potter and Randerson (1993), Wang et al. (2007), and Wang et al. (2010), into the photosynthesis-transpiration framework within HTGCM; and ii) Extension of biogeochemical processes modeling to include soil organic matter oxidation, nitrification and denitrification distributed soil solute transport based on Berlin et al. (2014), Hofmann et al. (2008), Jassal et al. (2004), and Wissmeier and Barry (2010), and linked to chemical equilibrium of AMD processes and pyrite oxidation (Plaza 2018; Xu 2013) using PHREEQC model (Wissmeier and Barry 2010).

The hydro-solute transport includes linking the biogeochemical cycles to stream transport in the HTCGM (Xu 2013). This formulation is implemented through two components: 1) Solute transport computation in the subsurface layers using DHSVM flow 8-directions routing following the general concept by Czuba and Foufoula-Georgiou (2014), and Gangodagamage et al. (2014). 2) Solute transport computation at surface level, similar to Mortensen et al. (2016) adopting the of

ADZ Model (Beer and Young 1984; Camacho and Gonzalez 2008; Mortensen et al. 2016) for stream solute transport into HTGCM-DHSVM.

We will use two coal refuse mine sites for which necessary data is available at this time. We have also performed field measurements of soil-water variables (i.e., water potential, soil moisture, soil temperature) and collected samples of vegetation. Calibration and validation processes of the model will be performed along with consistency and sensitivity analysis. Model will be applied to sites of study in different time horizons (i.e., 5, 10 to 100 years and beyond for resilience-recovery purposes). Finally, we will present the computational framework for replication of the ensemble model to be applied in any watershed.

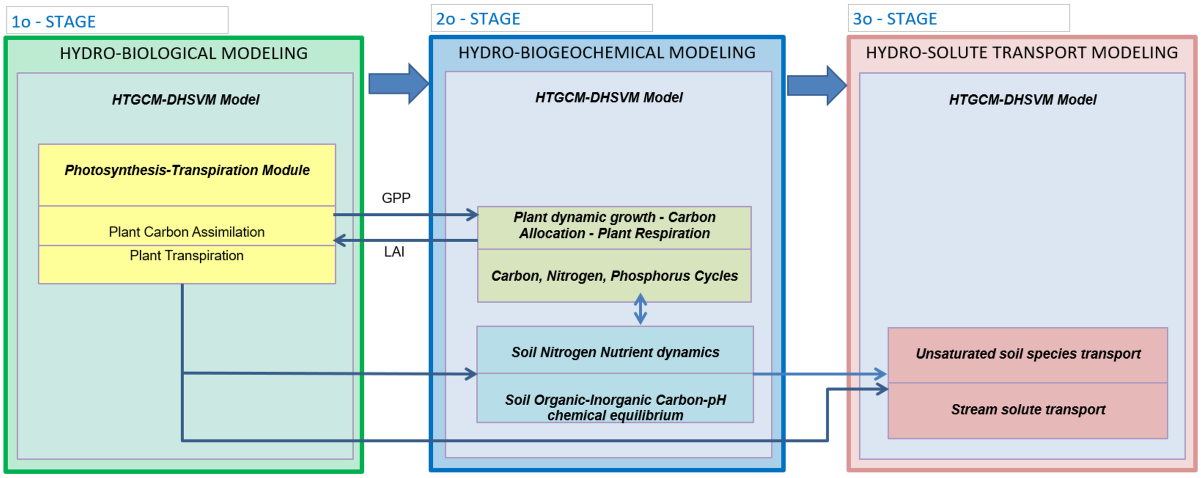

Figure 2 General scheme of the research method used in this study based on the three stages of model computational development: a) Hydro-biological modeling, b) Hydro-biogeochemical model and c) Hydro-solute-transport modeling.

1.3.2 Sites of Study

We focus our model analysis of Acid Mine Drainage in two similar abandoned coal pile sites: Mather and Ernest. Both located in Pennsylvania, United States. However, we use data from Oensingen site located in Switzerland, for the optimality extension analysis as an alternative validation site due to data availability.

1.3.2.1 Mather Site

This site corresponds to a coal refuse mine disposal in Mather, PA. This site is instrumented with chemical and hydrological data and it has the vegetation coverage (i.e. grass) as an implementation of the remediation of the AMD processes (Plaza 2018; Xu 2013). This site also has a meteorological station close to the piles of coal refuse. As part of the research collaboration we have implemented a field-lab experiments to understand the pirate oxidation and the effect of vegetation on the AMD processes.

The Mather site is a large vegetated pile of coal refuse from an abandoned mine that was in operation from 1917 to 1965, located nearby Mather Town, Greene County, Pennsylvania, USA bordering the Ten Mile Creek. In 2009, a reclamation program was implemented on the Mather pile with four plots, three portions with vegetated coverage with different subsurface specifications and one portion unaltered.

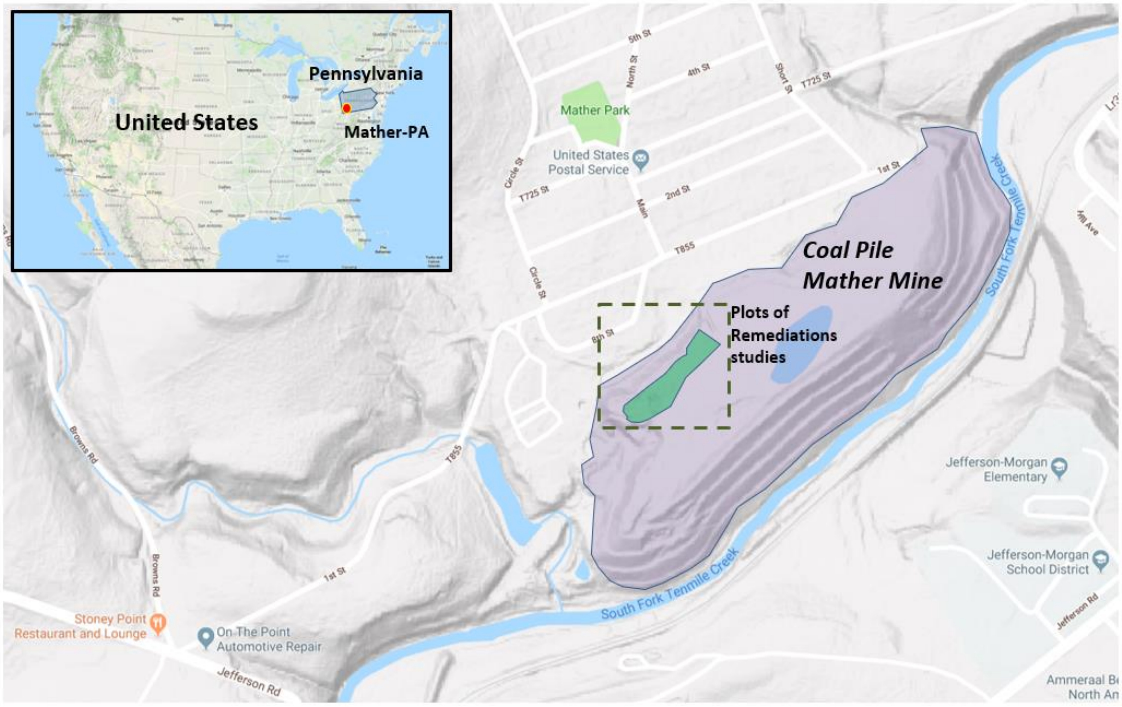

Figure 3. Location of Mather Site Mine [google maps].

The Mather site is under a temperate continental climate with warm summers, with a mean annual precipitation of 1148 mm (44.7 in), 85.2 precipitation days, mean annual temperature of 10 ^{o}C, with portions of alfalfa, white clover, red clover and tall fescue grass vegetation planted as pilot remediation studies.

1.3.2.2 Ernest Site

This site also has coal refuse piles and is located in Pennsylvania. Water quality data is available for the main stream. The general conditions for Ernest site are similar to Mather's.

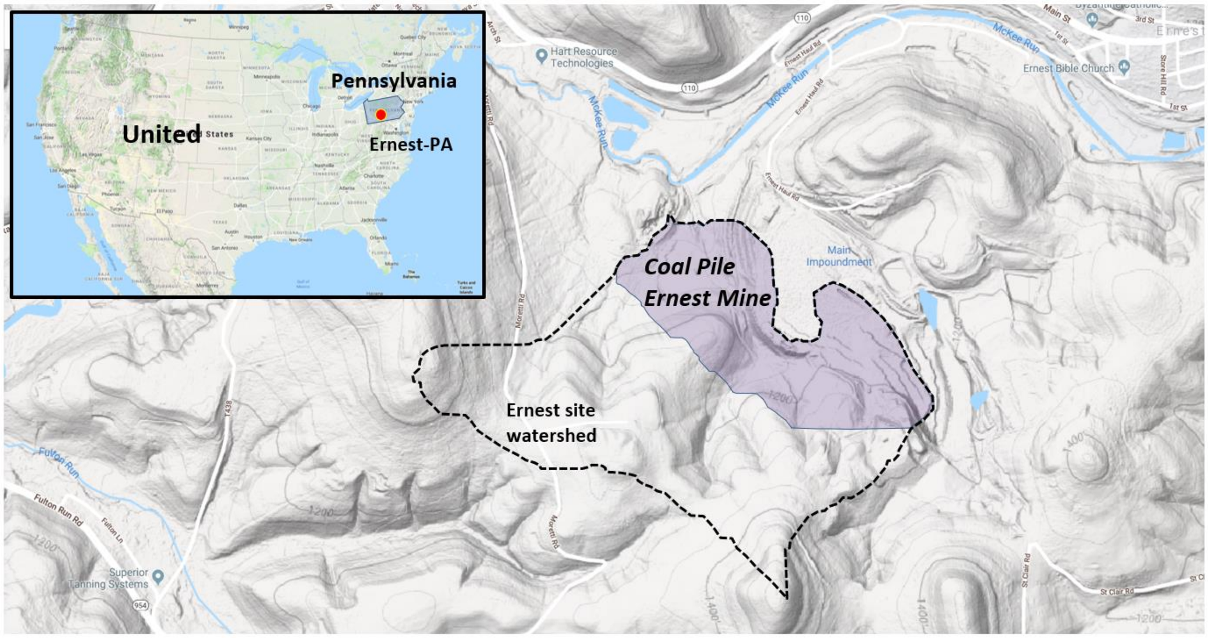

Figure 4 Location of Ernest Site Mine [google maps].

1.3.2.3 Oensingen Site

This site is located in Switzerland, at a crop plantation field where there is a Euro-Flux station to capture meteorological and plant physiological data. The site was taken from Molina-herrera et al. (2016) as validation for optimality analysis and possible reference for complete validation of biogeochemical computations.

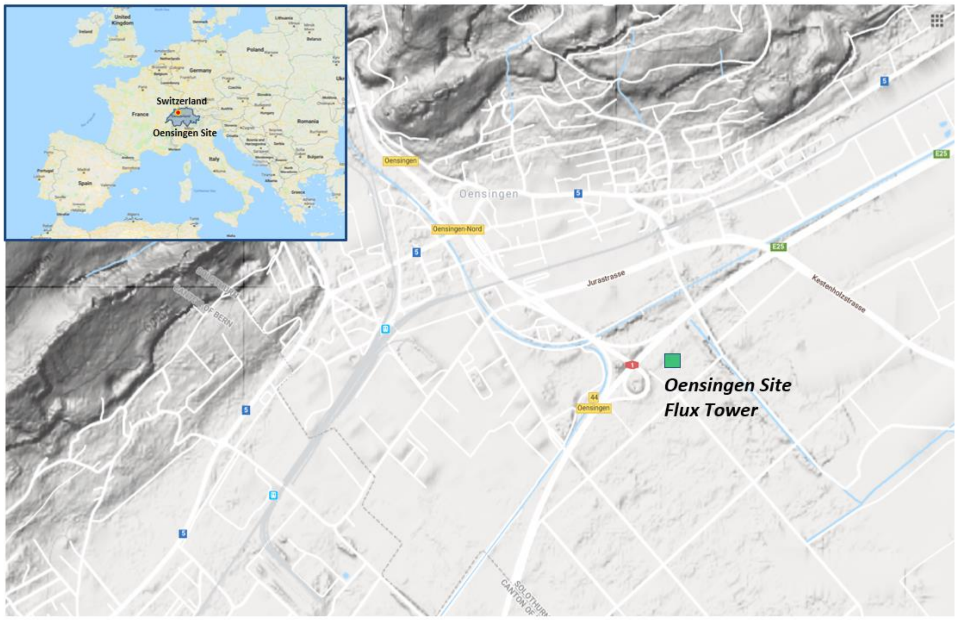

Figure 5 Location of Oensingen Site flux tower owned by ETH-Zurich [google maps].

1.3.3 Data Sets

Geospatial data is provided by USGS National Map project, and by local and states environmental websites. (http://nationalmap.gov/), The main source of information for precipitation, solar radiation, air temperature is NOAA website and Satellite information [http://www.noaa.gov/]. The vegetation information from the Mather, Ernest and Oensingen sites are retrieved by the satellite information (MODIS-NASA) (http://modis.gsfc.nasa.gov/). For the analysis of AMD processes, we have data of chemicals at 4 plots in Mather with record of chemical substances over time (Plaza 2018; Xu 2013). Additionally, we have access to chemical data for the Ernest site. For the Mather site, Plaza (2018) implemented column-lab tests for different scenarios of disposal coal refuse that serve to validate the model at controlled conditions scale.

1.3.4 Dissertation Organization

This dissertation is presented in four main chapters: Chapter 2 presents the methods and results of including plant physiological variables into the general model framework. This part is cited as the Hydro-biological stage and corresponds to the first research question. Chapter 3 presents the methods and simulation results of validation of integrating pyrite oxidation and biogeochemical processes as a description of vegetation bioremediation scenarios. This chapter corresponds to the Hydro-biogeochemical stage of the model development and intends to explore the second research question. Chapter 4 contains an estimate of capacity of pollution on the watershed scale using solute transport simplified methods and the previous column integrated pyrox-biogeochemical results. This portion of the dissertation is the Hydro-Solute Transport stage and corresponds to the third research question. Finally, Chapter 5 includes a general overview of the dissertation contributions and further proposed work.

2.0 Extending Unit Cost Function Optimal Theory to Include Interactions in Soil-Plant-Atmosphere under Water-Limited Conditions

2.1 Introduction

Plants play a central role in hydrology as well as in carbon and nitrogen cycles. Indeed, plants' physiology determine carbon assimilation, evapotranspiration and nutrient uptake at watershed level (Tague and Band 2004), which are key to explain and mitigate effects of acidification disturbances on soils and streams.

There are two main approaches to compute carbon assimilation and evapotranspiration as main physiological plant processes: using empirical equations and using optimality theory concepts (Medlyn et al. 2011; Porporato and Rodriguez-iturbe 2013). Empirical equations are often derived by measured data into regressions using explicit stomata conductance (Collatz et al. 1991; Medlyn et al. 2011). Use of the optimality approach is based on a general rationale of a fundamental physiology law followed by plants as an evolutionary mechanism (Eagleson 1982, 2001; Medlyn et al. 2011; Prentice et al. 2014).

Optimality theory has been widely used to explain plants physiology (Hatton et al. 1997; Kleidon 1997; Laio et al. 2001; Luo et al 2013; Manzoni et al. 2011, 2014; Zehe et al. 2011). According to the optimality principle theory the state of the system (i.e. plant-water) in a given time can be explained by maximizing or minimizing a system's generalized function (Liu 2014). There are two approaches to define generalized optimality functions related to the plant-water system: i) conceptual-based functions that use ideas from optimal control theory (Farquhar 1973); or ideas from microeconomic theory (Cowan et al. 1977; Prentice et al. 2014; Wright et al. 2003);

and ii) thermodynamic-based functions founded upon the Second Law of Thermodynamics, first stated by (Schroedinger 1944) and recently studied by Dewar (2010), Jesus et al. (2012), Marsland and England (2015), Perunov et al. (2014), Schymanski et al. (2010a), Volk and Pauluis 2010, Wang and Bras (2011), and Zehe et al. (2011). In a detailed summary of studies Porporato and Rodriguez-iturbe (2013) provide the eco-hydrological perspectives on the thermodynamic formulation of optimality.

Thermodynamic-based optimality functions use the Maximum Entropy Production principle (MEP), which has been shown to accurately represent the interaction within the plant-soil-atmosphere system (Dewar 2010; Schymanski et al. 2010a), but does not consider nutrient limitation, water-stress and atmospheric conditions (Porporato and Rodriguez-iturbe 2013). This work applies concepts of theory of statistical mechanics to include nutrient limitation and water-stress conditions in the optimality function to model the plant-water system. In 2010, in a special issue of The Philosophical Transactions of The Royal Society, the Maximum Entropy Production was postulated as the most appropriate alternative to model interaction between plant-soil-atmosphere and geomorphology (Dewar 2010; Schymanski et al. 2010a). This new perspective has led to research on this topic during most recent years tackling the modelling problem from the thermodynamic perspective, but real-world applications are still in development (Brunsell et al. 2011; Clark et al. 2016; Jesus et al. 2012; Kleidon et al. 2013). A thermodynamic perspective in conjunction with hydrology modeling has been developed by Dewar (2010), Eagleson (2001), Istanbulluoglu et al. (2012), Jesus et al. (2012), Martyushev (2010), Meysman and Bruers (2010), Porporato and Rodriguez-iturbe (2013), Schymanski et al. (2010a, 2010b), and Westhoff and Zehe (2013). However, this physical-based optimality theory requires some specific model interpretations of the entropy function to include a complete hydrological, biogeochemical and geochemical interactions in our general mathematical implementation. These requirements enable more the use of conceptual perspective of the optimality approach.

The optimality principle has been used extensively in plant physiology and in hydrology from the conceptual perspective (Dekker et al. 2012; Farquhar 1973; Farquhar et al. 2002; Manzoni et al. 2014; Schymanski et al. 2008; Wright et al. 2003) where a function invokes the physiological function over the intricate interrelations among the hydrology processes.

The conceptual approach is founded on control theory, and is the most used by researchers (e.g. Cowan et al. 1977; Farquhar et al. 2002; Katul et al. 2010; Manzoni et al. 2011; Manzoni et al. 2014; Wright et al. 2003). Farquhar's seminal work models the interaction between plant and environment as a linear dynamic system with a proportional control (Farquhar 1973).

Since the first modeling work of stomata conductance, the scientific community working on eco-hydrology has been advancing the empirical and the optimal approaches. The empirical approach pursues a more simple and data-based formulation for the stomatal conductance, based on the works of Bally-Berry-Leuning (Collatz et al. 1991; Daly, Porporato, and Rodriguez-Iturbe 2004; Laio et al. 2001; Leuning et al. 1995; Luo et al. 2016; Luo et al. 2013; Rodriguez-Iturbe and Porporato 2004; Tuzet et al. 2003; Wang et al. 2009). For example, Tuzet et al. (2003) promotes the use of the Leuning equation, which is capable of reproducing hysteresis cycles in stomata conductance. Similarly, Daly et al. (2004) use the Leuning equation to show the effect of soil moisture on the decline of carbon assimilation and evapotranspiration with time. These authors set the modelling framework of coupling vegetation physiology and hydrology processes for the next generation of models like those in Gilhespy et al. (2014), Ivanov et al. (2008), Luo et al. (2016), Luo et al. (2013). Models that are based on Tuzet et al. (2003) and Daly et al. (2004)'s approximation are able to include the constraint of plants in water-limited environments.

The optimal approach seeks different functions relating physiological variables to tackle the problem of uncertainty in the parameters of the empirical model (Farquhar et al. 2002; Farquhar and Sharkey 1982; Prentice et al. 2014; Wright et al. 2003). It represents plant physiology using the concept of production function, like that in microeconomic theory, with inputs being the stomatal conductance and the carbon concentration in-leaf difference and output being the carbon assimilation. The mathematical form of the carbon diffusion equation is similar to that of the Cobb-Douglas equation in the theory of maximization production of a firm in microeconomics; the plant searches to maximize the carbon assimilation subject to a cost function of a) the use of stomatal conductance; and b) the use of carbon concentration in-leaf. The inclusion of the role of nitrogen limitation and temporal analyses was developed by Farquhar et al. (2002) using optimal control theory to derive an optimality condition for the evolution of stomatal conductance. In sum, this approach has been focused on determining the evolution or the optimal behavior of the stomatal conductance under different conditions.

Overall, we can recognize in the conceptual optimality formulations, despite the objective functions based on minimizing evapotranspiration or maximizing carbon assimilation, that the mathematical decision variable can be stomatal conductance in the majority of the cases, as established by the seminal work (Cowan et al. 1977). Other authors use the stomatal conductance variable as the decision variable, including Bonan et al. (2014), Duursma et al. (2019), Franks et al. (2018), Héroult et al. (2013), De Kauwe et al. (2015), Manzoni et al. (2014), and Sperry et al. (2017). The focus on stomatal conductance follows from of its importance in plant physiology. However, there are novel formulations based on CO_2 in-leaf concentrations, such as those developed by Eller et al. (2018) and Prentice et al. (2014) which consider the optimization to be addressed jointly with stomatal conductance. For example, Dewar et al. (2018) and Mencuccini and Christoffersen (2019) have developed a summary review of the main optimal functions using either stomatal conductance or CO_2 in-leaf concentration.

Another important development was made by Medlyn et al. (2011). In this work, they test an explicit formulation for an optimal stomatal conductance that allows for consistency among the different results presented in the literature. This simple optimal stomatal equation has been used in several Land Surface Models (LSMs) as a replacement for the empirical equation, for example the BBL stomatal conductance equation. This exchange of equations has been proposed as an optimality formulation when it is integrated within hydrology models in LSM, as in Bloomfield et al. (2019), Kauwe et al. (2015), and Zhou et al. (2018). This dissertation expands this type of modeling approach by integrating the physiology, hydrology and biogeochemical processes. Expanding this modeling approach is fundamental to develop the mathematical framework necessary for this study.

In recent developments, the integration of plant hydraulics as a main conjunctive element of water-stress or drought-test conditions has been implemented in several conceptual optimal formulations, including Eller et al. (2018), Héroult et al. (2013), Kauwe et al. (2015), De Kauwe et al. (2015) and Manzoni et al. (2014). However, the only plant hydraulics development that includes dynamic formulation on water leaf potential is made by Manzoni et al. (2011), which does not include carbon and nitrogen cycling in its general formulation.

In other modeling works, there is an increasing interest accounting for interactions between the plant and nutrients, metals, pH, atmospheric humidity, and carbon dioxide. The mathematical framework of optimality-based models offers flexibility enough to include these interactions. One optimality-based model uses the concept of optimality including carbon availability and water stress but without explicit accounting of carboxylation capacity and nitrogen assimilation (Katul et al. 2010). A second optimality-based model framework has been developed by Dekker et al. (2012), Schymanski et al. (2007) and Schymanski et al. (2008) using optimality principle of the net carbon benefit to find a function, that is capable of modeling plant physiology and its dynamics. However, their work does not include any constraints to model water-controlled dynamics.

Researchers in botany science (Prentice et al. 2014), have proposed an innovative formulation for plant optimality that considers the photosynthesis process to be similar to the production function defined by the microeconomic theory of a firm. The production function is the focus of the optimality principle, and two variables as inputs. These authors report an optimality function similar to that in Manzoni et al. (2011) and Schymanski et al. (2008), but they introduce the concept of the carboxylation unit cost of photosynthesis. This is probably the most innovative concept in recent years of searching for a functional optimality to describe the physiology of photosynthesis. This dissertation employs the rationale of the optimality function stated in Prentice et al. (2014) and extends it to include water-stress conditions and nutrients limitations using additional constraints equations. This approach will allow us to study the impact of plants used to remediate acid mine drainage processes (AMD) in coal refuse pile sites.

The optimal approaches of both Prentice et al. (2014) and Medlyn et al. (2011) were formulated under wet water conditions and with a lack of comprehensive interaction in terms of soil hydrology and atmospheric processes (Porporato and Rodriguez-iturbe 2013). An intrinsic and integrated formulation of optimality has not yet been developed (Prentice et al. 2014; H. Wang et al. 2014). An opportunity is taken by this dissertation to reformulate the Prentice Optimality approach to integrate it with soil hydrology equations and account for water-stress conditions.

This chapter presents the details of optimality extension development as a Hydro-Biological model in three sections: a) The mathematical formulation comparing the empirical and the optimal approaches with the formalization of the modeling strategy used in this study b) the computational implementations for the solution of the system of equations; c) at proposed innovative geometrical and conceptual analysis of the integrated equations and approaches. d) a validation exercise of the model at the Mather and Oensingen sites; e) the simulation analyses of the model to explore its capabilities and limitations; and f) some features that show consistencies with original Prentice paper observations.

2.2 Mathematical Model Formulation

The interaction between plant photosynthesis processes and soil moisture dynamics is the focus of the model to be developed in this study as an extension of optimal theory under water limited conditions. This section shows the general mathematical model implementation for including vegetation into the pyrite oxidation processes. In general, the mathematical model developed in this part of the study is a system of five equations that include five unknowns: carbon assimilation (A_n), evapotranspiration (E), stomatal conductance (g_s), CO_2 in-leaf concentration (c_i) and water leaf potential (Ψ_L). Currently used in other models are two main approaches: the empirical approach and the optimal approach. We add a third, coupling the optimal to the empirical approach using a modeling strategy based on constraining the parameters of the model.

The first part of this section is devoted to the plant physiological processes and the corresponding equations. The second part provides information on the empirical approach for the computation of the physiological variables. Next, we present the formulation for plant processes via the unit cost optimality approach. Finally, we develop the modeling strategy for constraining parameters and application of this strategy to the optimality approach coupled with the empirical approach.

2.2.1 Processes Modeled

The main photosynthesis process that has been modeled is carbon assimilation, as formulated by Cowan et al. (1977), Daly et al. (2004), Tuzet et al. (2003). Such assimilation is the biochemical demand carbon by plants; this process is constrained by the capacity transfer of the carbon diffusion and can be calculated using a Fickian formulation presented by Daly et al. (2004), Luo et al. (2013), and Tuzet et al. (2003). Other processes are related to soil moisture and evapotranspiration. The soil moisture dynamics is defined by the Richards equation linked with the evapotranspiration computation through the soil column (Bonan et al. 2014; Luo et al. 2013). This evapotranspiration process is also tightly integrated with carbon assimilation as part of the plant photosynthesis by the stomata conductance. The effect of water limited conditions is computed using the water leaf potential as main variable in the evapotranspiration and the reduction of the carbon assimilation capacity.

The model for carbon assimilation A_n is based on the biochemical formulation by Farquhar and Sharkey (1982) and completed later by Collatz et al. (1991). The general equation for carbon assimilation is a bi-quadratic composite of three parts proposed by Collatz et al. (1991) each having different rates of assimilation: a) light-limited conditions, b) Rubisco carboxylation, and c) maximum capacity of carboxylation. The three different rates of carbon assimilation are computed according to Michaelis-Menten kinetics on the main variable of carbon in-leaf concentration, c_i with maximum rates on irradiance and rubisco capacity that depend on net short radiation and leaf-air temperature respectively. A function on water leaf potential Ψ_L is used as a lowering factor to carbon assimilation to represent the effect of dry soil conditions into the photosynthesis process, as formulated by Daly et al. (2004), and Luo et al. (2013).

The supply for carbon assimilation is the diffusion. This rate is the capacity of carbon transfer from the atmosphere into the leaf. The gradient between atmospheric carbon concentration and the CO_2 in-leaf concentration is the main factor responsible for the capacity of transfer. However, the openness of the stomata is the ultimate factor determining the transfer capacity. The measure of the stomata behavior is the conductance g_S. In the model for carbon diffusion, a series-coupled of stomata conductance and boundary-layer conductance is used as a factor for the concentration gradient, as formulated by Daly et al. (2004) and Luo et al. (2013).

The evapotranspiration, *E,* a mass-energy balance for water from the leaves to the atmosphere, is computed by the Penman-Monteith formulation (ASCE 2000; Daly et al. 2004; Luo et al. 2013). In this case, the potential capacity of evapotranspiration is reduced by a factor to convey the actual evapotranspiration, which depends directly on the stomata conductance, g_S, and leaf area index, *LAI*. The main inputs for this formulation are air temperature, radiation and vapor pressure deficit, *D,* among other meteorological parameters.

The transpiration process that drives water from soil to the leaves is also computed using an analog resistance-capacitance Ohm's law model (Katerji et al. 1986; Luo et al. 2013). In such a model, the water flows from high to low water potentials, from soil potential, Ψ_S, to leaf potential, Ψ_L, through the equivalent plan resistance. Also, the effect of water storage, Ψ_P, is computed using an equivalent capacitance of the plant based on water storage potential. Both the water flow in the xylem and the water storage can be equated to the total evapotranspiration given by the Penman-Monteith formulation.

So far in this section, there are four equations: one for carbon assimilation, one for carbon diffusion and two for actual evapotranspiration. However, we have five main variables for the coupled photosynthesis-evapotranspiration process: A_n, carbon assimilation; E, actual evapotranspiration; g_s, stomata conductance; ci, CO_2 in-leaf concentration and water leaf potential Ψ_L. The equation needed for the solution of the five variables can be either an empirical formulation given by Daly et al. (2004), Medlyn et al. (2011), and Tuzet et al. (2003) as employed in the study by Luo et al. (2013) or an optimality formulation for the plant behavior. The use of an empirical equation is called hereafter the empirical approach and the use of an optimal mathematical formulation is named the optimal approach. Both approaches are explained below.

2.2.2 Empirical Approach for Stomatal Conductance

There are many empirical relationships between stomatal conductance and carbon assimilation that define the intrinsic physiological behavior of plants. The Ball-Berry-Leuning (BBL) model (Leuning 1995; Leuning et al. 1995) shows a linear relationship between stomatal conductance and carbon assimilation with an inverse effect of CO_2 in-leaf concentration ci. In addition, the effect of water limited conditions can be incorporated via a factor function on carbon assimilation that depends on water leaf potential, Ψ_L. The empirical equation is shown below,

$$g_s = g_o + a' \frac{A_n(\Psi_L, c_i)}{c_i - \Gamma} f_v(\Psi_L) \qquad [\ 2.1\ ]$$

where, g_s [mol/m2/s] is stomatal conductance; g_o [mol/m2/s] minimum stomatal conductance; a' the empirical parameter; A_n [mol/m2/s] is net carbon assimilation; Ψ_L [MPa] water leaf potential;

c_i [mol/mol] CO_2 in-leaf concentration; f_v (Ψ_L) [-] function of stomata response to evapotranspiration and/or water stress; Γ [mol/mol] compensation point for CO_2 concentration.

The linear relation between stomatal conductance and carbon assimilation in Equation 2.1 shows a certain response of the stomata to carbon assimilation needs under the condition of the concentration in-leaf. This equation is broadly used in literature as a main explanatory formulation for stomata conductance. Using this equation makes it possible to address the problem of solving the five unknows describe above. However, its foundations are merely empirical and do not take into account the mechanistic or theoretical perspectives (Bonan et al. 2014; Medlyn et al. 2011). The following alternative approach provides a more general and mechanistic formulation.

2.2.3 Optimal Approach Using Unit Cost Function

Prentice et al. (2014) proposed a formulation for plant optimality, comparing the photosynthesis-transpiration processes with the production function used in microeconomic theory of a firm as the optimality principle with two variables as inputs (Prentice et al. 2014; Wright et al. 2003). The main contribution of the Prentice optimality is the Unit Cost Function, which involves two opposing processes, transpiration and carboxylation. This function searches for a minimum cost based on c_i variation rather than optimal stomata conductance. Also, this function includes an explicit physiological term for the carboxylation infrastructure V_{cmax}/A_n.

The application of this optimal approach to the complete system of equations is formulated as a mathematical optimization. The objective function is the Unit Cost as defined by Prentice et al. (2014), $Cost = aE'/A_n + bV_{cmax}/A_n$, with a measure of transpiration E', potential carbon assimilation V_{cmax} and actual carbon assimilation A_n. The equations for carbon assimilation and carbon diffusion can be considered as constraints. According to Prentice optimal theory, the CO_2

in-leaf concentration c_i is adopted as the main decision variable. However, the water leaf potential Ψ_L is needed as a variable for the system of equations, to make carbon assimilation and carbon diffusion variables equal through the stomata conductance g_s. The complete derivation of the integrated components of the optimality equation is presented in Appendix A (Equation 2.2 and Equation A34). The optimality condition equation for this formulation is obtained by taking the first derivative with respect to c_i as follows,

$$a\left[\frac{\partial E'}{\partial c_i}\frac{1}{A_n}-\frac{E'}{A_n^2}\frac{\partial A_n}{\partial c_i}\right]-b\left[\frac{V_{cmax}}{A_n^2}\frac{\partial A_n}{\partial c_i}\right]=0 \qquad [\ 2.2\ ]$$

where, $E' = 1.6\ G_s\ D$ [mol/m2/s] is the maximum evapotranspiration; G_s [mol/m2/s] is an equivalent total aerodynamic-boundary layer-stomatal conductance; D [Pa/Pa] is the vapor pressure deficit; a transpiration cost parameter; b carboxylation cost parameter; A_n [mol/m2/s] net carbon assimilation; Ψ_L [MPa] water leaf potential; c_i [mol/mol] CO_2 in-leaf concentration; and V_{cmax} [mol/m2/s] carboxylation maximum capacity.

From a purely mathematical perspective, the use of Equation 2.2 allows the complete solution of the system of equations for the five variables A_n, E, g_s, Ψ_L and c_i. Equation 2.2 plays the same role in the system of equations as the empirical Barry-Belly-Leuning (BBL) equation for stomatal conductance. To solve the equations in a more direct way, the optimization problem can be reduced to a compact formulation with three elements: a) an objective function using the Unit Cost, b) a constraint of equilibrium between carbon assimilation and carbon diffusion, and c) only one decision variable, c_i. The final formulation used in this dissertation is the reduction of the original optimization problem of five variables to a system of two variables, c_i and Ψ_L, with two equations: a) the optimality condition Equation 2.2 or Equation A44-Appendix A, and b) the equilibrium constraint equation for carbon assimilation and carbon diffusion Equation A27-Appendix A. The compact formulation can then be expressed by the following system of equations:

$$\boldsymbol{g_s} = \frac{a}{b}\frac{[g_{ab}+g_s]}{g_{ab}[c_a-c_i]}\left[\frac{\partial E\prime}{\partial c_i} - \frac{E\prime}{A}\frac{\partial A_n}{\partial c_i}\right]\frac{A_n}{V_{cmax}}\frac{A_n}{\partial A_n/\partial c_i} \qquad [\ 2.3\ ]$$

$$f(\psi_L)A_F(c_i) = G_s(\psi_L)[c_a - c_i] \qquad [\ 2.4\ ]$$

where, g_{ab} [mol/m2/s] represents aerodynamic-boundary layer conductance.

The above formulation enables a comparison between the optimal and empirical approaches. In the latter, the equations are the Ball-Barry-Leuning (BBL) equation for stomatal conductance and the equilibrium equation for carbon assimilation and carbon diffusion. The variables are the same as those used in the optimal method. Thus, the empirical approach can be formulated using Equation 2.1 and the same Equation 2.4. The details of the system of equations' formulation and the derivation are in Appendix A.

2.2.4 Strategy for Constraining Model Parameters

The strategy presented by Luo et al. (2013) for achieving use of representations from different perspectives or models to illustrate the same process, searching for reduction of a model's degree of freedom (Luo et al. 2013), is also employed here. We can establish the general formulation as a mathematical multi-generalized system of equations. In general, mathematical models are composed of non-linear algebraic equations linked to partial differential equations.

This implies the solution of instant variables based on the optimal or empirical approaches as dynamic variables to fit with better observed data. The problem arises when the number of processes and the corresponding number of parameters increases (Hernández 2019). Normally, the solution to fit parameters is solved by sophisticated heuristics or optimization methods which fit any combination of parameters to match observed and computed data (Beven and Binley 1992). However, this kind of solutions results in problems of equifinality among the parameters (Beven 2006; Beven and Binley 1992; Vrugt and Beven 2018). Such problems, which implies fitting observed data with different groups of parameters (Fatichi et al. 2016), are easily revealed by looking at strictly statistical criteria like the AIC index or Pareto curves among the parameters.

We formulate a strategy that can deal with this issue using the following statements. Let X_i and Y_j, be modeled variables (which can be computed in space and time). There are at least two different approaches to model Y_j based on X_i: *Model A* and *Model B*. Let *Model A* be represented by a generalized function $Y_j=M_A(X_i, \Pi^A{}_k,F_{ext})$ of non-linear algebraic and ordinary-partial differential equations based on X_i to get Y_j as an output. Let *Model B* be another system of equations $Y_j=M_B(Xi, \Pi^B{}_p,F_{ext})$ that could be similar to *Model A*, but with different parameters. Let $\Pi^A{}_k$ be the fitting parameters of *Model A* and $\Pi^B{}_p$ be the ones of *Model B*. Let F_{ext} be the forcing data or boundary conditions as fixed values in time and space for every model approach and constraints in the total system. Finally let X_{iobs} and Y_{jobs} be the observed data on the variables X_i and Y_j respectively as an additional element for the ideal formulation.

The problem is to find a solution for X_i, Y_j, $\Pi^A{}_k$ and $\Pi^B{}_p$ using the different model approaches (*Model A* and *Model B*), to match as closely as possible the observed data X_{iobs} and Y_{jobs}. Therefore, the solution has to use as many constraints as possible to represent physically or conceptually based relationships between X_i and Y_j through the observed data X_{iobs} and Y_{jobs}.

As a brief demonstration of the existence and uniqueness of the solution, we can address the following system of equations. Let X_i, Y_j, Π^{A}_{k} and Π^{B}_{p} be a group of vector variables. Then we need a system of four groups of equations. However, we have only *Model A* and *Model B* as different approaches to same solutions. In Figure 6, we can see a geometric representation of an ideal case of the problem. In plane X_i, Y_j the shaded area is the feasible solutions for *Model A* with variation of the parameter Π^{A}_{k}. We have to find a constraint $E_c(X_i,Y_j)=0$ that relates to observed data X_{iobs}, Y_{jobs}. The constraint intersects within the area of feasible solutions a line that contains the observed point X_{iobs}, Y_{jobs}. In the plane Π^{A}_{k} and Π^{B}_{p} of the parameters space, it is possible to build a pareto curve of equifinality with the parameters using the *Model A* and *Model B* equations as $\Pi^{A}_{k} = M^{-1}_{A}(X_i, M_B(X_i, \Pi^{B}_{p}, F_{ext}), F_{ext})$. The used constraint equation $E_c(X_i,Y_j)=0$ can be represented in the Π^{A}_{k} , Π^{B}_{p} space using the observed data. This constraint equation then determines a curve of validity in parameter space for the equifinality values of the observed data X_{iobs}, Y_{jobs}. The intersection between the constraint equation $Ec(X_{iobs},Y_{jobs}, \Pi^{A}_{k}, \Pi^{B}_{p})=0$ and $\Pi^{A}_{k} = M^{-1}_{A}(X_i, M_B(X_i, \Pi^{B}_{p}, F_{ext}), F_{ext})$ is the solution to the general system of equations for X_i, Y_j, Π^{A}_{k} and Π^{B}_{p}. Finally, the solution can be traced in the X_i,Y_j plane as the intersection between *Model A* and *Model B* with parameters Π^{A}_{k} and Π^{B}_{p} and the constraint equation $Ec(X_{iobs}, Y_{jobs})=0$.

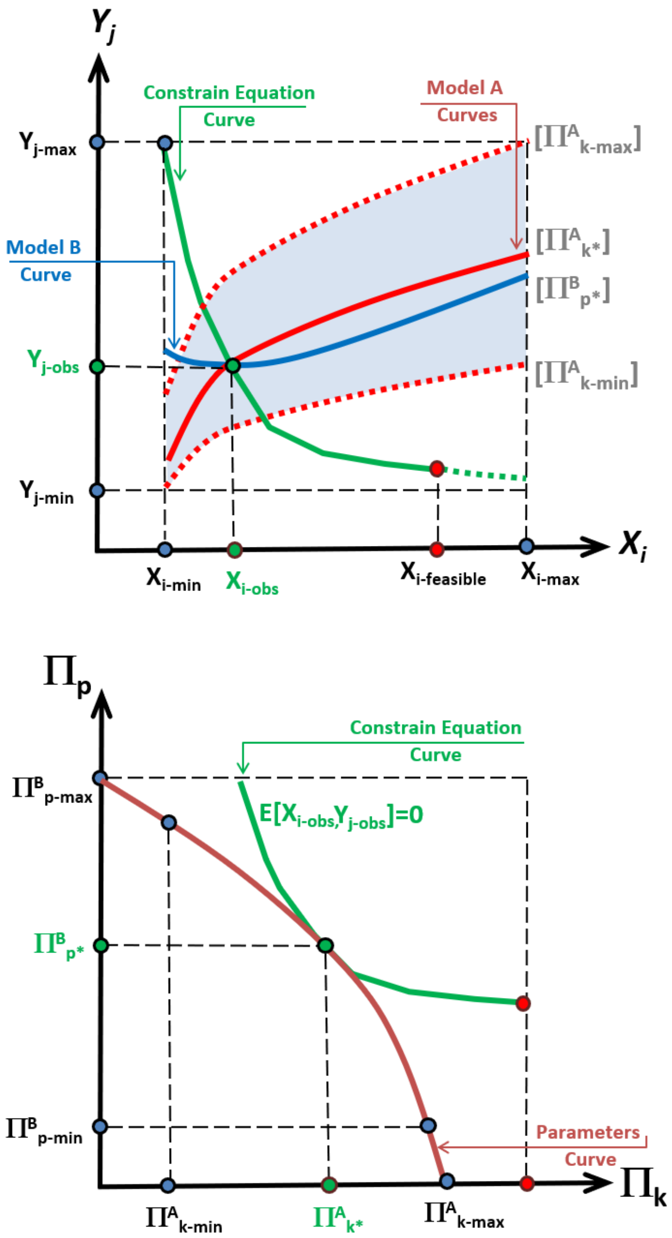

Figure 6 Geometrical representation of an ideal case of the general formulation of the modeling strategy of constraining parameters. a) Plane of X_i,Y_j variables with two model curves approaches: Model A in red dashed and continuous line and shaded blue area of feasible values, *Model B* in continuous blue. The green curve is the constraining equation for variables X_i and Y_j. b) Plane of Π_k, Π_p parameters of *Model A* and *Model B,* respectively. The red brown curve is the equifinality curve among the parameters and the green curve is the constraint equation in the parameters plane.

Lastly, the general strategy can be stated as finding constraining equations $Ec(X_{iobs},Y_{jobs}, \Pi^{A}_{k}, \Pi^{B}_{p})=0$ that intersect $\Pi^{A}_{k} = M^{-1}_{A}(X_i, M_B(X_i, \Pi^{B}_{p}, F_{ext}), F_{ext})$ which represents the relationship between differing models' parameters.

The model strategy formulation explains in general terms the solution for the problem of adding more processes to a modeled system with more equation parameters. In the next few paragraphs the application to soil-plant integrated modeling is addressed, again using two model approaches: the empirical and the optimal.

One procedure for the strategy for constraining parameters is to fit the results from one approach to the other via constant parameters in simulation time. For example, the results from the optimal approach computation can be fitted to the results from the empirical approach and vice versa. For this process, first, the empirical approach is computed using a constant *a'* parameter according to Equation 2.1; then the optimal approach results are computed searching for the *a/b* parameter into the Equation 2.2 to fit empirical results. The opposite would be now to search for the *a'* parameter to fit optimal results. As a first attempt, the use of literature reported values for the parameters *a'* and *a/b* are used to get the main differences between both methods. Further exploration is tested searching best parameters either in the optimal and empirical approach.

Another procedure that can be performed when using this strategy is to match the empirical and optimal results by varying the parameters for each time step. One option is to compute the empirical approach results using an *a'* constant-in time parameter while computing the *a/b* parameter from the optimal approach for each time step to get empirical results. Another option is to get optimal results using an *a/b* constant-in time parameter and get *a'* varying in time to match the optimal values. The computation of each of the time steps for the *a'* and *a/b* parameters is based on Equation 2.5 and Equation 6 respectively as indicated below,

$$a' = \frac{[c_i - \Gamma][g_s - g_o]}{A_n(\Psi_L, c_i) f_v(\Psi_L)} \qquad [\ 2.5\ ]$$

$$\frac{a}{b} = \frac{V_{cmax}}{A_n} \left[\frac{\partial E'}{\partial c_i} - \frac{E'}{A} \frac{\partial A_n}{\partial c_i} \right]^{-1} \frac{\partial A_n}{\partial c_i} \qquad [\ 2.6\ ]$$

As stated by the general formulation of the strategy, Equation 2.5 and Equation 2.6 correspond to the Π^A_k and Π^B_p inverse model equations in the case of parameters *a'* and *a/b*. The relationship between the *a'* and *a/b* parameters is explored by comparing results from both approaches while simultaneously varying these parameters. This exercise is an extension of the first fitting procedure. The first procedure of fitting searches for the fittest parameters; however, the second procedure compares the model results with fixed parameters. The next section provides more detailed information on the computational implementations used to solve the system of equations shown in this section.

2.3 Computational Implementations

In this section, the computational implementation of the system of equations of Section 2.2 is presented. The system of equations for both approaches, the empirical and the optimal, are linked to the soil moisture balance equation and to meteorological input variables. To ensure this general condition for the study, the algorithmic formulation developed is based on the use of a known Land Surface Model (LSM): The Distributed Hydrological Soil Vegetation Model (DHSVM) enhanced by Xu (2013) to include geothermal and geochemical processes of pyrite oxidation, which Xu (2013) called the Hydro Thermal Geochemical Model (HTGCM). LSM models are capable of executing all the computations for soil moisture and meteorological conditions while providing the capability of linking plant physiological variables to soil and hydrological processes in an integrated manner (Wigmosta et al. 2002; Wigmosta et al. 1994).

The computational implementation of the system of equations requires modifications to the original DHSVM-HTGCM code. Such modifications include: a) Links between new and old variables and b) new sub-modules in the original codes of the DHSVM-HTGCM. For instance, in the DHSVM-HTGCM code the algorithms for the empirical and optimal approaches need to be implemented within the sub-module of evapotranspiration. This means, for example, that it is necessary to transform the soil moisture variable computed inside DHSVM-HTGCM into water soil potential using Clapp and Hornberger (1978) equations. Further explanation of DHSVM-HTGCM coding modifications is provided in Subsection 2.3.4.

Section 2.3 contains four parts: First, the empirical approach algorithm implementation is presented. This algorithm is based on Luo et al. (2013), where carbon assimilation and evapotranspiration are computed as the empirical equation for stomata conductance constrains the variables.

Second, the optimal algorithm is shown as a numerical solution of the system of equations 2.3 and 2.4, the equilibrium equation and the optimality condition equation for the water leaf potential Ψ_L and CO_2 in-leaf concentration *ci*. The third part contains the modeling strategy for constraining parameters and the fourth part, the adjustments and modifications of the DHSVM-HTGCM model are explained.

2.3.1 Empirical Approach Algorithm

According to Luo et al. (2013), the numerical solution for the system of equations (Equation 2.1 and Equation 2.4) uses the bisection method to find the water leaf potential Ψ_L that makes carbon assimilation and carbon diffusion equal. The water leaf potential defines simultaneously stomatal conductance on carbon diffusion and a factor function on carbon assimilation represented by the equilibrium equation (Equation 2.4).

The algorithm code has a main loop containing four steps: 1) computation of evapotranspiration following the plant hydraulics-water transport model through a trial value for water leaf potential; 2) calculation of stomata conductance using the inverse and adjusted Penman-Monteith model with the evapotranspiration value computed in step 1; 3) use of a coupled equation linking the Ball-Barry-Luening BBL model and carbon diffusion to get the carbon concentration in-leaf *ci*; and 4) use of the Farquhar-Collatz complete model to determine carbon diffusion and carbon assimilation. The loop is considered completed once carbon diffusion and carbon assimilation are equal.

The condition for carbon diffusion to be equal to assimilation has a percentage tolerance of 1% but it could be as low as computationally possible. In this study the difference between the carbon assimilation and carbon diffusion values is reduced by conducting a finite number of iterations using the bisection method.

2.3.2 Optimal Unit Cost Function Algorithm

The numerical search of the minimum cost function using c_i and water leaf potential Ψ_L uses the solution of the system of equations (Equation 2.3 and Equation 2.4), which constrains the equilibrium-constraint equation and the optimal condition equation.

The system of equations (Equation 2.3 and Equation 2.4) is solved by a main, or outer, loop and a second, or inner, loop within the main loop, as shown in Figure 7. The purpose of the main loop is to determine the c_i variable by computing the optimal Equation 2.3 through its derivates to get the minimum cost function value. The inner loop calculates the water leaf potential Ψ_L using the ci value from the main loop. The calculations are based on the equilibrium equation (Equation 2.4), which is a similar procedure to that used in the empirical algorithm.

As with the empirical algorithm, the water leaf potential is found when the carbon assimilation and carbon diffusion are equal. Unlike the empirical algorithm, however, the BBL equation is not used in the optimal approach. The main loop is completed by computation of the detailed components of the derivates for the optimality equation and finally the condition for the minimum cost.

As a condition for the minimum cost for each tested c_i value, the bias for the optimality equation is computed and the minimum value for this deviation defines the optimal point for all variables. Another way to get the optimal point is direct computation of the unit cost using the variables from the equilibrium equation-water leaf potential loop and choosing the minimum cost along the c_i values tested. It is worth mentioning that there is an important constraint along the searching for the optimal values: the maximum feasible c_i. The equilibrium equation (Equation 2.4) is the main condition used along the testing of c_i values in searching for the minimum unit cost. However, if there is a point where it is not possible to find a stomata conductance (and its correspondent water leaf potential) that makes carbon assimilation and carbon diffusion equal, then this limit c_i value is the maximum feasible point to preserve the equilibrium equation.

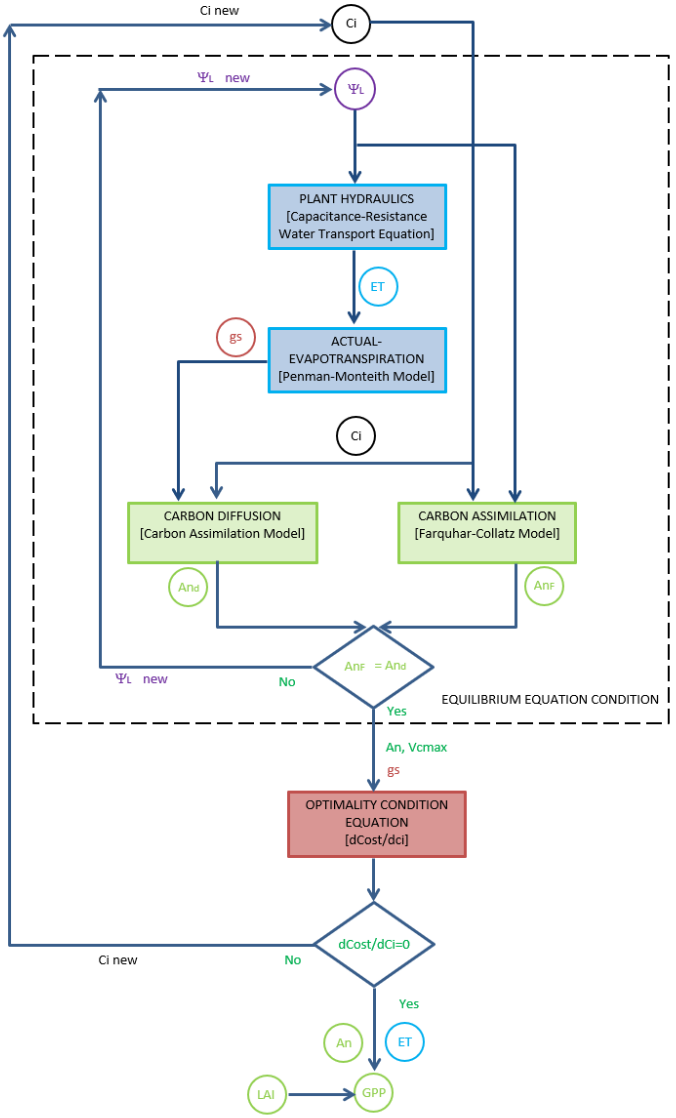

Figure 7 Scheme of optimal approach algorithm for the solution of the system of equations of section 2.2.3. The algorithm stars with initial values for c_i and Ψ_L in the upper portion of the scheme. The workflow moves downward solving for E, g_s, carbon assimilation and carbon diffusion as the equilibrium equation (Equation 2.4) and finally solving the optimality equation (Equation 2.2 or Equation 2.3) in the outer iteration loop on c_i.

2.3.3 Constrained Optimal Algorithm

The modeling strategy to constrain the parameters involves computing the optimal approach under a constant *a/b* parameter to match empirical values varying the *a'* parameter in BBL equation. In addition, two conditions are imposed within the algorithm of optimal approach: 1) on the physical limitation of stomata conductance values and 2) on the reported valid values for the *a'* parameter of the BBL equation.

The algorithm has three phases (Figure 8): i) the optimal computation as it is described above in subsection 2.3.2, with a double condition on the minimum cost that verifies the limit value for the computed stomata conductance in the outer c_i loop. This means that the minimum cost also has also stomata conductance values below the physical limit; ii) the computation of the equivalent *a'* parameter according to Equation 2.5 and the condition of the verification of this value under the reported literature limit. If *a'* parameter value is valid, the computed optimal results are used. If *a'* parameter is not valid, the computation of the c_i loop is carried out up to the point at what the *a'* parameter is verified as valid; and iii) the computation of the empirical approach algorithm using the computed *a'* from the second phase in order to match the optimal and empirical results.

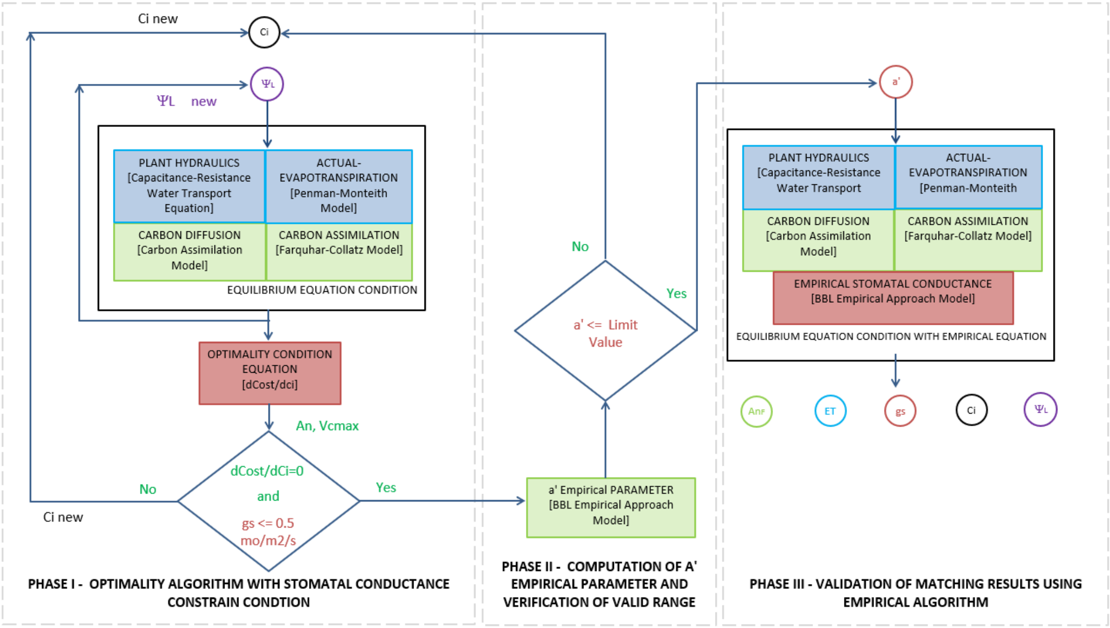

Figure 8 Scheme of the algorithm of the modeling strategy for constraining parameters applied to the optimality and empirical approaches. The workflow begins in the phase I with the optimality algorithm, moves with phase II of computing *a'* and finally phase III with use of the empirical algorithm.

2.3.4 Coding Adjustments in DHSVM-HTGCM for the Evapotranspiration Module

In this subsection, the required adjustments for more comprehensive physiological computations in the DHSVM-HTGCM are presented. The need for this comprehensive computation within DHSVM is mainly justified in the calculation of the Leaf Area Index (*LAI*) and the Gross Primary Productivity (*GPP*). The original DHSVM accounts for *LAI* as an input in the configuration file. However, *LAI* is not computed inside DHSVM. The *GPP* is not computed at all in the original DHSVM, but it is a main input for the carbon and nitrogen biochemical cycles model.

All the arrangements in the code are focused on the evapotranspiration module of the DHSVM model. In general, we had to include all the new physiological variables inside the evapotranspiration module although the original DHSVM could compute stomatal conductance using an empirical approach other than the BBL used in this study. The inputs included in the arranged evapotranspiration module are the resistance parameters R_p, and C_p of the plant to be used in the capacitance-water transport model and the soil water potential, Ψ_s, based on hourly soil moisture and derived from (Clapp and Hornberger 1978)'s equations. Other conventional inputs in the optimality algorithm, such as solar radiation, shortwave radiation, vapor pressure deficit and air temperature, are already inputs in DHSVM, so we use these within the code without changes. The evapotranspiration module first estimates the potential evapotranspiration; then it goes through the vegetation layers assigning transpiration values. We modify this structure to compute the overall evapotranspiration using the optimality algorithm and distribute the values over the layers. Finally, we add a daily accumulative variable for evapotranspiration and a spatial redistribution that later follows the biogeochemical model configuration, shown in Chapter 3.0.

On the main module, we added the required variables to enable printing of the results and a code line for a daily accumulation of *GPP* as the hourly carbon assimilation is computed.

2.4 Geometrical and Conceptual Analysis of the Models

We can analyze the solutions of the systems of equations (Equation 2.1 and Equation 2.4) and (Equation 2.3 and Equation 2.4) and the effects of the multiple constraints, including of water limited conditions, and atmospheric and soil hydrology interactions on the physiology plant variables, through the geometry of the curves of the equations and its conceptual implications. The process of analysis goes from simple to complex curves interactions among the equations. All the curves and intersection points correspond to an instant or one-time step under the external soil or meteorological conditions. First, we build the evapotranspiration model curves, combining the Penman-Monteith equation with the plan hydraulics model (capacitance-resistance water transport model). Then we analyze the equilibrium equation using carbon diffusion and carbon assimilation using the respective model curves. We next analyze the integrated empirical approach with the evapotranspiration and equilibrium constraints. The optimal approach is studied under the same linking of evapotranspiration and equilibrium constraints. Finally, we add more complexity to the analysis involving the variation in climate conditions to each approach and how they operate together under the modeling strategy explained in Section 2.2.4.

2.4.1 Constraining and Linking Evapotranspiration Models

This section explains how the Penman-Monteith equation and the capacitance-resistance equation (ASCE 2000; Daly et al. 2004; Luo et al. 2013) of plant hydraulics are combined in terms of the water leaf potential Ψ_L and stomata conductance g_s. The details of the equations are explained in Appendix A. This part is the first step in the complete analysis of the empirical and optimal approaches models. The first geometry curves analyzed are the Penman-Monteith equation for evapotranspiration E with stomatal conductance g_s, shown in Figure 9.

Figure 9 shows how evapotranspiration increases as stomatal conductance increases up to a limiting potential evapotranspiration value E_{pot}. The shape of the model curve is a hyperbola with a half value out of potential evapotranspiration linked to a constant stomatal conductance of $g_{so,1} = C_2/C_3$. The values for C_1, C_2 and C_3 are given by the Penman-Monteith Equation as shown in Appendix A (Equation A2): $C_1 = [S\,R + \rho_a\,C_p\,g_a\,D]\,LAI$; $C_2 = \rho_w\,\lambda_w\,\gamma_w\,g_a$; and $C_3 = \rho_w\,\lambda_w\,[S + \gamma_w]$

LAI. with $E_{pot} = C_1/C_3$. Based on these parameters, we can say that an increase of vapor pressure deficit *D* implies an increase of potential evapotranspiration and therefore all the possible values of actual transpiration for any stomatal conductance value. The plane [*D x E*] in the left part of the Figure 9 shows a type of linear relationship between vapor pressure deficit *D* and the potential evapotranspiration E_{pot-1} and E_{pot-0}, according to the C_1 coefficient in Penman-Monteith Equation, but not the actual non-linear relationship. Similarly, as radiation increases, the model curves move upward, representing an increase in actual transpiration for any stomatal conductance value.

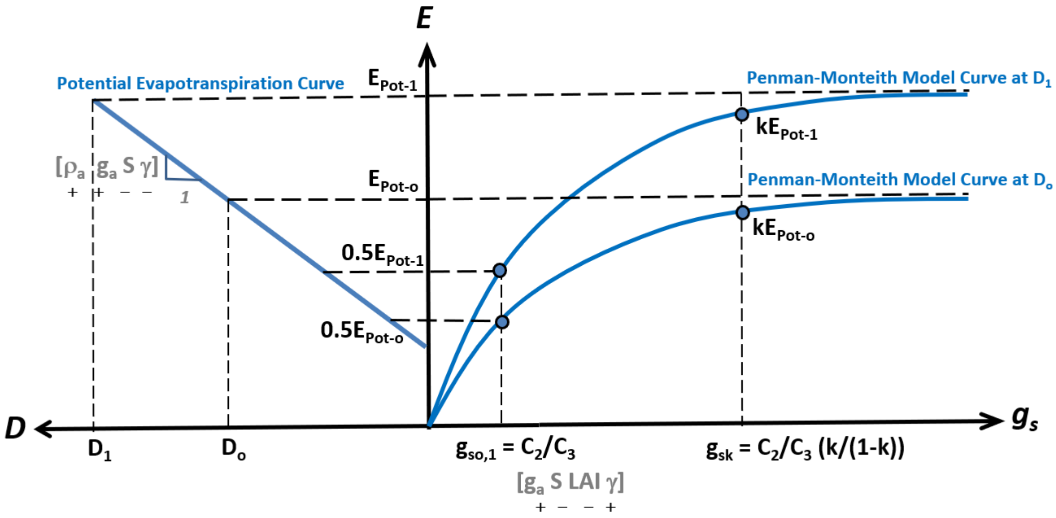

Figure 9 Penman-Monteith Model Curve and its variations under changing parameters. Left side: linear relationship between vapor pressure deficit *D* and potential evapotranspiration E_{pot}. Right side: the different evapotranspiration curves.

One special feature derived from the geometric shape of the model curve is that for any fraction $k = E/E_{pot}$ of the potential evapotranspiration kE_{pot-1} or kE_{pot-0}, we can get the corresponding stomatal conductance in terms of the fraction as $g_{sk}=C_2/C_3\ (k/(1-k))$. The derivation of this relationship between stomatal conductance and the potential evapotranspiration fraction is based on the Penman-Monteith Equation in terms of the fraction *k*. This formulation is an important result that we can use to extrapolate any stomatal conductance value based on the fraction *k* of the potential evapotranspiration.

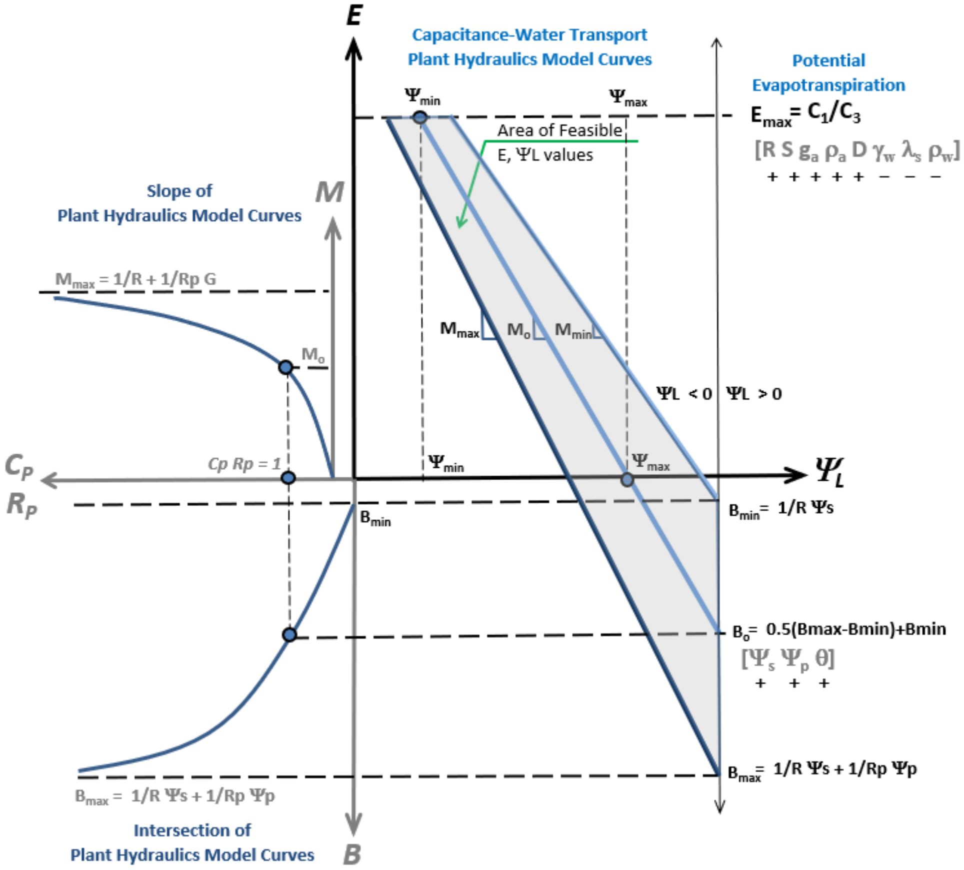

Figure 10 Plant Hydraulics or capacitance-resistance water transport model curves. Right plane [Ψ_L x E] shows the numerical model and its feasible area in shaded blue. Left planes [C_p x B] and [C_p x M] are the curve of the parameters of the numerical model in the right side plane.

We can also analyze the geometry of water-transport plant hydraulics model curves. The graphical representation of the model is derived from the linear relationship in Equation A7 in Appendix A. In Figure 10, we are showing three planes: a) Plane [Ψ_L x E] for the relationship between water leaf potential and transpiration E; b) Plane [C_p x B] for the relationship between C_p and B as the intercept parameter of the plant hydraulics model; and c) Plane [C_p x M] for the relationship between Cp and M as the slope parameter of the plant hydraulics model. The intercept $B = 1/R\ \Psi_s + 1/R_p\ \{(C_pR_p/\Delta t/(1+C_pR_p/\Delta t))\,\Psi_p\}$, and slope $M = \{-1/R+1/R_p\ [1/(C_pR_p/\Delta t)-1]\}$ are derived from Equation A7 in Appendix A.

The final equation from the numerical method to get E in time (see Appendix A, Section A.1 and Section A.2) is a linear relationship between water leaf potential Ψ_L and transpiration E. The slope M of this line is an inverse function of the total plant resistance and the capacitance resistance, as shown in plane [C_p x M] as a hyperbola curve relationship. The intercept B is also an inverse function of the resistances and direct function of the soil potential and storage potential. A simple analysis of variation of capacitance resistances and/or soil potential shows the feasible set of solutions (feasible area), shown in blue in Figure 10. Looking at the feasible area we can see that as soil moisture increases, the soil water potential increases and so the intercept B, which promotes a shift of the line E, Ψ_L to higher values of E.

The next analysis consists of integrating the Penman-Monteith curve and the plan hydraulics curve to get the relationship between water leaf potential Ψ_L and stomatal conductance g_s. The first step is to turn the plane [g_s x E] and to turn the plane [Ψ_L x E] left to be in the same E axis as shown in Figure 11. If we preserve all the features from Figure 9 and Figure 10 in the curves and bring them into the Figure 11, we can extrapolate the evapotranspiration line through the curves to the corresponding stomatal conductance g_s and water leaf potential Ψ_L values to build the Plane [Ψ_L x g_s] curve. Hence, the Ψ_L x g_s curve shows that as water leaf potential increases the stomatal conductance decreases to zero. Also, as the water leaf potential approaches the minimum value, the stomatal conductance goes to an unbounded value. This particular feature of the stomatal conductance explains much of its behavior within the optimal computations, as is shown in subsequent sections. Based on the situation when the Penman-Monteith curve is coordinated with the plant hydraulics line, we can infer that stomatal conductance has the tendency to be much higher as the solution's points approach to potential evapotranspiration values.

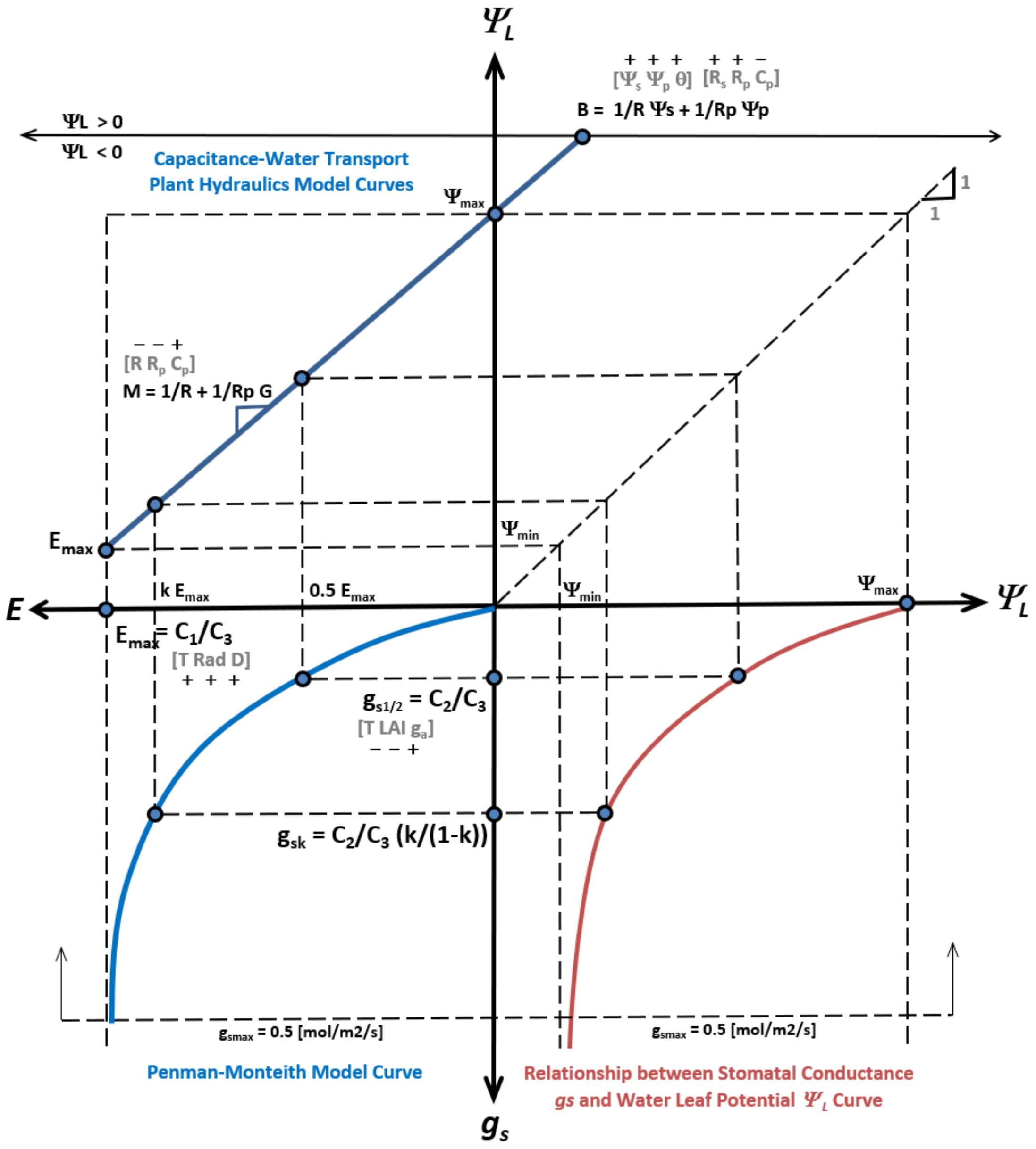

Figure 11 Integration of Plant Hydraulics and Penman-Monteith models curves. Plane [E x g_s] shows the Penman-Monteith curve. Plane [E x Ψ_L] shows the capacitance-resistance water transport or plant hydraulic model. Plane [Ψ_L x g_s] shows the resulting relationship between Ψ_L and g_s.

The next analyses are focused on the carbon assimilation models and how they are combined with the evapotranspiration curves to generate the equilibrium equation condition.

2.4.2 The Equilibrium Equation – Constraining Carbon Assimilation Models

The first step in the construction of the equilibrium equation (Equation 2.4) is analysis of the carbon assimilation model (G. D. Farquhar et al. 1980)-(Farquhar-Collatz model) using its curves interacting with the function factor $f(\Psi_L)$ to incorporate the effect of water stress on the biogeochemical rate of carbon assimilation A_n. In Figure 12, we combine the Rubisco-limited Farquhar curve model with the water stress function factor. In plane [c_i x A_n] the carbon assimilation model is shown with its hyperbola curve. The maximum value of the curve is given by the maximum carbon assimilation capacity V_{cmax}. At half of the maximum rate $V_{cmax}/2$, the corresponding CO_2 in-leaf concentration is $c_i = K^* + 2\Gamma$, which corresponds to the level of CO_2 saturation concentration within the leaf. The value of c_i at this point is dependent on the temperature and this point explains how carbon assimilation curves moves right along the c_i values as temperature increases. The effect of the water stress function on carbon assimilation is shown in plane [c_i x Ψ_L] where one can see how the decrease of water leaf potential impacts linearly the maximum carbon assimilation. The final result of this combined effect is the spectrum of carbon assimilation curves on the plane [c_i x A_n] from zero to V_{cmax}.

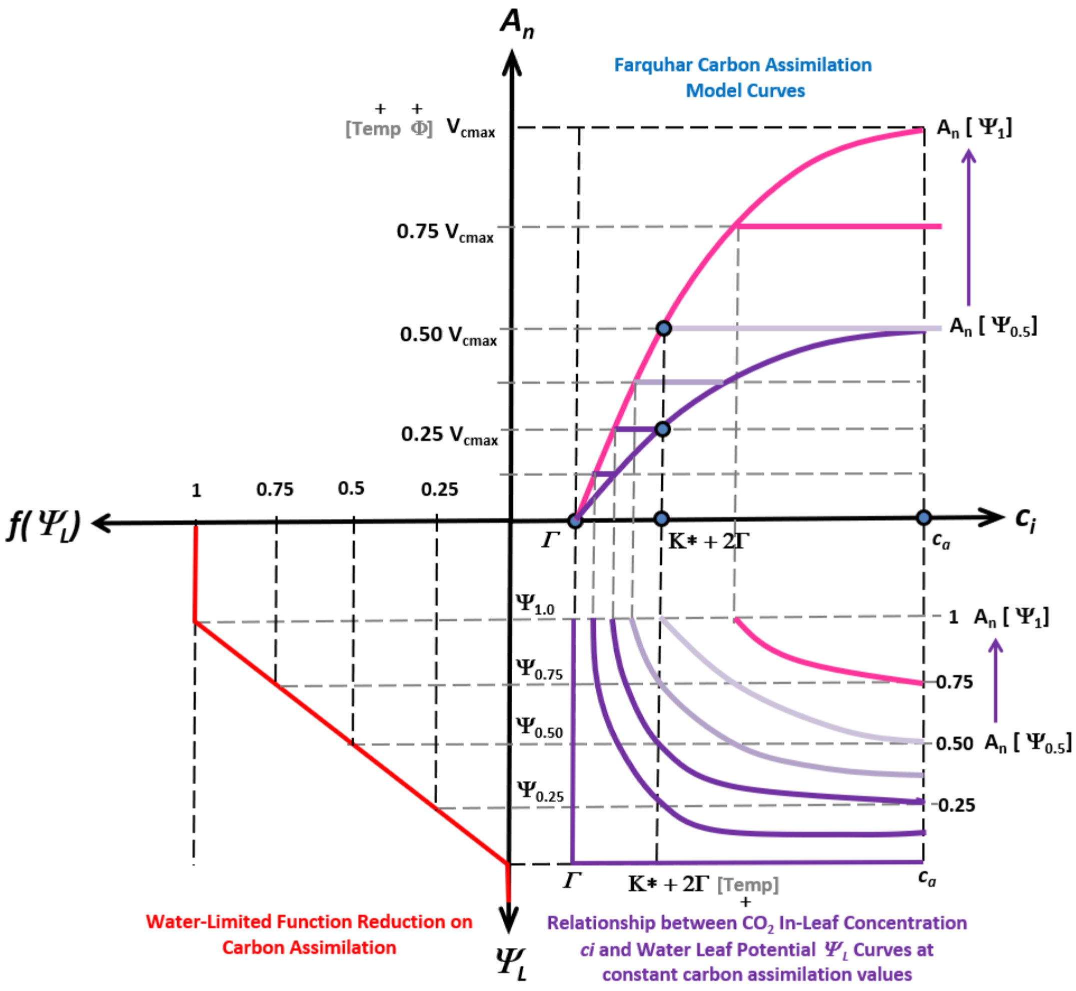

Figure 12 Carbon Assimilation Farquhar (Rubisco-Limited) Model Curve constrained by water limited condition factor.

The next analysis focuses on the carbon diffusion equation model. Carbon diffusion represents the availability of carbon uptake by plants. The linear equation that explains the supply of carbon to the plant is shown in Figure 13. The negative slope of the line is the total equivalent stomatal conductance $G_s = g_s\, g_{ab} /(g_s + g_{ab})$. Based on the equation and its graphical representation in Figure 13, we can establish the maximum capacity of carbon assimilation as $g_{ab}(c_a-\Gamma)$. This capacity links the atmospheric conditions to the physiological processes in plants. Furthermore, this curve allows us to understand the possible effect of temperature and atmospheric carbon changes on the carbon assimilation supply to plants. With higher temperatures the carbon compensation point Γ moves to the right, subtracting from the maximum capacity of carbon assimilation. Higher atmospheric carbon concentration is able to increase the maximum carbon availability while the conductance maintains its value.

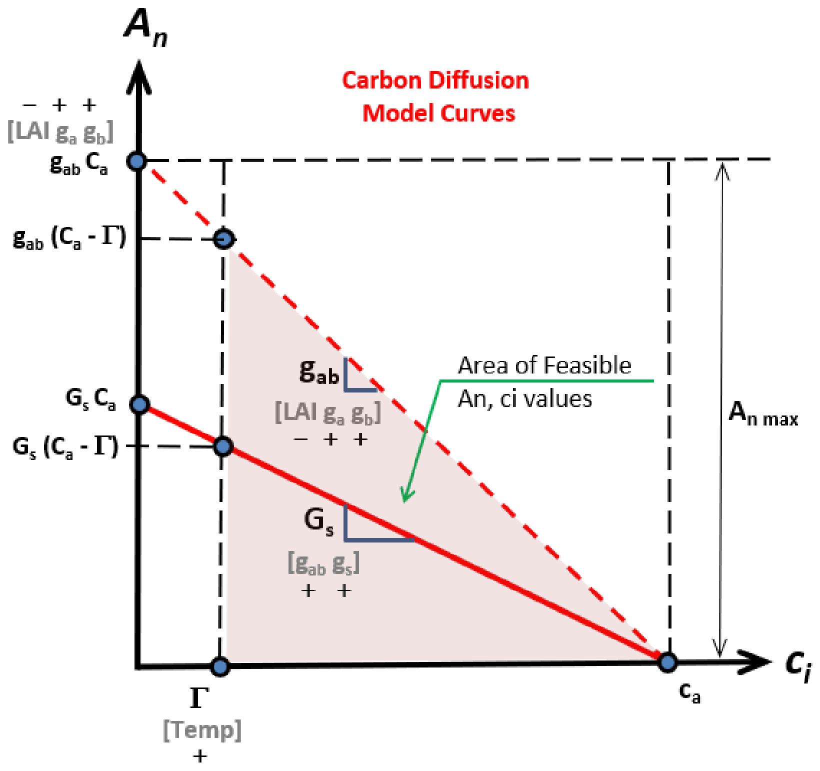

Figure 13 Carbon Diffusion Model curve constrained by atmospheric-boundary-layer conductance g_{ab}. The shaded area shows the feasible area of values where it is possible to have equilibrium conditions points.

The equilibrium condition (the supply-demand constraint according to Leuning (1995) is that in which carbon assimilation (demand) meets carbon diffusion (supply). In terms of our graphical analysis, an instant or one-time step equilibrium is the point where the carbon assimilation curve intersects the carbon diffusion line in the plane [c_i x A_n], as it is shown in Figure 14.

The equilibrium point marked in green, is considerably low in comparison to the maximum capacity of carbon availability g_{ab} $(c_a-\Gamma)$. In figure 14, the shaded area shows the set of points where it is actually possible to have equilibrium points given conditions of temperature and radiation. This type of area is shown in Figure 18-d) as the cloud of points that correspond to equilibrium points in a simulation of a typical year.

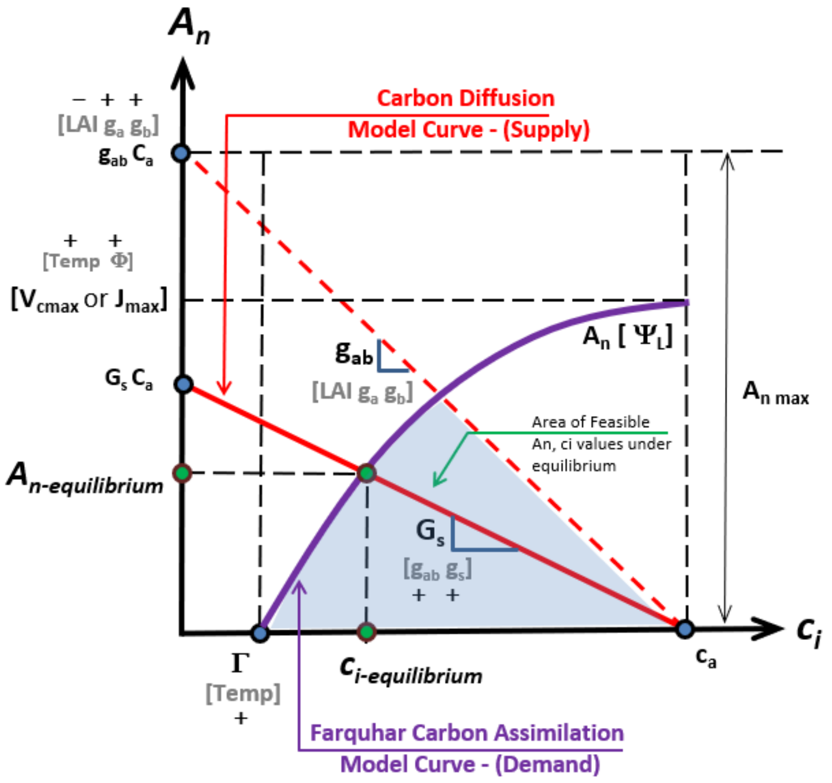

Figure 14 Equilibrium condition with constraining carbon diffusion as supply and carbon assimilation as demand for carbon by plants. Blue shaded area represents the set of points where the equilibrium points are possible for a range of temperature and radiation conditions.

Finally, we develop an integrated analysis of the equilibrium condition and its interaction with evapotranspiration models as discussed in subsection 2.4.1. Figure 15 shows the results of integrated analysis into one group of plots and the resulting equilibrium condition curve in the plane [c_i x Ψ_L]. Bringing in the two planes [E x Ψ_L] and, [E x g_s] from Figure 11 and arranging them on the plane [c_i x A_n] from Figure 14, we build the equilibrium condition curve from the carbon assimilation and carbon diffusion intersections points. For low values of CO_2 in-leaf concentration $c_{i-1/2}$, the carbon assimilation curve marks a low value $A_{n-1/2}$ (plane [c_i x A_n] in Figure 15). The carbon diffusion line in red closest to axis c_i (plane [c_i x A_n] in Figure 15) that intersects the carbon assimilation curve, has the smallest slope $G_{s1/2}$. This point of intersection at $c_{i-1/2}$, $A_{n-1/2}$ corresponds to lowest value of stomatal conductance $g_{s-1/2}$ because of lowest slope $G_{s1/2}$. The lowest stomatal conductance tracks the Penman-Monteith curve at $0.5E_{max}$ evapotranspiration value (plane [E x g_s] in Figure 15). The $0.5E_{max}$ transpiration value defines the green point of water leaf potential in the plant hydraulics line (plane [E x Ψ_L] in Figure 15). Finally, the intersection of the water leaf potential described before and the initial $c_{i-1/2}$ indicates the green point of equilibrium in the plane [c_i x Ψ_L]. The exercise of tracking all the points of intersection of carbon assimilation and carbon diffusion in the plane [c_i x A_n] through the planes [E x g_s] and, [E x Ψ_L] to [c_i x Ψ_L] builds the equilibrium curve in the plane [c_i x Ψ_L]. One of the conclusions we draw from this final curve is that it has a limit value at point red c_{i-max} where it is the highest CO2 in-leaf concentration that makes possible the equilibrium. The maximum equilibrium is due to the maximum slope G_{smax} of the carbon diffusion dashed red line in plane [c_i x A_n]. The maximum slope G_{smax} is defined by the atmospheric-boundary layer conductance g_{ab}. This limitation is already implemented as a constraint in the computational implementation of both the empirical and the optimal approaches. Another conclusion to be made from Figure 15 is that under the equilibrium condition the c_i increases as Ψ_L decreases close to a limit value, which corresponds to higher values of stomatal conductance.

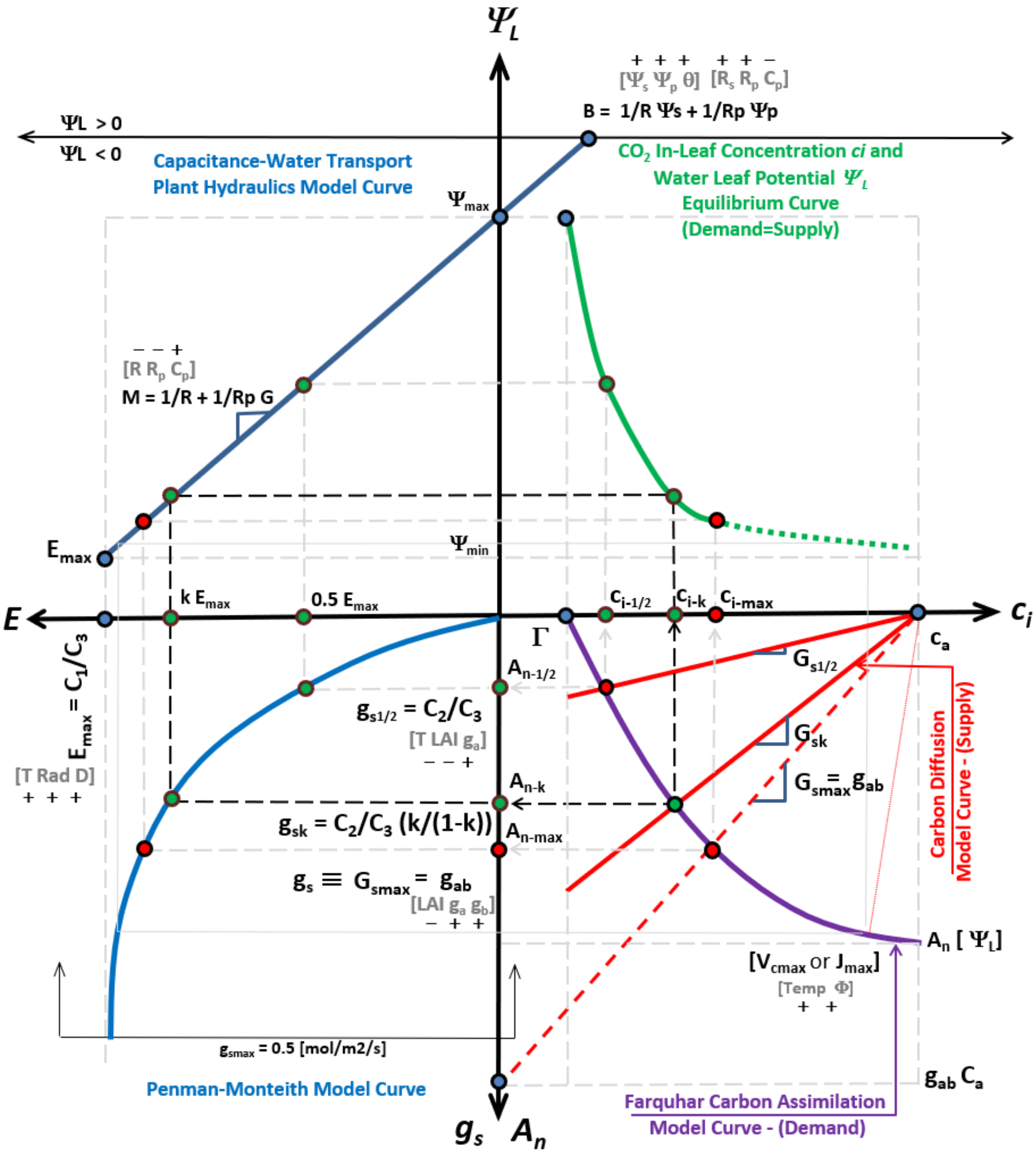

Figure 15 Equilibrium condition curve in plane [c_i x Ψ_L] in green and the corresponding points in the evapotranspiration-water transport curves. Plane [E x g_s] shows the Penman-Monteith curve. Plane [E x Ψ_L] shows the water transport-plant hydraulics line. Plane [c_i x A_n] shows the equilibrium condition from the intersection between carbon assimilation and carbon diffusion curves. Stomatal conductance g_s and carbon assimilation A_n are actually on different axes though sharing one here for graphical purposes.

2.4.3 Empirical Approach Integrated Model

Figure 16 represents the integration of the equilibrium condition and the empirical approach. In this particular case the plane [c_i x A_n] is replaced by the plane [c_i x g_s] to build the empirical equation curve. Equation 2.1 can be simplified by assuming water-stress factor functions $f(\Psi L)$ and $f_v(\Psi_L)$ close to 1. Also, we can use the Rubisco-limited version of the Farquhar biogeochemical model for carbon assimilation in terms of V_{cmax} to get a simpler representation of the empirical equation. Then the empirical equation for stomatal conductance can be expressed as $g_s = a'\ V_{cmax} / (c_i + K^*)$. This equation describes a decreasing curve with c_i in the plane [c_i x g_s] (this plane has g_s axis increasing downward). The projection of different points from this curve through the Penman-Monteith curve and plant hydraulics curve to the plane [c_i x Ψ_L] builds an increasing curve indicating that for the empirical approach as c_i increases, Ψ_L increases. Therefore, the intersection point P between the equilibrium condition curve in green and the empirical curve in white-red (plane [c_i x Ψ_L] in Figure 16) is the solution of the system of equations described in Section 2.2. This solution shows that if a' parameter increases the empirical stomatal conductance curve in plane [c_i x g_s] increases (the curve moves downward in the plane) and as a consequence the point of solution P moves right in the plane [c_i x Ψ_L]. The increase of a' implies that the empirical method's solutions approach to higher values of stomatal conductance, evapotranspiration and CO_2 in-leaf concentrations follow the equilibrium curve shown in green.

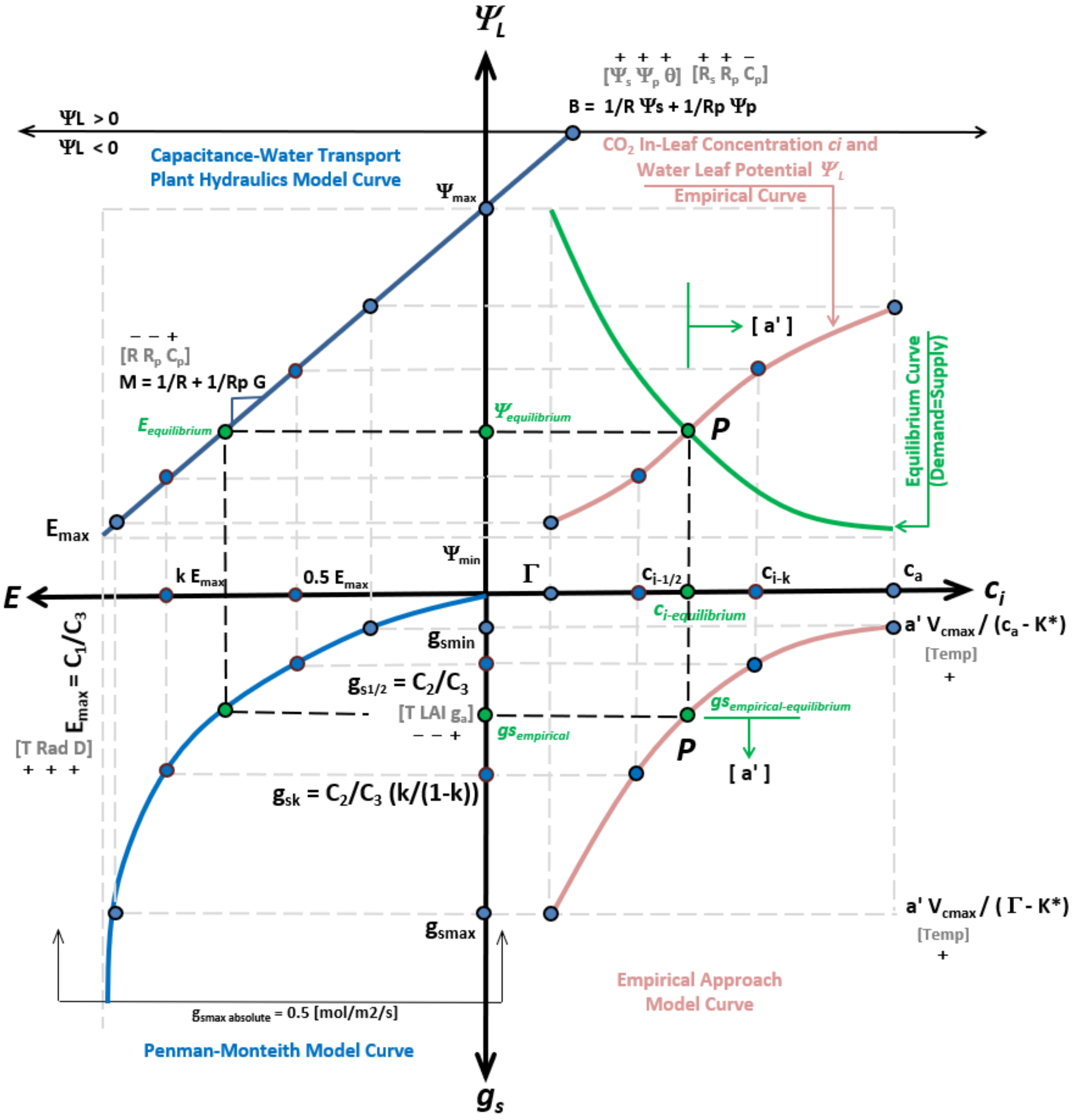

Figure 16 Integrated curves of evapotranspiration, plant hydraulics, carbon assimilation, carbon diffusion and equilibrium curve to empirical approach curve. The point *P* represents the solution of the two variable c_i, Ψ_L system of equations described in Section 2.2. The curve in the $c_i - g_s$ plane is a BBL equation (Equation 2.1) representation where carbon assimilation A_n changes.

The following analysis seeks to answer the question of how the empirical solution changes under two climate conditions (Figure 17): hot and cold. The system of planes and curves is similar to that in Figure 15 for the equilibrium condition, but in this case, we are adding the plane [c_i x g_s]

of Figure 16 in the bottom right of the planes to represent the climate changes in the empirical equation for stomatal conductance. Following the analysis explained in Figure 16, we add two types of curves in Figure 17: cold climate curves and hot climate curves. The higher curves in plane [E x g_s] Penman-Monteith evapotranspiration and in plane [c_i x A_n] carbon assimilation correspond to hot climate, because the curve parameters depend positively on the temperature and radiation. The lower curves represent the cold climate conditions. The equilibrium condition curve in plane [c_i x Ψ_L] for higher temperatures (hot climates) is the lower one. The cold equilibrium condition curve is the higher one in the plane [c_i x Ψ_L]. With higher temperatures the V_{cmax} is higher and the empirical curves are higher. According to the empirical curve analysis in Figure 17, the corresponding curve in plane [c_i x Ψ_L] for hot climates is the lower one. Then, the intersection points P_L (for low temperatures-cold conditions) and P_H (for high temperatures-hot conditions) between low and high empirical and equilibrium curves show the differences between cold and hot climate conditions for the empirical approach results. For cold climates carbon assimilation, evapotranspiration and stomatal conductance are lower than those for hot climates. However, the CO_2 in-leaf concentration $c_{i\text{-}empirical\text{-}low}$ is higher for cold conditions than that for hot climates, $c_{i\text{-}empirical\text{-}high}$. This is due to the shape of the equilibrium conditions curve in plane [c_i x Ψ_L] and the overlap in the empirical curves when changing from cold to hot climates when the values of stomatal conductance are the same. The general behavior predicted by the graphical analysis in Figure 17 can be seen in the numerical simulations for the Mather site in Figure 18. The cloud of points in Figure 18 for each plane similar to that in Figure 17 represents equilibrium points computed from a transient simulation over a year with real input forcing data for temperature, radiation and vapor pressure deficit. The red points correspond to temperatures below 15 ^oC and the blue points to temperatures over 15 ^{o}C. The multiple lines shown in Figure 18-a), are result of the variations in soil moisture computed by the simulation.

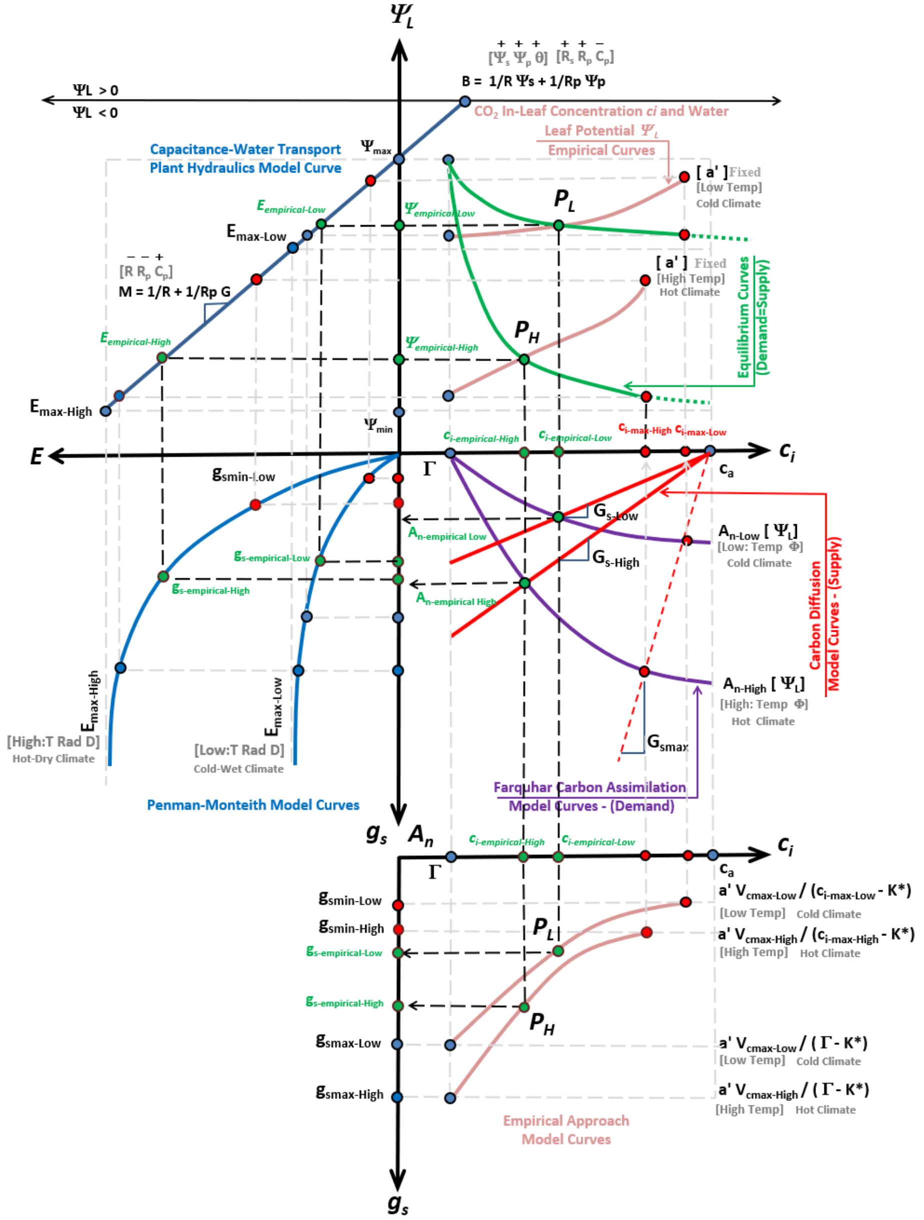

Figure 17 Variation of the empirical approach solutions under cold and hot climate conditions. Planes [c_i x Ψ_L] , [E x g_s] , [E x Ψ_L] and [c_i x A_n] are similar to those in Figure 15. Plane [c_i x g_s] right bottom is similar to that in Figure 16.

Finally, Figure 18, serves as a consistency verification of the analysis used in this section to understand the behavior of the empirical approach's solutions for different climate conditions. The cloud of points in each plot represents points of solutions under a simulation of a year at the Mather site. The similarity between the simulation points and the graphical analysis shows the coherence of the analysis developed. The next analysis focuses on the integrated optimal approach model.

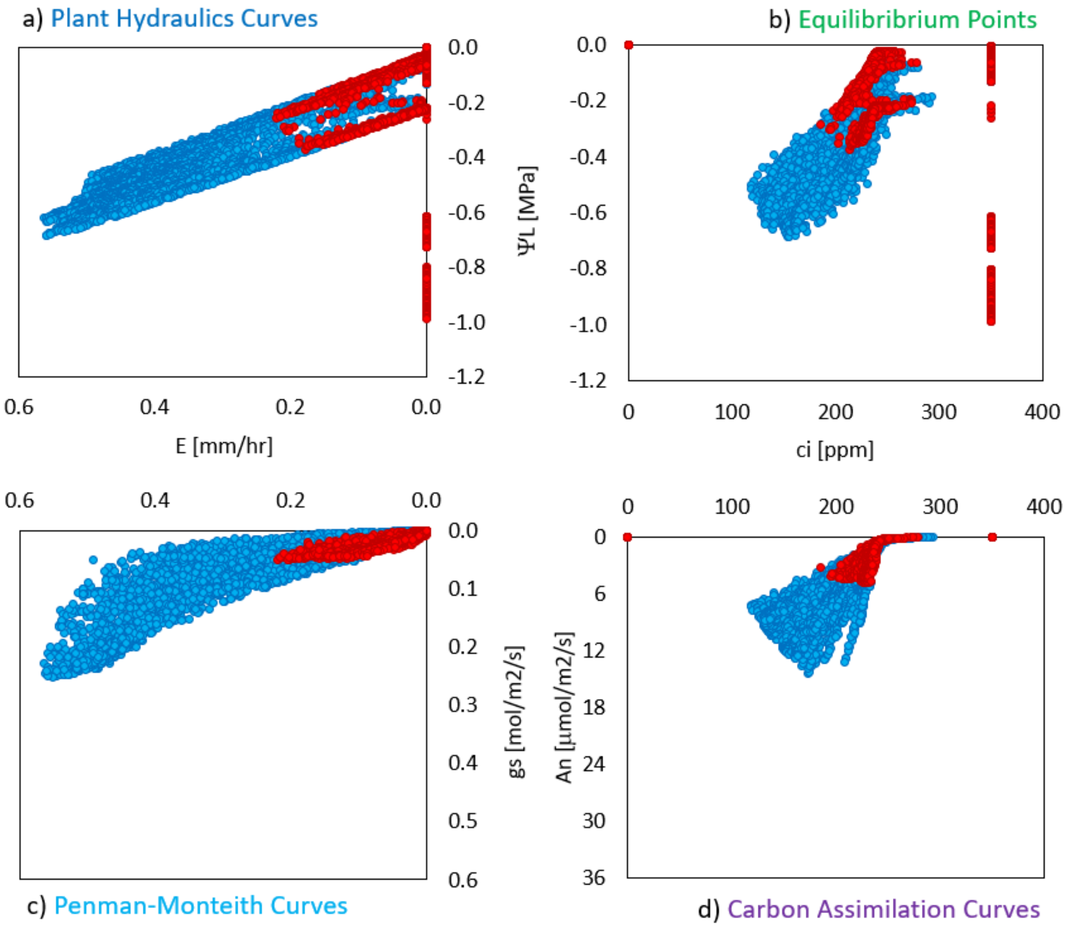

Figure 18 Empirical approach simulation data for carbon assimilation, evapotranspiration, stomatal conductance, CO_2 in-leaf concentration and water leaf potential at the Mather site, following the same axis arrangement as the graphical analysis in Figure 17.

2.4.4 Optimal Prentice Approach Integrated Model

The analysis of this approach begins with the unit cost function and how it operates to search for the optimal results. Figure 19 illustrates the total unit cost function and the minimum cost point *P* at $c_{i\text{-}optimal}$ where the two-component cost derivatives are equal $dCost_a/dc_i$ =-$dCost_b/dc_i$. The search for the minimum cost tests at each c_i value involves identifying what stomatal conductance value g_s makes the carboxylation derivative curve equal to the transpiration derivative curve. The resulting curve is an optimal condition relationship between c_i and g_s. As the g_s becomes higher, the carboxylation derivative curve goes lower and the intercept to the transpiration derivative becomes lower, as shown in plane [c_i *x* $dCost/dc_i$]. This is possible because the transpiration derivative curve is fixed, not depending on g_s. In normal conditions, transpiration unit cost component is expected to increase with c_i or the transpiration derivative is expected to be positive. In our numerical exploration of this component, the use of coordinated Penman-Monteith with plant hydraulics evapotranspiration produces decreasing transpiration unit cost in some cases, as explained in Subsection 2.6.2.

In Figure 20, the optimal condition curve can be projected from the plane [c_i *x* $dCost/dc_i$] to the plane [c_i *x* Ψ_L] through the evapotranspiration curves. The resulting curve shows that as c_i increases the stomatal conductance g_s decreases and the water leaf potential Ψ_L increases. In this integrated system of curves similar to the one for the empirical approach in Figure 16, the intersection point *P* between the equilibrium curve in green and the optimal condition curve in magenta represents the solution for the system of equation of the optimal approach. The intersection point *P* moves upward if we increase the optimal parameter *a/b*, because the transpiration derivative curve increases as the *a* parameter increases making the intersection point moves to the left. An increase in the *b* parameter works in the opposite direction moving the intersection point *P* to the right.

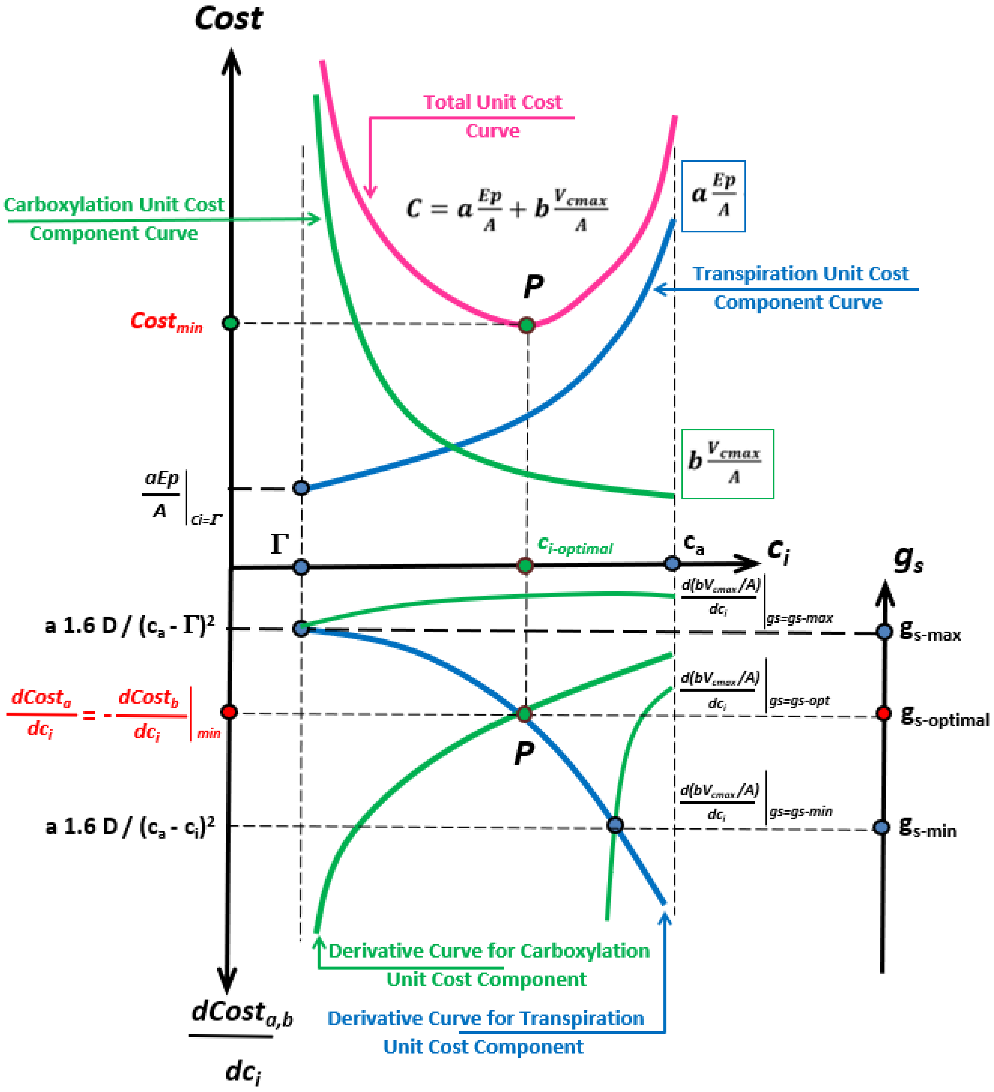

Figure 19 Total unit cost function with the two components: transpiration unit cost and the carboxylation unit cost. The Plane [c_i x $dCost/dc_i$] shows the derivatives for the unit cost components and the condition for minimum cost at intersection point *P*. The corresponding stomatal conductance is shown on external axis.

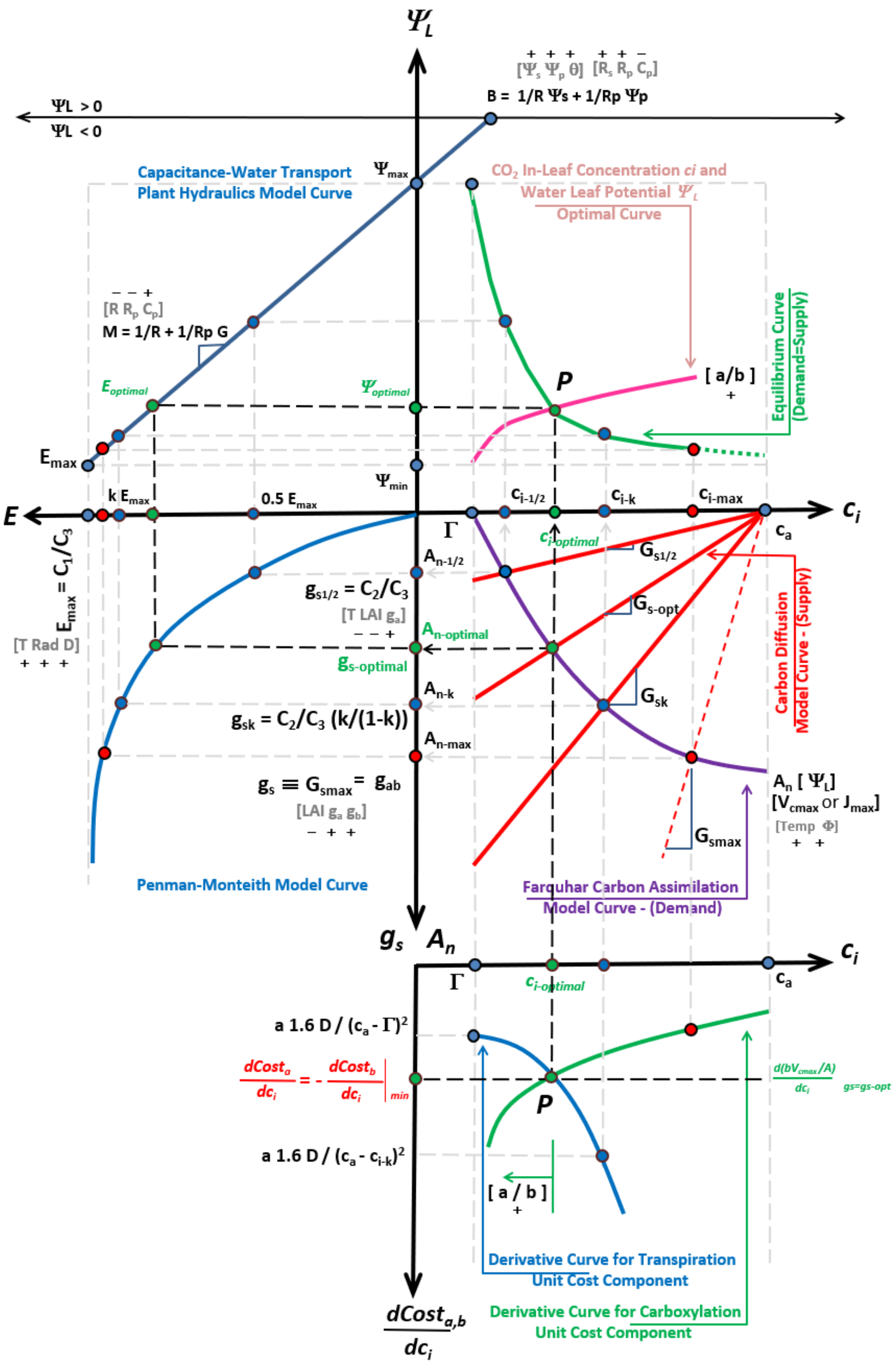

Figure 20 Integrated curves of evapotranspiration, plant hydraulics, carbon assimilation, carbon diffusion and equilibrium curve to the optimal approach curve. The point *P* represents the solution of the two variable *c_i*, *Ψ_L* system of equations described in Section 2.2.

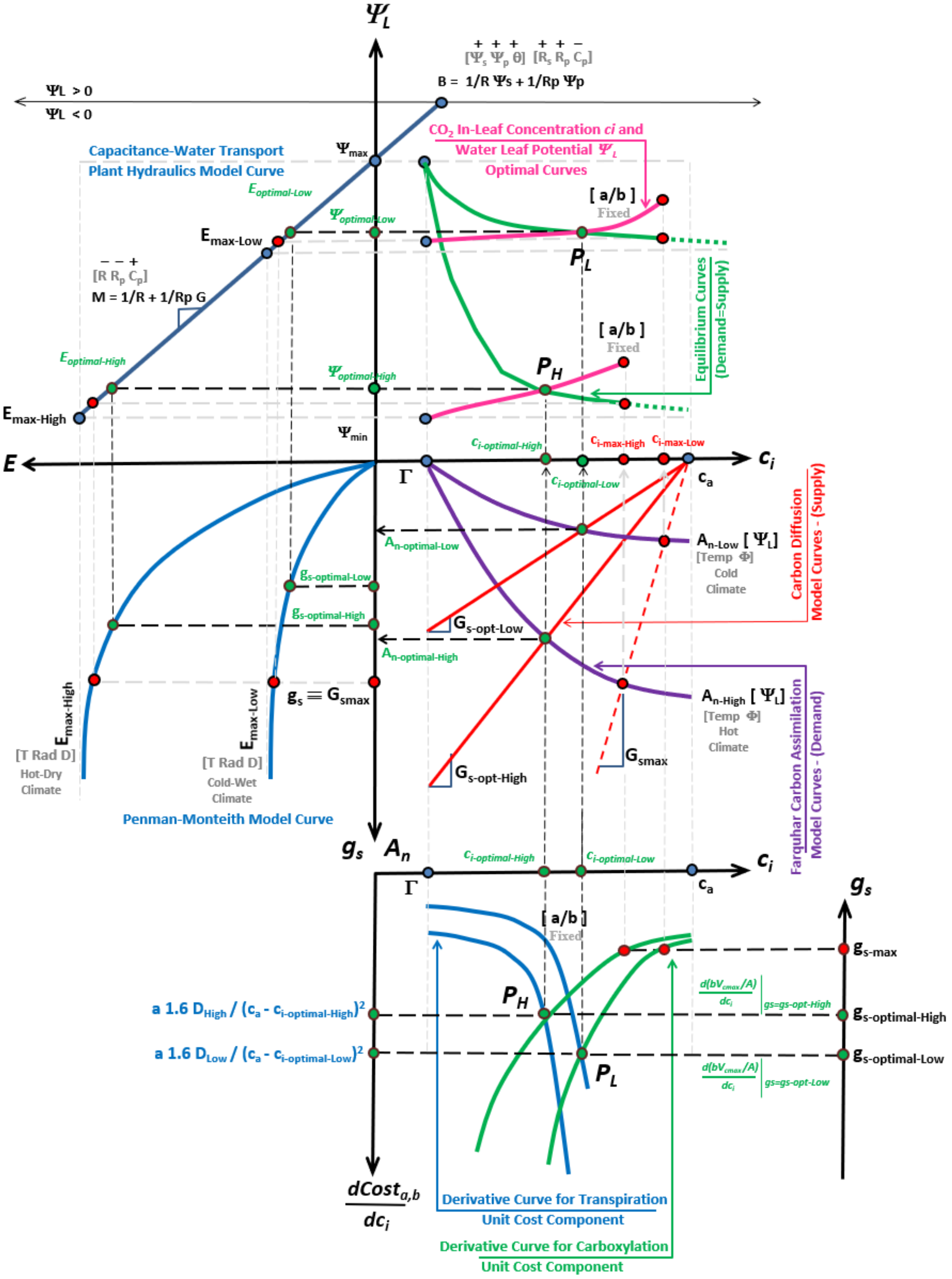

Figure 21 Variation in the empirical approach solutions under cold and hot climate conditions. Planes [c_i x Ψ_L], [E x g_s], [E x Ψ_L] and [c_i x A_n] are similar to those in Figure 15. Plane [c_i x $dCost/dc_i$] right bottom is similar to the one in Figure 20.

To sum up the optimal approach analysis, we can build an integrated system of curves with the two climate conditions in a similar fashion to that presented earlier for the empirical approach. In this case, the behavior of the solutions P_L and P_H (intersection points for cold and hot climates respectively) is similar to that in the empirical approach. Figure 22 portrays the coherence between the system of curve analyses and the numerical simulation. The cloud of points illustrates the shapes of the geometrical curves to be as the analysis predicted.

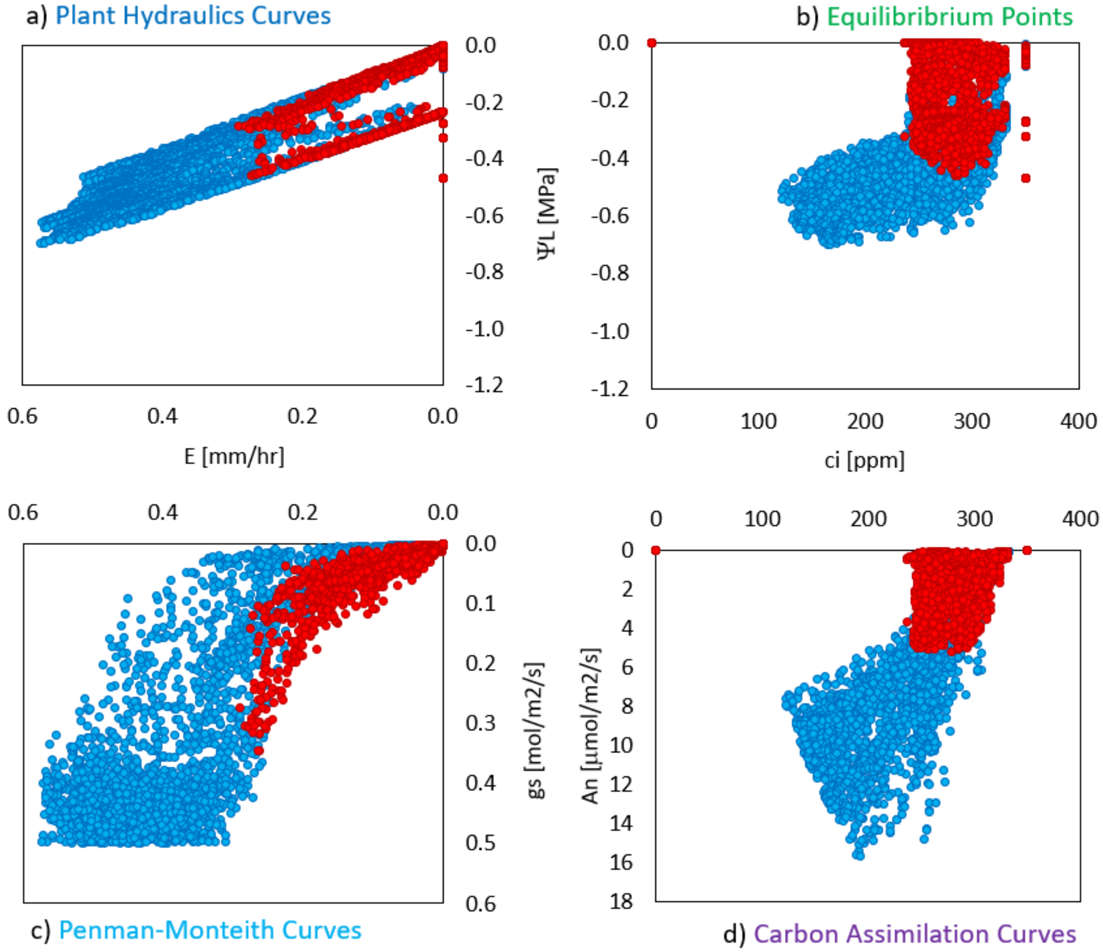

Figure 22 Optimal approach simulation data for carbon assimilation, evapotranspiration, stomatal conductance, CO_2 in-leaf concentration and water leaf potential a the Mather site, following the same axis arrangement the graphical analysis in Figure 21.

2.4.5 Empirical and Optimal Approaches Correspondences as Modeling Strategy

As a main part of the implementation in this study of the vegetation into the pyrite oxidation, the modeling strategy of constraining parameters is analyzed in this subsection using the general formulation in section 2.2.4. Figure 23 shows the intersection points P_L and P_H (cold and hot climates) for the optimal approach constrained by the empirical approach. Following the general formulation of the strategy, both methods intersect at the same points with a common constraint of the equilibrium curve. In this case, the empirical parameter a' is raised to move the empirical curves to the right to match the optimal curves. The movement of the empirical curves to intersect the optimal points explains the increase of a' in the hot climates.

A conceptual explanation of how the coupled optimal-empirical works according to Modeling Strategy is shown in Figure 24. Along the c_i, Ψ_L equilibrium curve, it is possible that empirical a', or upper boundary, limits the Optimal point. There are three conditions that constrain optimal approach by the empirical equation or by stomatal conductance: 1) Optimal c_i is lower than the corresponding empirical a' and g_s limiting ones; 2) when the g_s upper value is lower than the optimal and empirical parameter a' corresponding values then the g_s upper value determines the optimal-empirical results; 3) if the a' upper valid value point in the c_i, Ψ_L curve is lower than g_s and optimal, then the final result is given by the empirical equivalent a' value.

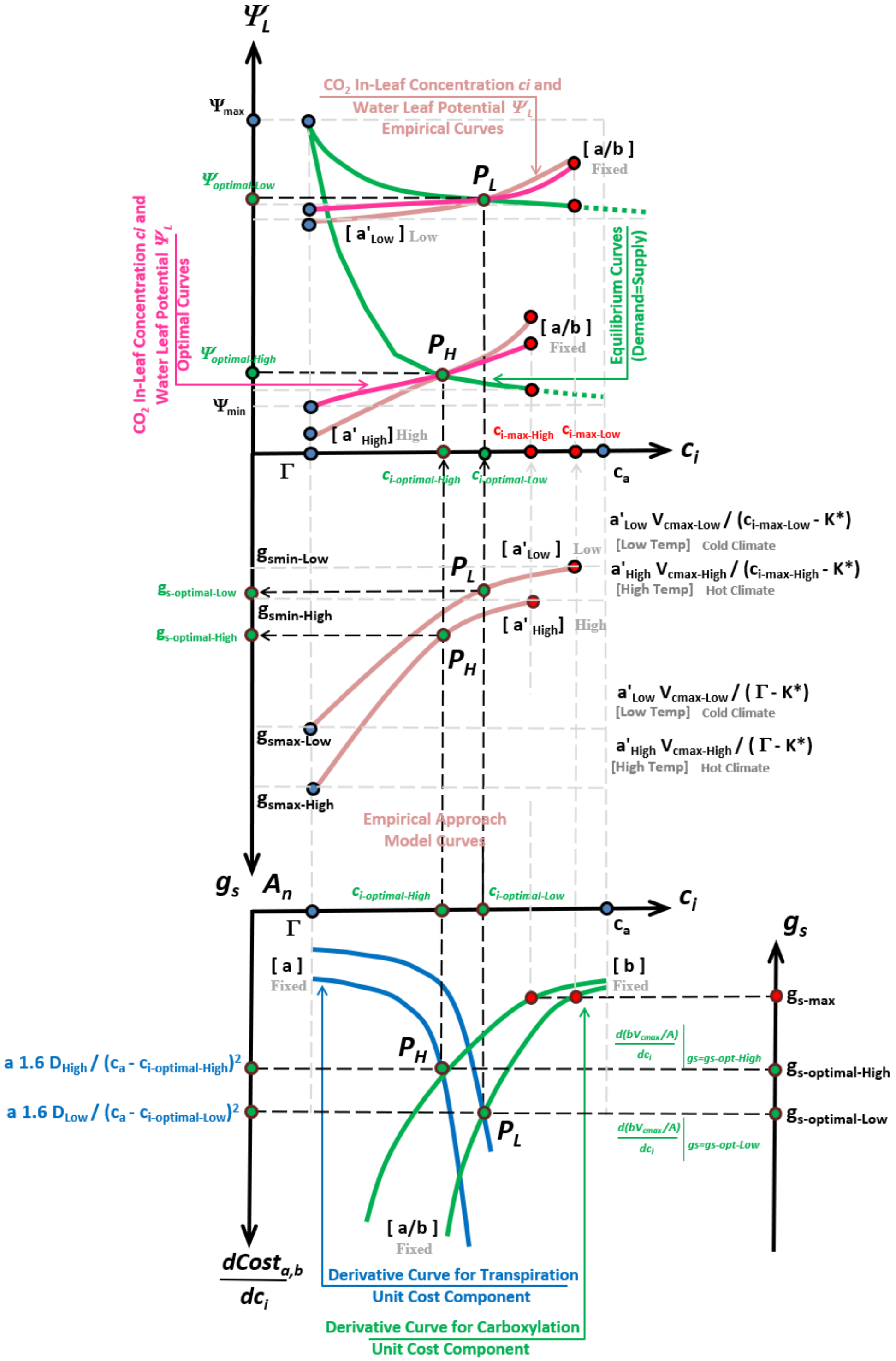

Figure 23 Correspondence between the optimal and empirical approach solutions under different climate conditions. Plane [c_i x g_s] shows the empirical approach curve. Plane [c_i x $dCost/dc_i$] shows the derivative conditions for the optimal approach.

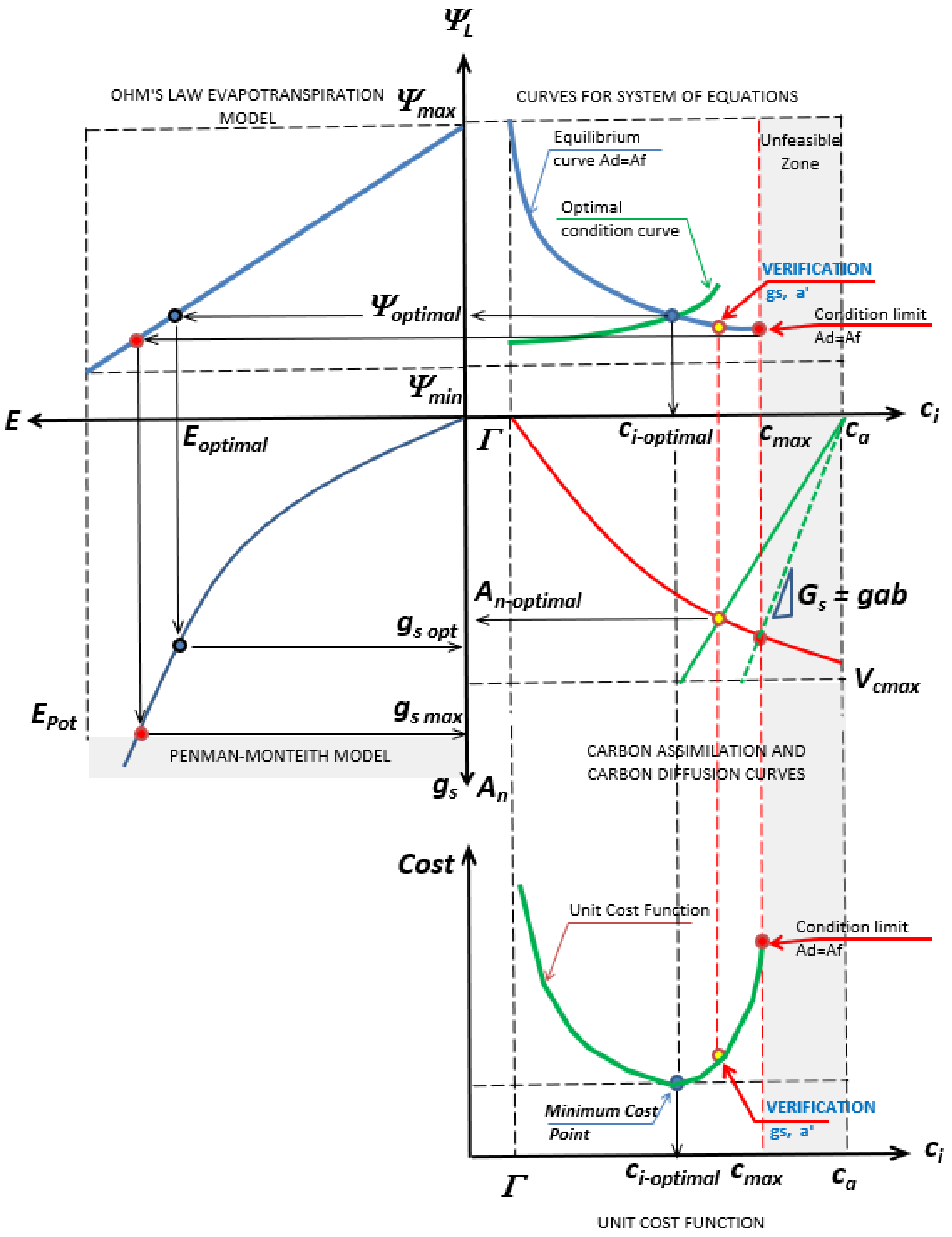

Figure 24 Geometrical and conceptual explanation of the three possibilities for optimal coupled with empirical approach: a) optimal by minimum cost point; b) constrained by g_s and *a'*; c) constrained by condition limit carbon diffusion = carbon assimilation. Plane [E x g_s] shows the Penman-Monteith curve. Plane [E x Ψ_L] shows the water transport-plant hydraulics line. Plane [c_i x A_n] show the equilibrium condition from the intersection between carbon assimilation and carbon diffusion curves. Plane [c_i x *Cost*] corresponds to unit cost function.

In summary, the geometrical analysis of the integrated empirical and optimal approaches leads us to the following main conclusions: a) both approaches have similar behavior in terms of the variation in carbon assimilation, evapotranspiration and CO_2 in-leaf concentration. However, the stomatal conductance computed by the optimal approach tends to be higher than that computed by the empirical approach; b) the CO_2 in-leaf concentration has the tendency to be lower in warmer climate conditions due to the shape and the slope of the equilibrium condition curve; and c) the use of the modeling strategy of constraining the optimal approach to be equal to the empirical approach makes that the empirical parameter *a'* has to be higher in hot conditions than in colder conditions. The variation in the empirical parameter *a'* is explained by the movement of the empirical curve to get the solution points given by the optimal approach from the left to right, thereby raising *a'* values.

The next section explains the validation exercise of both the empirical and the optimal approaches to observed data.

2.5 Model Calibrations

After the conceptual analysis presented in section 2.4, the comparison of simulations to observed data is necessary to calibrate the empirical and optimal models for the specific sites in this study.

2.5.1 Model Parameters

The models used in this study have a variety of parameters that depend on the type of plant, type of ecosystem, atmospheric conditions and soil properties. The range used in the validation of the parameters is given by the literature for each specific process model (Table 1). There are parameters for the empirical approach in the BBL equation (Leuning 1995; Medlyn et al. 2011; Miner et al. 2017), parameters for the unit cost function according to Prentice et al. (2014) and Wang et al. (2017), parameters for the physiological process of transpiration (Daly et al. 2004; Katerji et al, 1986; Luo et al. 2013; Tuzet et al. 2003) and parameters for soil properties from the soil moisture dynamics equation (Clapp and Hornberger 1978).

The parameters in empirical Equation 2.1 are obtained from regressions analysis over different species and environmental conditions (Leuning 1995); we develop a methodology in (outlined in Appendix B) to use the maximum empirical parameter *a'* as a bounded value for the optimal-empirical coupled approach. Values for the residual stomata conductance g_o, are 0.01mol/m2/s to 0.03 mol/m2/s (Daly et al. 2004; Leuning 1995; Luo et al. 2013; Tuzet et al. 2003). The factor function of water leaf potential Ψ_L in Equation 2.1 has two shape parameters, Ψf and *Sf*, for the sigmoidal function. These parameters serve to determine the maximum and minimum water soil potential, with values of 3.2 MPa and 1.9 MPa, respectively. The empirical parameter *a'* in the Equation 2.1 has a valid accepted range from 2 to maximum 250, depending on the plant species or ecosystem conditions (Leuning 1995; Medlyn et al. 2011; Miner et al. 2017). For our analysis with the empirical approach we use *a'*=2, and for the optimal-empirical coupled approach we adopt *a'*=17 for the Mather site and *a'*=24 for the Oensingen site, according to the analysis presented in Appendix B and, based on literature species values.

The main unit cost function parameters a and b are related to the cost of respiration for each component (Prentice et al. 2014). The parameter a is the unit cost related to transpiration. Prentice et al. (2014) propose a useful equation and Wang et al. (2017) demonstrate an explicit dependence of a on water viscosity and temperature in. The parameter b, related to carboxylation cost, is suggested by Prentice et al. (2014) and Wang et al. (2017) to be considered constant. The relation a/b (or as defined by Wang et al. (2017) b/a) is considered constant and equals 1/240 at 25^oC under standard conditions.

Among the plant-transpiration process parameters are whole-plant resistance; plan capacitance, C_p with an original value 0.0000026 MPa/m; and Root-Leaf Resistance, R=1/50 m (Katerji et al. 1986). The plant-atmosphere conductance is $g_a = 1/ R_a$ with R_a = 221 s/m (Luo et al. 2016). The Farquhar biochemical model for carbon assimilation (Farquhar 1980) has parameters maximum carboxylation with an initial value of V_{cmax} = 50 μmol/m2/s and K_{O2} = 0.256 mol/mol and J_{max} = 75 mmol/m2/s used in this study. The soil properties used in the soil moisture balance equation are encapsulated in the potential and hydraulic conductance equations parameters according to Clapp and Hornberger (1978).

Table 1 Parameters used in validation for Empirical and Optimal Constrained Approaches

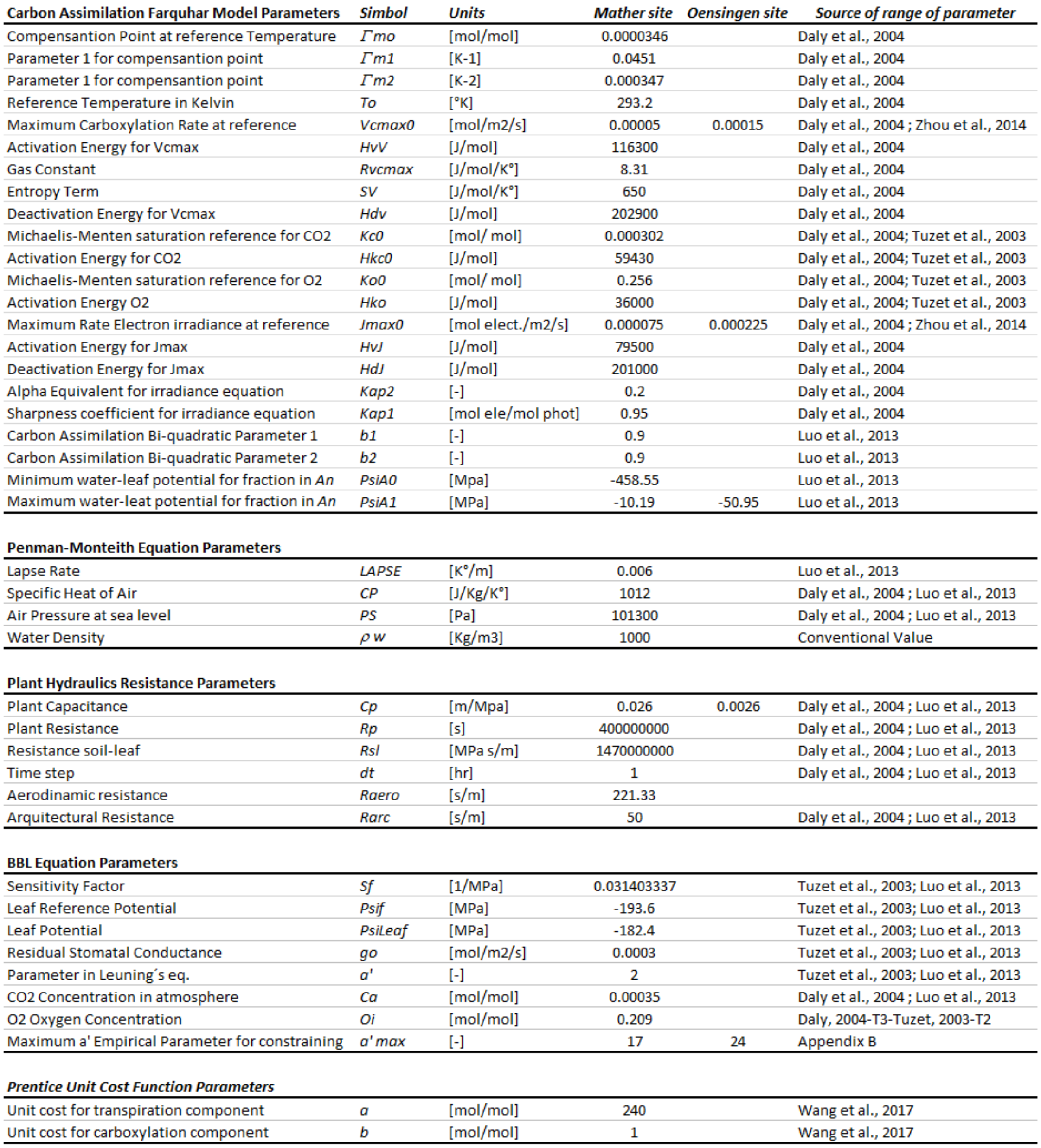

Carbon Assimilation Farquhar Model Parameters	***Simbol***	***Units***	***Mather site***	***Oensingen site***	***Source of range of parameter***
Compensantion Point at reference Temperature	*Γmo*	[mol/mol]	0.0000346		Daly et al., 2004
Parameter 1 for compensantion point	*Γm1*	[K-1]	0.0451		Daly et al., 2004
Parameter 1 for compensantion point	*Γm2*	[K-2]	0.000347		Daly et al., 2004
Reference Temperature in Kelvin	*To*	[°K]	293.2		Daly et al., 2004
Maximum Carboxylation Rate at reference	*Vcmax0*	[mol/m2/s]	0.00005	0.00015	Daly et al., 2004 ; Zhou et al., 2014
Activation Energy for Vcmax	*HvV*	[J/mol]	116300		Daly et al., 2004
Gas Constant	*Rvcmax*	[J/mol/K°]	8.31		Daly et al., 2004
Entropy Term	*SV*	[J/mol/K°]	650		Daly et al., 2004
Deactivation Energy for Vcmax	*Hdv*	[J/mol]	202900		Daly et al., 2004
Michaelis-Menten saturation reference for CO2	*Kc0*	[mol/ mol]	0.000302		Daly et al., 2004; Tuzet et al., 2003
Activation Energy for CO2	*Hkc0*	[J/mol]	59430		Daly et al., 2004; Tuzet et al., 2003
Michaelis-Menten saturation reference for O2	*Ko0*	[mol/ mol]	0.256		Daly et al., 2004; Tuzet et al., 2003
Activation Energy O2	*Hko*	[J/mol]	36000		Daly et al., 2004; Tuzet et al., 2003
Maximum Rate Electron irradiance at reference	*Jmax0*	[mol elect./m2/s]	0.000075	0.000225	Daly et al., 2004 ; Zhou et al., 2014
Activation Energy for Jmax	*HvJ*	[J/mol]	79500		Daly et al., 2004
Deactivation Energy for Jmax	*HdJ*	[J/mol]	201000		Daly et al., 2004
Alpha Equivalent for irradiance equation	*Kap2*	[-]	0.2		Daly et al., 2004
Sharpness coefficient for irradiance equation	*Kap1*	[mol ele/mol phot]	0.95		Daly et al., 2004
Carbon Assimilation Bi-quadratic Parameter 1	*b1*	[-]	0.9		Luo et al., 2013
Carbon Assimilation Bi-quadratic Parameter 2	*b2*	[-]	0.9		Luo et al., 2013
Minimum water-leaf potential for fraction in *An*	*PsiA0*	[Mpa]	-458.55		Luo et al., 2013
Maximum water-leat potential for fraction in *An*	*PsiA1*	[MPa]	-10.19	-50.95	Luo et al., 2013

Penman-Monteith Equation Parameters					
Lapse Rate	*LAPSE*	[K°/m]	0.006		Luo et al., 2013
Specific Heat of Air	*CP*	[J/Kg/K°]	1012		Daly et al., 2004 ; Luo et al., 2013
Air Pressure at sea level	*PS*	[Pa]	101300		Daly et al., 2004 ; Luo et al., 2013
Water Density	*ρ w*	[Kg/m3]	1000		Conventional Value

Plant Hydraulics Resistance Parameters					
Plant Capacitance	*Cp*	[m/Mpa]	0.026	0.0026	Daly et al., 2004 ; Luo et al., 2013
Plant Resistance	*Rp*	[s]	400000000		Daly et al., 2004 ; Luo et al., 2013
Resistance soil-leaf	*Rsl*	[MPa s/m]	1470000000		Daly et al., 2004 ; Luo et al., 2013
Time step	*dt*	[hr]	1		Daly et al., 2004 ; Luo et al., 2013
Aerodinamic resistance	*Raero*	[s/m]	221.33		
Arquitectural Resistance	*Rarc*	[s/m]	50		Daly et al., 2004 ; Luo et al., 2013

BBL Equation Parameters					
Sensitivity Factor	*Sf*	[1/MPa]	0.031403337		Tuzet et al., 2003; Luo et al., 2013
Leaf Reference Potential	*Psif*	[MPa]	-193.6		Tuzet et al., 2003; Luo et al., 2013
Leaf Potential	*PsiLeaf*	[MPa]	-182.4		Tuzet et al., 2003; Luo et al., 2013
Residual Stomatal Conductance	*go*	[mol/m2/s]	0.0003		Tuzet et al., 2003; Luo et al., 2013
Parameter in Leuning´s eq.	*a'*	[-]	2		Tuzet et al., 2003; Luo et al., 2013
CO2 Concentration in atmosphere	*Ca*	[mol/mol]	0.00035		Daly et al., 2004 ; Luo et al., 2013
O2 Oxygen Concentration	*Oi*	[mol/mol]	0.209		Daly, 2004-T3-Tuzet, 2003-T2
Maximum a' Empirical Parameter for constraining	*a' max*	[-]	17	24	Appendix B

Prentice Unit Cost Function Parameters					
Unit cost for transpiration component	*a*	[mol/mol]	240		Wang et al., 2017
Unit cost for carboxylation component	*b*	[mol/mol]	1		Wang et al., 2017

2.5.2 Calibration at the Mather Site using DHSVM

We applied the empirical and optimal-empirical coupled (optimal constrained) approach to the Mather site within the DHSVM-HTGCM model, for a period of Jan-2010 to Dec-2010, using observed *GPP* and *ET* from MODIS-NASA data (Figure 25).

It is valuable to note that the modeling strategy used in this study makes the calibration process more rigid in terms of tuning parameters to fit observed data. This rigidity means that the more sensitive parameters are constrained, at least in terms of range, and it is not possible to use them easily to match computed results to observed data. In consequence, this conditionality of constrained parameters shows the strength of the model in representing observed data, because just from the initial simulations is possible to get very close results to observed ones. Hence, the final refinement to fit the model to observations is to find other parameters with low sensitivity in the final results.

In this particular calibration with the optimal approach constrained by the empirical model to observations at the Mather site, the only parameters used for the final fit were the capacitance of water storage parameter and the upper water leaf potential in the water-limited function on carbon assimilation. The first parameter adjustment, C_p, indicates that water plant storage is greater than for the original parameter and implies less flux of storage in summer seasons. The second parameter adjustment $\Psi_{L\,max}$ shows that the model has a tendency to avoid the effect of water stress conditions under optimal searching.

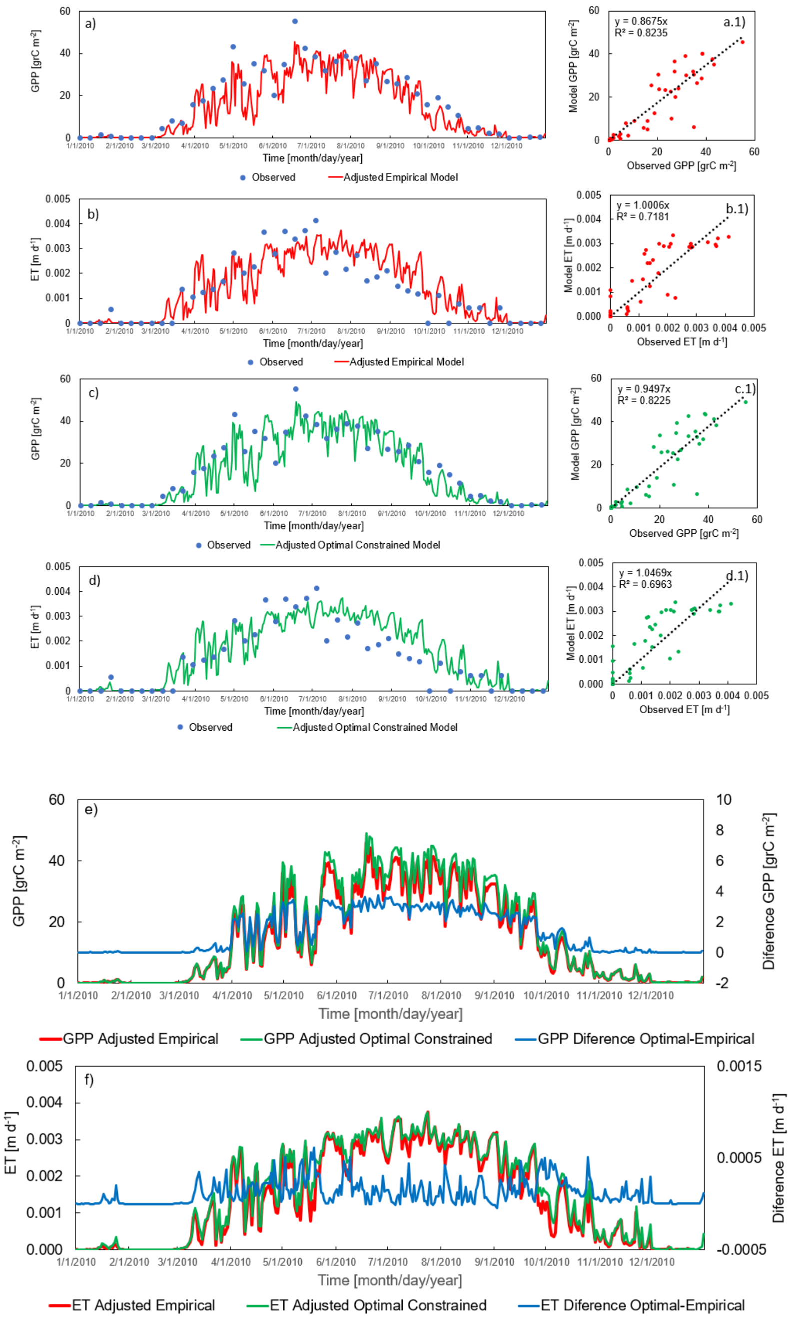

Figure 25 Comparison of modeled results with the observations at Mather site for the year 2010 using the empirical and optimal constrained approaches. a) Gross primary productivity (GPP) using the empirical approach; b) Evapotranspiration using the empirical approach; c) Gross primary productivity (GPP) using the optimal constrained approach; d) Evapotranspiration using the optimal constrained approach. e) Comparison of gross primary productivity of the empirical and optimal constrained approaches. f) Comparison of evapotranspiration of the empirical and optimal constrained approaches.

2.5.3 Calibration at Oensingen-Switzerland Site using DHSVM

Oensingen observed data were also used to compare the empirical and optimal-empirical coupled (optimal constrained) approaches, for a period of Jan-2004 to Dec-2004, in which the observed GPP and ET from MODIS-NASA data were also used. The results are shown in Figure 26. Both models also show fit with observed data.

The adjustments of the model for the Oensingen site were performed using the carbon assimilation parameters and the capacity of water storage parameter. The carbon assimilation parameters were the carboxylation capacity V_{cmax} and the maximum light irradiance capacity J_{max}. The final adjusted values of these two parameters indicate that the fertilization of the type of crop species in the field can explain the high capacity of carbon assimilation. These adjusted carbon assimilation parameters make possible to fit the observed GPP data. The final adjusted value for the water storage parameter indicates highly productivity of the species at the site with a value of $V_{cmax} = 3 * V_{cmaxo}$ and $J_{max} = 3 * J_{maxo}$, three times the original parameter values.

Once we calibrate the models for each site, we can work on them to compare the empirical and the optimal simulation results. The next section shows these comparisons of the empirical and optimal approaches with the implications of the optimal constrained approach.

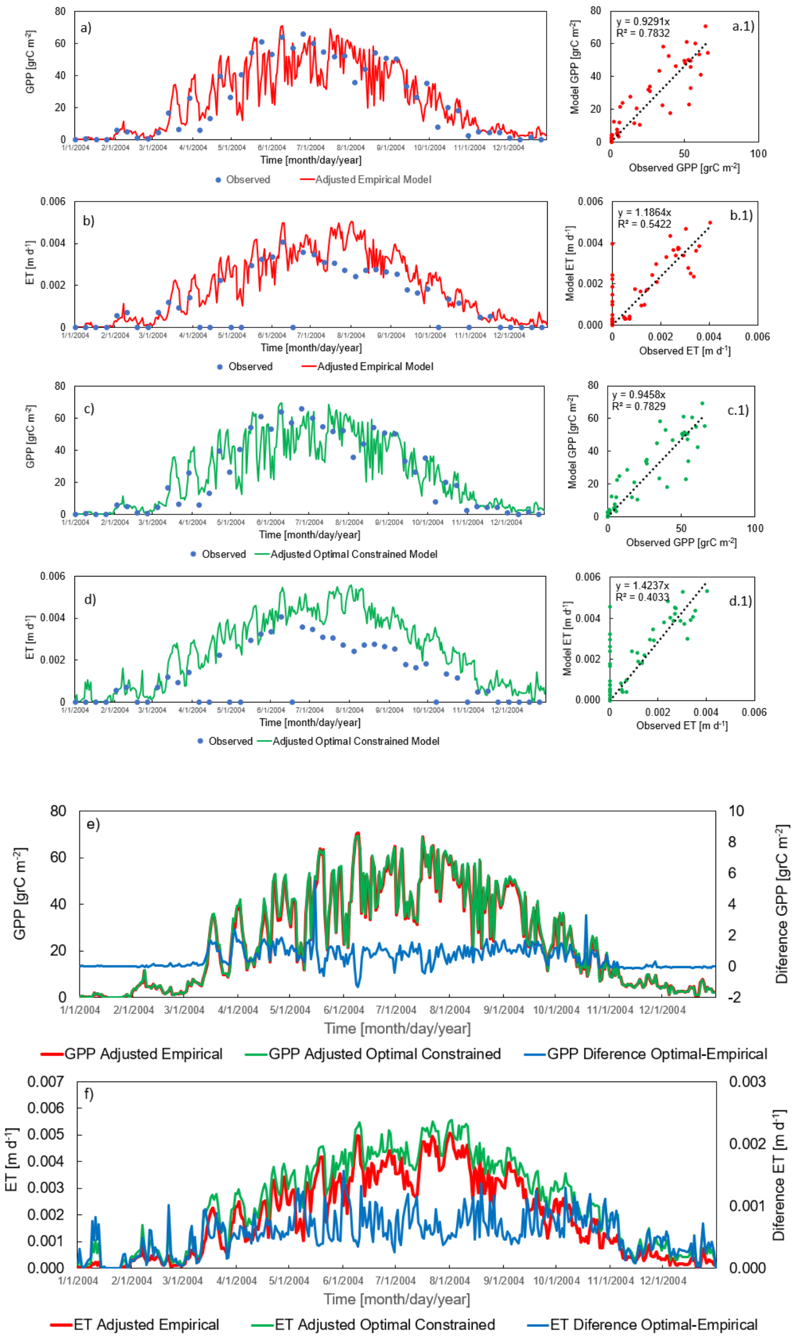

Figure 26 Comparison of modeled results with the observations at the Oensingen site for the year 2010 using the empirical and optimal constrained approaches. a) Gross primary productivity (GPP) using the empirical approach; b) Evapotranspiration using the empirical approach; c) Gross primary productivity (GPP) using the optimal constrained approach; d) Evapotranspiration using the optimal constrained approach. e) Comparison of gross primary productivity of the empirical and optimal constrained approaches. f) Comparison of evapotranspiration of the empirical and optimal constrained approaches.

2.6 Simulations and Analyses

Comparative simulations of the empirical and optimal approaches were developed using the same site conditions, including input on meteorological data, soil types and vegetation parameters. The parameter reduction of computability strategy was used as a basis for the comparative simulations. One purpose of these comparative numerical exercises is to verify the order of magnitude and range of validity of the parameters under the strategy. The comparative simulations aim to establish a general relationship between the empirical and optimal approaches under water-limited conditions using validated soil-plant-atmosphere land surface models. The integration of soil-plant-atmosphere processes implies the modeling extension and adaptation of the optimal theory to the Mather and Oensingen specific conditions. This explorative numerical exercise with different comparisons and the implications which can be made regarding the plant physiological and hydrological processes was done to illustrate elements of applicability and limitations of each the empirical and the optimal theory.

Applying the optimal theory to water-limited conditions was also useful for investigating its consistency with respect to observed relationships between environmental variables, physiological traits and concentration in leaf expressed as the ratio c_i/c_a (Prentice et al. 2014; Wang et al. 2017). In this study, these relations were tested in local and detailed modeling configurations as a contribution to previous works in validating the optimal theory (Wang et al. 2017).

In this section, the first part is devoted to describe the comparison between the empirical and optimal unit cost functions using the *a/b* parameter in the analysis. The second part shows the examination of the *a/b* parameter as a strategy for matching the empirical and optimal approaches. The third part treats the comparison between the empirical and optimal approaches using fixed parameters. The fourth part shows the use of *a'* parameter in the strategy of matching both approaches. The remaining parts present the results of constraining g_s and *a'* in the matching strategy with *a'* parameter.

2.6.1 Empirical and Optimal Unit Cost Functions

In applying and adapting optimal theory to water-limited conditions, unit cost parameters values must be determined properly. For the transpiration component parameter, (Prentice et al. 2014) propose the unit cost *a* as a cost of respiration related to water flow formulation through the xylem or as a function of the viscosity of fluid and height of the plant. For the unit cost of carboxylation, parameter *b*, the authors suggest a constant value that is driven by the effect of temperature on the kinetics of the biochemical reactions of the photosynthesis processes. In De Kauwe et al. (2015) and Wang et al. (2014), the formulation of the optimal c_i / c_a, requires the definition of the ratio a/b parameter under water-no limited conditions. Wang et al. (2014) proposes a simplified formulation for *a/b* parameter which cannot be directly applied to this study. Based on these formulations (Prentice et al. 2014; Wang et al. 2014), a parameter value exploration was made to establish the order of magnitude related to cited papers (Prentice et al. 2014; Wang et al. 2014) and to explore the effect of the parameter being put into the total unit cost function in comparison to the empirical approach one. At this level of exploration, the actual evapotranspiration was used in the evapotranspiration part of the unit cost function, represented as aE'/V_{cmax}.

For $a/b=1$ the average value of the unit cost function computed using the optimal theory approach [8.2 mol/mol] is lower than that computed using empirical approach [9.3 mol/mol] in 12%. Carbon assimilation, evapotranspiration and stomata conductance computed using optimal approach are, in most cases of time step simulations points, lower than the corresponding values computed using the empirical approach when conventional parameters are used. The difference between mean values of carbon assimilation computed using [2.68 mmol/m2/s] optimal and empirical [2.36 mmol/m2/s] empirical approaches is 13%, for evapotranspiration the difference is 21%, at [3.3 mm/d] optimal and [2.75 mm/d] empirical. The highest difference found is between the values for stomata conductance, [275.14 mm/s] for optimal and [1.05 mm/s] for empirical. The average values for water leaf potential are [-1.28 MPa] for optimal and [-0.538 MPa] for empirical, with the corresponding concentration in-leaf at [289 ppm] for optimal and [269 ppm] for empirical showing consistency in terms of the general difference between optimal and empirical results. The values for stomata conductance given by optimal theory, out of maximum capacity reported by the literature of [20 mm/s or 0.02 m/s] show some limitation for using $a/b = 1$ as a ratio parameter in the optimal theory.

In the cases $a/b<1$, the average unit cost function decreases to a limit value of [7.6 mol/mol] with a/b values lower than 1. In general, the increment of carbon assimilation values computed using the optimal approach is low with lower values of $a/b < 1$, while the average value for evapotranspiration computed using the optimal approach is almost constant with the variation of $a/b <1$. The average value of stomata conductance is high, up to [414.3 mm/s] with $a/b = 0.1$;

however, for lower values of *a/b <1*, the increment value stays stable, with average values of [191 mm/s]. In general, when using the optimal approach, with lower values of *a/b < 1*, more time step points present a total unit cost with lower values than those found using the empirical approach. This condition of *a/b < 1* shows a tendency of the general results using the optimal approach to get close to a limit value as *a/b* becomes smaller.

For *a/b >1*, the average unit cost using the optimal approach increases [12.3 mol/mol] in relation with the previous conditions of the ratio *a/b* as expected. However, the increment value does not change its relationship to the empirical unit cost value; it is still lower in comparison to the new empirical unit cost with new *a/b* ratio. The average values for carbon assimilation [2.6 mmol/m2/s], evapotranspiration [3.0 m/s] and stomata conductance [210 mm/s] using the empirical approach decrease, consistent with the effect of *a/b* in the optimal computation, with a noticeable proportionality as *a/b>1* with higher orders of magnitude.

Overall, as the ratio *a/b* increases, the optimal results show a sustained decrease for carbon assimilation, evapotranspiration and stomata conductance, according to the mathematical condition for optimal computation. However, for most of the cases the values of stomata conductance computed by optimal theory are higher than the corresponding empirical ones. This fact provided motivation to explore not only the details of what specific conditions explain higher values for stomata conductance using optimal theory compared to empirical values and even for the physical limitations, but also explore how to adjust the optimal computation to get more feasible results.

In a first attempt to adjust the optimal computation, a limitation on the minimum computable water leaf potential was set to limit the relation between evapotranspiration and stomata conductance and consequently get lower values of stomata conductance. This limitation could be on the percentage of potential evapotranspiration that the algorithm uses to compute the minimum water leaf potential. In consequence, the effect of lowering the maximum computable evapotranspiration is the decrease of the minimum water leaf potential for the computation to limit greater values of stomata conductance in the Penman-Monteith equation.

The effect of lowering $a/b < 1$ shows that stomata conductance gets high values as evapotranspiration still increases in concordance to optimal computation. In this case, the adjustment generates low values for stomata conductance that are feasible but still a little higher than empirical values. For instance, the average value for stomata conductance computed using the optimal approach is 1.55 mm/s at $a/b=0.1$, or 1.65 mm/s at 0.01 mm/s, with an empirical value of 1.05 mm/s. As $a/b > 1$, it is to possible to get optimal values for stomata conductance closer to the empirical ones but with some important difference in carbon assimilation. This adjustment produces a relatively equality between optimal and empirical unit cost functions.

2.6.2 Strategy for *a/b* Optimal Parameter to Constrain Optimal

The parameter strategy for matching empirical and optimal theory models is conducted by means of an analytical framework using the empirical and optimal equations. Once these analytical equations are established, the empirical model is run and the results so obtained are plugged into the equation for the *a/b* parameter. The direct computation of the *a/b* parameter is based on Equation 6. The equation for the *a'* parameter using the empirical approach is Equation 2.5.

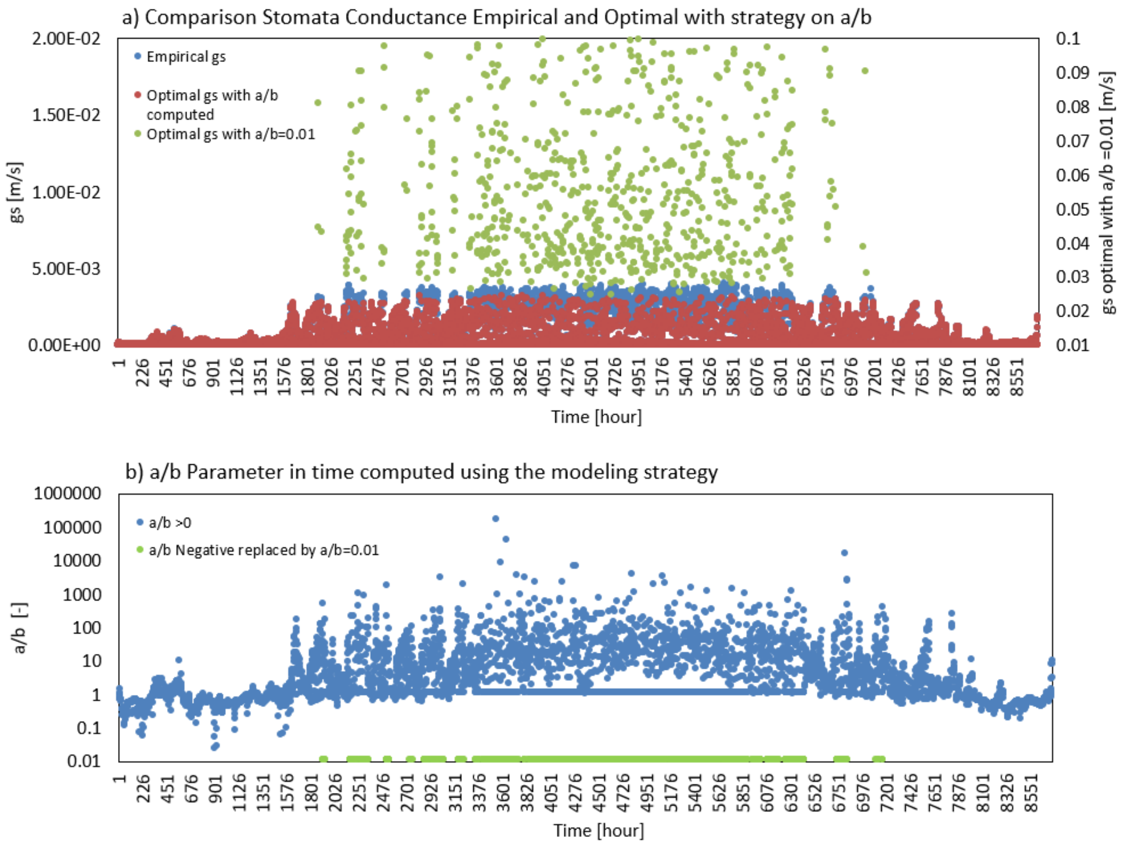

Figure 27 Stomatal conductance and a/b behavior in time using the modeling strategy on a/b optimal parameter.

Figure 27 shows the annual variation of *a/b* parameter values with temperature, VPD and radiation. This graph depicts two main findings. First, in most cases, the *a/b* parameter values are higher during the warm seasons (late spring, summer and early fall) than in the cold seasons. A second finding is that some negative values do still occur during the warm season.

The first finding above can be explained in terms of low and high values of meteorological conditions. Empirical and equilibrium equations intersect at high concentration in-leaf and water leaf potential values. This empirical result gives a high value for stomata conductance because the matching equilibrium equation at high concentration in-leaf values, despite low carbon assimilation. For this type of empirical result, it is possible to get the same values using the optimality approach by decreasing the *a/b* parameter. Meanwhile, under high values of meteorological conditions, the empirical intersection with equilibrium equation (Equation 2.4) gives low concentration in-leaf values and higher water leaf potential than the case above. Hence, the *a/b* parameter that allows matching of the optimal approach to the empirical approach is higher than one at low meteorological conditions.

Negative values of *a/b* are the result of applying the inverse optimal equation (Equation 6) for matching to empirical values. These negative values are due to the negative derivate of transpiration unit cost component. It has been found that for low carbon assimilation values, the transpiration unit cost component increases with concentration in-leaf, while for average carbon assimilation values transpiration unit cost component has a minimum value. For high values of carbon assimilation, the transpiration unit cost part decreases, which implies that the minimum cost is always at maximum concentration in-leaf, indicating no effect of *a/b* on the total unit cost. This special case computes negative *a/b* with a derivate of transpiration lower than the derivate for carbon assimilation.

These negative *a/b* values indicate that actual evapotranspiration, as a variable in the total unit cost, does not increase with c_i on the aE'/A component as the theory expects. Therefore, the estimate of transpiration $E'=1.6G_sD$ is used instead of actual evapotranspiration E in examining the total unit cost in the following development of the optimal approach.

2.6.3 Comparison of Empirical and Optimal Approaches Results

Fixed, literature-reported parameter values were used to compute the simulations under the empirical and optimal approaches separately. Simulations were performed in equal conditions of forcing inputs for both methods. Note that the optimal approach applied in this section, with fixed *a/b* and maximum evapotranspiration in the unit cost function as used in Prentice et al. (2014) is called the unconstrained optimal approach.

Figure 28 shows that the carbon assimilation and evapotranspiration computed by both empirical and optimal (unconstrained version) approaches are similar. However, the stomatal conductance g_s computed using the optimal approach is much higher than the stomatal conductance computed using the empirical approach. For both the Mather site and the Oensingen site, the carbon assimilation computed using the optimal approach is higher than that computed using the empirical approach. The average difference between the optimal and the empirical approach carbon assimilation series is 0.2 μmol/m2/s, for the Mather site, which represents a 2% difference; at the Oensingen site the average difference is 0.3 μmol/m2/s, or 3%. For the Mather site, the difference in the actual evapotranspiration average of the optimal and empirical approaches is 0.5 μmol/m2/s, equivalent to a 1% difference. For the Oensingen site, the difference is 2.5 μmol/m2/s, or 1.8%.

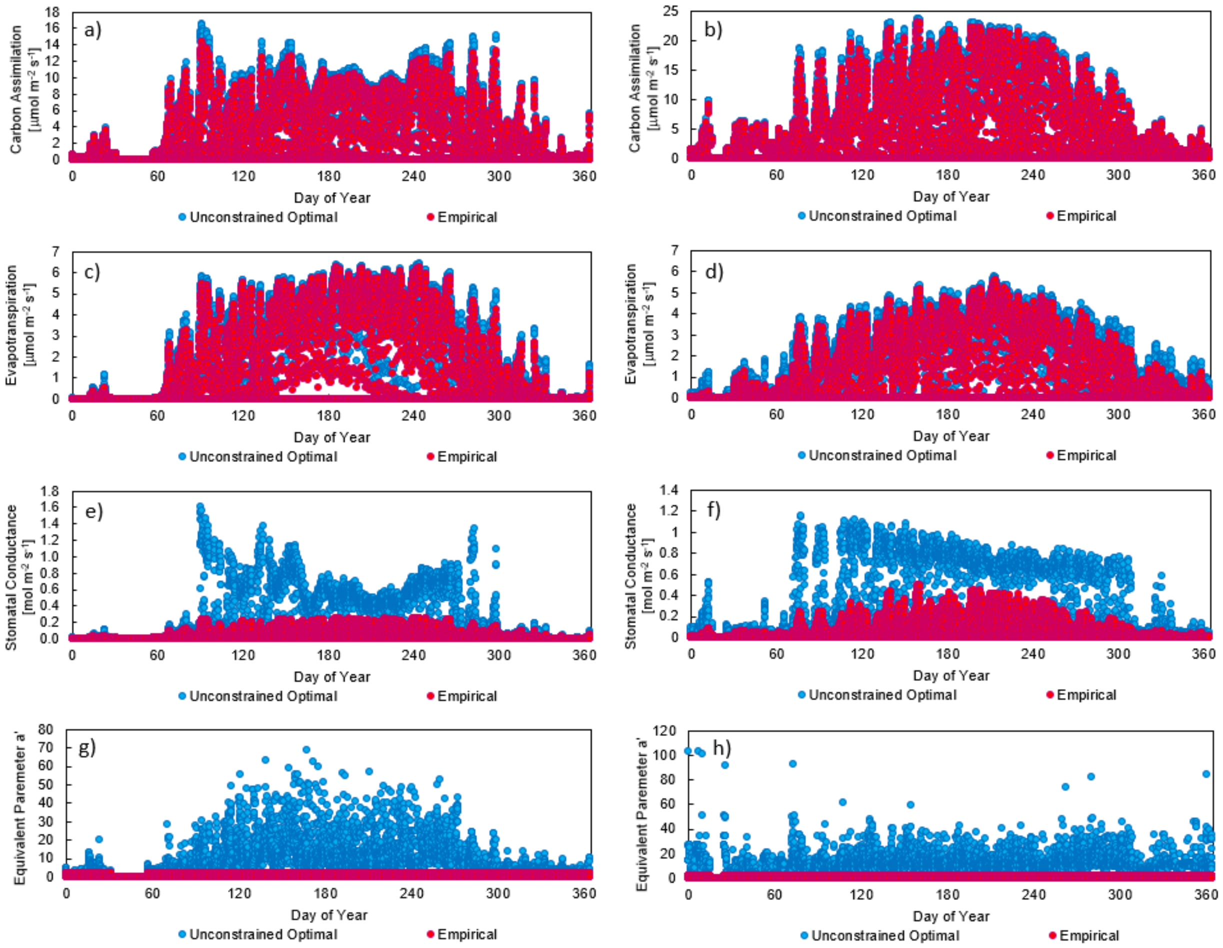

Figure 28 Comparisons of empirical (red points) and unconstrained optimal (blue points) approach simulations over the course of a year. a) and b) Carbon assimilation; c) and d) Evapotranspiration; e) and f) Stomatal conductance: g) and h) Equivalent empirical parameter a'. Mather site (Left-side panels) and Oensingen site (Right-side panels).

The stomatal conductance computed using the optimal approach is higher than that computed using the empirical approach for warm seasons. The average difference is 0.3 mol/m2/s, or 570%, for the Mather site, and 0.2 mol/m2/s, or 270%, for the Oensingen site in warm seasons (April through August) whereas cold seasons (January to March, September to December) the average difference is only 0.1 mol/m2/s, or 1%, for the Mather site, 0.5 mol/m2/s, or 2%, for the Oensingen site.

Figure 28-g) and Figure 28-h) show that equivalent empirical parameter *a'*, computed by Equation 2.5 based on optimal approach results, follows stomata conductance. In cold seasons the average *a'* value is 10 for the Mather site. In warm seasons, the average *a'* is 32 for the Mather site, which is greater than the limit value of 17.

Figure 28-h) also shows that equivalent parameter *a'* for the Oensingen site, in contrast to that for the Mather site, has a uniform distribution of *a'* along the year of simulation, with no seasonal pattern easily recognizable.

The higher values computed using the optimal approach in comparison with the empirical approach is due to Optimality solutions' search for higher c_i, values. One reason explaining these higher values is that the *a/b* parameter used is a low value, less than 1, which makes the transpiration cost component lower in comparison to the carboxylation cost component. This means that the total unit cost is mostly explained by the carboxylation cost component. As the carboxylation unit cost is monotonically decreasing with c_i, the minimum total unit cost is at higher c_i values.

The similarity of carbon assimilation and evapotranspiration values obtained by these approaches is due to relative similarity of G_s in the equilibrium equation (Equation 2.4) under both approaches. The G_s similarity is directly related to the Ψ_L similarity, because both variables are mapped one-to-one through an inverse Penman-Monteith (PM hereinafter) equation and equivalent stomatal-atmospheric conductance equation. As Ψ_L is lower using the optimal approach than when using the empirical approach, G_s is a little higher when using optimal approach than empirical approach. Another reason for this similarity is that at higher c_i values for both the optimal and empirical approaches, dA/dc_i decreases and hence the difference in optimal and empirical c_i values is not substantial for carbon assimilation.

However, a low increment in G_s implies a higher increment in g_s as an effect of the equivalent stomatal-atmospheric conductance equation and the inverse PM equation. Even with the higher g_s computed using the optimal approach, evapotranspiration tends to be close to Potential evapotranspiration. The PM equation means a much higher optimal g_s, so optimal evapotranspiration is higher than empirical evapotranspiration but constrained to be much closer to Potential evapotranspiration.

These results mean that under Optimal theory plants open stomata at higher values than the empirical theory would predict. The optimal stomatal conductance is higher because plants look for higher c_i values that allow to minimize total unit cost. The atmospheric limitation of CO_2 transfer to inside the leaf, given by the supply of CO_2 in the diffusion equation, forces a correspondence between higher c_i with much higher g_s and higher evapotranspiration closer to Potential evapotranspiration.

Although the BBL equation in Leuning (1995) is, similar to Equation 2.1, constrained by the equilibrium equation (Equation 2.4), it was not formulated for water-limited conditions, and it does not use the PM equation as an additional constraint for evapotranspiration and water leaf potential Ψ_L. In Medlyn et al. (2011), the USO (Eq. 11, page 2735) Equation proposed is valid for wet conditions and is constrained neither by the evapotranspiration equation nor water leaf potential. Other studies such as De Kauwe et al. 2015 and Zhou et al. 2018 use only the BBL empirical equation for the USO Equation or the basic Prentice et al. (2014) Equation, however they do not reformulate the equations as we do in this study.

Optimal theory, as formulated by Prentice et al. (2014) under dry conditions and the PM equation, shows large values of stomatal conductance, sometimes even values out of feasible physical range. Also, a computation of an equivalent empirical parameter a' shows large values out of an upper bound value of 17 for the Mather site and 24 for the Oensingen site. The maximum *a'* values are explained in Appendix B.

To overcome these two issues, the parameter strategy is used to match (or couple) both optimal and empirical results under a reduction of degree of freedom for the equivalent parameter *a'* and constraining g_s under valid ranges. This is the so-called optimal coupled to empirical approach, to our best knowledge, not used before in previous optimality formulations such as Mencuccini and Christoffersen (2019), which is a revision of different optimality versions. Results under this modified (coupled with empirical) Prentice optimal approach in comparison to an unconstrained optimal approach is shown next in subsection 2.6.4.

2.6.4 Strategy for *a'* Empirical Parameter Constraining g_s and *a'* in Optimal Approach

Figure 29 shows a strong similarity of carbon assimilation and evapotranspiration in the optimal coupled with empirical and optimal unconstrained approaches, with a difference of only about 1% between them for the Mather site and 2% for the Oensingen site. The overall difference in c_i and Ψ_L is 1% for the Mather and Oensingen sites, which it shows that both results are virtually equal.

However, the reduction in g_s under the constrained condition in 39% at the Mather site and 48% at the Oensingen site, which implies that the optimal unconstrained approach could double the g_s value in comparison to an optimal computation coupled with empirical. Also, the equivalent parameter *a'* is reduced by the optimal-empirical approach; for Mather to 27% and for Oesningen 28%.

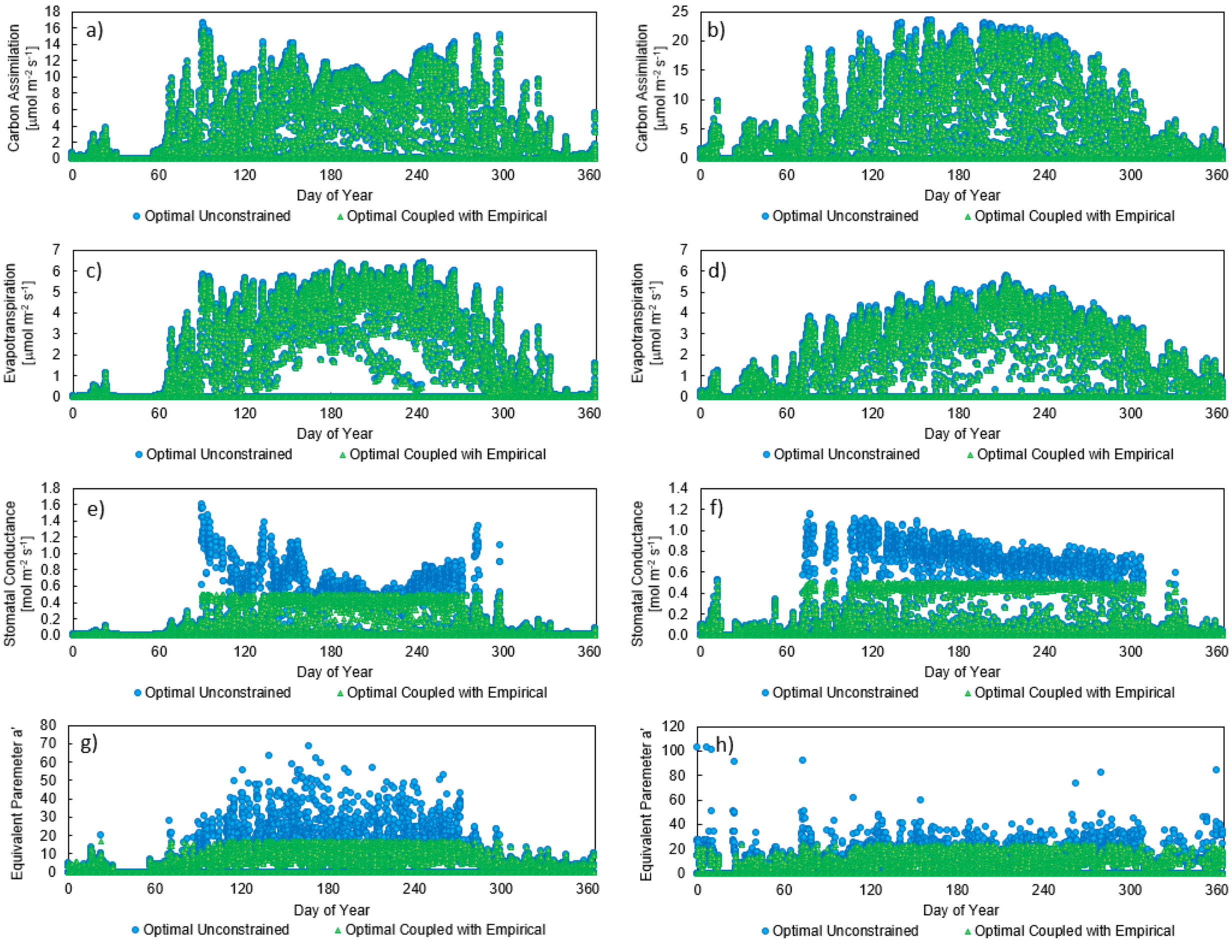

Figure 29 Comparisons of unconstrained optimal (blue points) and optimal coupled with empirical (green points) approaches simulations over the course of a year. a), b) Carbon assimilation; c), d) Evapotranspiration; e), f) Stomatal conductance: g), h) Equivalent empirical parameter a'. Mather site (Left-side panels) and Oensingen site (Right-side panels).

The last three possibilities show in Section 2.4.5 that under certain environmental conditions, plants do not behave optimally, but instead open their stomas up to the maximum physical value or follow a behavior described by empirical conditions. The next section explores possible hypotheses on the optimal unconstrained and empirical applicability.

2.6.5 Exploring Hypotheses about the Implications of Optimal Approaches

This section is intended to establish hypotheses on the limitations of both the empirical and optimal approaches with respect to explaining feasible results. These hypotheses rise as a first meaning of the implications of the overestimated results of g_s and equivalent a' computed by the optimal unconstrained approach. In this context, an exploration of the hypotheses, based on the main causes of the overestimated results, is carried out through interpretation of the computed data and conceptual analyses of the optimality approach equations.

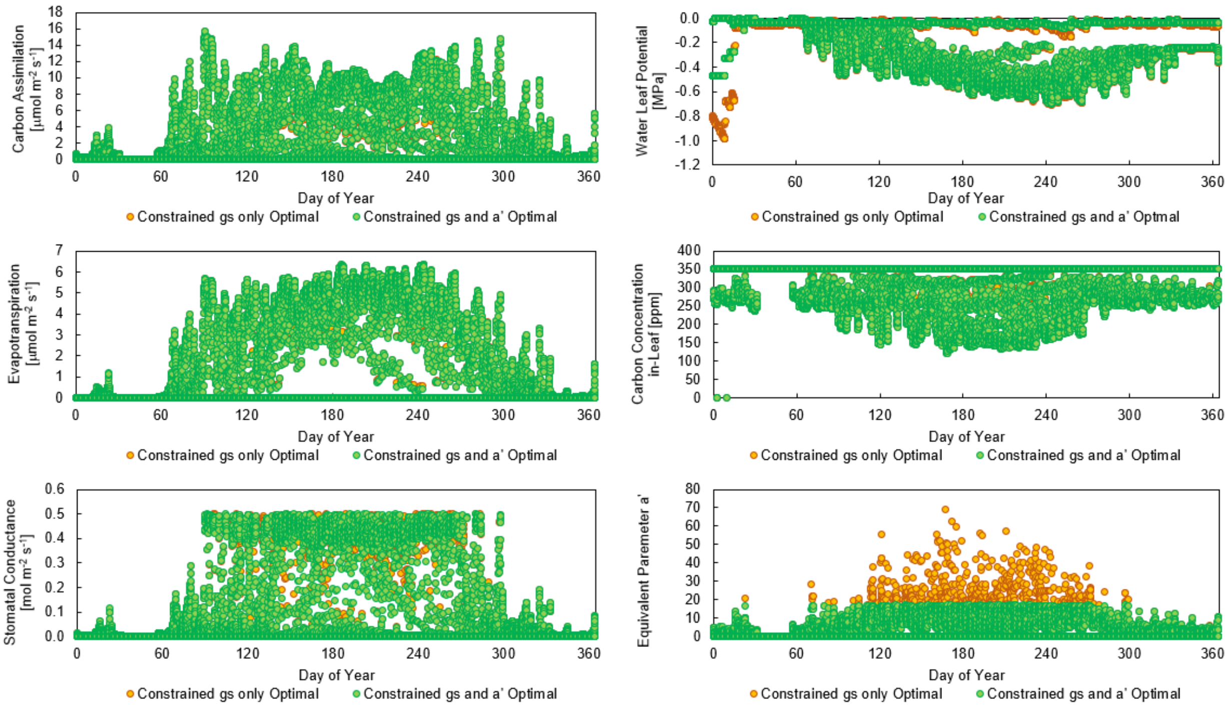

Figure 30 Comparisons of constrained optimal using g_s only (yellow points) and constrained optimal using g_s and *a'* (green points) approaches simulations in a year at the Mather site. a) Carbon assimilation; b) Evapotranspiration; c) Stomatal conductance; d) Water leaf potential; e) Carbon concentration in-leaf; f) Equivalent empirical parameter *a'*.

Figure 30 shows that even when g_s is constrained, there are still equivalent *a'*s above the maximum value. The effect of constraining only g_s does not change carbon assimilation, evapotranspiration, CO_2 in-leaf concentration or water leaf potential substantially. The evidence shows that stomata conductance changed from its initial large values computed by using unconstrained optimal approach to feasible lower values. These new stomata conductance values limit an important amount of *a'* values below the limit of 24. However, some other *a'* values re-computed with the new stomatal conductance are higher than the maximum 24 value. Indeed, there are cases of original high *a'* values with low g_s values.

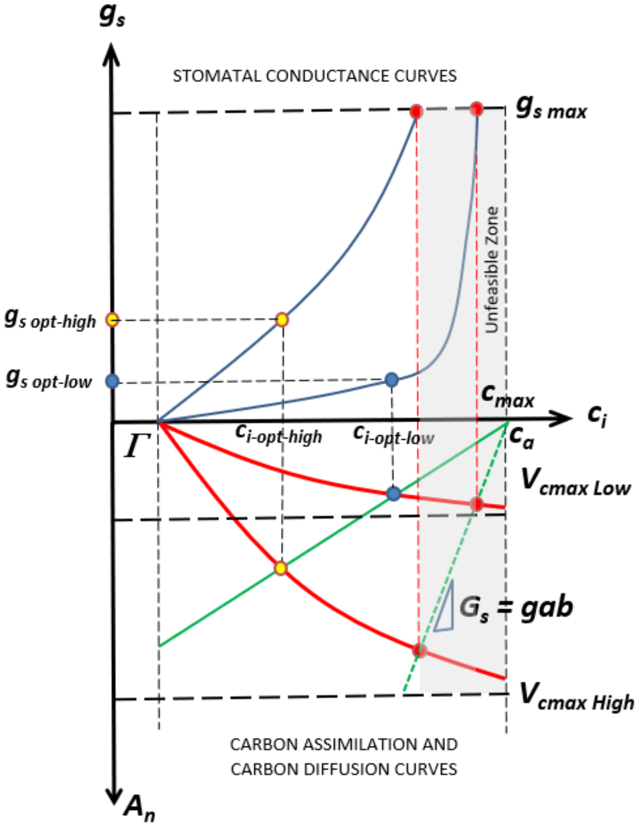

Figure 31 Geometrical and conceptual explanation of stomatal conductance variation with ci under hot and cold climate conditions. Plane [c_i x A_n] shows the equilibrium condition from the intersection between carbon assimilation and carbon diffusion curves at high and low temperature conditions. Plane [c_i x g_s] corresponds to stomatal conductance curves.

As a consequence, this constrained-g_s only optimal approach reveals that the equivalent *a'* parameter is affected strongly by CO_2 in-leaf concentration c_i and, carbon assimilation A_n, not only by stomata conductance g_s.

A graphical-conceptual analysis of stomatal conductance is presented in Figure 31. Figure 31 shows that as c_i increases g_s increases, following the equilibrium equation. But the range of c_i goes up to a maximum value that corresponds to maximum total equivalent conductance G_s, which is determined by the atmospheric-boundary layer conductance g_{ab}. Likewise, Figure 31 also illustrates that the stomata conductance curve is higher for warmer and hot climates than for cold conditions. Consequently, this implies that for any c_i value stomata conductance is higher in warmer-hot climates (or when meteorological condition values are higher) than for cold climates (or when meteorological conditions values are lower).

As presented in the Section 2.4.4 of this dissertation, the optimal approach searches for the minimum unit cost condition for high c_i values in cold-low meteorological conditions and lesser c_i values for hot-high meteorological conditions. Therefore, stomata conductance has the tendency to be lower in cold conditions than in warmer conditions (Figure 31). This difference in stomatal conductance g_s values can be observed in Figure 32-a) and Figure 32-b). For instance, stomatal conductance at hot-humid conditions are higher than those at cold conditions because the corresponding evapotranspiration values depend on high temperatures and radiation.

These relationships between g_s and c_i lead to the conclusion that the unconstrained optimal approach tries to overestimate stomatal conductance at warmer-hot climates (or higher meteorological condition values) especially where actual evapotranspiration *ET* is close to potential evapotranspiration *PET*, which means water-stress for the plants (Bonan et al. 2014; Dewar 2010; Manzoni et al. 2014).

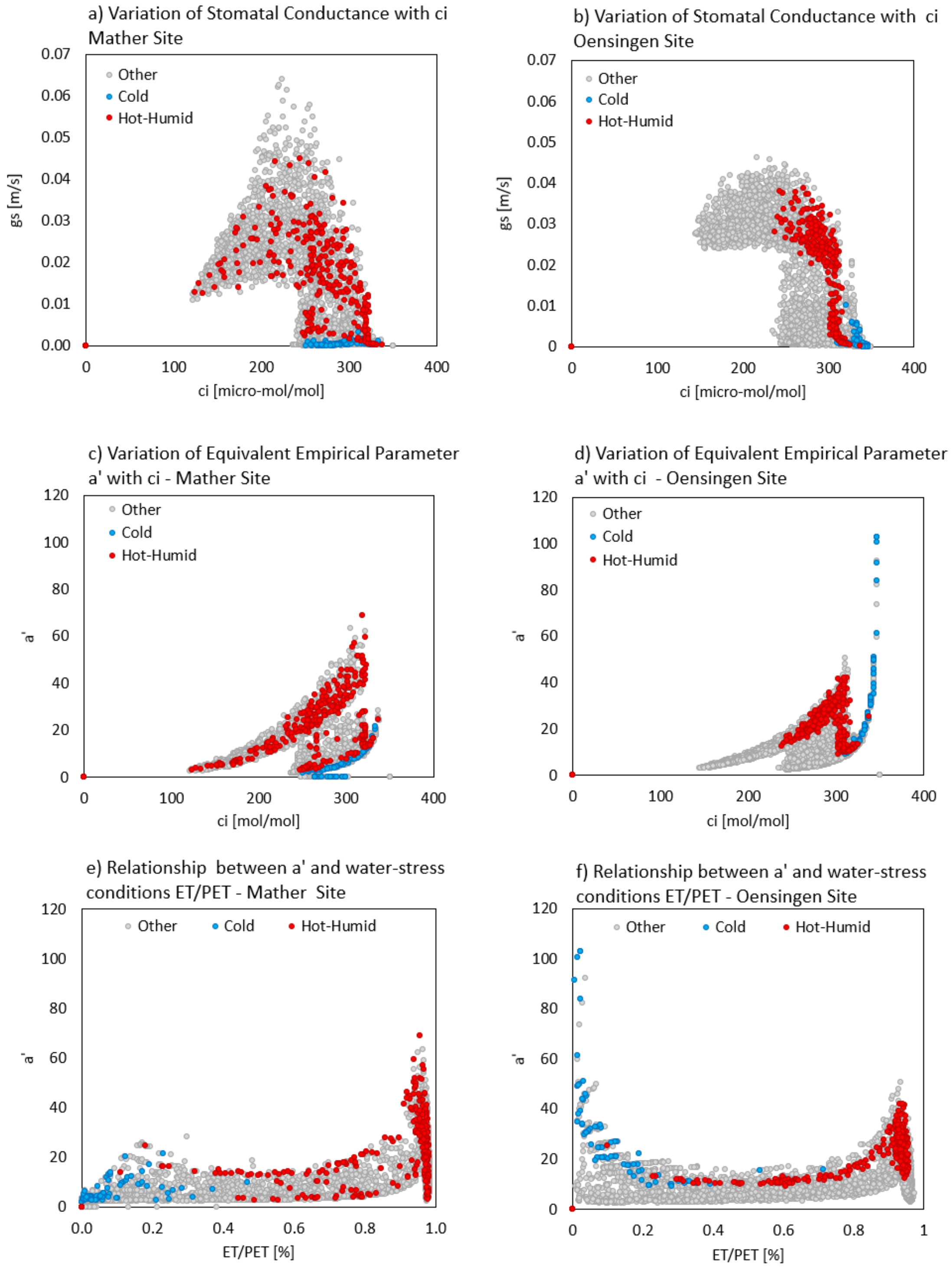

Figure 32 Conditions that explain high Equivalent Parameters a' values at the Mather and Oensingen sites in red and blue points. All the points shown are simulation results from optimality unconstrained without any bounding on g_s or *a'*.

An analysis of the variation of equivalent *a'* is detailed through Figure 32-c), Figure 32-d) and the empirical equation. First of all, the empirical equation (Equation 2.1 or Equation 2.5) describes clearly what the main factors of *a'* variation. We can consider that they are: Stomata conductance g_s, CO_2 in-leaf concentration c_i, carbon assimilation and water-stress functions $f(\Psi_L)$, $f_v(\Psi_L)$. Figure 32-c) and Figure 32-d) present that, in general, *a'* increases as ci increases, what is easily interpreted from the empirical equation. This relationship between *a'* and c_i is also presented in the same manner in Franks et al. (2018) for different conditions.

Nevertheless, there are two distinguishable peaks in Figure 32-c) and Figure 32-d) that correspond to the extreme cold and hot temperature conditions. The middle peak in both Figure 32-c), and Figure 32-d), represents the effect of the highest g_s values, in warmer conditions, on the higher *a'* values. At the same time, this same effect is jointly caused by the maximum c_i values, that are in turn determined by the equilibrium equation (Equation 2.4) at warmer conditions.

At these warm and hot climate conditions, the highest g_s values correspond to the highest actual evapotranspiration values. In addition, these evapotranspiration values are close to the potential evapotranspiration values which indicates some state of water-stress conditions. The correspondence between the highest *a'* values and highest ratio *ET/PET* are shown in Figure 32-e) and Figure 32-f).

Moreover, close to the highest *ET/PET* values, there is an additional effect of rising *a'* value due to lower values of factor functions $f(\Psi_L)$ and $fv(\Psi_L)$ on carbon assimilation. The lower values of the factor functions correspond to the lower values of water leaf potential which are the result of optimal points where the evapotranspiration is close to the highest values indicating water-stress conditions. In some cases where *ET/PET* is low, the *a'* value is high because the effect of low carbon assimilation increases the *a'* value, according to the Equation 2.5.

On the other hand, carbon assimilation has an opposite effect on *a'*. For higher A_n values at warmer conditions *a'* has a tendency to decline, while at very low carbon assimilation values in cold conditions, *a'* increases substantially, as present at the Oensingen site in Figure 32-d).

At this point, it can be concluded that high values of equivalent *a'* are present in both warm and cold seasons at high and low *ET/PET* ratios respectively, as shown in Figure 32-e) and Figure 32-f). These high *a'* values are above the boundaries reported in the literature for these sites and species application. This means that the empirical approach cannot replicate the results obtained by the optimal unconstrained approach.

In addition to the above analysis, a set of scatter plots representing the meteorological conditions for high g_s and *a'* is presented in Figure 33. These representations help to demonstrate the coherence between the above described relationships and environmental conditions for higher g_s and *a'* values out of valid ranges. All of these points are computed using the unconstrained optimal approach. The points that represent g_s values higher than feasible ones, are located in the region of high temperatures (more than 10^{o}C) independent of other meteorological variables.

The points corresponding to *a'* higher values than reported limits are superimposed on several points with high g_s values, showing that some of these points are related each other. However, this relationship is not one-to-one; as is demonstrated in Figure 32, there are *a'* high values points which implies low g_s values and vice versa.

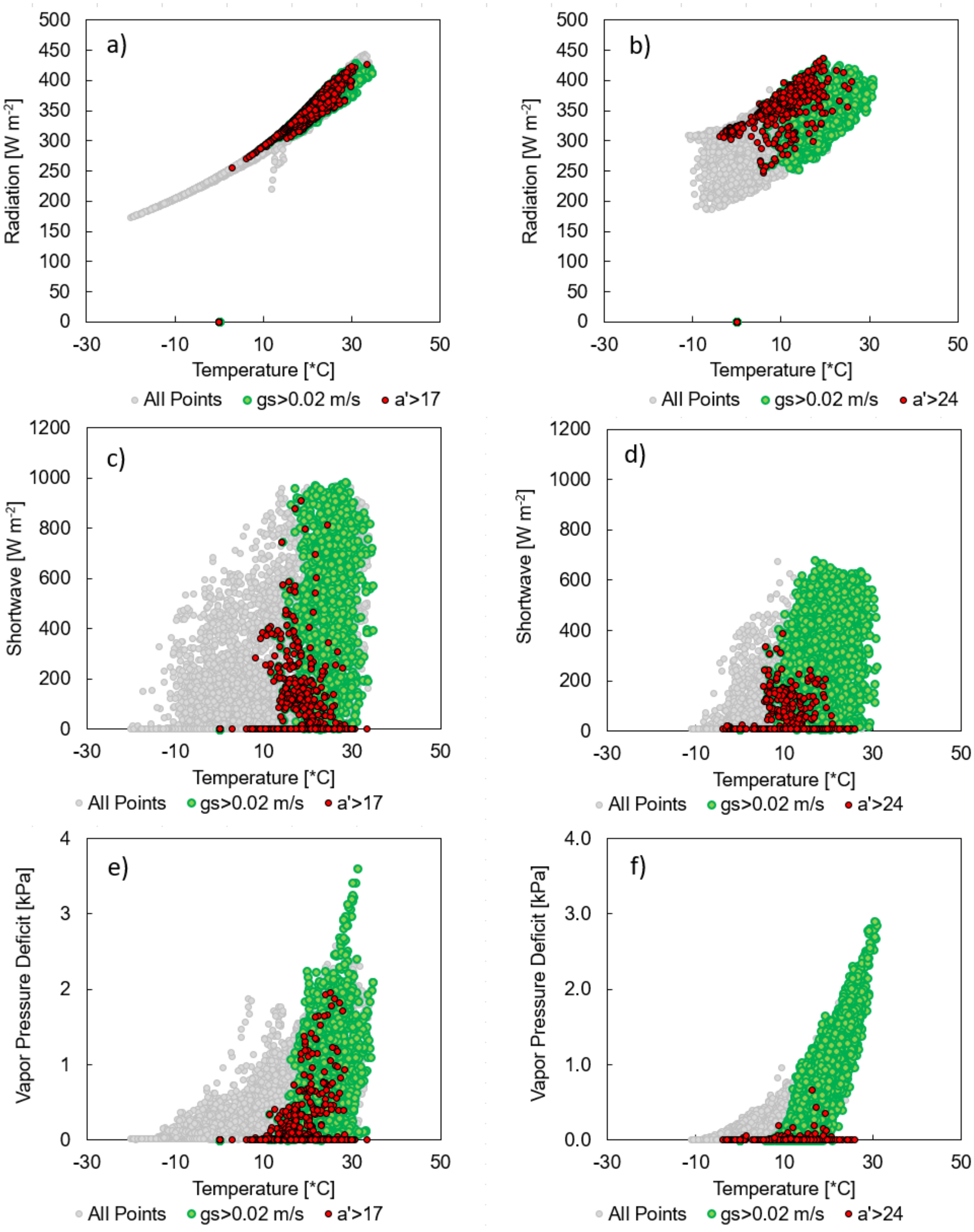

Figure 33 Scatter Plots of forcing meteorological data showing relationships with unconstrained optimal approach (grey points), with constrained by g_s (green points) and with constrained by *a'* (red points). a) and b) temperature vs radiation; c) and d) temperature vs shortwave; e) and f) temperature vs vapor pressure deficit. Left plots a), c) and e) are for Mather site. Right plots b), d) and e) for Oensingen site.

The scatter plots of these high *a'* value points reveal that they spread to include a wide broader range of temperatures than the g_s points do. The plots also describe that the majority of high *a'* points correspond to middle and lower values of Shortwave radiation (below 500 W/m2), and middle to lower values of vapor pressure deficit, or VPD (below 1 kPa). For example, at the Oensingen site, the *a'* points are located at very low values of VPD than those at the Mather site. Hence, the very low values of carbon assimilation at the Oensingen site can explain the higher values in the peak of *a'* vs c_i /c_a or *a'* vs *ET/PET* in cold conditions in comparison to the Mather site peak in the same cold season.

In addition, high radiation explains more *a'* points than g_s points, despite the fact these both types of points are located in the same high radiation region.

The above explanations led us to formulate the following hypotheses about the physiological implications of the application of the optimal approach and the limitations of the empirical approach explaining plant behavior in extreme conditions:

One hypothesis is that under the optimality approach, the stomatal conductance values are unbounded, implying some of lack of capacity of plants to reach the minimum unit cost (or behave completely optimal) under high temperatures and water-stress conditions. Another hypothesis is that some of the empirical *a'* values are higher than the specie-related limit implying that the empirical BBL Equation approach cannot explain optimal results at certain extreme conditions of lowest temperatures, lowest radiation values and highest temperatures and highest water-stress values.

The next section describes how the results from the unconstrained optimal and optimal approaches coupled with the empirical approach agree with tendencies of observed plant variables.

2.6.6 Review of c_i/c_a Relationships under Optimal Theory

In this section, examinations of certain relationships between the ratio c_i/c_a and other variables are presented. Most of the relationships show some agreement with observed data. We first examine how the optimal approach (both unconstrained optimal and optimal coupled with empirical) conveys the unit cost function theory as a hyperbola-like curve. We then examine how c_i/c_a evolves over time. Then we look at the relationship between c_i/c_a and temperature. Finally, we present the relationships between c_i/c_a, vapor pressure deficit, VPD and carboxylation capacity, V_{cmax}.

2.6.6.1 Hyperbola Curve in Unit Cost Trade-off

Figure 34 shows the trade-off between carboxylation capacity, denoted as $V=V_{cmax}/A_n$, and transpiration, expressed as $G = g_s/A_n$, as predicted by the unit cost concept formulated by Prentice et al. (2014), in the shape of a hyperbola curve. This relationship, between essential variables representing unit cost components, is similar to that presented in Prentice et al. (2014) in Figure 3-page 88, which is a representation of how observed data of carboxylation and transpiration substitute for each other.

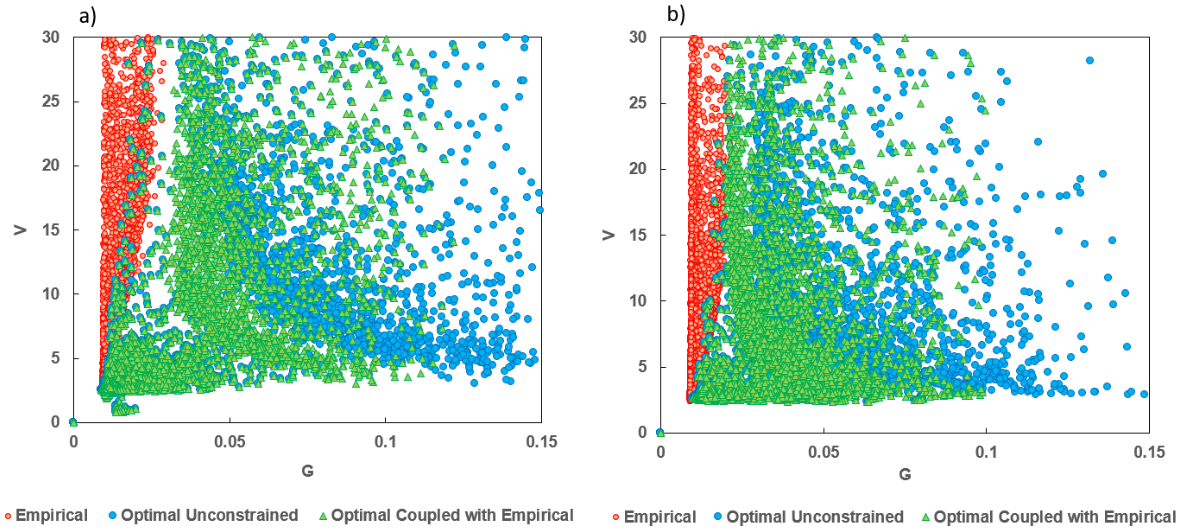

Figure 34 Comparison among hyperbola curves for empirical. Optimal unconstrained and optimal constrained (optimal coupled with empirical in the figure) approaches where $V=V_{cmax}/A_n$ and $G= g_s/A_n$. a) Hyperbola curves for the Mather site; b) Hyperbola curves for the Oensingen site.

In the optimal approach results developed in this study, the trade-off between carboxylation and transpiration (represented by g_s value) is more widespread in the G variable than in the Prentice et al. (2014) curve. These higher values of G are due to the higher values of g_s computed by the unconstrained optimal and optimal coupled with empirical approaches. Although the optimal coupled with empirical approach has constrained g_s values, its stomatal conductances are higher than those computed using the empirical approach and reported in Prentice et al. (2014). The results reported by Prentice et al. (2014) show the hyperbolic shape trade-off based on average data for four types of climates.

On the other hand, the empirical approach does not show a similar trade-off between carboxylation and transpiration variables. The reason for this might be the lower values of g_s computed using the empirical approach and the thin range of computation of all variables with only one specified a' parameter.

2.6.6.2 Time variation of c_i/c_a

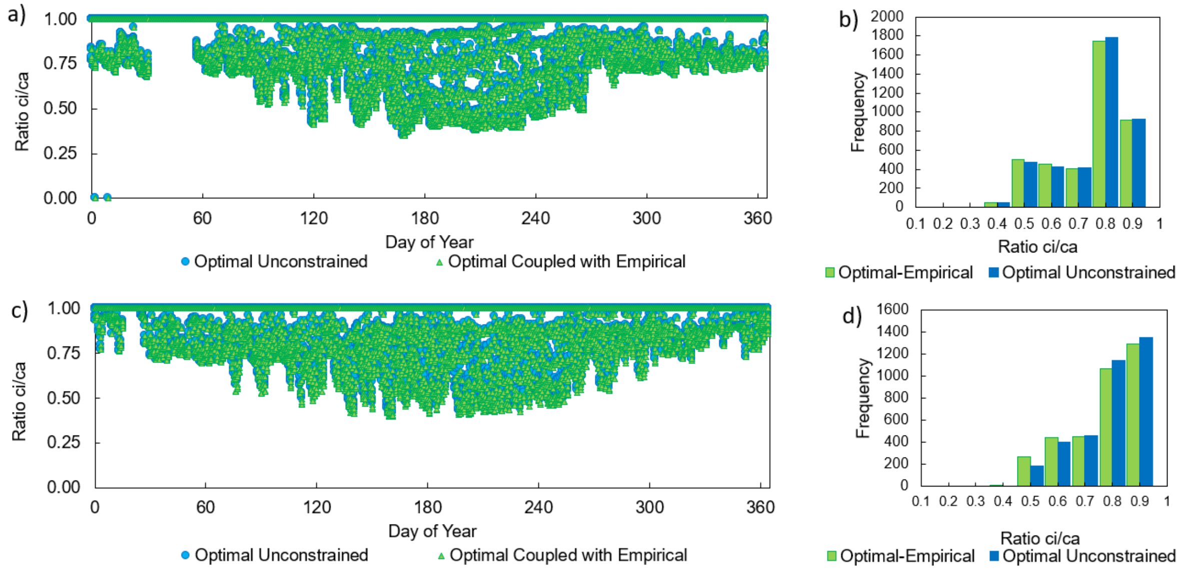

Figure 35 *Ci/Ca* Relationship with Time. a) Ratio *Ci/Ca* vs time comparing optimal unconstrained and optimal constrained (optimal coupled with empirical in the figure) approaches for the Mather site; b) Frequency distribution of ratio *Ci/Ca* over time at the Mather site; c) Ratio *Ci/Ca* vs time comparing optimal unconstrained and optimal constrained (optimal coupled with empirical in the figure) approaches for the Oensingen site; d) Frequency distribution of ratio *Ci/Ca* over time at the Oensingen site.

Figure 35 exhibits that c_i/c_a is lower in warm seasons than in cold ones. The evolution over time is smoother in the summer-fall transition than in the winter-spring one. The reduction of c_i/c_a in warm climates is also reported by Prentice et al. (2014) as observed data. The results computed using the optimal approaches confirm this relationship of c_i/c_a with cold and warm-hot climates.

However, Prentice et al. (2014) report, based on data, how c_i/c_a increases from cold-dry sites to hot-wet sites. This variation on c_i/c_a is not predicted completely by original unit cost formulation in terms of $X=c_i/c_a$ (Equation 2.2 in Prentice et al. (2014)). Section 2.6.6.3 explores this possibility under the developed optimal formulation in this study, based on Equation 2.2 and considering c_i and Ψ_L as main variables.

Both optimal approaches, unconstrained and coupled with empirical, present almost equal c_i / c_a values throughout the year. The frequency distributions in Figure 35-b) and Figure 35-d) indicate a concentration of c_i / c_a values around 0.8 and 0.9 at the Mather site and Oensingen site respectively. According to Prentice et al. (2014) the ratio c_i / c_a has little tendency to vary. This trend is supported by the high concentration of c_i / c_a values shown in Figure 35-b) and Figure 35-d).

2.6.6.3 Relationships Between c_i / c_a and Temperature

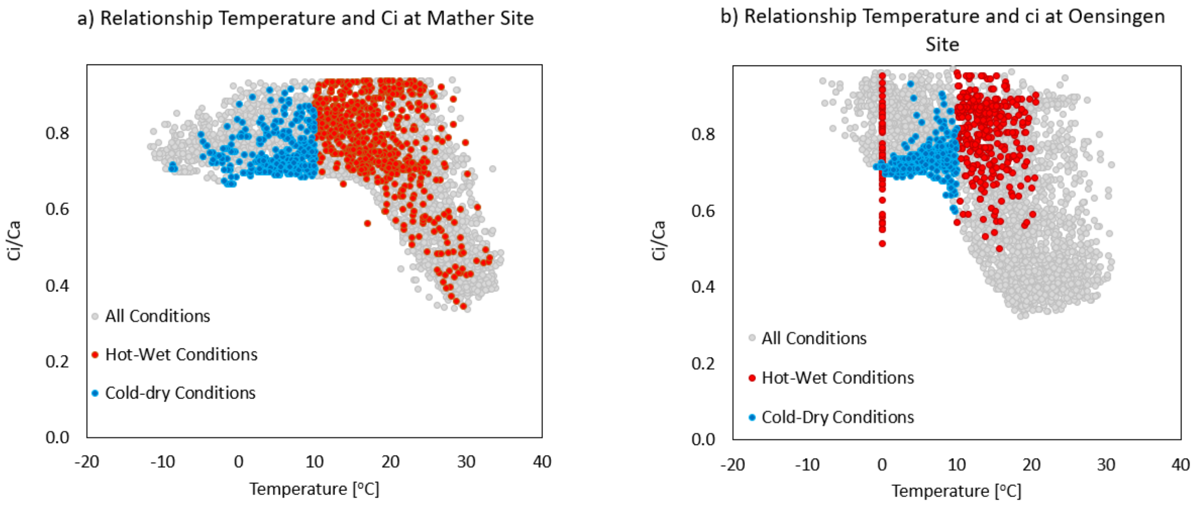

Figure 36 *Ci/Ca* Relationship with Temperature.

Figure 36, displays how c_i / c_a is usually constant with temperature until one specific value, where it begins decreasing as temperature increases, shown by the in grey dots. This behavior is consistent with Prentice et al. (2014) observations for general cases. The decrease in c_i / c_a moving from lower to higher temperatures is due to the increase in absolute value of the slope of the transpiration unit cost component, which makes the minimum cost seeks lower values of c_i.

However, Prentice et al. (2014) also report special conditions where the there is an increase in c_i/c_a from cold-dry sites to hot-wet sites. The optimality extension model developed in this study, shows that is able to replicate the special conditions of increasing c_i/c_a from cold-dry to hot-wet climates, as shown by the blue (cold-dry) and red (hot-wet) dots in Figure 36. These particular conditions computed in the simulations are explained by the effect of the increase of the slope of the carboxylation cost component on the increase in the optimal c_i. The increase of the slope of the carboxylation unit cost component is due mainly to the increase of V_{cmax} with temperature. The change in the carboxylation curve slope seeks a minimum cost in higher c_i values.

2.6.6.4 Relationships Between c_i/c_a with Vapor Pressure Deficit and Carboxylation Capacity

Figure 37 describes how c_i/c_a decreases as V_{cmax} and VPD increase. The decline of c_i/c_a with V_{cmax} has a tendency to be asymptotic to a middle below 0.5. The c_i/c_a behavior with respect to V_{cmax} is similar to its behavior with respect to temperature, which is consistent with the direct effect of temperature on V_{cmax}.

On the other hand, the decrease in of c_i/c_a as VPD decreases is more evident at the Oensingen site than the Mather site, despite both sites presenting similar linear regression coefficients. This type of relationship is in agreement with observed data as reported by Prentice et al. (2014), and is also consistent with Leuning (1995) and Medlyn et al. (2011) formulations between c_i/c_a and VPD. The main explanation of the effect of VPD on c_i/c_a, is the direct incidence of VPD on maximum transpiration *E*' as used in unit cost function. As VPD increases, the maximum transpiration increases in linear proportion. These higher values of maximum transpiration imply that the minimum cost searches for lower c_i values and in consequence lower c_i/c_a.

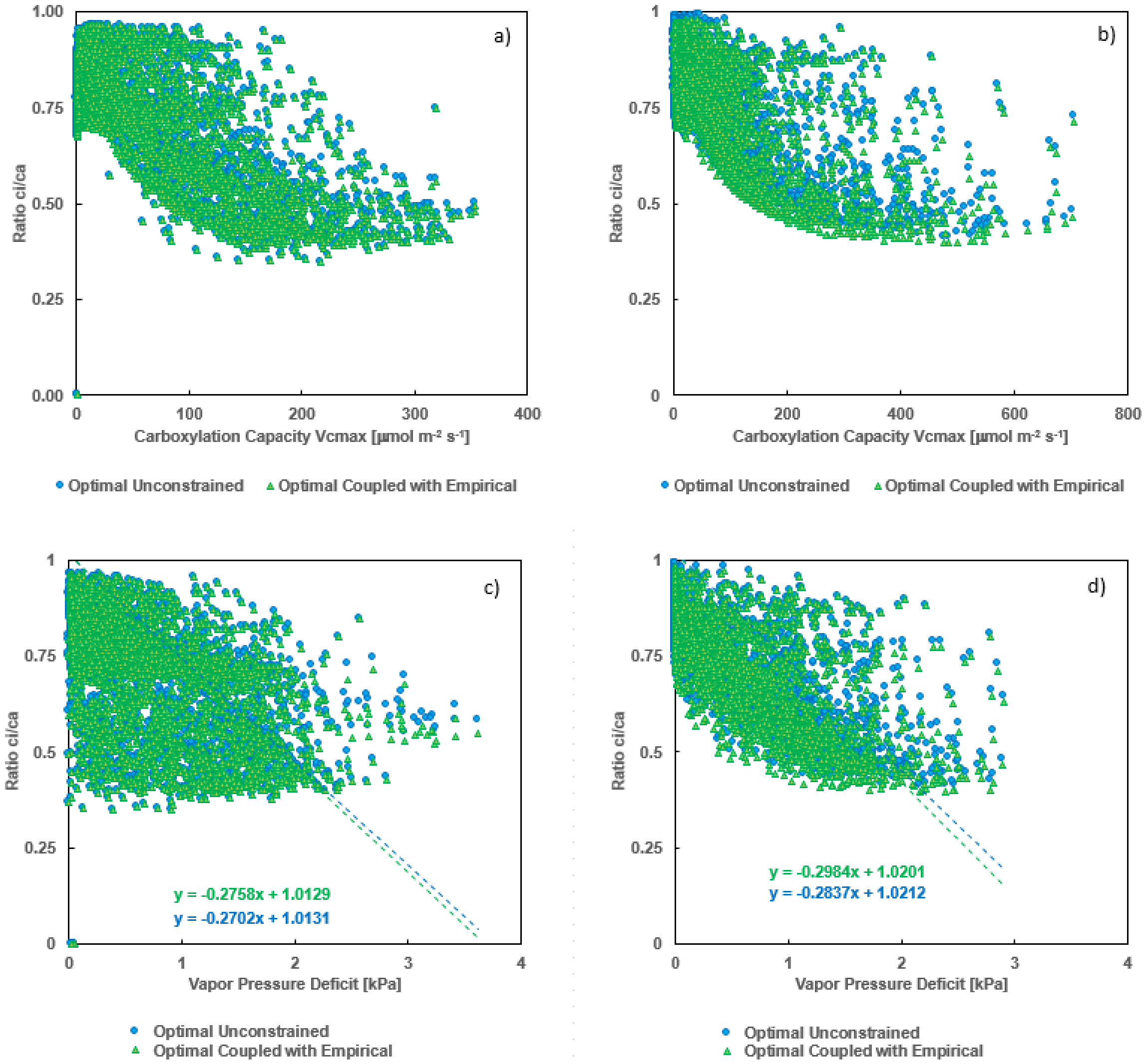

Figure 37 *Ci/Ca* relationships with carboxylation capacity V_{cmax} and Vapor Pressure Deficit *VPD*. a) Ratio *Ci/Ca* vs V_{cmax} comparing optimal unconstrained and optimal constrained approaches for the Mather site; b) Ratio *Ci/Ca* vs V_{cmax} comparing optimal unconstrained and optimal constrained approaches for the Oensingen site; c) Ratio *Ci/Ca* vs VPD comparing optimal unconstrained and optimal constrained for the Mather site; d) Ratio *Ci/Ca* vs VPD comparing optimal unconstrained and optimal constrained approaches for the Oensingen site. Optimal constrained is labeled optimal coupled with empirical in the figure.

2.7 Conclusions

The Prentice et al. (2014) optimality formulation developed in this dissertation based on minimum unit cost function can be integrated with Penman-Monteith and plant hydraulics evapotranspiration, including water-limited conditions (by using the water leaf potential as explicit variable). This integration of the Prentice et al. (2014) modeling is tied to soil-plant-atmosphere processes in a more constrained manner than the majority of optimal formulations presented in the literature. The formulation developed in this dissertation was able to represent properly the unit cost concept of trade-off between carboxylation capacity and transpiration, unlike the empirical approach, which has some limitations when address this feature. This trade-off representation by the optimal approach simulation results was possible by substituting the transpiration formulation used by Prentice et al. (2014) in the unit cost function instead of using the actual evapotranspiration given by the Penman-Monteith equation. That trade-off is possible because the slope of the transpiration unit cost component $d(aE'/A)/dci$ is always positive for all meteorological conditions. This characteristic of the transpiration cost component makes carboxylation capacity unit cost V_{cmax}/A and transpiration E'/A unit cost substitutable for each other as predicted by the theory and observed by data.

The strategy presented in Luo et al. (2013) to have as many possible constraints to reduce parameter equifinality as possible has been applied in the formulation of this study. Also, it has been proven effective in producing more reliable and reasonable model simulation results in terms of the uniqueness of the results through matching or coupling together the same processes from two perspectives: the empirical and the optimal perspective. In this manner, the parameters values (e.g., g_s and a') are automatically bounded in valid ranges resulting in more physically meaningful values.

The modeling work in this study, is able to represent accurately the Prentice et al. (2014) observed c_i / c_a relationships with time, temperature, vapor pressure deficit and carboxylation capacity. This feature promotes the optimal coupled with empirical approach model, formulated in this dissertation, as another valid tool to predict general plant responses to the environment.

The application of the unconstrained optimality model showed overestimated results that convey the following concluding hypotheses: i) The results of stomatal conductance out of bounding values under the optimality theory could be interpreted as a lack of capacity of plants to reach the minimum unit cost (or behave optimally) under high temperature and water-stress conditions. ii) Some empirical a' parameter values, as a constraining of the optimality approach, were computed out of valid ranges, implying certain limitation of the empirical approach to explain optimal results at lowest and highest extreme climates conditions.

Finally, the use of this developed optimality formulation shows a need to investigate some theoretical background from a purely biological perspective to explain the limitations at extreme conditions.

3.0 Development of a Pyrox+Hydro-Biogeochemical Model linked to AMD Processes Modeling

3.1 Introduction

Acid Mine Drainage is still a significant environmental issue resulting from the mine industry in almost all countries (Nordstrom 2011). A sustainable solution is passive remediation using vegetation planted over the coal piles of abandoned mines (Johnson and Hallberg 2005; Liu et al. 2018; Rodríguez et al. 2019). The main technologies offered by phytoremediation as categorized in Karaca et al. (2018) are: a) phytoextraction of metals to be allocated into different part of the plants; b) phyto-stabilization to modify the ability of pollutants to react and stabilize them within the rhizosphere (Karaca et al. 2018; Yao et al. 2012); and c) phytovolatilization to transport soil solutes into the air using plant xylem systems (Karaca et al. 2018). Other mechanisms related to rhizosphere processes are suitable when using vegetation to degrade organic or inorganic contaminants in the presence of bacteria-plant-soil interactions.

In general, phytoremediation relies on the interaction of biogeochemical processes triggered by the plants or by the microbes in the soil (Skousen et al. 2017). In particular, the use of wetlands has been proven effective in remediating AMD through the use of biological interactions with metal (Crafton et al. 2019). In other studies, the use of special sludges offers biochemical passive treatment under AMD (Escobar et al. 2016). For example, the mechanisms of ferric oxidation are related to the microbial activity of *Terris Ferrooxidans* (Skousen et al. 2017). All of the above passive remediation techniques imply that biochemical mechanisms are involved.

However, the underlying interactions processes of phytoremediation are not well understood (Karaca et a. 2018; Liu et al. 2018; Nordstrom 2019b). At the same time, an appropriate assessment is crucial to develop feasible engineering applications on economic efficiency (Nordstrom 2019b). Therefore, the modeling of more detail-based processes is needed to not only enable the understanding of many processes but also enable an assessment of remediation techniques for engineering purposes (Nordstrom 2011, 2019c). In general, the modeling work has been focused on assessment based on particular sites and on pilot experimental remedial works (Nordstrom 2011, 2019a). Four approaches to this modeling have been enacted (Nordstrom, 2018): a) geochemical acid-base speciation modeling, b) reactive transport solutes modeling, c) dynamic oxygen and shrinking core modeling, and d) dynamic acidification modeling.

Most of the modeling work on AMD pollution is built on acid-base speciation or chemical equilibrium models (Cosby et al. 2001). This is a basic platform performing conventional computations related to ion exchange and pH determination (Cosby et al. 2001). Reactive-transport modeling receives more use in AMD research, with special emphasis on hydrodynamic modeling and water quality analysis, such as in Myers (2016). The shrinking core approach is a specific modeling description of pyrite oxidation through the internal oxygen diffusion mechanism and coal coat formation of the pyrite as proposed by Wunderly et al. (1996). Under this modeling approach Gerke et al. (1998) developed long term simulations and added a reactive-transport description. Following the Gerke et al. (1998) formulation, Wright et al. (2006) perform a study of biochemical integration with pyrite oxidation to explain acidification reinforcement. Doulati Ardejani et al. (2013) carry out the incorporating of biological solid-liquid interaction to explore microbial ferric oxidations. Based on this work, Jodeiri et al. (2016) developed a geochemical model that incorporate acid-base speciation and shrinking core. Subsequent work was performed by Bahrami and Doulati Ardejani (2016) in which an analytical formulation for oxygen was integrated with bacterial activity. Overall, the shrinking core approach has been developed more from geochemical perspective than a biochemical inclusion perspective.

Including the biochemical process as a main factor of the modeling is accomplished mainly with the dynamic soil acidification approach. In Cosby et al. (2001) the integration of nitrogen dynamics into acidic description equations is developed in a more comprehensive manner than other previous studies but without a hydrological-physiological inclusion of plants. In a following study Posch and Jan (2009) introduces the Very Simple Dynamic (VSD) concept for soil acid modeling and expresses the need for a better inclusion of vegetation into the dynamic acidification models. In response, Holmberg et al. (2018) formulates a vegetation growth with organic matter turnover and acid-base dynamics, but still describing the plant growth simply. It is only in Bonten et al. (2016) where a more detailed description of nutrient uptakes, carbon and nitrogen dynamics are used still using a simple growth model. Guided by inclusion of the main biogeochemical processes, subsequent modeling works focus on long term and climate change analysis of soil acidification (Holmberg et al. 2018). However, Gustafsson et al. (2018) have remarked the limitations of VSD modeling that a more complex model might be able to overcome, especially in terms of a aluminum long term analysis. In summary, dynamic acidification modeling is the only approach to include biogeochemical processes, but it still uses simple physiological plant formulations, and simple descriptions of interaction with hydrology and lacks a description of the shrinking core concept.

From the biogeochemical modeling perspective, on the other hand, biogeochemical cycles have been included as part of the theoretical, field and experimental research in eco-hydrology in the last decade. The most recognized model for carbon, nitrogen and phosphorus is the DNDC model, developed by Li et al. (1992). DNDC has been proved to be well calibrated and has also been improved to include a module for photosynthesis, developed by Aber et al. (1992;) and Li et al. (2000). However, the equations of the DNDC are not completely physically based. The processes of nitrification, denitrification and organic matter oxidation are modeled using conceptual equations and not chemical kinetics or chemical equilibrium. The SWAT model, developed by Neitsch et al. (2011), includes chemical kinetics and chemical equilibrium equations; however, biogeochemical processes are not tied to the gross primary production.

Recently, other simulation codes have been developed for different environmental issues and with different capabilities. VELMA, by Abdelnour et al. (2013), is a complete environmental code model for carbon, nitrogen and hydrology cycles in the soil matrix, but it does not have an optimality principle for modeling, especially modeling plant physiology in photosynthesis and carbon allocation. DayCENT is another code model by Hartman (2009). It includes elements to those in VELMA, but it does not include photosynthesis modeling. Finally, the tRIBS+VEGGIE model by Ivanov et al. (2008) offers an innovative formulation for topography and flow at the watershed level. The formulation of the entire system of watershed processes is similar to that in DHSVM, but it improves on DHSVM’s formulation by adding triangle modeling of the spatially distributed processes in the watershed, computing carbon allocations explicitly, and being coupled to the carbon assimilation Farquhar model. However, tRIBS+VEGGIE does not account for the nitrogen process or carbon diffusion and does not use any optimality formulation. Other models, such as Johnson et al. (2014) and Quijano et al. (2012), use an empirical approach to estimate stomatal conductance and do not couple chemical equilibrium in the dynamical equations for organic matter oxidation, nitrification-denitrification and dissolved carbon dioxide efflux. Nevertheless, these models do not use an optimality framework; instead they use an empirical approach to represent stomata conductance, and the effect of pH on the biochemical cycles is not completely modeled as proposed by Hofmann (2009) and Hofmann et al. (2008). Therefore, this work plans to bring together the optimality principle and carbon and nitrogen cycles modeling, to describe vegetation growth dynamics and to have it coupled to chemical equilibrium for pH and pyrite oxidation, in an integrated mathematical framework.

Because a more comprehensive biogeochemical-pyrite oxidation modeling is needed to gain more insight on interacting phytoremediation processes and to act as a tool to assess bioremediation, the work of this part of the dissertation develops and explores the modeling details of vegetation cover as one part of a remediation tool on coal piles of abandoned mines. We focus our modeling work on two main questions: a) how do the interactions between biogeochemical and pyrite oxidation processes operate within AMD; and b) what are the remediation effects on of using grass or higher types of vegetation species as trees on reducing AMD pollution.

This chapter presents the formulation, an analysis and the results of the Hydro-Biogeochemical model stage of the dissertation in three sections: a) The mathematical components and formulation of the interactions between biogeochemical and pyrite oxidation processes; b) the description of the codes used and the components of the computational implementations for the general mathematical model; c) a qualitative system dynamics analysis of the main processes derived from the mathematical components equations; d) a validation of the model using a combination of laboratory experiments data and Mather site data; e) simulations analyses of each interaction separately and f) scenarios of remediation with grass vegetation and tree vegetation as an overall assessment of the combined biogeochemical and pyrite interactions.

3.2 Mathematical Model Formulation

The aim at this second stage of the model development is a more physical and chemical based representation of integrated hydrological and biogeochemical processes interacting with pyrite oxidation. In general, the model implementation is intended to make comprehensible the effect of vegetation as a passive remediation on coal piles refuse through the internal feedbacks among said processes (Johnson and Hallberg 2005; Plaza et al. 2017; Plaza 2018; Xu 2013; Xu et al. 2020). The main modeling task is to extend the Hydro-Thermal-Geochemical HTGCM model developed by Xu (2013) and Xu et al. (2020) to involve biogeochemical processes as representation of the vegetation phytoremediation. We introduced a general description of plant physiology including the soil moisture dynamics coordinated with carbon assimilation and evapotranspiration variables. The plant growth as allocation of carbon and nitrogen is represented and is closely linked to soil pools of carbon and nitrogen cycles. In the soil matrix, we developed a representation of biogeochemical processes such as organic matter oxidation, nitrification and solute plant uptake considering more comprehensive interactions with pyrite oxidation, acidic ions formations and metals chemical equilibrium. Figure 38 is a schematic representation of all interactions among the hydrology, plant-biogeochemical processes (shown in the upper part of the figure) and the pyrite oxidation and contaminant transport processes (shown in the lower part of the figure).

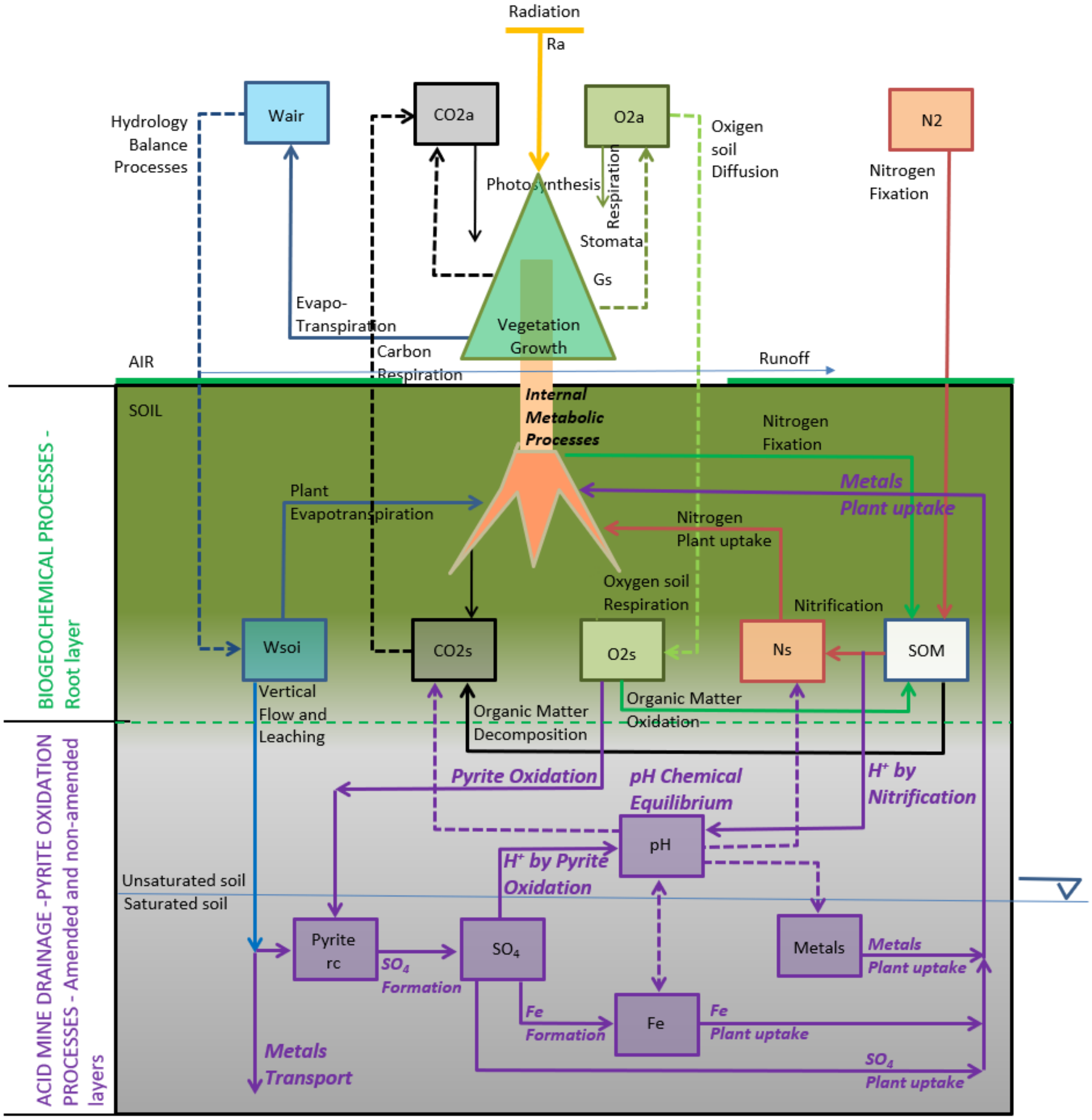

Figure 38 Schematic representation of the main interactions between Acid Mine Drainage with pyrite oxidation (Xu 2013; Xu et al. 2019) and biogeochemical processes (included in this study as a contribution) using vegetation as passive bioremediation. The violet arrows represents the fluxes between pyrox processes and biogeochemical processes. Dashed violet arrows show the effect of pH chemical equilibrium over metals and biogeochemical species. The mathematical model aims to describe the above processes.

The complete mathematical model at this stage could be summarized as a system of ordinary-partial differential and algebraic equations linked to describe such hydrological, biogeochemical and chemical variables as they evolve. The first component of the model is the non-linear algebraic system of equations described in Chapter 2, used for the description of soil moisture dynamics integrated with plant physiological variables. The second component is devoted to the plant growth and biochemical cycles, using linear differential equations that represent lumped carbon and nitrogen pools in both plant allocations and soil matrix. The third component of the model is formed by a system of partial non-linear differential equations to represent in a more detailed manner the transport and reaction dynamics of the biogeochemical processes of organic matter oxidation, nitrification and plant uptake within the soil matrix. The fourth and last component is integrated system of non-linear partial and algebraic equations as described in Gerke et al. (1998), Wunderly et al. (1996), Xu et al. (2019) and Xu (2013) to compute the pyrite oxidation and chemical equilibrium.

The following subsections detail the components described in the above paragraph: a) each process modeled, b) the system of equations and c) the connections used to represent the interactions among the processes.

3.2.1 Plant Physiology Processes and Soil Moisture Dynamics

This first component of the general model represents an interaction between plant physiology processes (carbon assimilation and evapotranspiration) and soil moisture conditions. The effect of evapotranspiration on soil moisture is the key to such interaction and is the basis for further interactions later in the model. The main soil hydrology process modeled is the unsaturated zone flow which follows the Darcy Law and considers two main components: soil moisture conditions and water soil potential as the driving force for the flux movement. The Richards Equation allows the unsaturated flow, representation based on balance mass, using soil moisture and water leaf potential as main variables. We also use Clapp and Hornberger (1978) equations to define relationships between soil moisture θ and water soil potential Ψs. In the mass balance equation, we include evapotranspiration as computed by the optimal-empirical approach developed in Chapter 2. The equations used for soil moisture and water soil potential are described as follows,

$$\frac{\partial\theta}{\partial t} = \frac{\partial}{\partial z}\left[K_s\left(\frac{\partial\Psi_s}{\partial z} - 1\right)\right] - E_z \qquad [\ 3.1\ ]$$

$$K(\theta) = K_s\left[\frac{\theta}{\theta_s}\right]^{2b+3} \qquad [\ 3.2\ ]$$

$$\Psi_s(\theta) = \Psi_s^*\left[\frac{\theta}{\theta_s}\right]^{-b} \qquad [\ 3.3\ ]$$

where θ [m^3/m^3] is soil moisture content; θ_s [m^3/m^3] porosity; K [m/s] actual vertical conductivity; K_s [m/s] vertical conductivity at saturation; Ψ_S [MPa] soil water potential; Ψ^*_S [MPa] soil water potential at saturation, a and b are soil parameters. E_z [m/s/m] is the actual evapotranspiration distributed along the soil depth.

In addition to soil moisture and water soil potential, we include plant physiology processes to complete the first component of the model. Carbon assimilation, evapotranspiration, stomatal conductance, water leaf potential and CO_2 in-leaf concentration are the main plant processes introduced in the equations as explained in Chapter 2. The optimal-empirical approach is the method by which the equations are solved. Carbon assimilation is a measure of the photosynthesis of plants and is represented by the Collatz-Farquhar biochemical model (Farquhar et al. 1980).

Carbon diffusion is the limiting supply for carbon assimilation and is described by a Fickian law equation using stomatal conductance and driving force based on the difference between atmospheric CO_2 concentration and CO_2 in-leaf concentration (Daly et al. 2004; Leuning 1995; Luo et al. 2013; Medlyn et al. 2011; Prentice et al. 2014; Tuzet et al. 2003). Evapotranspiration is related to the stomatal conductance Leaf Area Index and main meteorological forcing data using the Penman Monteith equation (ASCE 2000; Wigmosta et al. 2002). Evapotranspiration is also computed using a capacitance-resistance equation of the plant hydraulics that relates water soil potential and water leaf potential (Katerji et al. 1986; Luo et al. 2013). The Prentice Optimal Theory (Prentice et al. 2014) is adapted to use the above equations and constrained by the empirical equation for stomatal conductance. The above described equations lead to a compact form of a system of equations with Equation 2.2 (or Equation 2.3), Equation 2.4 and Equation 2.5 as shown in chapter 2.

Therefore, the system of equations of the first component of the model is composed of a partial differential equation on soil moisture (Equation 3.1) and two non-linear algebraic equations on water leaf potential and CO_2 in-leaf concentration (Equation 2.2 and Equation 2.4). The other equations (Equation 3.2 and Equation 3.3) are auxiliary constraints of the system, as explained in Chapter 2.

Lastly, there are four interactions with other components of the model: a) the Gross Primary Productivity *GPP*, an output from this part of the model, is the main input for the plant growth biochemical component, explained in the next subsection, 3.2.2; b) the soil moisture computed in this component is used in the third and fourth parts of the model for the chemical and biogeochemical vertical transport-reactive equations; c) the evapotranspiration computed in soil layers is used for metal and biochemical solutes plant uptakes; d) this component of the model uses the Leaf Area Index *LAI* computed in the second component in the Penman-Monteith equation for evapotranspiration and in the *GPP* computation. The general equation for *GPP* is shown as follows,

$$GPP = LAI \int_{day} A_n \, dt \qquad [3.4]$$

where *GPP* [grC/m^2/day] is gross primary production; LAI [m^2/m^2] leaf area index; and A_n [mol/m^2/s] net carbon assimilation.

3.2.2 Carbon and Nitrogen Biochemical Cycles Processes

The second component of the model computes plant carbon storage pools, carbon fluxes, plant nitrogen storage pools, nitrogen fluxes, surface litter and soil organic components following Potter and Randerson (1993), Schaefer et al. (2008), Wang et al. (2010) and Wang et al. (2007), which model is known as the CASACNP (Carnegie-Ames-Stanford-Approach – Carbon-Nitrogen-Phosphorus) model. This portion of the entire model represents the gross carbon assimilation by plants and the subsequent carbon allocation into the three plant components: a) carbon leaf, b) carbon wood and c) carbon root. Moreover, this component of the model describes the nitrogen plant uptake and its allocation within the nitrogen plant components: a) nitrogen leaf, b) nitrogen wood and c) nitrogen root. Both plant carbon and plant nitrogen pools can be considered as a description of plant growth. Plant carbon pool is affected by plant nitrogen leaf pool through a limitation of the *GPP* in the Net Primary Productivity *NPP* as representation of plant respiration. On the other hand, plant nitrogen pools are affected indirectly by plant carbon leaf pool via Leaf Area Index *LAI* through evapotranspiration. This component of the model also computes the carbon and nitrogen pools of surface litter from the plants. Consequently, this part of the model describes the organic carbon and nitrogen soil storage which come from the respective litter pools.

In this study, we used a system of multi-connected linear ordinary differential equations for the pools described in the last paragraph, similar to that in the CASACNP model (Wang et al. 2010). Furthermore, we added two constraints equations to the system of differential equations computing two pools variables (carbon soil microbial and mineral nitrogen) in the following component of the model (the biogeochemical transport-reactive part in subsection 3.2.3). The main input forcing data for the system of equations is the *GPP* computed by the first component, as shown in subsection 3.2.1. The carbon storage pools for plants are represented by linear differential equations with *GPP* as an external source and a decay term. The computation of *LAI*, used in the later component of the model (subsection 3.2.1), is computed at this point based on the carbon leaf pool Equation 3.7. The nitrogen plant pools have the mineral nitrogen uptake term (computed in the third component of the model, subsection 3.2.3) as a main external source and also decay terms to describe plant turnover. Each external source term has a fraction factor which corresponds to the allocation portion of each part of the plant. The differential equations (Equations 3.5 and 3.6) for plant carbon and nitrogen pools are similar to those described in the CASACNP model and are shown as follows.

$$\frac{dC_{Plant\ i}}{dt} = F_{AlloC\ i}\ GPP - k_{Plant\ i}\ C_{Plant\ i} \tag{3.5}$$

$$\frac{dN_{Plant\ i}}{dt} = F_{AlloN\ i}\ F_{Uptake} - k_{Plant\ i}\ N_{Plant\ i}\ F_{NP-L\ i} \tag{3.6}$$

$$LAI = S_{LAI}\ C_{Plant-Leaf} \tag{3.7}$$

where $C_{Plant\ i}$ [grC/m^2] is carbon plant pools with i = *Leaf, Wood and Root*; $F_{AlloC\ i}$ [%] fraction of carbon allocation to i pool; $k_{Plant\ i}$ [day^{-1}] decay coefficient or turnover rate for plant pool i; $N_{Plant\ i}$ [grN/m^2] nitrogen plant pools; F_{Uptake} [grN/m^2/d] mineral nitrogen plant uptake; $F_{AlloN\ i}$ [%] fraction of nitrogen allocation to i pool; $k_{Plant\ i}$ [day^{-1}] decay coefficient or turnover rate; $F_{NP\text{-}L\ i}$ [%] fraction transfer from nitrogen plant i to nitrogen litter pools; S_{LAI} [m^2/m^2] specific leaf area index; $C_{Plant\text{-}Leaf}$ [grC/m^2] carbon leaf pool.

The litter storage pools for carbon and nitrogen are: a) metabolic, b) structural and c) coarse woody debris (CWD). The differential equations for the litter pools have the decay terms of the plant pools equations as external sources. The litter pools equations also have decay terms which represent mass transfer to soil organic pools. The following equations correspond to the carbon and nitrogen litter pools:

$$\frac{dC_{Litter\ j}}{dt} = F_{FluxCj} - k_{Litter\ j}\, C_{Litter\ j} \qquad [3.8]$$

$$\frac{dN_{Litter\ j}}{dt} = F_{FluxN\ j} - k_{Litter\ j}\, N_{Litter\ j} \qquad [3.9]$$

where $C_{Litter\ j}$ [grC/m^2] is carbon litter pools where j = *Metabolic, Structural and CWD*; $F_{FluxC\ j}$ [grC/m^2/day] flux of carbon to litter pool j; $k_{Litter\ j}$ [day^{-1}] decay coefficient or turnover rate for litter pool j; $N_{Litter\ j}$ [grN/m^2] nitrogen litter pools; and $F_{FluxN\ j}$ [grN/m^2/day] flux of nitrogen to litter pool j.

As the final part of this second component of the model, the carbon and nitrogen organic soil differential equations have three pools: a) microbial, b) slow and c) passive. The source terms of each of the soil organic differential equations are composed of litter decay terms. Similar, to the equations presented in the above paragraphs, these soil organic pools equations have decay terms which represent carbon and nitrogen oxidation. As special cases, the carbon soil microbial and mineral nitrogen pools are computed in the third component of the model (explained in subsection 3.2.3) such that we can assume these two variables as inputs for this second component of the model. The special computation of these two variables (mineral nitrogen and organic carbon matter) is an improvement over the original formulation of the CASA model (Wang et al. 2010). The differential equations (Equations 3.10 and 3.11) for carbon and nitrogen soil pools are presented below,

$$\frac{dC_{Soil\,k}}{dt} = F_{FluxC\,k} - k_{Soil\,k}\, C_{Soil\,k} \qquad [3.10]$$

$$\frac{dN_{Soil\,k}}{dt} = F_{FluxN\,k} - k_{Soil\,k}\, N_{Soil\,k} \qquad [3.11]$$

$$C_{Soil-mic} = A_{cell} \int_{z=0}^{z=RootDeptH} C_{OM}(z)\, \theta(z)\ dz \qquad [3.12]$$

$$N_{min} = A_{cell} \int_{z=0}^{z=RootDeptH} [C_{NO3}(z) + C_{NH4}(z)]\, \theta(z)\ dz \qquad [3.13]$$

where $C_{Soil\ k}$ [grC/m^2] is carbon soil pools with k = *Microbial, Slow and Passive*; $F_{FluxC\ k}$ [grC/m^2/day] flux of carbon to soil k pool; $k_{Soil\ k}$ [day^{-1}] decay coefficient or turnover rate for soil pool k; $N_{Soil\ k}$ [grN/m^2] nitrogen soil pools; $F_{FluxN\ k}$ [grN/m^2/day] flux of nitrogen to soil k pool; $C_{Soil\text{-}mic}$ [grC/m^2] carbon soil microbial pool representing the soil organic matter; C_{OM} [mg/L] organic matter concentration; N_{Min} [grN/m^2] mineral nitrogen pools; C_{NO3} [mg/L] nitrates concentration; and C_{NH4} [mg/L] ammonium concentration.

There are four other interactions between this component of the model and the other three. The first and second interactions are the use of the nitrogen plant uptake and nitrogen leaching rates, computed in the inorganic biogeochemical component of the model (Subsection 3.2.3), as part of internal fluxes for nitrogen pools in this component. The third interaction is the use of flux of carbon from litter to soil, computed at this point as an upper boundary condition for the organic matter concentration equation in the third component of the model (Subsection 3.2.4). The fourth interaction is transferring the mineral nitrogen fluxes such as deposition and mineralization to be used as spatially distributed sources for the subsequent partial differential equations (third component of the model, Subsection 3.2.3).

3.2.3 Soil Inorganic Biogeochemical Dynamics and Chemical Equilibrium of pH

In this third component of the model, the computation of the spatially distributed and dynamic biogeochemical processes is presented linked to carbon and nitrogen cycles and to soil moisture dynamics. The computation of microbial soil carbon and mineral nitrogen in this component replaces the original CASACNP estimation (the use of partial differential equations in our study instead of the lumped ordinary differential equation used in CASA) as an improvement over the CASA model. This improvement of the original formulation of the CASA model is needed due to the lack of explicit modeling of nitrification and denitrification processes (Wang et al. 2010). In addition, we are including the interactions between the biogeochemical processes and the pH using the chemical equilibrium equations among inorganic carbon and nitrogen species as well as representing the plant uptake of solutes (nutrients and metal pollutants) in an integrated manner along with the reactive and transport dynamics.

At this point in the model, the general form of the equations to describe the details of transport, organic matter oxidation, nitrification and denitrification is based on a partial differential equation that includes soil moisture, vertical discharge, external sources and reactions terms. The general concept we used to build this configuration of the equations is specifically based on

Hofmann (2009) and Hofmann et al. (2008) to capture the effect of biogeochemical reactions on the pH and based on Berlin et al. (2015) and Berlin et al. (2014) to describe nitrogen solute transport with nitrification and denitrification. We can arrange the partial differential equations in three groups: a) The oxidation-nitrification processes equations, b) the ammonia equations and c) the inorganic carbon equations. The pH chemical equilibrium equations are the final portion of this third component of the model. The numerical solution of the biogeochemical reactive-transport model is explained in Appendix C.

The first group of partial differential equations (Equations 3.14, 3.15 and 3.16) is devoted to model soil organic matter concentration (spatially distributed variable equivalent to carbon soil microbial pool), nitrates and generation of hydrogen ions by nitrification. The computation of soil organic matter replaces the microbial soil carbon in CASACNP; the summation of nitrates and ammonium replaces the mineral nitrogen computation in CASACNP. All these computations are coordinated within the CASACNP model to compute internally other soil carbon and nitrogen pools and fluxes. The equations include soil unsaturated vertical transport of the solutes, reaction terms and external sources. The description of the equations, the special terms, and the initial and boundary conditions are shown below,

$$\frac{\partial(\theta C_{OM})}{dt} = -\frac{\partial(qC_{OM})}{\partial z} - R_{ox} + F_{OM} \qquad [3.14]$$

$$\frac{\partial(\theta C_{NO3})}{dt} = -\frac{\partial(q\,C_{NO3})}{\partial z} + R_{nit} - R_{denit} + F_{NO3} \qquad [3.15]$$

$$\frac{dH^{+}_{nit}}{dt} = 2R_{nit} \qquad [3.16]$$

where C_{OM} [mg/L] is organic matter concentration; C_{NO3} [mg/L] nitrates concentration. R_{ox}, R_{nit} *and* R_{denit} [mg/L/d] are organic oxidation, nitrification and denitrification rates, respectively; F_{OM}

[mg/L/d] source of organic matter; F_{NO3} [mg/L/d] source of nitrates; and H^{+} Hydrogen Ion concentration [mg/L].

Among the parameters, $R_{ox} = - r_{ox} C_{OM} [C_{O2}/(C_{O2}+K_{MO})]$ obtained with initial conditions C_{OM} ($t=0$, z) = $C_{Soil\text{-}mic}$ (t=0) A_{cell} /(A_{cell} dZ θ) $Fracc_{z}$, and boundary conditions F_{OM} (t, z=0) = $F^{CASA}_{CSoil,\, mic}$ A_{cell}; F_{OM} (t, z>0) = - $E_{z} A_{cell} C_{OM}$. Also, $R_{nit} = r_{nit} C_{NH4} [C_{OX}/(C_{OX}+K_{O})]$; $R_{denit} = - r_{dnit} C_{OM} [C_{NO3}/(C_{NO3}+K_{OM})]$ having initial conditions C_{NO3} ($t=0$, z) = 0.5 N_{min} (t=0) A_{cell} /(A_{cell} dZ θ) $Fracc_{z}$; and boundary conditions F_{NO3} (t, z=0) = 0.5 F^{CASA}_{Ndep} $A_{cel..}$ *Finally,* F_{NO3} (t, z>0) =0.5 ($F^{CASA}_{Nfix} + F^{CASA}_{Nnet} + F^{CASA}_{Nloss}$) $A_{cell}\, Fracc_{z} - E_{z} A_{cell} C_{NO3}$; F_{NO3} (t, z=$Depth_{bio}$) = - q(z=$Depth_{bio}$) A_{cell} C_{NO3}(z=$Depth_{bio}$).

The second group of equations (Equations 3.17 and 3.18) correspond to ammonia nitrogen species (ammonia and ammonium ion). The equations represent the vertical transport and the effect of oxidation and nitrification interaction with organic matter and nitrates. The computation of ammonia nitrogen species is key to represent nutrient plant uptake and the soil chemical equilibrium pH linked to pyrite oxidation. This computation is coordinated with the effect of nitrification on the pyrite oxidation by the Hydrogen Ion production. The equations with special terms, initial values and boundary conditions are cited as follows,

$$\frac{\partial(\theta C_{NH3})}{dt} = -\frac{\partial(q\ C_{NH3})}{\partial z} + R_{ox} + F_{NO3} \qquad [3.17]$$

$$\frac{\partial(\theta C_{NH4})}{dt} = -\frac{\partial(q\ C_{NH4})}{\partial z} - R_{nit} + F_{NH4} \qquad [3.18]$$

where C_{NH3} [mg/L] is ammonia concentration; C_{NH4} [mg/L] ammonium concentration. C_{NH3} *has* initial conditions C_{NH3} ($t=0$, z) = 0 and boundary conditions F_{NH3} (t, z>0) = - $E_{z} A_{cell} C_{NH3}$; C_{NH4} has initial conditions C_{NH4} ($t=0$, z) = 0.5 N_{min} (t=0) A_{cell} /(A_{cell} dZ θ) $Fracc_{z}$, and boundary conditions F_{NH4} (t, z=0) = 0.5 $F^{CASA}_{Ndep}\ A_{cell}$; F_{NH4} (t, z>0) =0.5 ($F^{CASA}_{Nfix} + F^{CASA}_{Nnet} + F^{CASA}_{Nloss}$) $A_{cell}\ Fracc_{z}$ - $E_{z}\ A_{cell}\ C_{NH4}$; F_{NH4} (t, z=$Depth_{bio}$) = - q(z=$Depth_{bio}$) $A_{cell}\ C_{NH4}$(z=$Depth_{bio}$).

The third group of partial differential equations (Equations 3.19, 3.20 and 3.21) represent the inorganic carbon species (carbon dioxide, bicarbonate and carbonic acid). The equations below describe the transport and the oxidation effect on carbon sub products:

$$\frac{\partial(\theta C_{CO2})}{dt} = -\frac{\partial(q\ C_{CO2})}{\partial z} + \gamma\ R_{ox} + F_{CO2} \qquad [3.19]$$

$$\frac{\partial(\theta C_{HCO3})}{dt} = -\frac{\partial(q\ C_{HCO3})}{\partial z} + F_{HCO3} \qquad [3.20]$$

$$\frac{\partial(\theta C_{CO3})}{dt} = -\frac{\partial(q\ C_{CO3})}{\partial z} + F_{CO3} \qquad [3.21]$$

where C_{CO2} [mg/L] is carbon dioxide concentration; C_{HCO3} [mg/L] bicarbonate concentration; C_{CO3} [mg/L] acidic carbon concentration; F_{CO2} [mg/L/d] source of carbon dioxide; F_{HCO3} [mg/L/d] source of bicarbonate; F_{CO3} [mg/L/d] source of acidic carbon; and γ stochiometric relation between nitrates and carbon dioxide. These equations have the initial conditions, C_{CO2} ($t=0$, z) = C_{HCO3} ($t=0$, z) = C_{CO3} ($t=0$, z) = 0; and boundary conditions F_{CO2} (t, z>0) = - $E_{z}\ A_{cell}\ C_{CO2}$; F_{HCO3} (t, z>0) = - $E_{z}\ A_{cell}\ C_{HCO3}$; and F_{CO3} (t, z>0) = - $E_{z}\ A_{cell}\ C_{CO3}$.

The final part of this system of equations (Equations 3.22, 3.23, 3.24, 3.25 and 3.26) is intended to show the effect of the pH (produced by the pyrite oxidation and metals chemical equilibrium as explained in subsection 3.2.4) on the inorganic carbon and nitrogen species chemical equilibrium. Mass action equations (Equations 3.22, 3.23, 3.24) and total balance of species equations (Equations 3.25 and 3.26) are used at this portion of the component and are shown below,

$$[C_{NH4}] - \frac{[C_{NH3}][H^+]}{K_{NH4}} = 0 \quad [3.22]$$

$$[C_{HCO3}] - \frac{[C_{CO3}][H^+]}{K_{HCO3}} = 0 \quad [3.23]$$

$$[C_{CO2}] - \frac{[C_{HCO3}][H^+]}{K_{CO2}} = 0 \quad [3.24]$$

$$[C_{TN}] = [C_{NH3}] + [C_{NH4}] \quad [3.25]$$

$$[C_{TC}] = [C_{CO2}] + [C_{HCO3}] + [C_{CO3}] \quad [3.26]$$

where C_{TC} [mg/L] is total carbon mass concentration; C_{TN} [mg/L] total nitrogen mass concentration; K_{NH4} [mg/L] ammonium equilibrium constant. K_{HCO3} [mg/L] bicarbonate equilibrium constant; and K_{CO2} [mg/L] carbon dioxide equilibrium constant.

In summary, this component of the entire model constrains the computation of the second component (the carbon and nitrogen biogeochemical cycles component) via the microbial soil carbon pool and mineral nitrogen. This interaction includes the input flux of carbon soil from the carbon-nitrogen cycles model and the deposition-fixation-mineralization input flux of mineral carbon, which also form the second component. Finally, nitrification and organic matter oxidation is computed to be transferred to the pyrite oxidation process.

3.2.4 Pyrite Oxidation and Transport Metals Processes

This fourth and last component of the whole model is devoted describing pyrite oxidation (as the main chemical reaction part of Acid Mine Drainage AMD) alongside transport of metals and the chemical equilibrium as formulated in Gerke et al. (1998), Wunderly et al. (1996) and Xu (2013). In this context, the oxidation of pyrite (sulphide mineral) and its sub products can be described using the next chemical equations, where Equation 3.28 summarizes the two step reaction equations Equation 3.27 and Equation 3.28 as follows,

$$FeS_2 + H_2O + 7/2\ O_2 \rightarrow Fe^{2+} + 2SO^{2-}_4 + 2H^+ \qquad [3.27]$$

$$Fe^{2+} + 1/4\ O_2 + H^+ \rightarrow Fe^{3+} + 1/2\ H_2O \qquad [3.28]$$

$$FeS_2 + 1/2\ H_2O + 15/4\ O_2 \rightarrow Fe^{3+} + 2SO^{2-}_4 + 2H^+ \qquad [3.29]$$

The process of oxidation of pyrite, i.e. the formation of Ferric sub products, Sulfate ions and hydrogen ions, can be explained by the depletion of dissolved oxygen in the soil matrix (the coal refuse tailings) and the internal oxygen diffusion into the quasi-spherical particles of pyrite (Wunderly et al. 1996; Xu 2013). As the oxygen can get into the pyrite particles, an oxidized coat is formed around the unreacted inner core of the particle. Therefore, a reduction of the inner core particle is expected as the oxidation progress. Based on this description, Xu (2013) developed the equations for pyrite oxidation using a partial differential equation (Equation 3.30) for the dissolved oxygen and an ordinary differential equation (Equation 3.31) for the shrinking core of the unreacted particle through. We added some terms to include interactions with biogeochemical processes. The equations for the pyrite process are shown below,

$$\frac{\partial(\theta_a\,[O_2])}{\partial t} = \frac{\partial}{\partial z}\left[\theta_a D_a\ \frac{\partial[O_2]}{\partial z}\right] - D_w\,\frac{3\,(1-\theta)}{R^2}\left[\frac{r_c}{R-r_c}\right]\frac{[O_2]}{H} - R_{ox} \qquad [3.30]$$

$$\frac{dr_c}{dt} = -D_w\,\frac{(1-\theta)}{\varepsilon\,\rho_s}\,\frac{R}{r_c\,(R-r_c)}\,\frac{[O_2]}{H} \qquad [3.31]$$

where $[O_2]$ [mg/L] is dissolved oxygen concentration; θ_a [m^3/m^3] void space ratio; θ [m^3/m^3] soil moisture ratio; D_a [m/s] oxygen dispersion in gas phase; D_w [m/s] oxygen dispersion in liquid phase into the pyrite particle; r_c [m] shrinking core particle radius; R [m] initial pyrite particle radius; H [-] Henry equilibrium constant; ε chemical proportion; and ρ_s [Kg/m^3] soil density.

Once the dissolved oxygen and the equivalent radius of the shrinking core are computed, it is possible to quantify the formation of sulfate ions, the ferric ions and the Hydrogen ion as follows:

$$\Delta SO_4 = \frac{\rho_s]_m \left(\left(r_c]_m^{t+\Delta t}\right)^3 - \left(r_c]_m^{t}\right)^3\right)}{(R]_m)^3} \qquad [3.32]$$

$$\Delta Fe = \frac{W_{Fe}\,\Delta \mathrm{SO}_4}{2.0\,W_S} \qquad [3.33]$$

$$\Delta H^{+}_{pyrox} = 2.0\,\frac{\Delta \mathrm{Fe}}{W_{Fe}}\,ratio + \frac{\Delta \mathrm{Fe}}{W_{Fe}}\,(1 - ratio) \qquad [3.34]$$

$$Eq\big[[SO_4],[Fe],[Ca],[Na],[Mg],[K],[Si],[P],[Al],[Cl],[Mn],[H^+]\big] = 0 \qquad [3.35]$$

where ΔSO_4 [mg/L/d] is sulfate production by pyrite oxidation in a time step; ΔFe [mg/L/d] ferric ions production by pyrite oxidation in a time step; ΔH^{+}_{pyrox} [mg/L/d] hydrogen ions production by pyrite oxidation in a time step; W_{Fe} [gr/mol] Ferric ion molecular weight; W_S [gr/mol] Sulfate ion molecular weight. [SO_4] [mg/L] sulfate ion concentration; [Fe] [mg/L] ferric ion concentration; [*Ca*] [mg/L] Calcium concentration; [*Na*] [mg/L] Sodium concentration; [*Mg*] [mg/L] Magnesium ion concentration; [*K*] [mg/L] Potassium concentration; [*Si*] [mg/L] Silica ion concentration; [*P*] [mg/L] Phosphorus concentration; [Al] [mg/L] Aluminum concentration; [Cl] Chlorine concentration; [Cl] [mg/L] Manganese concentration; and [H^+] [mg/L] Hydrogen ion concentration.

After the formation of Hydrogen ions, sulfates and ferric ions, the other metals are transported vertically along the unsaturated soil matrix according to the next partial differential equations of transport used in Xu (2013):

$$\frac{\partial(\theta\,[C_i])}{\partial t} + \frac{\partial \rho_s}{\partial t} = \frac{\partial}{\partial z}\left[\theta\, D_w\, \frac{\partial [C_i]}{\partial z}\right] - \frac{\partial q [C_i]}{\partial z} - S_i \qquad [3.36]$$

$$S_H = \frac{dH^+_{pyrox}}{dt} + \frac{dH^+_{nit}}{dt} \qquad [3.37]$$

$$S_i = -E_z\, C_i \qquad [3.38]$$

where $[C_i]$ [mg/L] is solute concentration i; θ [m^3/m^3] soil moisture ratio; D_w [m/s] dispersion coefficient in liquid phase within soil matrix; S_H [mg/L/d] source of hydrogen ions in pyrite oxidation time step – daily; S_i [mg/L/d] source-sink of solute i concentration in pyrite oxidation time step – daily; E_z [m/s] plant evapotranspiration distributed in the root depth; H [-] Henry equilibrium constant; ε chemical proportion; ρ_s [Kg/m^3] soil density; q vertical unsaturated discharge; H^+_{pyrox} and H^+_{nit} hydrogen ions production over time from pyrite oxidation and nitrification, respectively.

Finally, we incorporate explicit modeling interactions between pyrite oxidation processes and the biogeochemical processes to quantify some of the effect of vegetation as a passive remediation to the AMD process within coal refuse piles. In Equation 3.30, we added the organic matter oxidation into the original pyrite oxidation equation (Xu 2013; Xu et al. 2020) as the explicit sink term R_{ox}. Moreover, the hydrogen ions production by nitrification is added to pyrite hydrogen ions production in the source term of transport in Equation 3.37 and the metals uptake is also computed using daily evapotranspiration from the physiological component of the model and added to the source term of transport in Equation 3.38. The Appendix D contains the numerical solution of all the components of the model.

3.3 Computational Implementations

This section shows the main algorithm code implementations and uses of predefined codes for the mathematical model solution. The first part outlines the carbon assimilation-evapotranspiration module with the optimal-constrained algorithm as explained in Section 2.3.3 in Chapter 2. The second portion contains the code for biochemical cycles Carnegie-Ames-Stanford-Approach (CASA-CNP). The third discusses is the biogeochemical reactive-transport coding implementation model. The fourth part of this section provides information about the pyrox-Phreeqc and transport component in the DHSVM-HTGCM. The Appendix D shows the mathematical formulation of the numerical solution of the complete system of equations that is implemented in this study using the DHSVM-HTGCM code.

We implement most of the four parts of the mathematical model using DHSVM-HTGCM (Plaza 2018; Xu 2013) as the basic platform code. The original DHSVM model is a computer code for computing hydrology in a spatially distributed watershed (Wigmosta et al. 2002), and it is used in our study to compute the soil moisture dynamics. An improvement to the DHSVM model was developed by Xu (2013) to incorporate pyrite oxidation, transport and chemical equilibrium of pollutant metals, and the effect of soil heat into the reactions. In our improvement of the original DHSVM-HTCGM model (Xu et al. 2019; Xu 2013), we include basic plant physiological, biochemical cycles and soil biogeochemical processes tightly linked to AMD processes. These added processes required modifications in the *evapotranspiration* module, in the *massEnergybalance* module, in the *unsaturatedflow* module and in the general requirements on the *main* part.

Finally, we present the general workflow scheme of coding interactions for the entire system developed in a single column 1D computation.

3.3.1 Carbon Assimilation-Evapotranspiration Module in DHSVM-HTGCM

The implementation of the optimal-empirical approach formulation derived in Chapter 2 within DHSVM-HTGCM is carried out with some input-output interactions added to the pyrox-Phreeqc code. Specifically, the original *evapotranspiration* module is modified including the algorithm explained in Section 2.3.3. The module modification produces as main outputs: a) Gross Primary Production GPP to be used in the carbon biochemical cycle in the code component CASA-CN in the *massEnergybalance* module; and b) computation of daily and distributed evapotranspiration to compute the solute plant uptake for the Pyrox-Phreeqc-Transport model in the initial part of the *unsaturatedflow* module. The first output *GPP* is the main input in the code development of the CASA-CN model. The evapotranspiration output is the key result for the soil moisture, transport and plant uptake computations moving forward within the *unsaturatedflow* module.

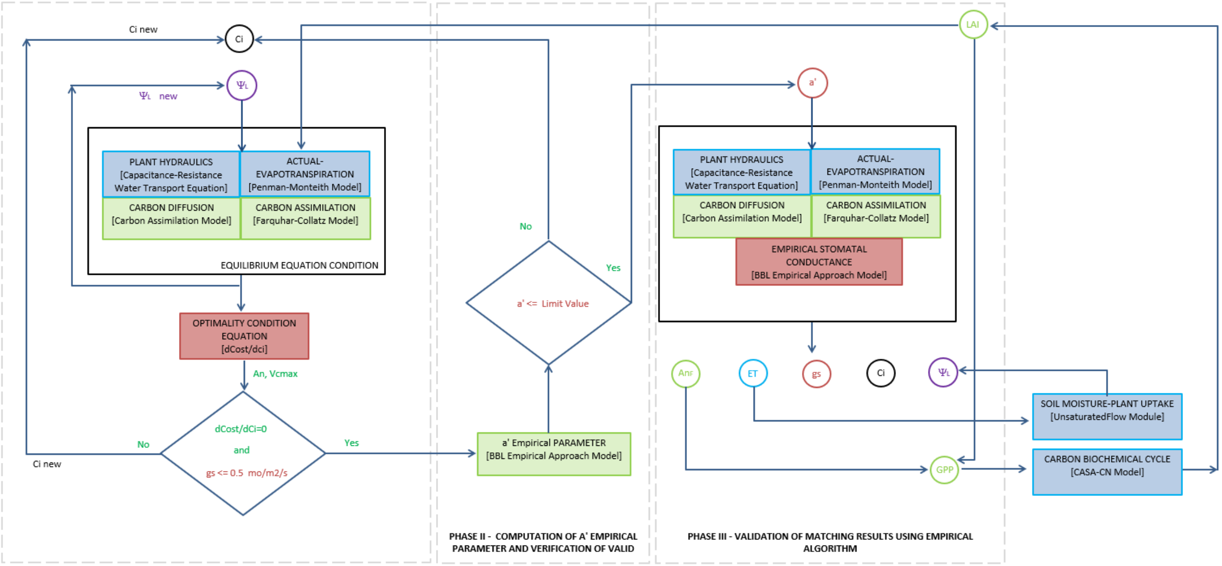

Figure 39 Schematic workflow of computational implementation of carbon assimilation-evapotranspiration module using the optimal-empirical algorithm within the DHSVM-HTGCM model interacting with the unsaturated flow computation part (*unsaturatedFlow* module) and carbon biochemical cycle computation module (CASA-CN) Section 3.3.2.

3.3.2 CASA-CN Model implementation within DHSVM-HTGCM

We implement the CASA-CN code in a comprehensive manner to compute the biochemical carbon and nitrogen cycling within the *massenergybalance* module in DHSVM-HTGCM. We follow the complete equations proposed in Wang et al. (2010) with the following interactions to the others parts of the DHSVM-HTGCM code: a) *GPP* is computed by the *evapotranspiration* module with the optimal constrained algorithm is used as main input and b) CASA-CN variables carbon soil microbial pool and mineral nitrogen pool are taken from the biogeochemical reactive-transport computation as an input each time-step. The parameters defining the CASA-CN pools behavior are taken from the DHSVM-HTGCM model as soil temperature and soil moisture.

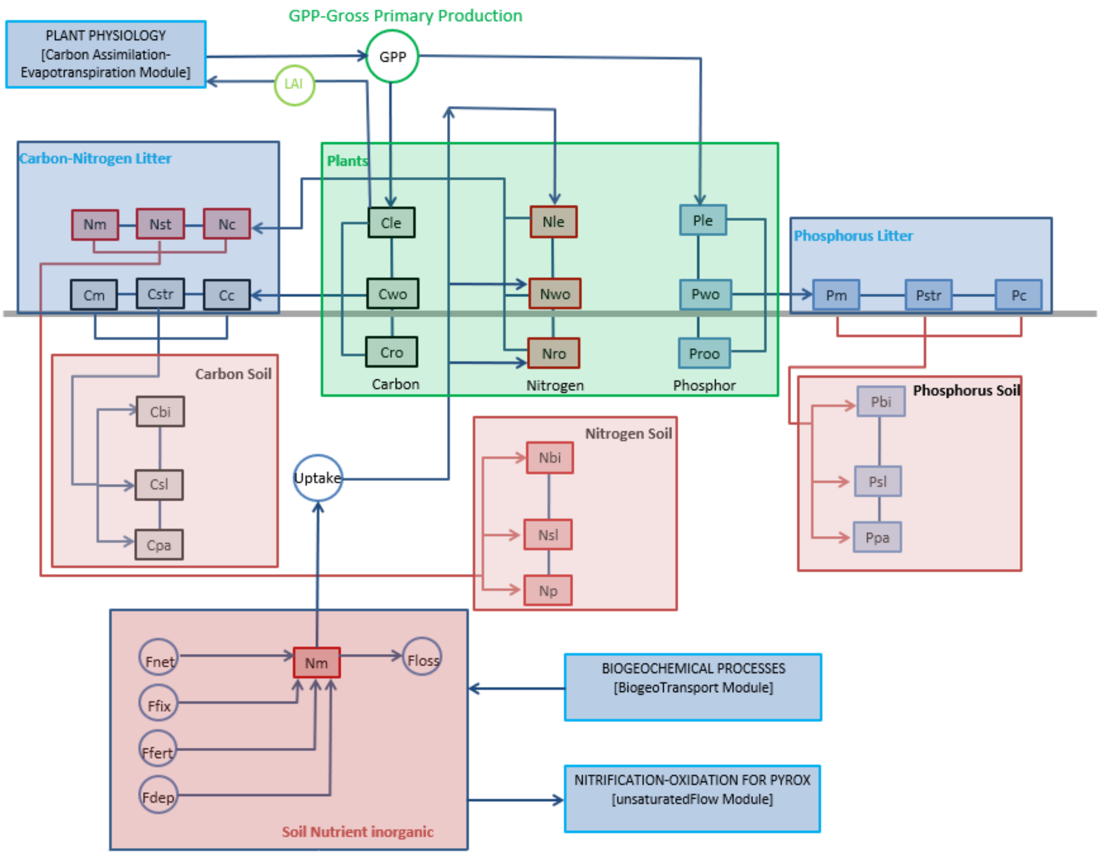

Figure 40 Schematic workflow of computational implementation of biochemical cycles processes in the CASA-CNP model (Wang, 2010) within the DHSVM-HTGCM model interacting with the carbon assimilation-evapotranspiration module Section 3.3.1, unsaturated flow computation part (*unsaturatedFlow* module) and biogeochemical inorganic transport model, Section 3.3.3.

3.3.3 Biogeochemical Transport-Reaction Module

The biogeochemical reactive transport module, one the special features originally developed in this dissertation, is built inside the *unsaturatedflow* module. The general dynamic relationships between soil organic matter, nitrates, ammonia species and inorganic carbon species are computed using a numerical scheme explained in Appendix C. There are three main groups of inputs for the operation of this code: a) The soil hydrology conditions, soil moisture, vertical discharge, and the distributed plant evapotranspiration as computed from the evapotranspiration module; b) the carbon soil and mineral nitrogen fluxes from CASA-CN as external distributed sources in the partial differential equations for organic matter and nitrogen species; and c) the pH and the Oxygen concentration from the pyrox computation. Additionally, the code delivers the following computations to other modules within DHSVM-HTGCM: a) carbon soil microbial pool and total mineral nitrogen as the summation of nitrates and ammonium as a replacement of the soil carbon and mineral nitrogen originally computed in CASA-CN. b) the rate of plant uptake for carbon and nitrogen species to be used in CASA-CN; c) the nitrogen leaching rate also to be used in CASA-CN; d) the rate of Hydrogen Ion production produced by the nitrification process into the pyrite oxidation; and e) the rate of organic matter oxidation also affecting the pyrite oxidation process.

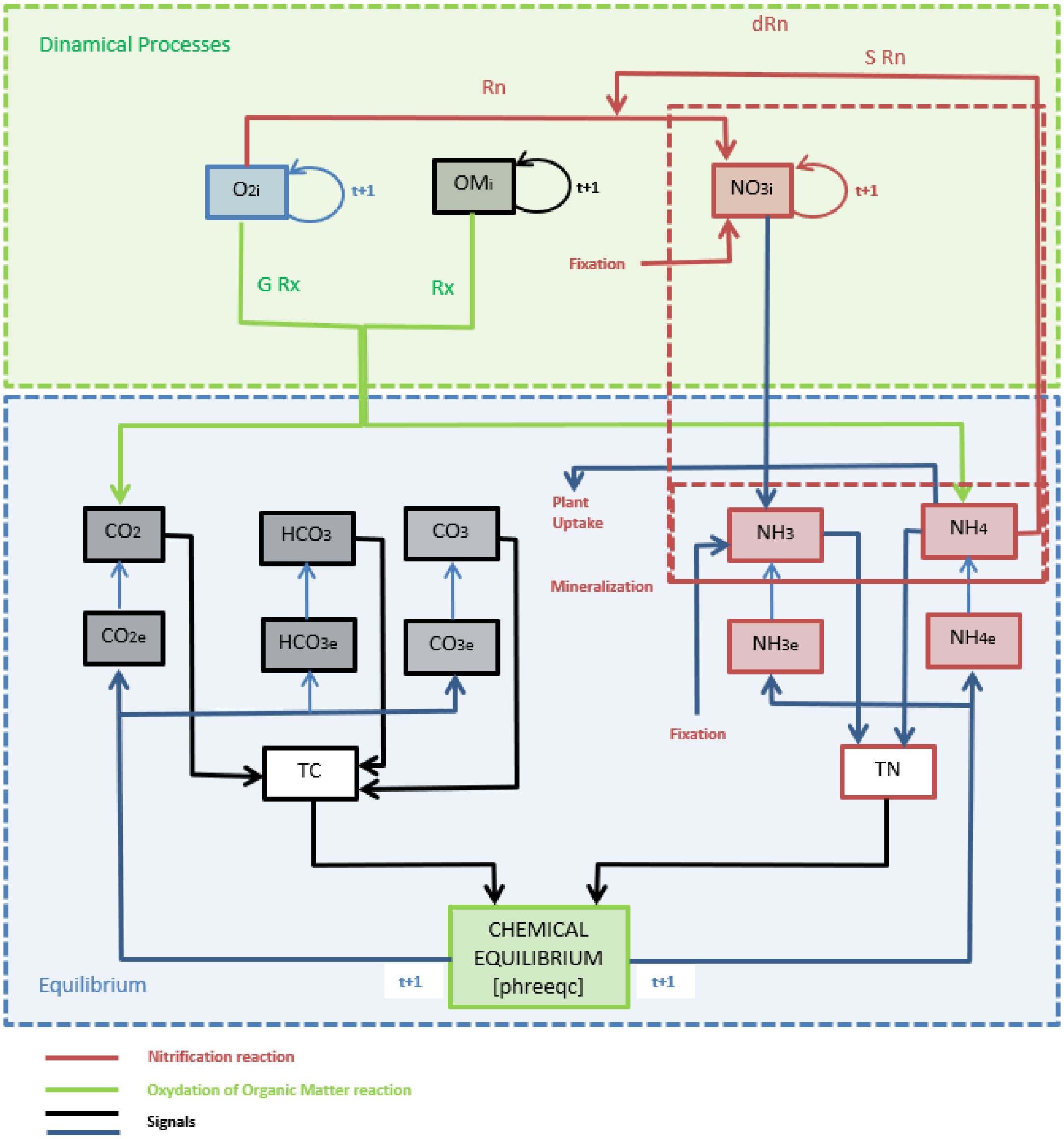

Figure 41 Schematic workflow of computational implementation of biogeochemical inorganic transport model within the DHSVM-HTGCM model interacting with carbon-nitrogen cycles processes (CASA-CN) model, Section 3.3.2, and pyrox module, Section 3.3.4.

3.3.4 Pyrox Module and Phreeqc Model (iPhreeqc version)

The code for the pyrite oxidation and transport processes is built into the *unsaturatedflow* module and includes three other submodule codes: the *oxidation* module, the *soiltransport* module and *Call_prheeqc* module. We initialize and coordinate interaction variables at the beginning of the module using an estimation of biogeochemical nitrification, oxidation and plant uptake before inputting into the *oxidation* module and the *soiltransport* module.

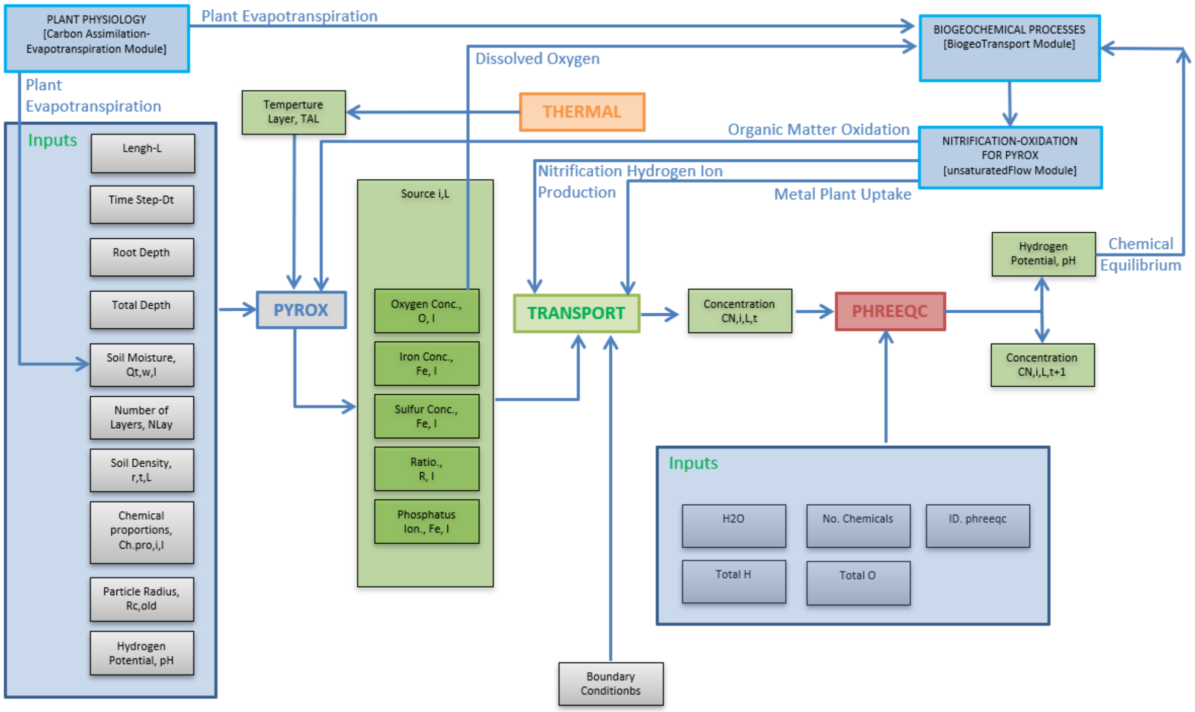

Figure 42 Schematic workflow of computational implementation of pyrite oxidation and metals transport model within the DHSVM-HTGCM (Xu, 2013) model interacting with plant physiology processes module Section 3.3.1, and biogeochemical transport model, Section 3.3.3.

3.3.5 Complete Model Framework Workflow

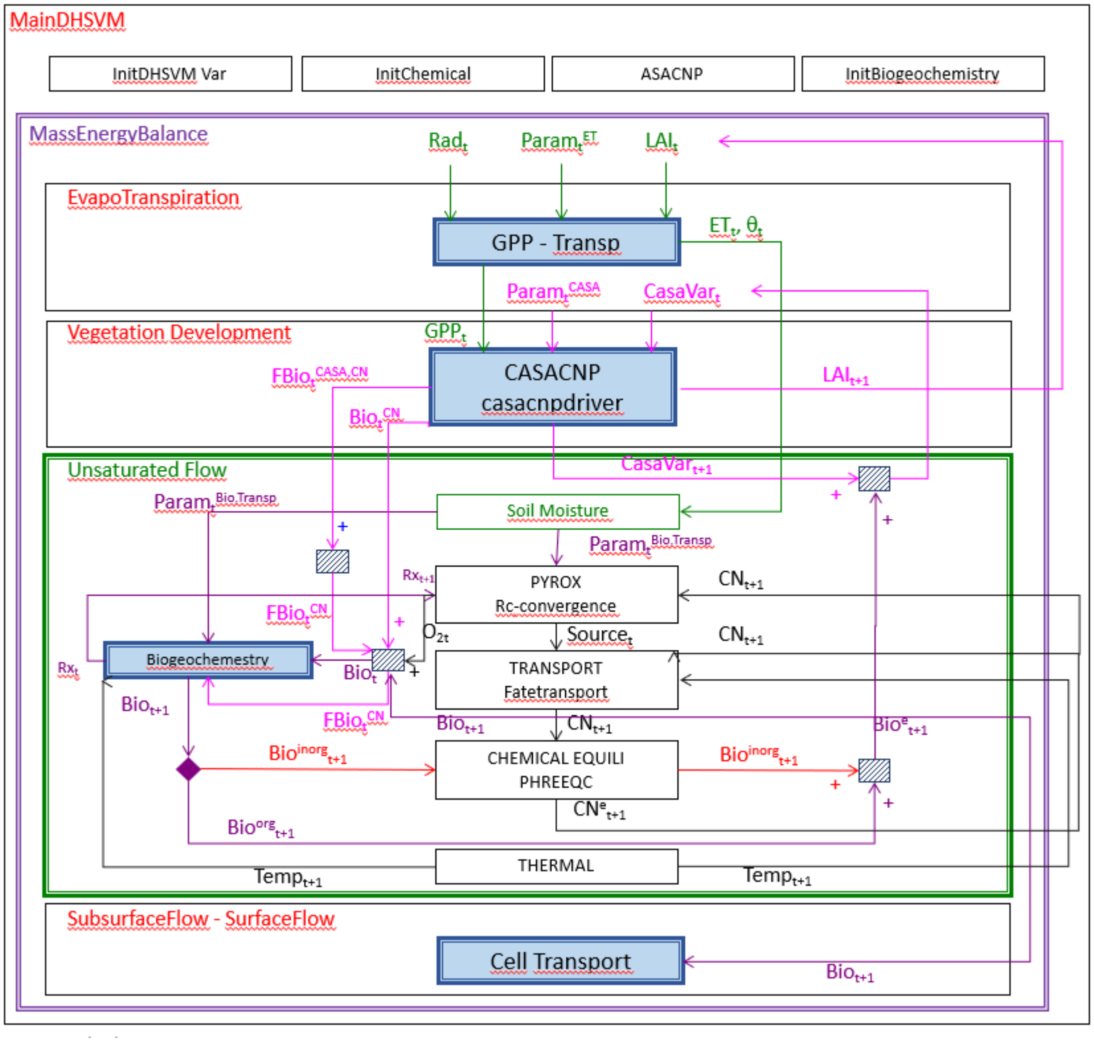

Figure 43 Complete schematic workflow of computational implementation of inclusion of vegetation as bioremediation into DHSVM-HTGCM (Xu 2013) model. The boxes show the general module structures of DHSVM-HTGCM. The blue boxes are the main modifications developed in this study. The arrows represent the flow of variables and data inside the general computational development.

We can explain the sequence of information for the computation as follows. First the DHSVM-HTGCM initializes all the variables in the *initmodelstate* module. The carbon assimilation and evapotranspiration rates are computed in the *evapotranspiration* module. These rates are used to computed the *GPP* to be transferred to CASA-CN in the *massenergybalance* module and to be transferred into the *unsaturatedflow* module, which will be used by the pyrox-Phreeqc-transport code. The biogeochemical variables are computed inside the *unsaturatedflow* module and in the *biogeotransportF* module to be passed to CASA-CN. At the end of the *unsaturatedflow* module, the chemical equilibrium is computed for the biogeochemical solutes and for the metals by the *Call_prheeqc* module. At this stage, the computations are updated for the time step and the cycle is repeated again.

3.4 Qualitative Mathematical Analysis of the Dynamics of the Model

As done in Section 2.4 in Chapter 2.0, we can make an approximation to the behavior of the solution of the model by performing a graphical and qualitative analysis of the main equations (Strogatz S H 1995). The interactions among the processes modeled can be visualized in the same manner using graphical representation of the equations (Strogatz S H 1995). In this section, we extract the relevant portions from the equations that explains the dynamics of each process to build simple equations and their graphical representations. By examining these simple equations and their dynamics using portrait curves we can address the main interactions between biogeochemical process and pyrite oxidation.

We present an analysis for three groups of processes: a) the dynamics of plant growth using leaf carbon and leaf nitrogen pools; b) the dynamics of the interaction between soil organic matter oxidation and pyrite oxidation; c) the dynamics of pyrite oxidation and interactions with biogeochemical processes.

3.4.1 Dynamics of Plant Growth

The dynamics of plant growth can be represented by Equations 3.10 for plant carbon pools and by Equation 3.11 for nitrogen pools. We can focus our analysis on the leaf carbon and nitrogen pools equations because they represent the core of the vegetation growth and because the main interactions with pyrite oxidation depends on leaf vegetation growth according to Plaza et al. (2018). Based on Equation 3.10 and 3.11, we can represent the dynamics of the leaf carbon and leaf nitrogen jointly with *GPP* as the main input for carbon allocation. This dynamical system helps to represent the effects of the carbon pool on the nitrogen pool via the *LAI* through the mineral nitrogen plant uptake, which is determined by the evapotranspiration.

Using Equation 3.10 with *i* =Leaf for carbon leaf pool and Equation 3.11 with *i* =Leaf for nitrogen leaf pool we can build the phase portrait of both variables [C_{Plant} x N_{Plant}], as shown in Figure 44. The steady curve for leaf nitrogen pool follows the evapotranspiration and *LAI* relationship defined by the Penman-Monteith equation. Hence, the carbon leaf pool has an effect on the nitrogen leaf pool dynamics through the evapotranspiration and *LAI*. However, Equation 3.10 implies that the carbon leaf pool depends only on *GPP*. Based on the intersection of the nitrogen and carbon steady curves, we found four regions on the dynamics plane [C_{Plant} x N_{Plant}]: a) region A, which has positive rates of growth in the carbon leaf pool but negative rates for nitrogen pool with flows toward the steady point; b) region B, which shows negative rates for both variables, also with flows to the steady point; c) region C, the only region with positive rates for carbon and nitrogen pools; and d) region D, with positive nitrogen pool rates and negative carbon pool rates. The flows in the regions configure a fixed point (attractor) at the intersection of the nitrogen and carbon steady curves. The phase portrait has as parameters mineral nitrogen N_{min} for nutrient plant uptake and gross primary production *GPP*, which together change over time and move the fixed point. The moving fixed point represents the non-equilibrium condition for vegetation growth.

The remaining consideration for plant leaf dynamics is the two effects of vegetation on pyrite oxidation: a) the solute plant uptake and soil moisture changes produce lower values of solute concentrations. Both processes are determined by carbon leaf pool in terms of Leaf Area Index as a factor of evapotranspiration and b) soil organic matter, through the ulterior fluxes of litter and soil organic pools, that reduces the dissolved oxygen availability slowing the pyrite oxidation. The next subsection, 3.4.2, illustrates the dynamics of the interaction between organic matter and pyrite oxidation.

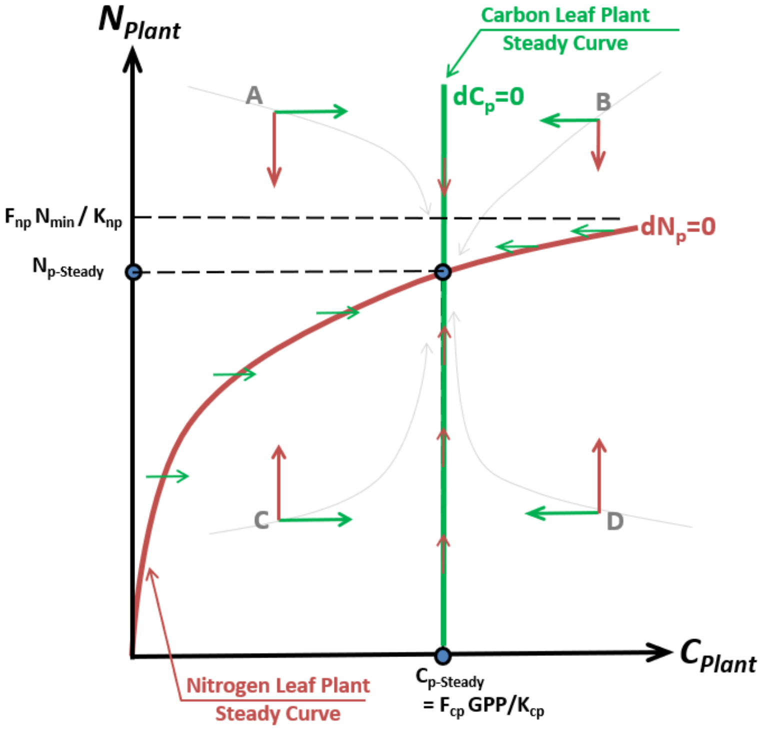

Figure 44 Phase portrait of carbon C_{Plant} and nitrogen N_{Plant} leaf pools dynamics. The green line and red brown curve correspond their respective to steady-dynamics points. The arrows represent the direction of flows of the variables dynamics. Point $C_{p\text{-}Steady}$,$N_{p\text{-}Steady}$ is the equilibrium point, which is an attractor.

3.4.2 Dynamics of Organic Matter and Dissolved Oxygen

The simplified version of the equations for the interaction between organic matter oxidation and the dissolved oxygen resulting from the pyrite process can be established as follows:

$$\frac{dOM}{dt} = OM_{ext} - q\ OM - r_{ox}\ OM\ f(O_2) - E\left(C_p, g_s\right)OM \qquad [3.39]$$

$$\frac{dO_2}{dt} = D[O_2^{ext} - O_2] - D_w \frac{3\,(1-\theta)}{R^2}\left[\frac{r_c}{R-r_c}\right]\frac{O_2}{H} - r_{ox}\ OM\ f(O_2) \qquad [3.40]$$

This organic matter equation formulation (Equation 3.39) is a simplification of the partial differential equation (Equation 3.14) into an ordinary differential equation. In Equation 3.39, the transport component is represented by the $q\ OM$ term, the boundary conditions by an external source OM_{ext}, the organic matter oxidation by a linear reaction term $r_{ox}\ OM\ f(O_2)$, and the plant uptake organic matter by the effect of root flux transpiration in the $E(C_p, g_s)\ OM$ term.

The first term OM_{ext} in Equation 3.39 stands for the external source of organic matter, which depends on the ulterior dynamics of the carbon plant, litter and carbon soil pools of Equations 3.5, 3.8 and 3.10 in the biochemical cycles' formulations. The second term in Equation 3.39 describes the transport process, the third term is the oxidation of organic matter and the final term is the organic matter plant uptake, which has the plant evapotranspiration computed in the first component based on the physiological variables carbon assimilation A_n, and stomatal conductance g_s coupled with Carbon Leaf Plant Pool C_p through the Leaf Area Index *LAI*. Equation 3.39 shows that the only source of organic matter is the vegetation growth development; the other components reduce the availability of organic matter.

Equation 3.40 is also an adaptation of the partial differential equation (Equation 3.30) into an ordinary differential equation with an explicit diffusion term $D\,[O^{ext} - O_2]$ and the sink term for organic matter oxidation.

The interaction between organic matter and oxygen dynamics can be analyzed using the curves derived by Equations 3.39 and 3.40 when the derivatives are zero. Then, the curve for organic matter steady state is given by the following equation,

$$OM = \frac{OM_{ext}}{q\;OM + r_{ox}\;OM\;f(O_2) + E\left(C_p, g_s\right)OM} \tag{3.41}$$

The oxygen steady state curve can be shown as follows,

$$OM = \frac{D\;O_2^{ext}}{r_{ox}\;f(O_2)} - \frac{[\;D + D_w\;3\;(1-\theta)/R(r_c/(R-r_c))/H\;]O_2}{r_{ox}\;f(O_2)} \tag{3.42}$$

The phase portrait in Figure 45 of both curves determine the non-linear dynamics of the organic matter and the dissolved oxygen using main transport, pyrite oxidation, organic matter oxidation and organic matter plant uptake. In the plane the intersection of the steady state curves generates four regions: a) region A, which has a positive derivative for oxygen and negative rates for organic matter pool with flows toward the steady point; b) region B, which shows negative derivatives for both variables, also with flows to the steady point; c) region C, which is the only region with positive derivatives for both organic matter and dissolved oxygen; and d) region D, which has a positive derivative for organic matter and nitrogen rates and a negative one for oxygen. The flows in the regions configure a fixed point (attractor) at the intersection of the organic matter and oxygen steady state curves.

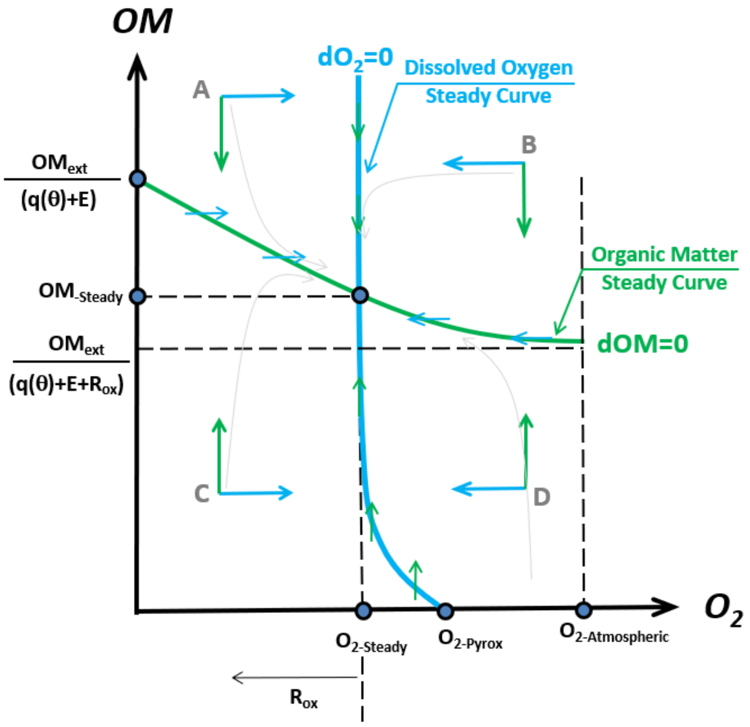

Figure 45 Phase portrait of Organic Matter pool *OM* and Dissolved Oxygen pool O_2 dynamics as a representation of Equation 3.39 and Equation 3.40. Green and blue curves correspond to their respective steady-dynamics points. Arrows represent the direction of flows of the variables' dynamics. Point $OM_{-Steady}$,$O_{2\text{-}Steady}$ is the equilibrium point, which is an attractor.

According to the coupled dynamics of organic matter and oxygen, the steady oxygen is reduced by the organic matter oxidation lowering the rate of shrinking of the core, which delays the pyrite process cessation, thereby increasing the particle radius over time and ultimately increasing the production of sulphates, ferric ions and hydrogen ions.

The next subsection presents details regarding pyrite oxidation dynamics and interactions with direct biogeochemical processes.

3.4.3 Dynamics of Pyrite Oxidation and Interactions with Biogeochemical Processes

The first pyrite process dynamics to explore is sulphate ions SO_4 production determined by the shrinking core radius r_c. SO_4 behavior is primary determined by Equation 3.32, which is formulated in the explicit time version using a third power exponent. If we try an expansion of the quadratic exponent, we can get an approximation for a discrete version of Equation 3.32 as follows,

$$\frac{dSO_4}{dt} = \frac{\rho_s}{R}[\,A - B\,r_c + C\,r_c^2\,] \qquad [3.43]$$

The time integration of Equation 3.43 can be approximated assuming a constant rate of declining of the shrinking core radius $r_c=(R\text{-}kt)$. The result of the time integration can then be reported in the following form:

$$SO_{steady} - SO_{initial} = \frac{\rho_s}{R}C\ \int_{to}^{T}[R - kt^2\,]dt \qquad [3.44]$$

This type of integral is easy to solve in terms of time. In our case, more important than the final solution is the general shape of the SO_4 curves in a phase portrait shown in Figure 46, with r_c as crossed variable. The main deduction derived from Equation 3.44 is that SO_4, Fe and H^+ production is high at the beginning of the pyrite oxidation process and will decline monotonically according to a quadratic function. The second important inference from Figure 46 and Equation 3.44 is that the evolution of SO_4 is strongly dependent on the initial condition as it increases the steady state as increases and vice versa. This simple approximation to only a pyrite formation equation, excluding transport, organic matter oxidation and plant uptake, helps to illustrate pyrite oxidation SO_4 production and is consistent with the concept of potential system dynamics described by Bahrami and Doulati Ardejani (2016).

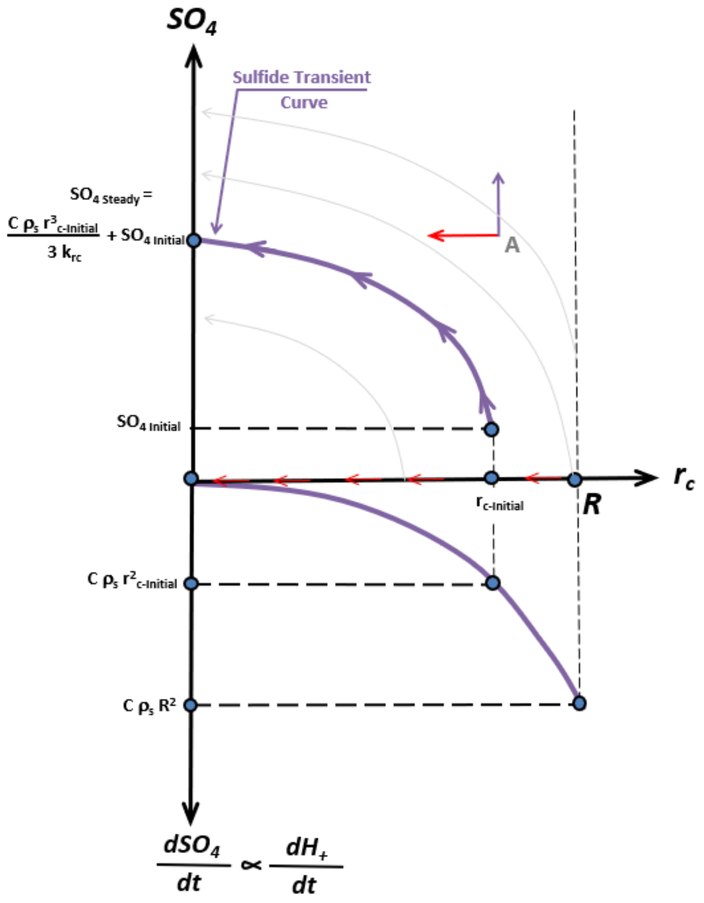

Figure 46 Phase portrait of Sulfate SO_4 ions production driven by the Pyrite Particle Radius r_c. The violet curve in plane [SO_4 x r_c] shows a transient trajectory of the variables. The violet curve in plane [dSO_4/dt x r_c] represents the production rate of SO_4 and H^+ ions depending on r_c.

The pyrite oxidation process as indicated in the system of Equations 3.30 and 3.31, can be explored in a simple manner using Equation 3.40 for oxygen and Equation 3.31 for r_c. Similarly, for organic matter oxidation analysis, the steady state curve for oxygen can be described as follows,

$$r_c = R \frac{[\, D\, O_2^{ext} + D\, O_2 - r_{ox}\, f(O_2) OM)\,]}{D_w^*\, O_2 + [\, D\, O_2^{ext} + D\, O_2 - r_{ox}\, f(O_2) OM)\,]} \tag{3.45}$$

Specifically, the steady state condition for r_c is only the first horizontal axis because the derivative is zero at $r_c = 0$. This explains why the pyrite process is slow and only ceases at the total consumption of the entire coal particle, or $r_c = 0$.

The phase portrait in Figure 47 shows two regions of dynamics: region A, where the oxygen tends to increase toward the fixed point; and region B, where the oxygen decreases to follow the steady state curve. In both regions, the shrinking core radius declines to ultimately vanish. The pyrite oxidation dynamics described by Figure 47, shows that the rate at which the shrinking core decreases is enlarge by oxygen availability. In other words, contrary to intuition about the effect of oxygen in the process, the more oxygen that is present, the faster oxidation is carried out, and the shrinking core is lowered producing less by-products or finishing the pyrite oxidation earlier.

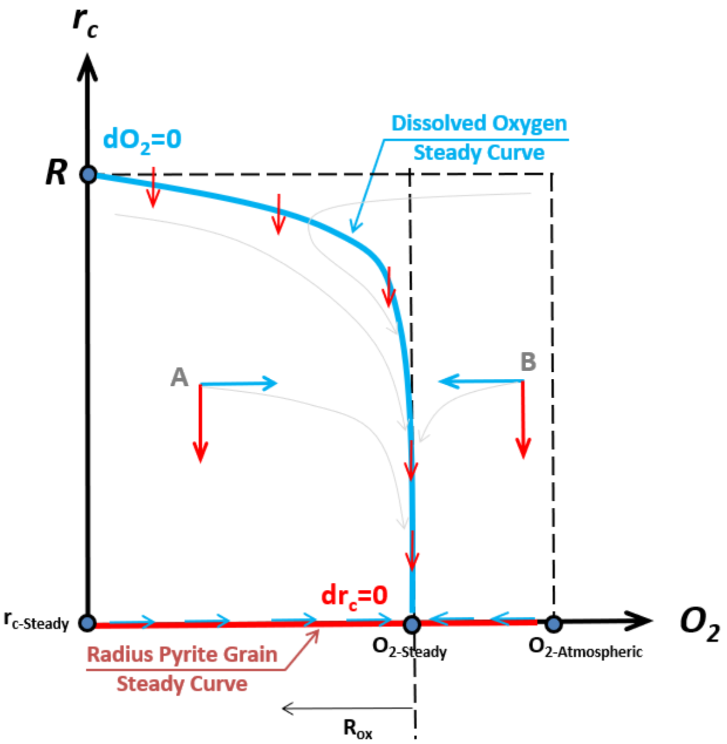

Figure 47 Phase portraits of pyrite oxidation dynamics with dissolved oxygen O_2 and pyrite particle radius r_c as described by Equation 3.40 and Equation 3.47. Blue and red curves correspond to respective steady-dynamics points. Arrows represent the direction of flows of the variables' dynamics. The point at $r_c=0$ and $O_2= O_{2\ Steady}$, is the equilibrium point which is an attractor.

To complete the pyrite oxidation analysis, we can use Equation 3.43 to incorporate the sulfate production component plus the dispersion, transport and plant uptake effect on SO_4 dynamics. The simplified ordinary differential system of equations for the analysis can be represented as follows,

$$\frac{dSO_4}{dt} = D_w[SO_{4\,ext} - SO_4\,] + \frac{\rho_s}{R}[C\,r_c^2\,] - qSO_4 - E(C_p, g_s)\,SO_4 \qquad [3.46]$$

$$\frac{dr_c}{dt} = -\boldsymbol{K}\,\frac{R}{r_c(R-r_c)} \qquad [3.47]$$

Equation 3.46 is a composite of the dynamics of SO_4 using elements of diffusion through the D_w $[SO_{4\ ext} - SO_4]$ term, the pyrite oxidation SO_4 production from Equation 3.43, and solute plant uptake using root transpiration as represented by the $E(C_p, g_s)\ SO_4$ term. Equation 3.47 is a version of Equation 3.31 where the K term condenses the parameters independent of the r_c variable.

The phase portrait in Figure 48 shows the dynamics of SO_4 without the biogeochemical interaction in plot a) and with biogeochemical interaction in plot b). In both planes there are two regions: a) region A, with decreasing sulfate and b) region B, with increasing SO_4. Both regions have flows toward the steady point determined by an external source of SO_4, the dispersion transport coefficient D_w and the vertical discharge $q(\theta)$ directly dependent on soil moisture θ. The effect of biogeochemical interaction implies a decrease in the long-term steady state point from $S_{ext}\ D_w/(D_w + q(\theta))$ to $S_{ext}\ D_w/(D_w + q(E)+E)$. Therefore, the system dynamics analysis demonstrates that solute plant uptakes effectively reduce pollution concentrations.

The final equations to explore are those related to hydrogen ions H^+. These are similar to Equation 3.46 but with inclusion of hydrogen ion production through nitrification. The ordinary differential equation for H^+ in this case is presented below,

$$\frac{dH}{dt} = D_w[H^+_{ext} - H^+] + K_{H+} \frac{\rho_s}{R} [C\ r_c^2] - qH^+ \qquad [3.48]$$

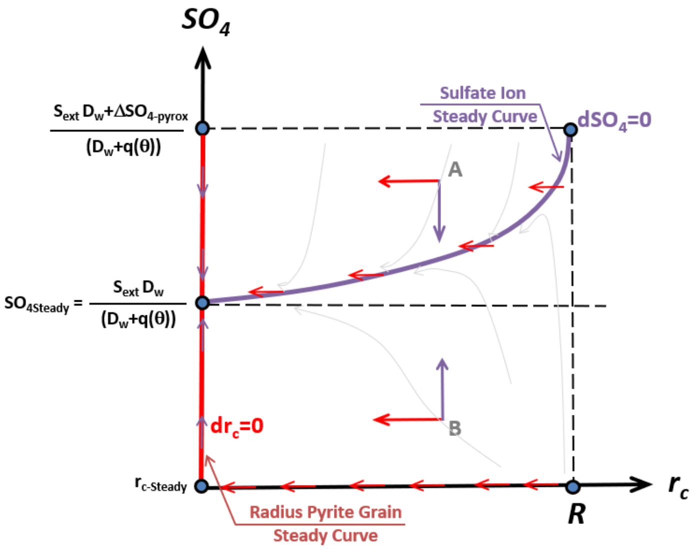

a) Pyrite oxidation with not interactions

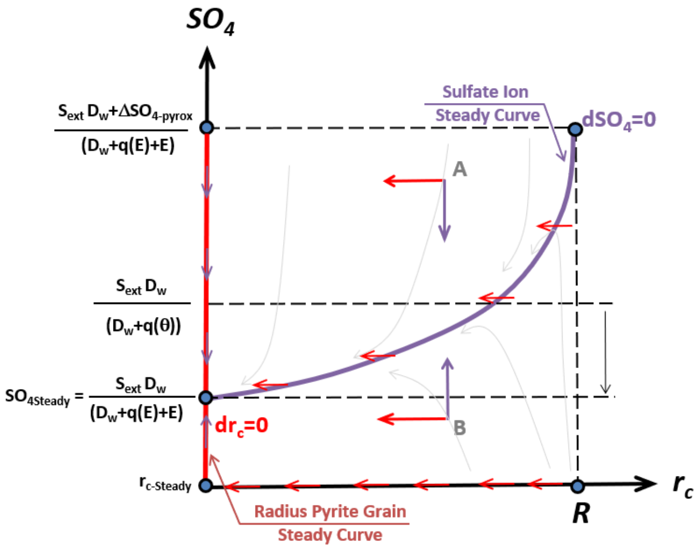

b) Pyrite oxidation interacting with Biogeochemical Processes

Figure 48 Phase portraits of Sulfates SO_4 with Pyrite Particle Radius r_c as dynamics using the unsaturated soil transport described by Equation 3.46 and Equation 3.47 without a) and with b) biogeochemical interactions. Violet and red curves correspond to respective steady-dynamics points. Arrows represent the direction of flows of the variables' dynamics. The point at $r_c=0$ and $SO_4 = SO_{4\,Steady}$, is the equilibrium point, which is an attractor.

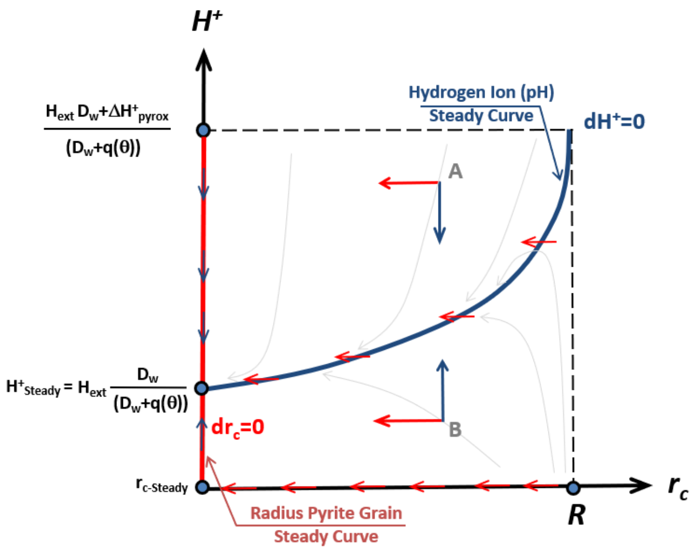

a) Pyrite oxidation with not interactions

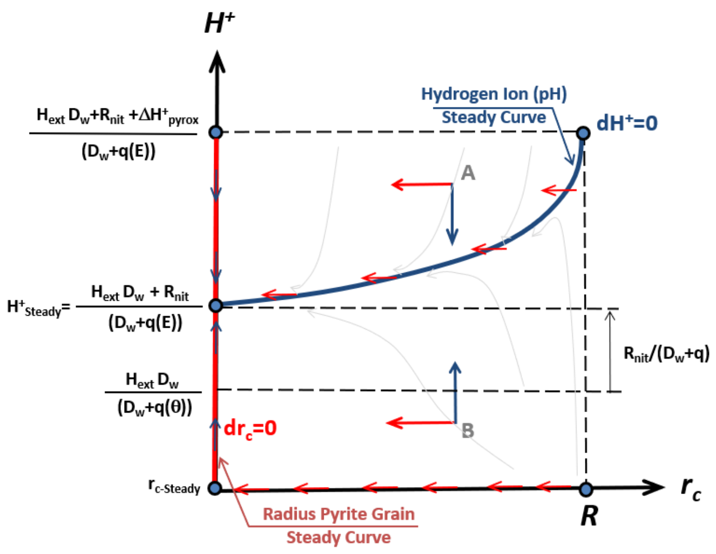

b) Pyrite oxidation interacting with Biogeochemical Processes

Figure 49 Phase portraits of Hydrogen Ions H$^+$ with Pyrite Particle Radius r_c as dynamics using the unsaturated soil transport described by Equation 3.47 and Equation 3.48 without a) and with b) biogeochemical interactions. Blue and red curves correspond to respective steady-dynamics points. Arrows represent the direction of flows of the variables' dynamics. The point at $r_c=0$ and $H^+ = H^+_{Steady}$, is the equilibrium point, which is also an attractor.

The phase portrait of the H^+ equation in Figure 49 shows similar behavior to those for SO_4 (or generic solutes under AMD). The main difference between the Hydrogen ions and sulfates is the effect of biogeochemical processes on the long-term steady point. An increase in Hydrogen ion concentration is expected in the long term (implying low pH), which can be explained by the effect of the Hydrogen ions produced by nitrification.

In summary, we can see by the qualitative system dynamic analysis that the interaction between biogeochemical processes and pyrite oxidation are: a) the effect of the vertical discharge and soil moisture on the accumulation of metals produced by acid mine drainage. b) The effect of organic matter oxidation on the oxygen concentration of stabilization by pyrite oxidation. c) The effect of the nitrification on the increase of hydrogen ion production during the pyrite oxidation process. and d) The effect of metals solute plant uptake on steady concentrations of sulfates and pH in the long term.

3.5 Model Calibrations

This section shows the results of the calibration of the model under two conditions: a) laboratory experiments of the pyrite oxidation process using grass as phytoremediation under controlled conditions columns developed by Plaza (2018) and Plaza et al. (2018). b) using the Mather site observed data in the period June 2009 to December 2014. Table 2 shows the main features and conditions for the components of the model for the four calibration situations. Table 3 shows the change in parameters used for laboratory data and field data.

Table 2 Modeling setup for calibration of lab experiments and Mather site observations

Site-Lab Experiment	Model Configuration	Initial Conditions	Forcing Data	Simulation Time
Lab Column Experiment A1 (90%CR+10%AC) Amended Plot 2 Mix No-Vegetation [Plazas, 2018]	6-Soil Layers Amended Plot 2 soil properties Total Depth: 0.15 m	Soil Moisture θo: 0.26 Observed SO4: 2800 mg/L pH: 4.2 Other metals: According to experiment	Lab internal Data Radiation: 150 W/m2 Temperature: 20 ºC Humidity: 70 % Precipitation: 100 mL/week	1400 days
Lab Column Experiment A2 (90%CR+10%AC) Amended Plot 2 Mix Grass-Vegetation [Plazas, 2018]	6-Soil Layers 6-Root Layers Amended Plot 2 soil properties Total Depth: 0.15 m	Soil Moisture θo: 0.26 Observed SO4: 5200 mg/L pH: 5.5 Other metals: According to experiment	Lab internal Data Radiation: 150 W/m2 Temperature: 20 ºC Humidity: 70 % Precipitation: 100 mL/week	800 days
Lab Column Experiment B1 (90%CR+10%AC) Non-Amended Plot 1 Mix No-Vegetation [Plazas, 2018]	6-Soil Layers Non-Amended Plot 1 soil properties Total Depth: 0.15 m	Soil Moisture θo: 0.26 Observed SO4: 12800 mg/L pH: 2.2 Other metals: According to experiment	Lab internal Data Radiation: 150 W/m2 Temperature: 20 ºC Humidity: 70 % Precipitation: 100 mL/week	800 days
Mather site (90%CR+10%AC) Amended Plot 2 Layer Grass Vegetation [Plazas, 2018] [Xu, 2013]	6-Soil Layers 3 Soil Layers-Amended Plot 2 (61 cm) 3 Soil Layers Non-Amended Plot 1 (>61 cm) Total Depth: 10.3 m Root Depth: 1 m	Soil Moisture θo: 0.22 Observed SO4: 2000 mg/L (Amended) 8000 mg/L (Non-amended) Fe: 20 mg/L (Amended) 10000 mg/L (Non-amended) pH: 4.5 Other metals: According to Observed data	Jefferson Weather Station Data [Jun 2009 - Dec 2014] Radiation (Average): 300 W/m2 Temperature (Average): 12 ºC Humidity (Average): 90 % Precipitation (Average): 1400 mm/yr	2000 days

The next sections show the results of calibration for the two conditions describe above.

Table 3 Parameters for lab experiments and Mather site calibration

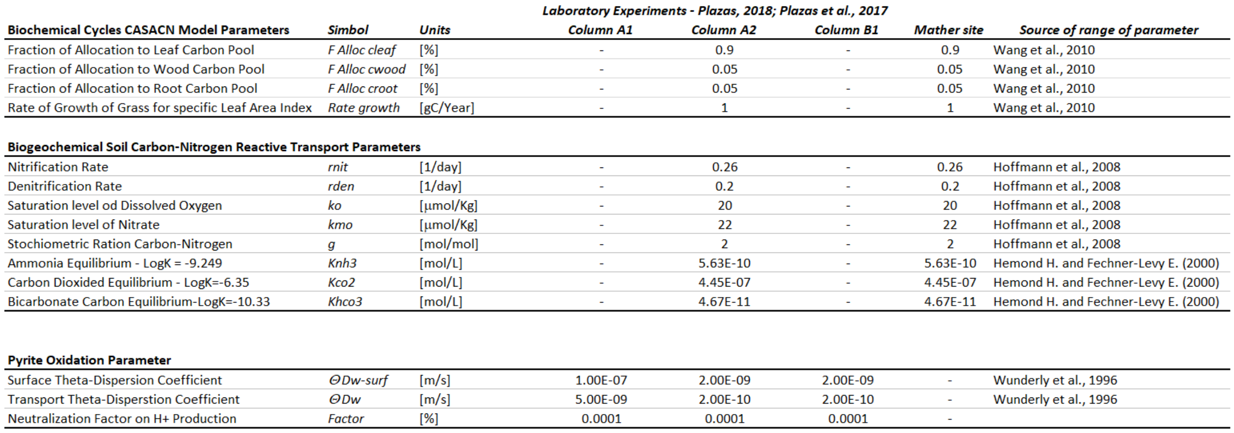

			Laboratory Experiments - Plazas, 2018; Plazas et al., 2017				
Biochemical Cycles CASACN Model Parameters	***Simbol***	***Units***	***Column A1***	***Column A2***	***Column B1***	***Mather site***	***Source of range of parameter***
Fraction of Allocation to Leaf Carbon Pool	*F Alloc cleaf*	[%]	-	0.9	-	0.9	Wang et al., 2010
Fraction of Allocation to Wood Carbon Pool	*F Alloc cwood*	[%]	-	0.05	-	0.05	Wang et al., 2010
Fraction of Allocation to Root Carbon Pool	*F Alloc croot*	[%]	-	0.05	-	0.05	Wang et al., 2010
Rate of Growth of Grass for specific Leaf Area Index	*Rate growth*	[gC/Year]	-	1	-	1	Wang et al., 2010
Biogeochemical Soil Carbon-Nitrogen Reactive Transport Parameters							
Nitrification Rate	*rnit*	[1/day]	-	0.26	-	0.26	Hoffmann et al., 2008
Denitrification Rate	*rden*	[1/day]	-	0.2	-	0.2	Hoffmann et al., 2008
Saturation level od Dissolved Oxygen	*ko*	[µmol/Kg]	-	20	-	20	Hoffmann et al., 2008
Saturation level of Nitrate	*kmo*	[µmol/Kg]	-	22	-	22	Hoffmann et al., 2008
Stochiometric Ration Carbon-Nitrogen	*g*	[mol/mol]	-	2	-	2	Hoffmann et al., 2008
Ammonia Equilibrium - LogK = -9.249	*Knh3*	[mol/L]	-	5.63E-10	-	5.63E-10	Hemond H. and Fechner-Levy E. (2000)
Carbon Dioxided Equilibrium - LogK=-6.35	*Kco2*	[mol/L]	-	4.45E-07	-	4.45E-07	Hemond H. and Fechner-Levy E. (2000)
Bicarbonate Carbon Equilibrium-LogK=-10.33	*Khco3*	[mol/L]	-	4.67E-11	-	4.67E-11	Hemond H. and Fechner-Levy E. (2000)
Pyrite Oxidation Parameter							
Surface Theta-Dispersion Coefficient	*ϴDw-surf*	[m/s]	1.00E-07	2.00E-09	2.00E-09	-	Wunderly et al., 1996
Transport Theta-Disperstion Coefficient	*ϴDw*	[m/s]	5.00E-09	2.00E-10	2.00E-10	-	Wunderly et al., 1996
Neutralization Factor on H+ Production	*Factor*	[%]	0.0001	0.0001	0.0001	-	

3.5.1 Calibration of Biogeochemical-Pyrox Processes using Experimental Column Lab Data

The model is first tested under controlled laboratory conditions that mimic, coal refuse conditions, amended conditions and bioremediation (90%CR+10%AC+Grass) conditions. Plaza (2018) implemented column-lab tests of disposal coal refuse in different scenarios. They measured the decay over time of levels of ion metals and pH after simulation of rain is passed through the system using a column-lab test. Figures 50, 51 and 52 present a comparison of the modeled and lab experimental data.

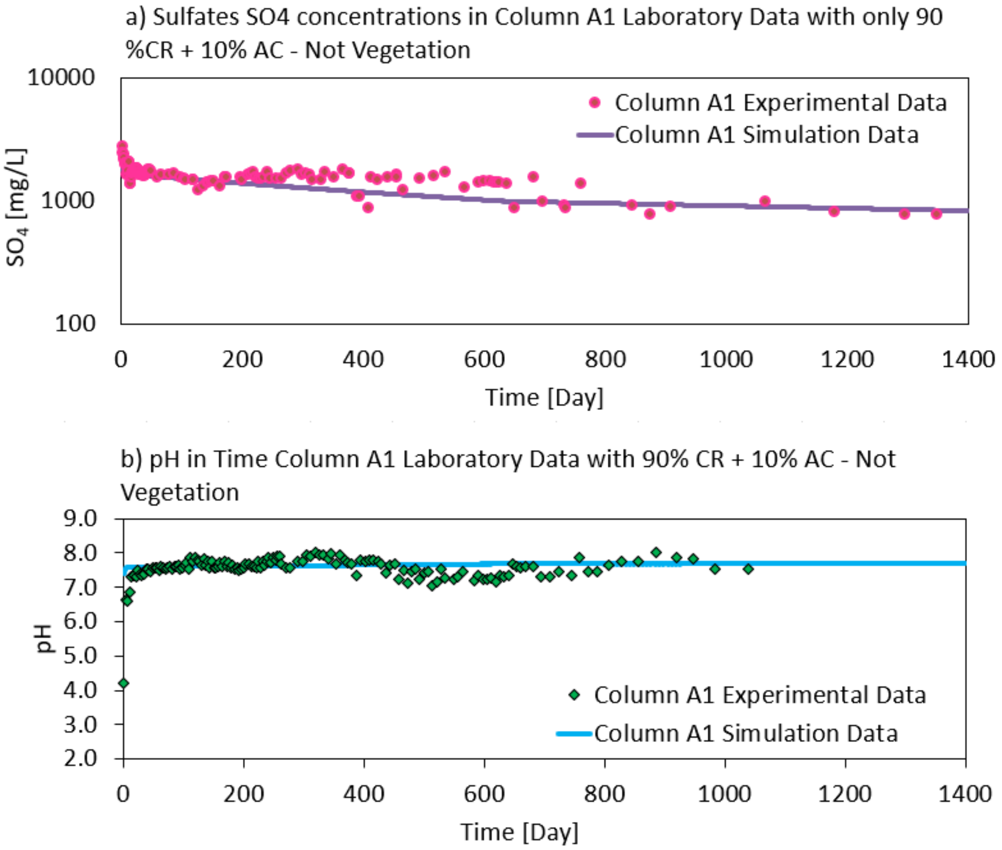

Figure 50 Comparison between observed and simulated data for SO_4 and pH at Lab Column Experiment A1 amended 90%CR+10%AC no bioremediation. Simulation time: 1400 days.

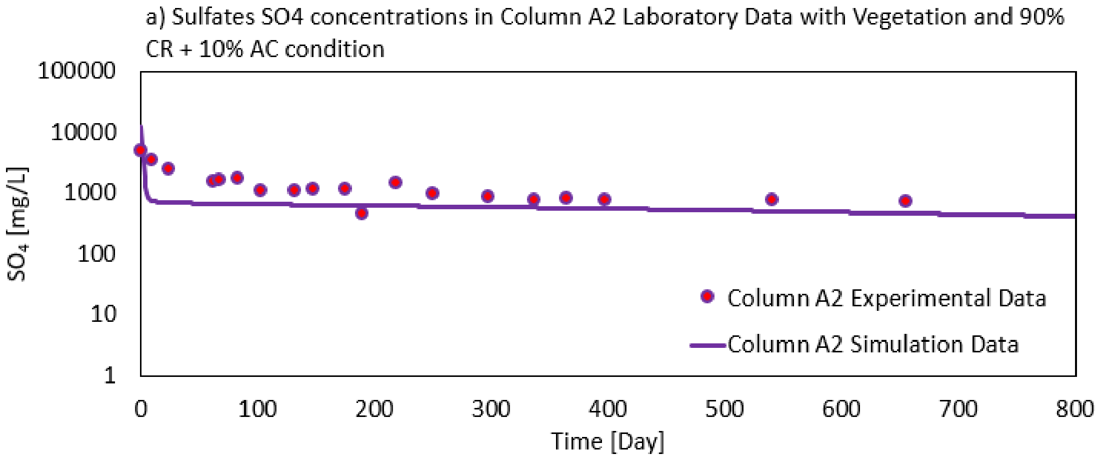

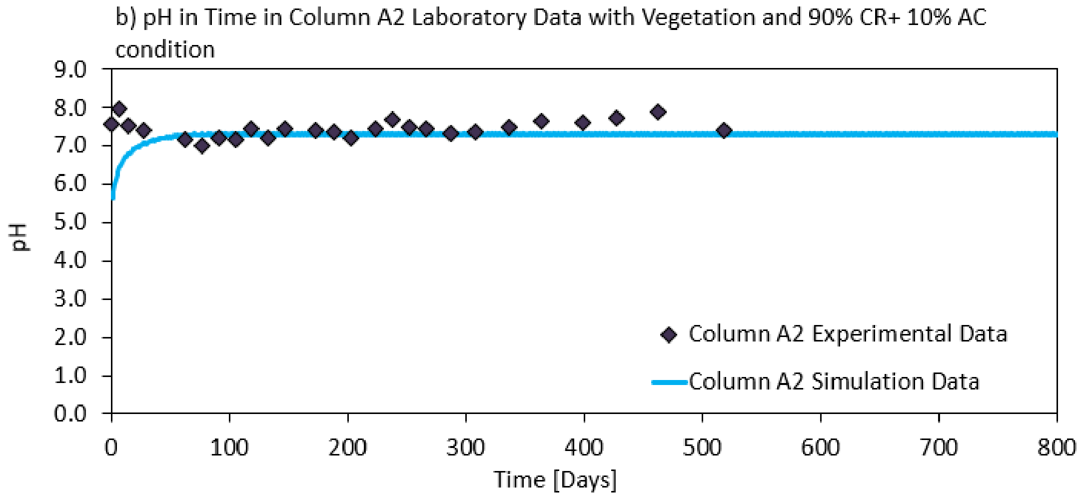

Figure 51 Comparison between observed and simulated data for SO_4 and pH at Lab Column Experiment A2 amended 90%CR+10%AC with grass as bioremediation. Simulation time: 800 days.

For lab column experiment A1 and A2 the implementation of solute plant uptake made possible the reduction of SO_4 in the simulation model to replicate the lab measured data. However, it was necessary to adjust the dispersion coefficient and the soil vertical conductivity to establish higher values of steady state concentrations in A2 and control the decay shape of the SO_4 simulation curve.

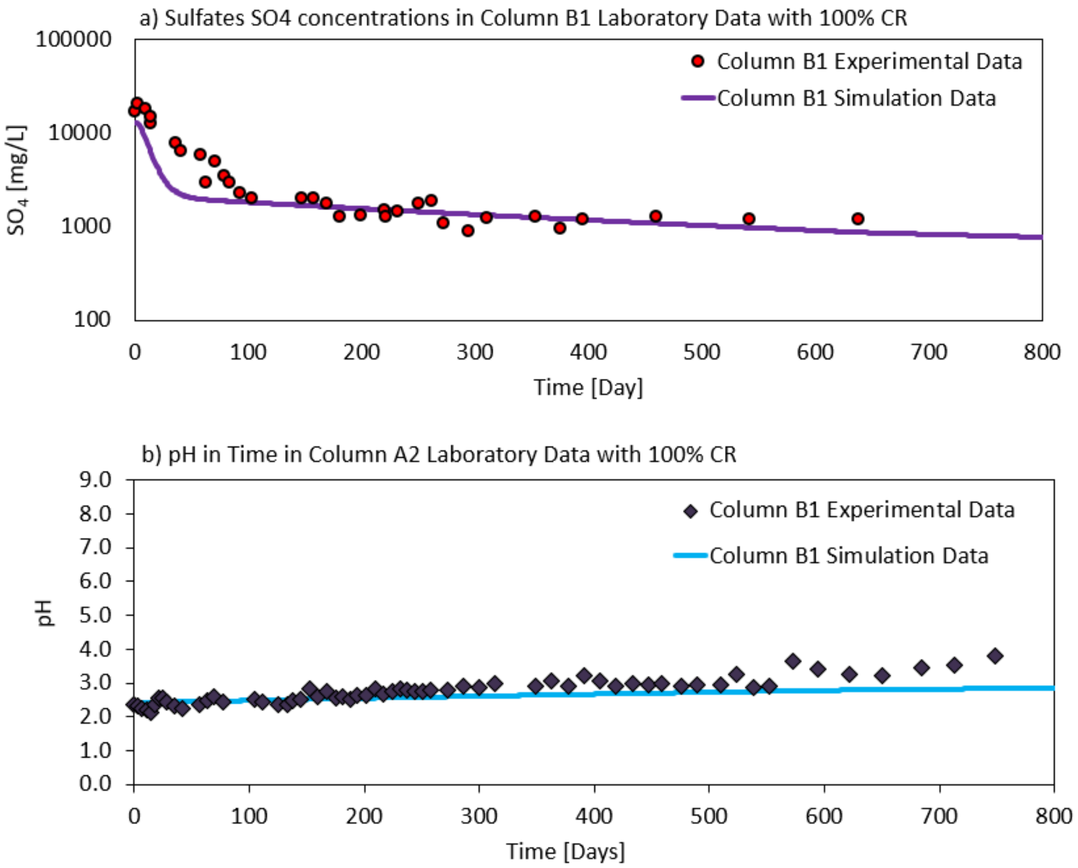

Figure 52 Comparison between observed and simulated data for SO_4 and pH at Lab Column Experiment B1 non-amended 100%CR no bioremediation. Simulation time: 800 days.

The parameters adjustments indicate that the potential of sulfate production is already consumed as indicated by the initial condition for the grain radius. The increase in pH values can be explained by the neutralization effect of the alkalinity potential on the hydrogen ions produced by the pyrite oxidation. In addition, the simulation shows with the high dispersion coefficients that the redistribution of solutes due to dispersion transport increase the final steady state of the final concentration on sulfates and hydrogen ions, as it was shown in the qualitative mathematical analysis in Section 3.4.3.

3.5.2 Calibration Biogeochemical-Pyrite Oxidation Processes at Mather Site

The validation of the model using Mather site data shows good agreement with the observed data, especially in the non-amended layer (see Figure 53). In the amended layer, the underestimation of SO_4 concentrations by the model might be caused by the effect of the capacity of acid neutralization of $CaCO_2$ ions, which can generate bias that forces variations in the final ion exchange. However, the model can still partially describe the high variation in ferric ions and the sustained increase of pH along the five years of the observed and simulated data. One important feature in the simulations is the seasonal pattern determined by the plant uptake over the ferric and pH dynamics presented in plots c) and e) for the amended layer. This shows the capacity of the model to mimic the biochemical processes.

In the non-amended bottom layers, the model can replicate with a better fit the decline of both sulfate and ferric ions due to the acidic neutralization of the alkaline clay mixture in part of the transport of the solutes and the capture some of ions by the plants. Indeed, we consider that even though the alkalinity effect of the mixture is greatly responsible of the elevation of pH in the amended zone, the plants can contribute by capturing enough solute metals to force additional increments on pH or at least by generating acid-base disbalances that change the bottom-layer conditions on the non-amended layers.

The non-amended layers simulation results are similar to those presented in Plaza (2018), with decay for SO_4 and Fe. The simulations of pH increase captured by our simulations are also similar to those in Plaza (2018), with more oscillations due to our including vegetation-biogeochemical processes effects. The amended layer simulation results for SO_4 are different from those in Plaza (2018) in their tendency to decrease. In the Fe simulations our simulations tend to capture more variations than present in Plaza (2018), which shows some steady values. While both

Plaza (2018)'s and ours show increases in pH in the amended layer, our results can better describe the changes in tendencies.

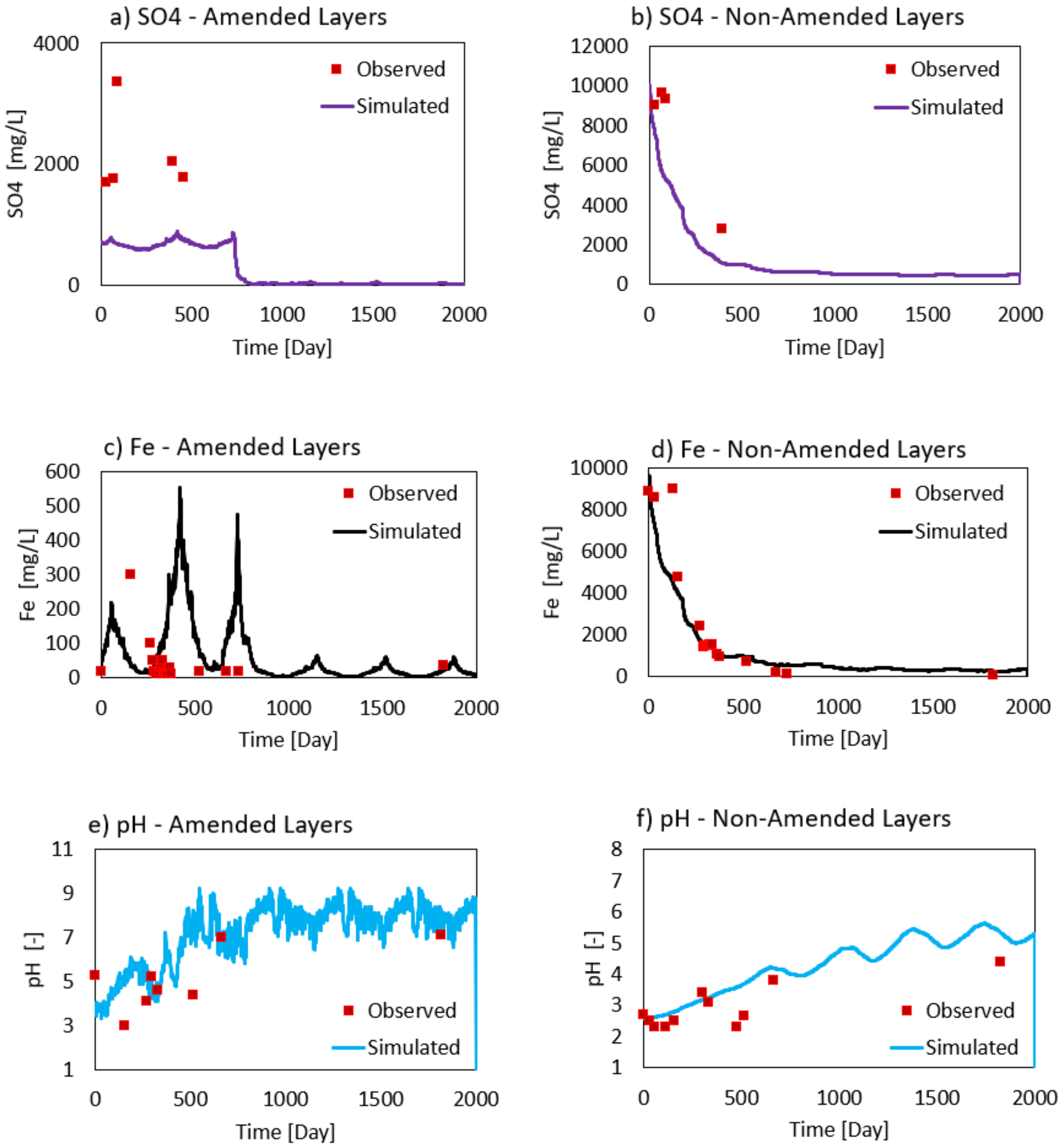

Figure 53 Comparison between observed and simulated data for SO_4, Fe and pH at amended and non-amended layers at the Mather site as validation process of the mathematical model. Dates of simulation: Jun 2009 to Dec 2014, equal to 2000 days.

3.6 Simulation Analysis of Interactions

This section is devoted to interpret the results of the main interaction between biogeochemical processes and AMD processes such as pyrite oxidation using the scenario simulations of implementation of passive remediation with grass vegetation. We focused on five main interactions, which are driven by the explicit formulations in equations 3.35, 3.36, and 3.37 and by the effect of evapotranspiration on soil moisture and vertical discharge. The five interactions are: a) the interaction between soil hydrology and pyrox solutes concentrations; b) the effect of pyrite oxidation pH on nitrogen pool; c) the effect of organic matter oxidation on the pyrite process; d) The effect of nitrification on the pyrox process and e) the effect of metals plant uptake on pyrite oxidation. The following sections illustrate in more detail each of the above interactions.

3.6.1 Interactions Between Soil Hydrology and Pyrite Oxidation

The first interaction driven by the soil hydrology over the solute concentrations levels is caused by the mass balance of the absolute quantity of solutes within the water content in the soil. As the total of mass of a solute could be constant for a certain period, the soil moisture explains the final concentration rise in inverse proportion to soil moisture. The effect of plant transpiration on the soil moisture causes significant changes in concentration levels. Figure 54 shows how the variation in soil moisture contributes to substantial changes in the solute concentration levels; as the soil moisture declines, the number of sulfate ions SO_4 increases from 1500 [mg/L] to 9000 [mg/L]. Consequently, the plant evapotranspiration interacts with the pH levels only in terms of mass balance, which induces changes in the overall chemical equilibrium of the other metals and inorganic carbon and nitrogen species. However, the potential pollution of pyrite hydrogen, sulfate and Ferric ions production is only dependent on the level of the shrinking core, given by the pyrite grain radius.

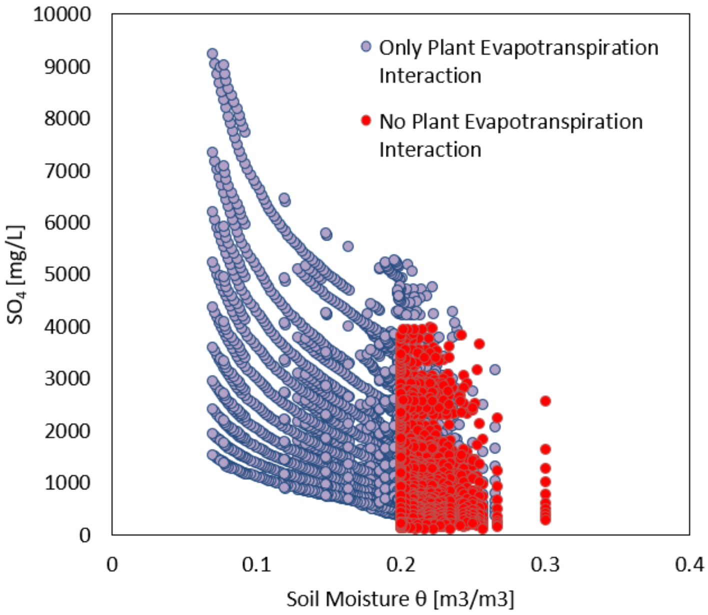

Figure 54 Relationship between soil moisture and sulfate concentration SO_4 as product of pyrite oxidation under the effect of plant evapotranspiration. The points are a 10-year simulation at 61 cm of the amended layer with 10%AC+90%CR.

The radius of the unoxidized core grain can be considered an indicator of remnant pyrite oxidation and it is strongly dependent on the oxygen availability within the soil matrix and its diffusion through the shrinking core (Plaza et al. 2018; Wunderly et al. 1996).

Figure 55 exhibits the increase of solutes concentration as an effect of plant transpiration either in the amended or non-amended layers. Also, there is a variation effect, since without the plant evapotranspiration the oscillations over time are less than those with plant evapotranspiration. Plots in Figure 55 are arranged using the same axis system as in Figure 48 and

49 of the qualitative analysis in Section 3.4.3. The purpose of the plot arrangement is to display the dynamic behavior on the planes [$r_c \ x \ SO_4$] and [$r_c \ x \ H^+$]. The dynamic behavior in both plot planes portrays the slow process of pyrite oxidation if one considers that the shrinking core radius is not zero yet after 10 years, according to the simulation. Also, the plotted planes highlight the tendency for both SO_4 and H^+ to be approaching a limiting value, as indicated by the analysis in Section 3.4.3.

Another important feature of the simulations emphasized in this subsection, is the difference in concentration levels between the amended and non-amended layers for the same soil column. In the amended layer with 90%CR+10%AC, the concentrations of SO_4 and H^+ are lower than those in the non-amended layers (100% CR). In general, one might think that, as the non-amended layers receive the flux of solutes from the upper layers (in this case, the amended ones), the transport process between both layers supports the increase of solutes concentration in the bottom layers. However, the actual main reason for the difference is the level of production of sulfate SO_4 and hydrogen H^+ ions within each layer. The rate of decline of the shrinking core radius on the amended layers is considerably higher than in the non-amended layers. As the leftovers of pyrite oxidation are given by the grain radius, bigger pyrite particles imply more sulfate, ferric and hydrogen ions production and higher sulfate concentrations SO_4 and low pH values.

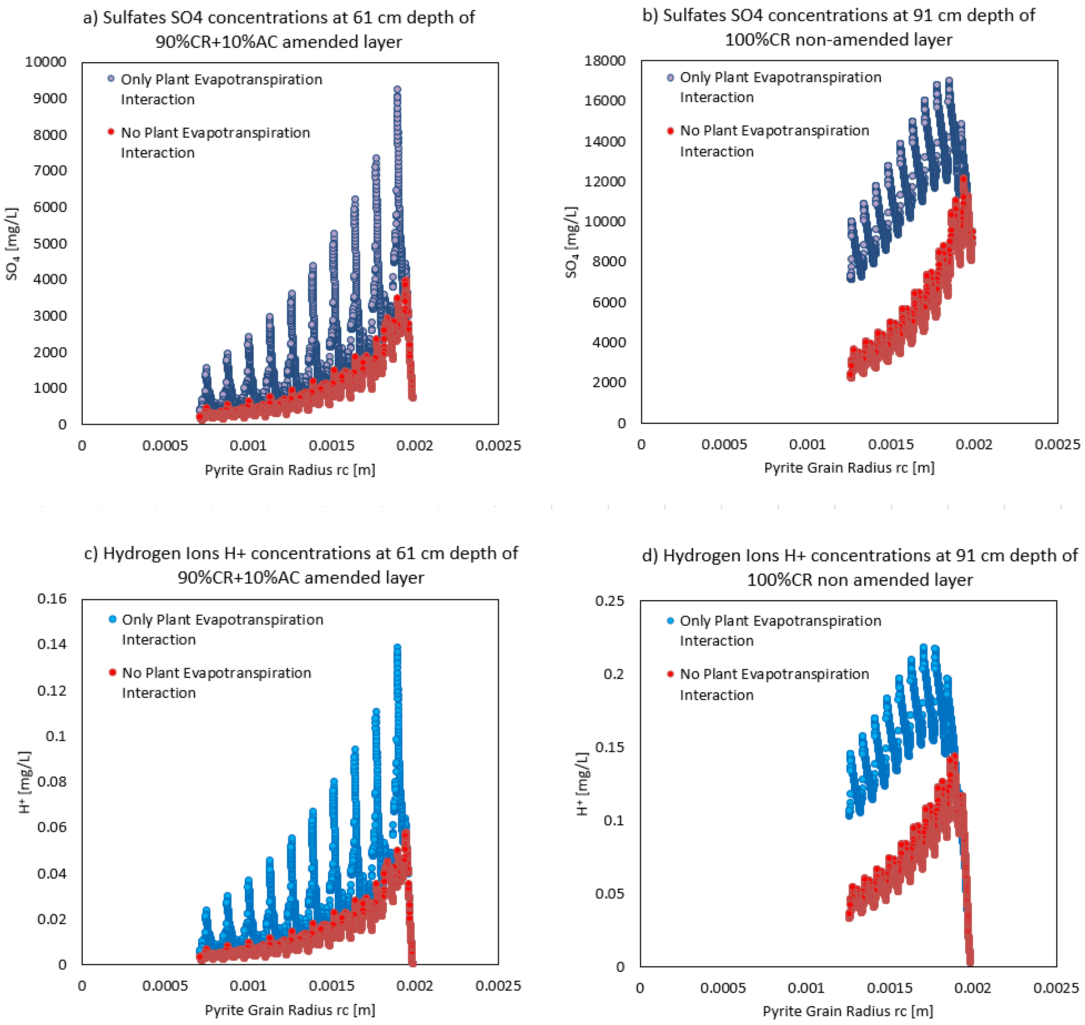

Figure 55 Plots of pyrite grain radius with sulfate SO_4 and H+ ions following the dynamical analysis phase portrait plots of the qualitative analysis in Section 3.4.3. The points are a 10-year simulation at 61 cm of the amended layer with 10%AC+90%CR and at 91 cm of the non-amended layer with 100%CR composition.

Figure 56 confirms the tendency of the sulfates SO_4 and pH to be reduced as a result of the transport process, as leaching and dispersion among the soil layers.

a) Sulfates SO4 concentrations at 61 cm depth of 90%CR+10%AC amended layer and Potential Pyrite Oxidation

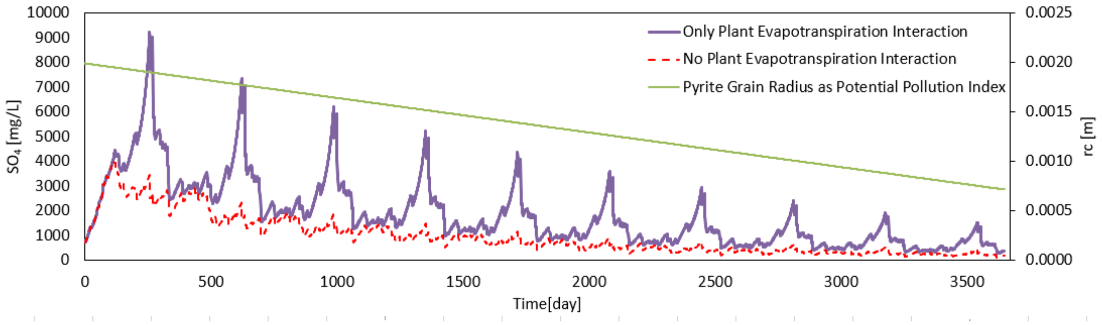

b) pH at 61 cm depth of 90%CR+10%AC amended layer and Potential Pyrite Oxidation

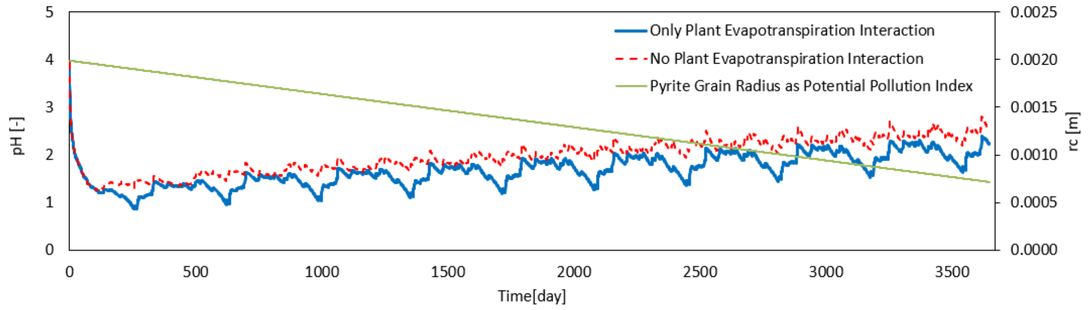

Figure 56 Comparison of sulfates SO_4 and pH time series under the effect of plant evapotranspiration through the change of soil moisture levels. The simulation series represent a 10-year simulation at 61 cm of the amended layer with 10%AC+90%CR.

3.6.2 Effect of pyrite oxidation induced pH on Nitrogen Pools

As the pyrite oxidation generates hydrogen ions H^+, the resulting values in pH drives the chemical equilibrium over all solutes within the soil matrix, including the inorganic nitrogen species: ammonium HH_4 and ammonia NH_3. This acidic environment changes the internal composition of mineral nitrogen as a pool that interacts with the biochemical nitrogen cycle. Low pH values convert ammonia NH_3 into ammonium ions, NH_4, and vice versa. Thus, mineral nitrogen composed primarily of nitrates, NO_3, change to be mostly composed of ammonium, NH_4, after the effect of chemical equilibrium is reached. As the mineral nitrogen increases with low pH values, the nutrients plant uptake enhances the nitrogen plant pools because plants are the main input.

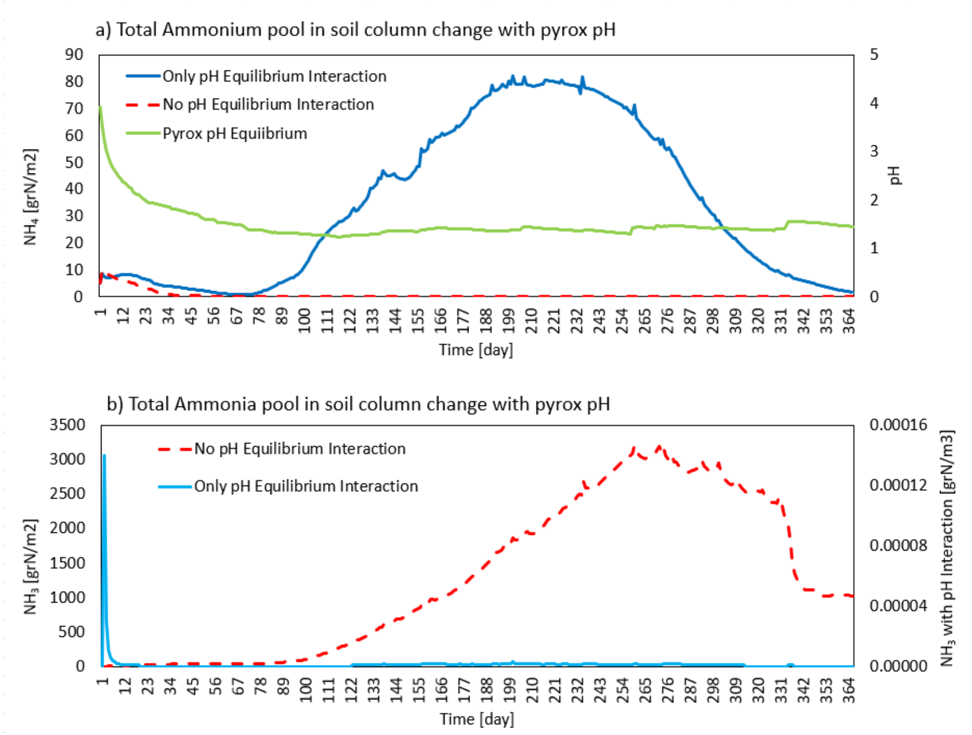

Figure 57 Comparison of annual simulated behavior of ammonia NH_3 and ammonium ions NH_4 through the effect of pH chemical equilibrium under pyrite oxidation.

Figure 57 depicts how the pyrite oxidation's dominant low pH forces the reduction of ammonia into ammonium ions, not only reducing the availability of total mass of inorganic nitrogen but also changing the annual behavior of the mineral nitrogen composed mostly of ammonium.

3.6.3 Effect of Organic Matter Oxidation on Pyrite Oxidation Process

Under biogeochemical environment processes, the dissolved oxygen is taken by pyrite and by the soil organic matter. When taken by pyrite, the original oxygen availability is reduced by the organic matter oxidation. As pyrite oxidation is strongly dependent on oxygen diffusion, the rate of the shrinking core declines, leading to higher values for pyrite grain radius. In Figure 58 phase portrait a) shows that the dynamics of interaction between organic matter and oxygen gradually diminish the availability of dissolved oxygen in the soil. Phase portrait b) illustrates how lower oxygen amount imply higher values for pyrite radius as the declining rate lessens.

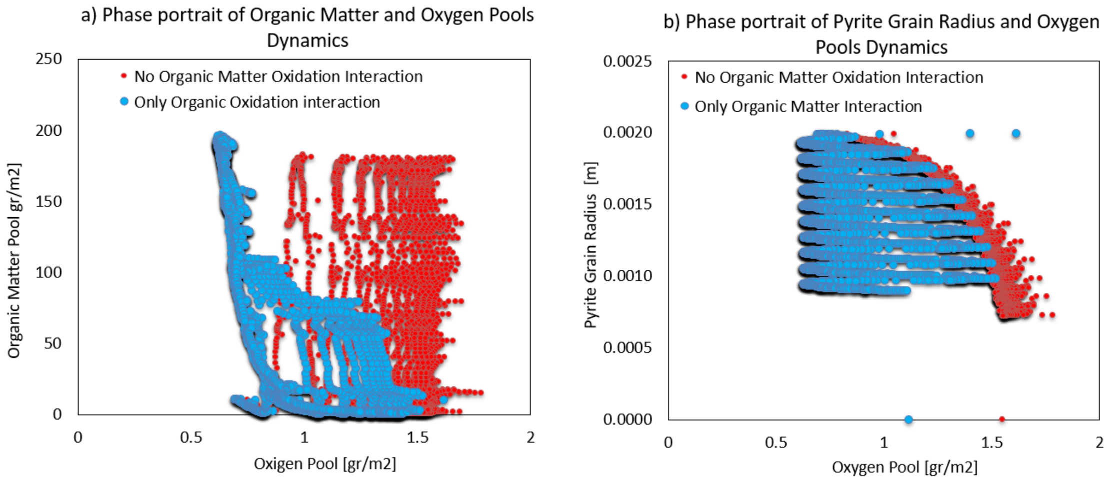

Figure 58 Phase portraits of dynamics of interaction among organic matter, oxygen and shrinking core radius, following the dynamical system phase portrait plots of the qualitative analysis in Section 3.4.2 and Sections 3.4.3.

In Figure 59, the 10-year simulation of the interaction between organic matter and pyrite oxidation depicts the annual variation in the total oxygen pool induced by the organic matter decay, which contrast with the asymptotical behavior of oxygen under only the pyrite process. Figure 59-

a) also illustrates the tendency of lower values for oxygen with the organic matter interaction than without the biogeochemical interaction. Figure 59-b) and Figure 59-c) illustrate the main implication of higher values of the grain radius on pyrite oxidation. The effect is a slow increase of sulfates, ferric and hydrogen ions production over time. Hence, pyrite oxidation could continue more time with the potential for more acidic production in the long term.

a) Dissolved Oxygen O_2 concentrations at 61 cm depth of 90%CR+10%AC amended layer and Potential Pyrite Oxidation

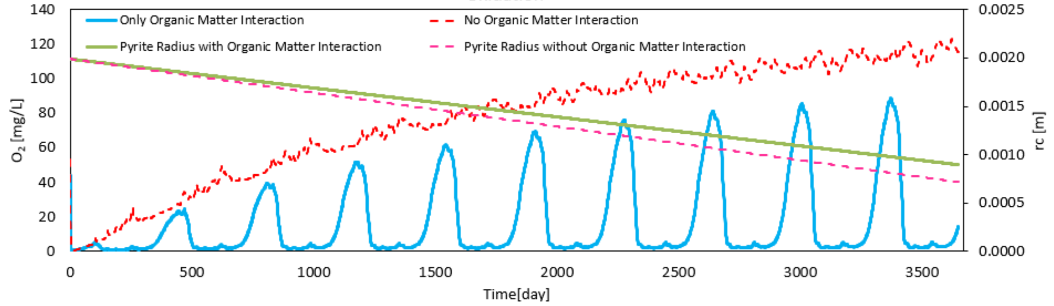

b) Production Rate of Sulfates SO_4 at 61 cm depth of 90%CR+10%AC amended layer

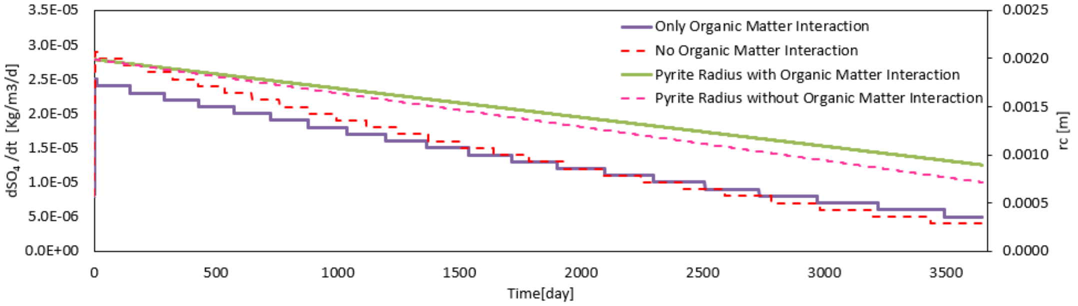

c) Production Rate of Hydrogen Ions H^+ concentrations at 61 cm depth of 90%CR+10%AC amended layer

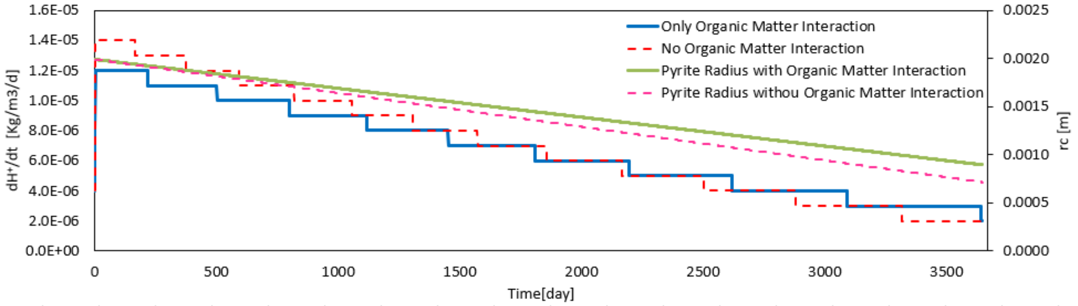

Figure 59 Comparison of dissolved oxygen, sulfates SO_4 and pH production and pyrite grain radius time series under the effect of organic matter oxidation. Simulation series represent a 10-year simulation at 61 cm of the amended layer with 10%AC+90%CR.

3.6.4 Effect of Nitrification on Pyrite Oxidation Process

The nitrification process generates hydrogen ions at a modeled rate that depends on ammonium and dissolved oxygen concentrations (Berlin et al. 2014; Hofmann et al. 2008); therefore, including biogeochemical processes implies additional hydrogen ions production in the soil matrix. The additional hydrogen ions can increase the acidic potential decreasing the pH. The effect of nitrification on decreasing the pH has been reported by literature when nitrogen fertilizers have been used (Cardoso et al. 2019; Zeng et al. 2017).

The simulation of the production of hydrogen ions only by nitrification shows that production is weak in comparison to that when pyrite oxidation is also present. Figure 60 illustrates the minor effect of nitrification on the hydrogen ions production compared with that of pyrite oxidation. There are few conditions where hydrogen ions concentrations are higher with nitrification than with pyrite oxidation.

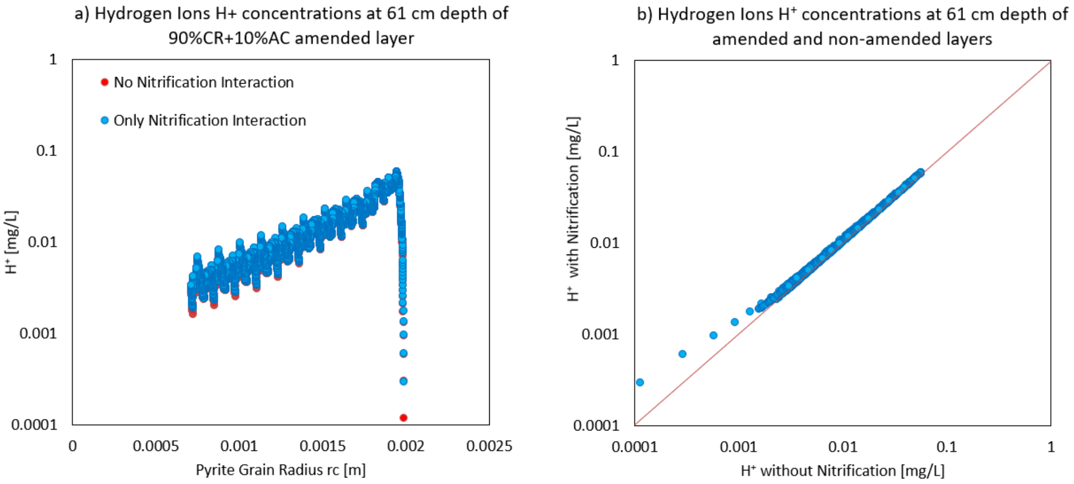

Figure 60 Hydrogen ions dynamic behavior under only nitrification effect. a) Plot of phase portrait of H^+ ions and pyrite radius dynamics, b) Comparison of H+ content between condition with nitrification and without nitrification. The points are a 10-year simulation at 61 cm of the amended layer with 10%AC+90%CR.

Similarly, Figure 61, describes the small difference in pH as a result of nitrification compared to that in a condition of only pyrite oxidation. The nitrification causes a moderate fall in pH along the year of simulation. The explanation for the small difference is the scant surplus production of hydrogen ions by the nitrification of each layer.

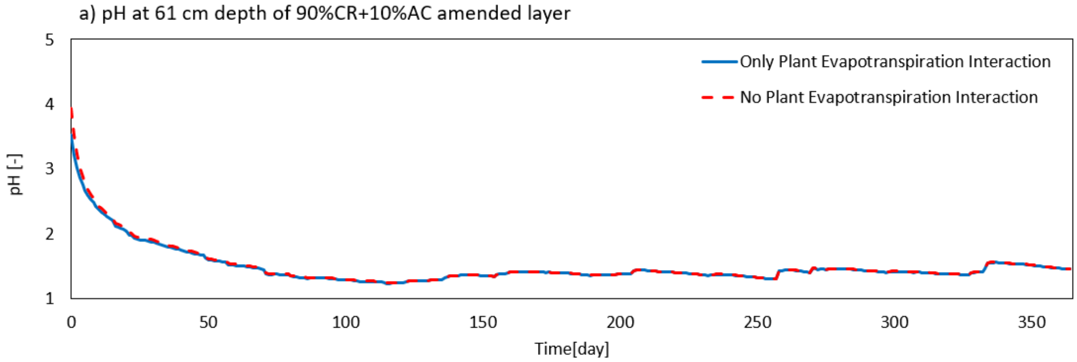

Figure 61 Comparison of pH time series between nitrification environment and without nitrification. Simulation series represent a 10-year simulation at 61 cm of the amended layer with 10%AC+90%CR.

3.6.5 Effect of Metal Plant Uptake on Pyrite Oxidation Process

According to Plaza et al. (2018), one of the tested effects in column-lab experiments comparing vegetation and pyrite oxidation is the capture of metals by the plants through the root-soil interaction. For example, Sas et al. (2001) describes how the plant uptake ions can trigger excretion of hydrogen ions promoting acidification in the soils.

The interaction can be modeled with mass transfer of metal solutes using the daily evapotranspiration of plants, as shown in Equation 3.38. The conceptual analysis in Section 3.4.3, through Figure 48 and Figure 49, illustrates that solute plant uptake reduces transient and steady state concentration by a factor of $1/(q(E) + E)$. The decrease in solutes concentration given by plant uptake is also moderated by the pH chemical equilibrium in a second stage. Figure 62, depicts the first stage of the decline of solutes concentration (SO_4 in this case) by metal plant uptake. In particular, the reduction is intensive within the amended layer where the root zone has its major influence. However, Figure 62-b) presents the transport effect of abatement of concentrations as a result of a consequent fall of solutes in the non-amended layer, which is out of the influence of root plant uptake. Figure 63 highlights the effect to the annual peaks and valleys of the warmer-colder seasons of physiological evapotranspiration of plant uptake on the solute concentrations. Warmer seasons imply higher values of evapotranspiration with low values of concentrations before pH chemical equilibrium. The peaks correspond to drops in evapotranspiration in colder seasons, also before pH equilibrium. The dissipation of the effect of metal plant uptake is due to the reduction of pyro by-products over time, as indicated by the pyrite particle radius.

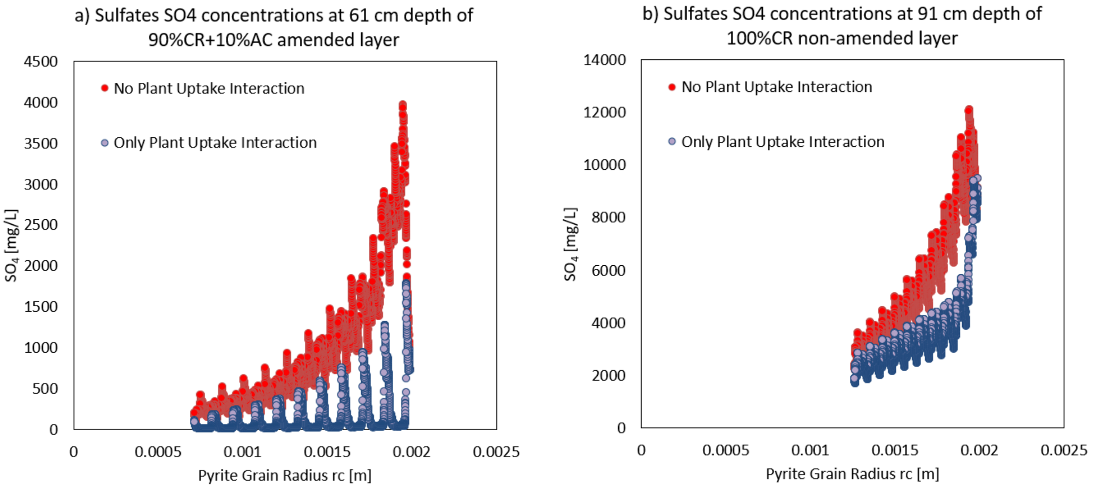

Figure 62 Phase portraits of pyrite grain radius with sulfate SO_4 and H+ ions following the dynamical analysis phase plots of the qualitative analysis in Section 3.4.3 under metals plant uptake only effect. The points are a 10-year simulation at 61 cm of the amended layer with 10%AC+90%CR and at 91 cm of non-amended layer with 100%CR composition.

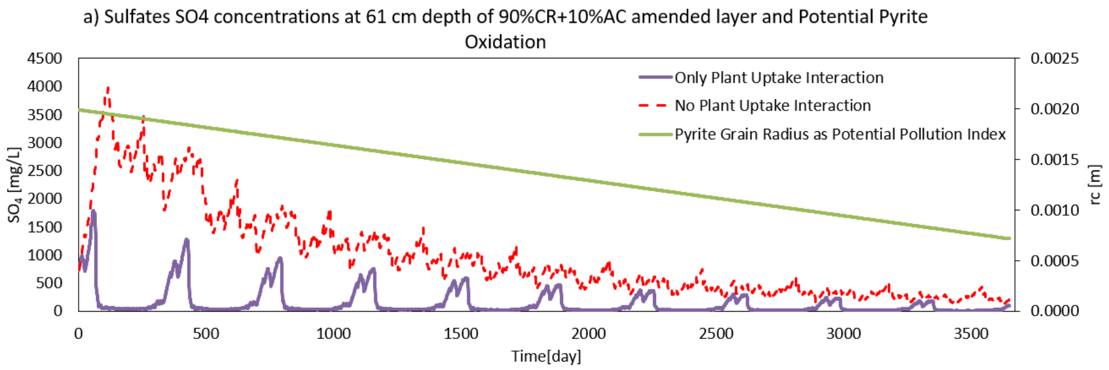

Figure 63 Comparison of sulfates SO_4 time series under the effect of only metals plant uptake before chemical equilibrium given by pH. Simulation series represent a 10-year simulation at 61 cm of the amended layer with 10%AC+90%CR.

In a second stage, the chemical equilibrium impacts all the solutes within the soil matrix layers causing a redistribution of the final concentrations of all species, especially the metals. Figure 64, confirms a decline in almost all concentrations of metals over the simulation time after the chemical equilibrium effect. However, the shape of these time series is different from those before the chemical equilibrium. After chemical equilibrium is reached, the annual oscillations of metals concentrations are more stable because there is a feedback effect between the amount of species available after the plant uptake and the final concentration after the chemical equilibrium. Figure 64-b) marks a similar behavior of simulated time series on pH and SO_4 solutes, with stable annual oscillations and lesser values of Hydrogen ions concentrations with plant uptake than those without the interaction.

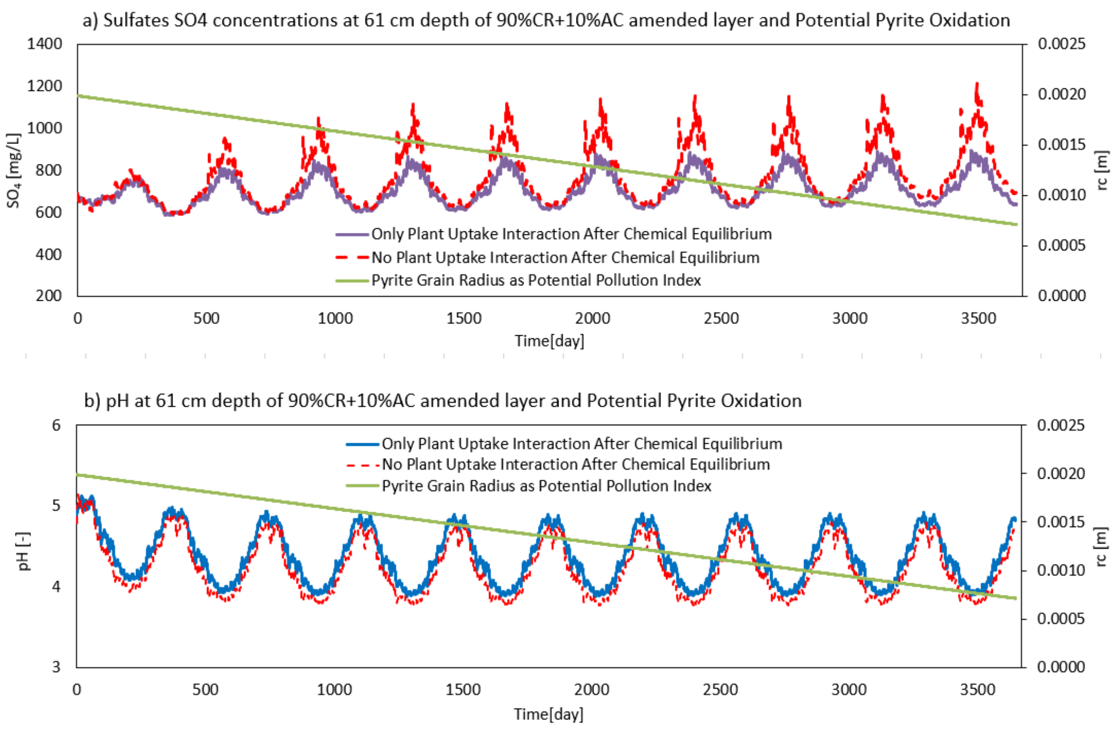

Figure 64 Comparison of sulfates SO_4 and pH time series under the effect of only metals plant uptake after chemical equilibrium by pH. Simulation series represent a 10-year simulation at 61 cm of the amended layer with 10%AC+90%CR.

In brief summary, we can distinguish among the five effects of the entangled interactions between biogeochemical processes and pyrite oxidation, the annual oscillations of solutes concentrations due to biophysiological evapotranspiration, nitrification and oxidation. We also, can recognize lower values of solutes concentration in the presence of biogeochemical processes mainly due to plant uptake.

Based on the findings on this section, we can proceed to analyze the combined effects of passive bioremediation of vegetation on the general Acid Mine Drainage Processes in the following sections.

3.7 Simulation Scenarios of Bioremediation

In this section, we present the simulation scenarios of passive bioremediation for two main types of vegetation: a) grass over the amended layer with 90% Coal Refuse (CR) and 10% Alkaline Clay (AC) b) tree vegetation (represented by forest vegetation species) also over the amended layer with 90%CR+10%AC, with a deeper root zone influence down to non-amended layer of 100%CR as recommended by Plaza (2018) and Xu (2013). The simulations were performed for a long term of 100 years for both vegetation scenarios. The five interactions described in Section 3.6 are combined to describe the final effect of vegetation on the acid mine drainage processes. As a benchmark scenario we include the simulation condition without vegetation as no bioremediation.

3.7.1 Remediation Scenario with Grass, Alkaline Clay and Coal Refuse

Figure 65 displays a lower SO_4 concentration when grass vegetation is present passive bioremediation only in the realm of the amended layer as a combined result of the biogeochemical processes interacting with pyrite oxidation as explained in Section 3.4.3. The reduction of the main trigger pollutant, SO_4, is directly related to pyrite particle radius through the computation of sulfate production. The relationship between SO_4 ions production and pyrite radius is the main reason for reduction of SO_4 concentration during the first 14-16 years (5000-6000 days). With grass bioremediation, organic matter oxidation promotes higher values of pyrite particle radius, making the reduction of SO_4 under bioremediation last longer. The reduction of SO_4 concentration in the 91 cm non-amended layer is driven also by the pyrite particle radius Figure 65-b). SO_4 concentrations in the bottom layer show an initial increase, up to a maximum value of 30000 mg/L around 25 years after the initiation of the pyrite oxidation processes, and a sustained and slow decline over the rest of the years of the simulation. However, higher values of SO_4 concentrations are computed with grass bioremediation in the non-amended layers (including the bottom layer) below the influence of the root zone, shown in Figure 65-b) and Figure 65-c). The explanation of those higher SO_4 concentrations values is the transport of more SO_4 and H^+ ions from the upper amended layer to the deeper ones. The higher amount of SO_4 produced in the amended layer is consistent with the organic matter effect through the pyrite particle radius. Also, higher amounts of Hydrogen ions are related to the nitrification interaction that also takes place in the amended layer.

Figure 66, shows consistency of pH values with SO_4 concentrations under the effect of grass bioremediation. In the amended layer, the pH is higher with grass remediation for almost the entire the simulation time. However, there are annual periods of similar pH values with grass and no remediation, especially in colder seasons when the plant evapotranspiration effect is low. Lesser values of pH in the non-amended and bottom layers are the result of higher values of SO_4 and other acidic ions being transported down to the lower layers (see Figure 65). The more significant increases in pH over the simulation time are related to times when the core ceases shrinking, meaning the pyrite radius is finally zero. The times when the pyrite radius become zero are longer with the depth of the layer as closer to the surface more oxygen is available and the shrinking core more rapidly decreases the radius. The last pyrite radius having a pollution effect is expected to finish at the 55th year after initiating the whole acid mine process. At that time, the SO_4, Fe and H^+ ion production ceases and the chemical equilibrium substantially changes the distribution of all solutes.

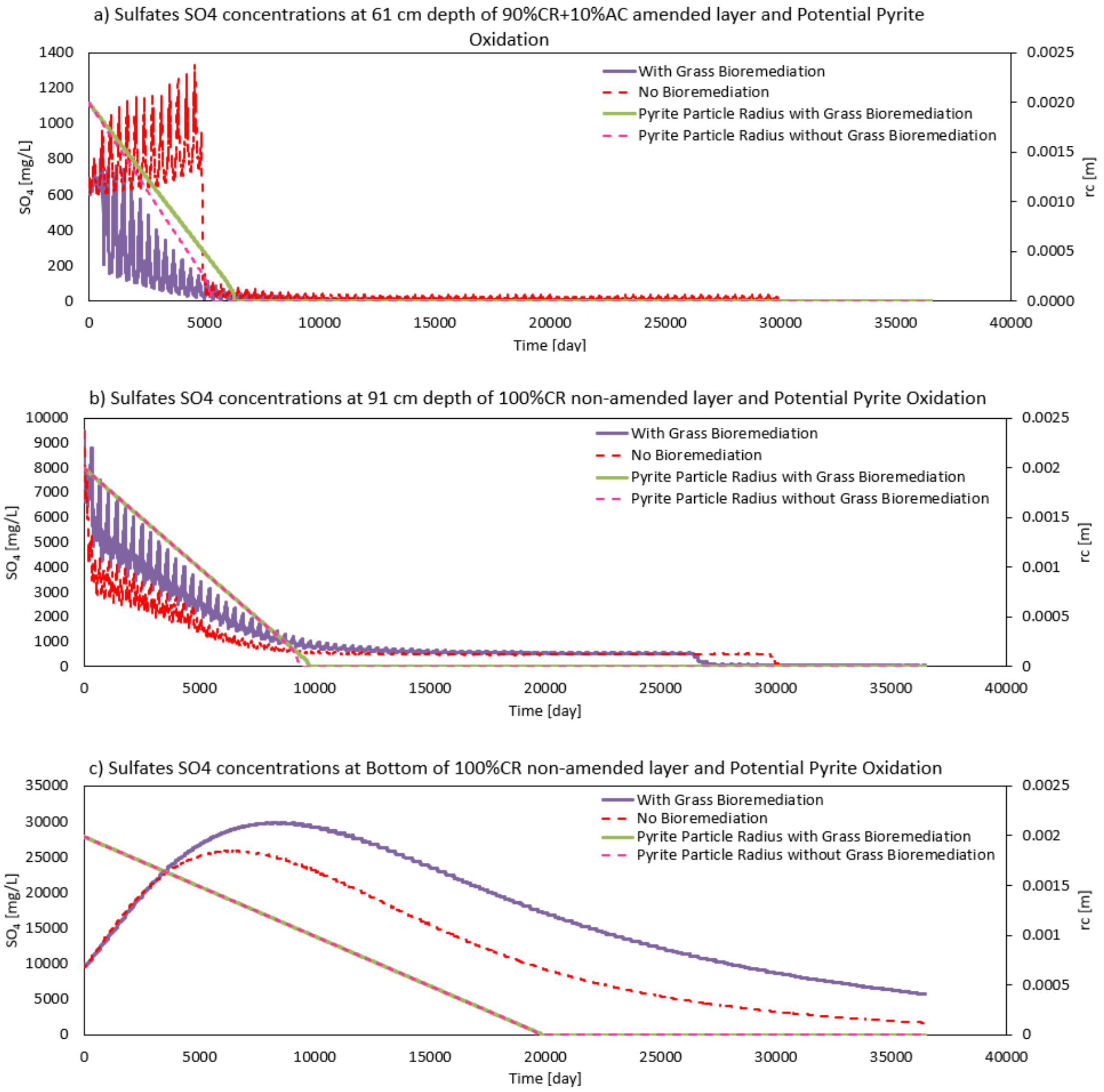

Figure 65 Comparison of sulfates SO_4 time series with and without grass bioremediation scenarios at three different amended conditions layers: a) at 61 cm of the amended layer with 10%AC+90%CR. b) at 91 cm of the non-amended layer with 100% and c) at the bottom layer of the non-amended layer with 100%CR. Also, Pyrite Particle Radius is shown as a measure of potential pollution. Time series represent a 100-year simulation.

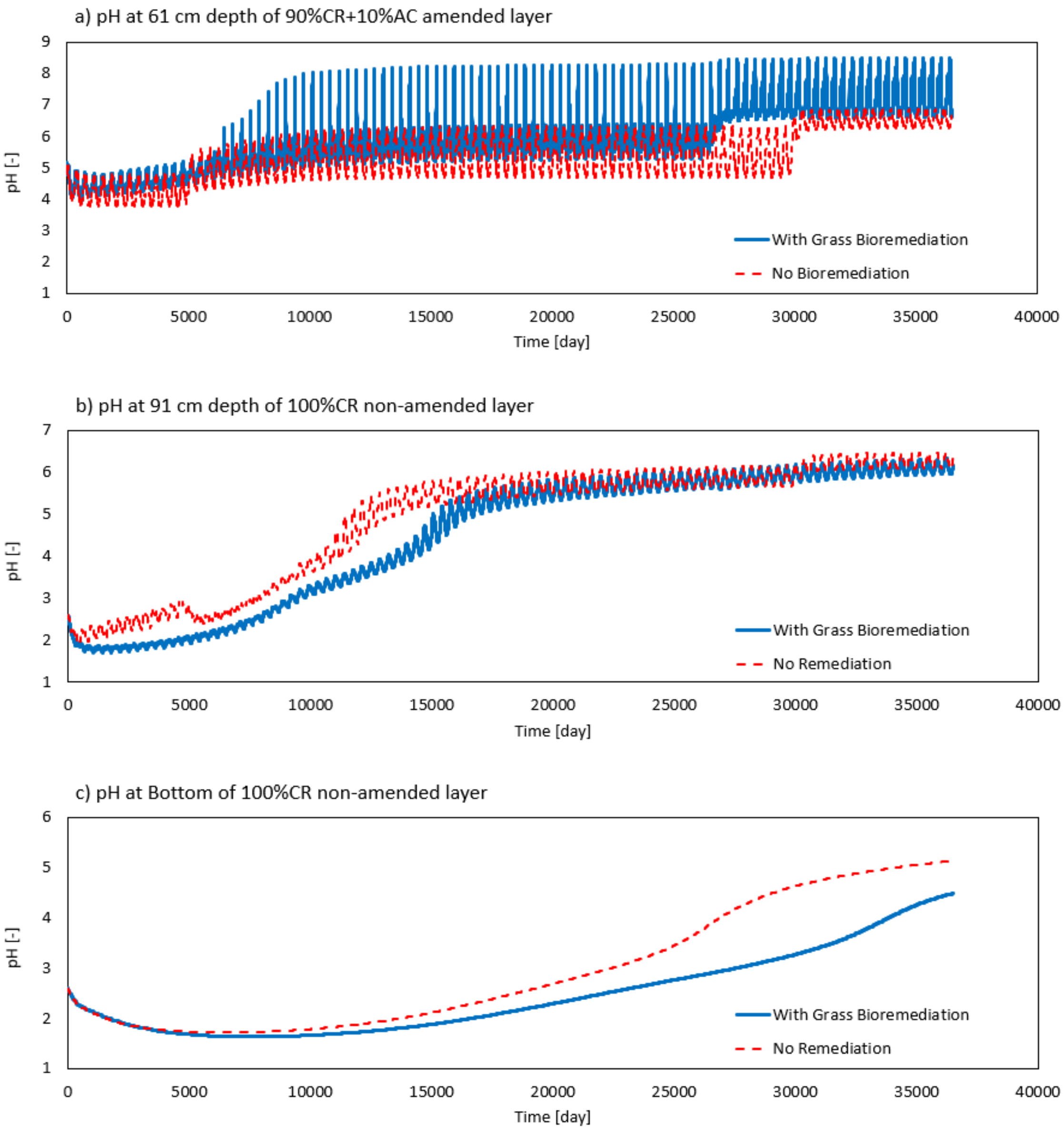
a) pH at 61 cm depth of 90%CR+10%AC amended layer

b) pH at 91 cm depth of 100%CR non-amended layer

c) pH at Bottom of 100%CR non-amended layer

Figure 66 Comparison of pH (as logarithm of Hydrogen ions concentration activity) time series with and without grass bioremediation scenarios at three different amended conditions layers: a) at 61 cm of the amended layer with 10%AC+90%CR. b) at 91 cm of the non-amended layer with 100% and c) at the bottom layer of the non-amended layer with 100%CR. Time series represent a 100-year simulation.

Figure 67 displays the low effect of grass bioremediation on SO_4 concentration and pH at deeper layer along the simulation time. For the first year, the depth distributions of SO_4 and pH with and without bioremediation are similar. The depth distributions in posterior years describe a major effect of grass bioremediation in the amended layers (from 0 to 61 cm depth). For deeper layers the opposite effect is shown. The reason for the general behavior at different times of depth distributions is the transport of SO_4, Fe and H^+ ions from the upper to the lower layers, which is only interfered with the basic chemical condition of the Alkaline Clay.

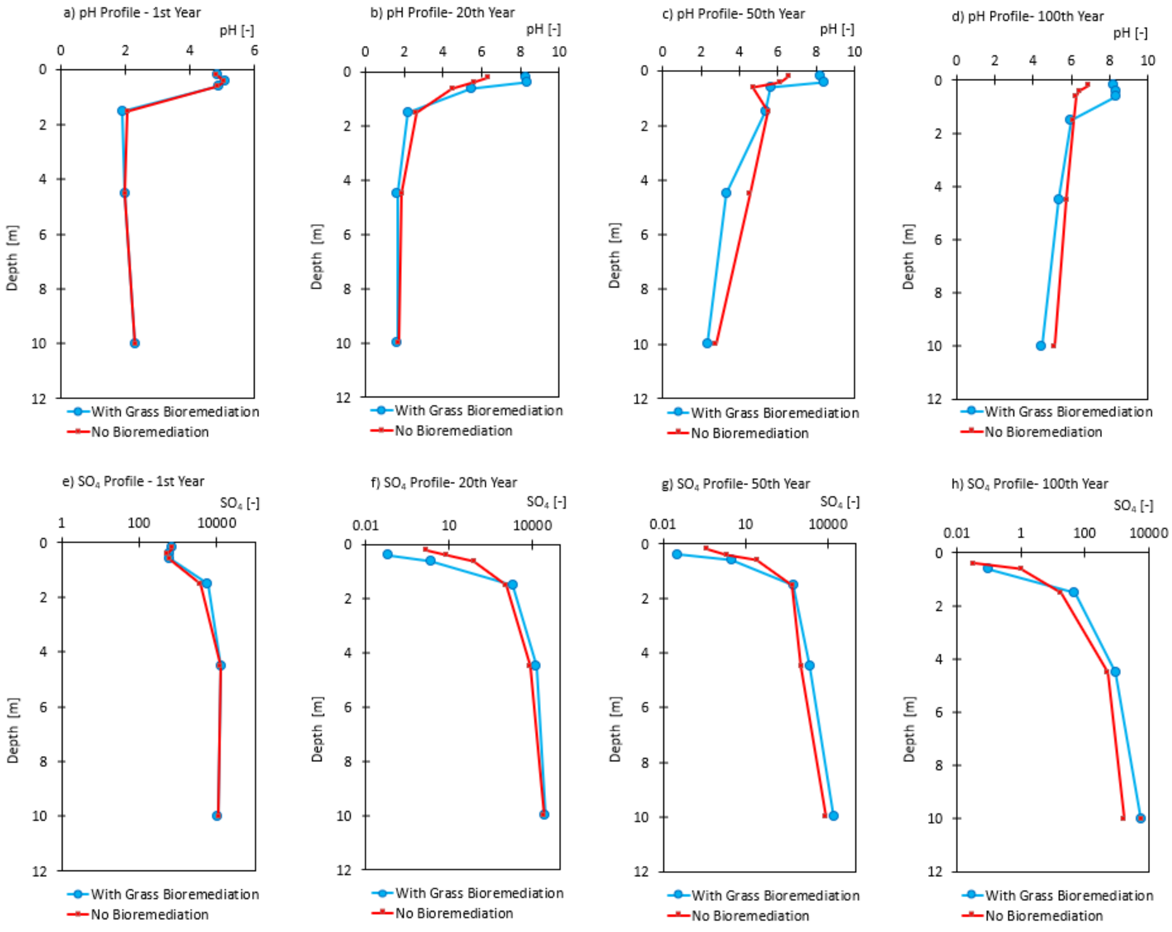

Figure 67 Comparison of Sulfates pH and SO_4 depth distributions with and without grass bioremediation at four different simulation times: 1st Year, 20th Year, 50th Year and 100th Year.

Figure 68 and Figure 69 reveal a similarity of behavior over time among the majority of solutes involved in the acid mine drainage process. With a few exceptions, the majority of solute ion decrease over time in all layers. The effect of grass vegetation is high within the amended layer, with solutes showing lesser concentrations in amended layers with grass vegetation remediation in comparison to those ones with no bioremediation. Strong acidic ions such as Fe, P and Cl trigger higher concentration values at the bottom layer. Base ions with high acid neutralization potential such as Ca, K, Si and Al have different behaviors. Over the long term, the reduction in Hydrogen ions, as the shrinking core vanishes, allows higher levels of acidic neutralization, such as with $CaCO_3$, with a consequent increase in solute concentrations over time and more stable concentration values in comparison to the case without bioremediation.

According to our simulations, the use of grass vegetation as a form of passive bioremediation promotes beneficial reduction of acidic conditions only the amended layer. The biogeochemical effect is not completely clear for deeper layers and we can assume that the general behavior within the non-amended layers is a result of the alkaline chemical interactions being transported vertically by the unsaturated flow.

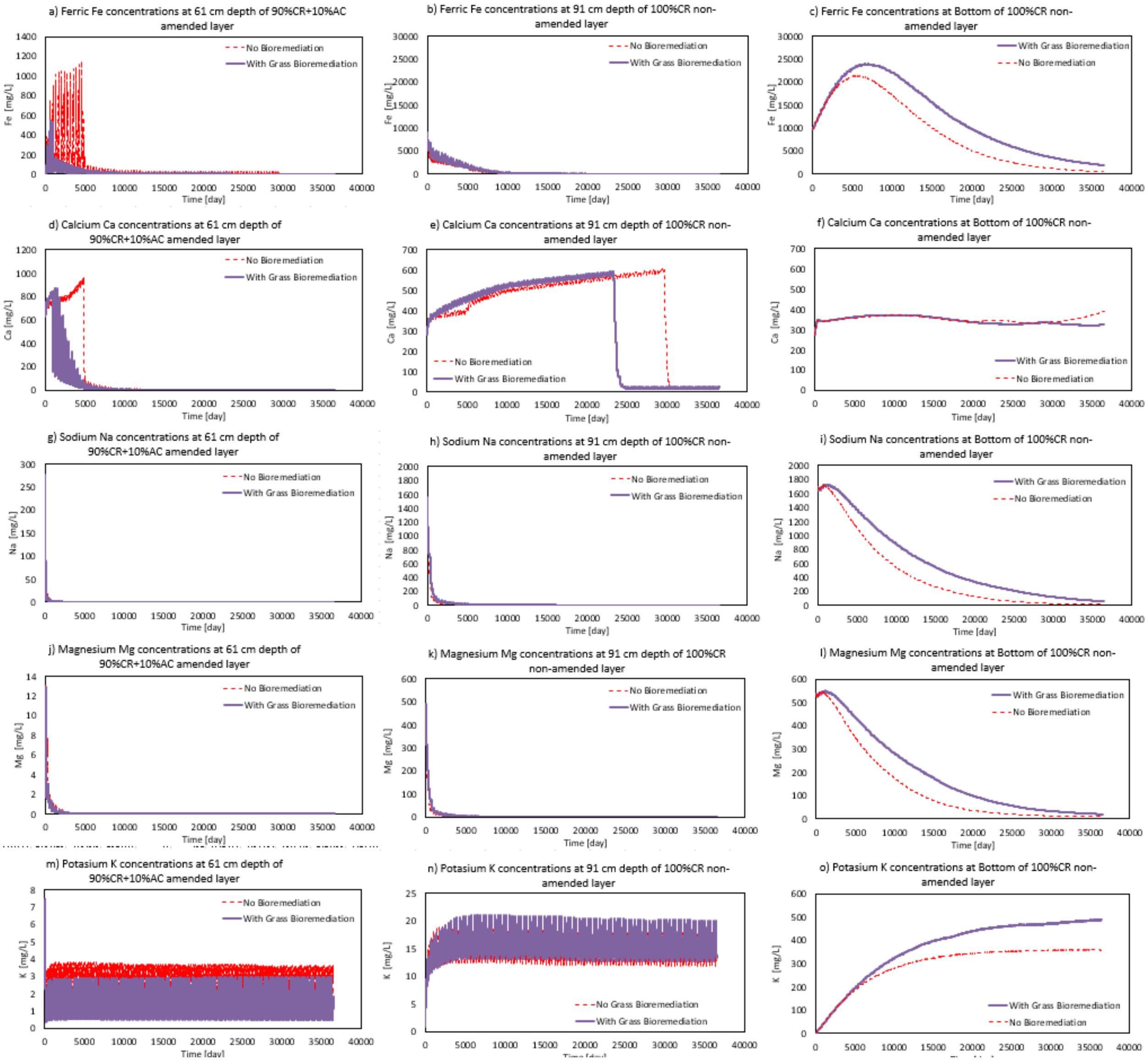

Figure 68 Comparison of Ferric Fe, Calcium Ca, Sodium Na, Magnesium Mg and Potassium K concentrations time series with and without grass bioremediation scenarios at three different amended conditions layers: a) at 61 cm of the amended layer with 10%AC+90%CR. b) at 91 cm of the non-amended layer with 100% and c) at the bottom layer of the non-amended layer with 100%CR. Time series represent a 100-year simulation.

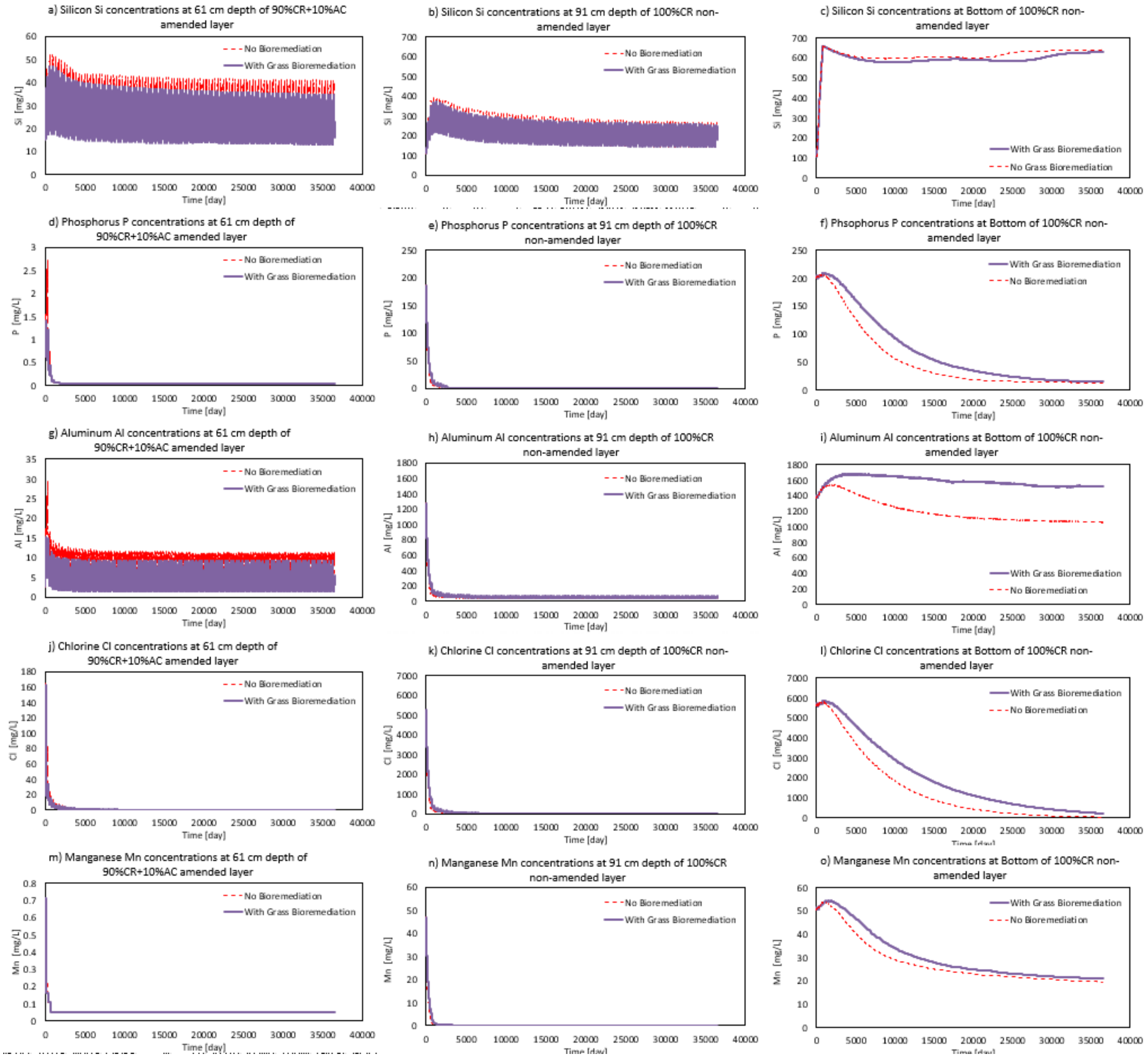

Figure 69 Comparison of Silicon Si, Phosphorus P, Aluminum Al, Chlorine Cl, and Manganese Mn concentrations time series with and without grass bioremediation scenarios at three different amended conditions layers: a) at 61 cm of the amended layer with 10%AC+90%CR. b) at 91 cm of the non-amended layer with 100% and c) at the bottom layer of the non-amended layer with 100%CR. Time series represent a 100-year simulation.

3.7.2 Remediation Scenario with Tree Vegetation Types and AC-CR.

The environmental effect of planting of tree vegetation as a forest species on coal refuse piles is examined in this section. In this particular case, there are two changes expected in the interactions between acid mine and biogeochemical processes: a) an increase in the rate of carbon assimilation potential for the proposed type of vegetation which, according to Smith et al. (2019), has an indirect effect on the organic soil processes and b) a deeper root zone than that in the grass scenario, which implies a stronger influence of plant evapotranspiration along the soil column and a stronger plant uptake effect, even in the non-amended layers.

Figure 70 describes a remarkable effect of tree vegetation as bioremediation over time in both the amended and non-amended layers. Lesser SO_4 concentrations are computed by the long term 100-year simulation in comparison to those show for grass in Figure 65, showing improvement with the use of trees as a form of phytoremediation. Even in the bottom layer, the SO_4 concentrations are lower than the benchmark condition of no bioremediation. The main explanation for the decrease in concentrations at all chemicals with tree vegetation is the deeper influence of metal plant uptake, including in the non-amended 100% CR layer. Also, as with the SO_4 concentrations shown for grass in Figure 65, there is a progressive reduction of the solute over time, defined by the shrinking core radius. The annual oscillation patterns are the same as those computed with only grass vegetation.

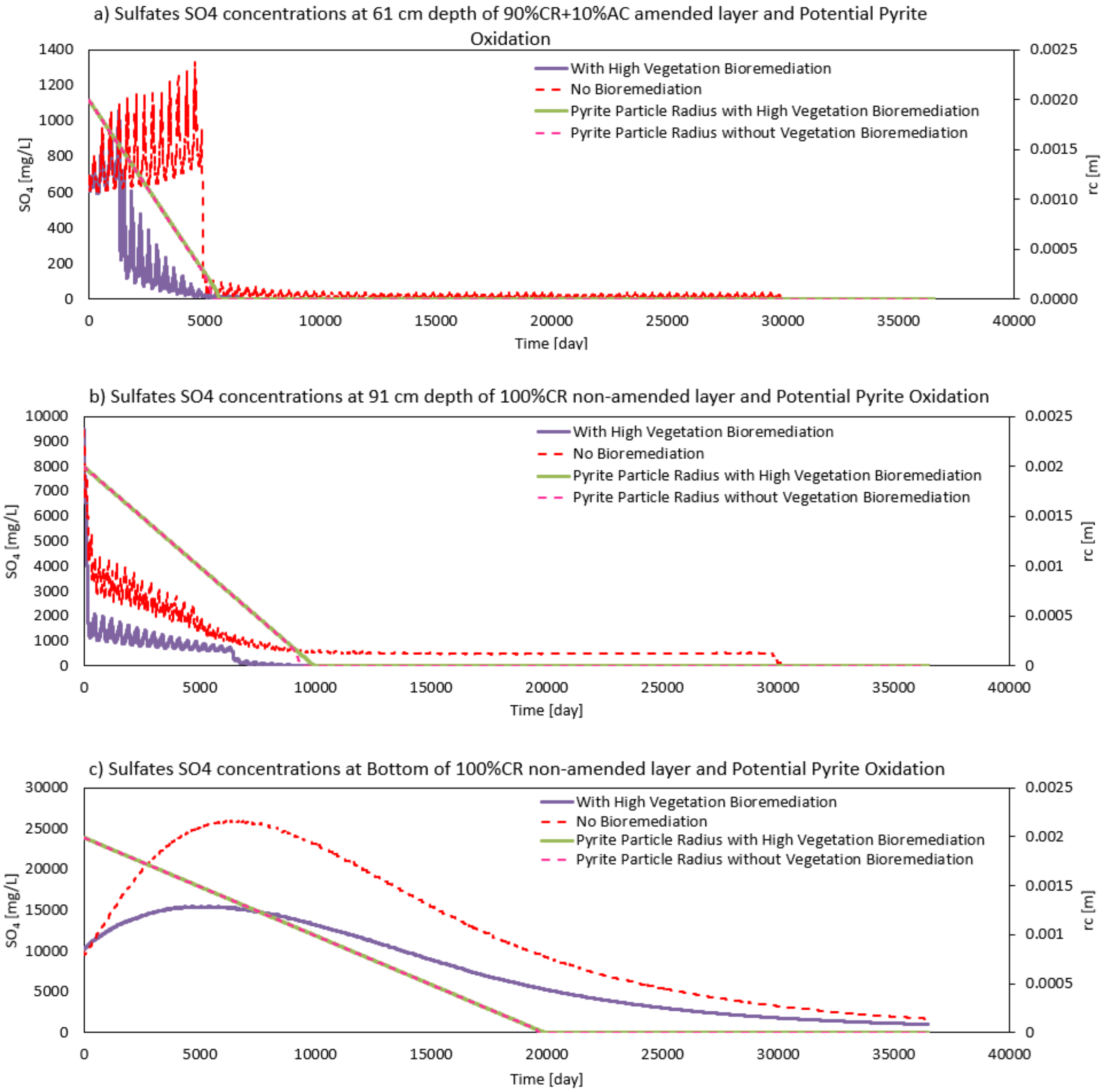
a) Sulfates SO4 concentrations at 61 cm depth of 90%CR+10%AC amended layer and Potential Pyrite Oxidation

b) Sulfates SO4 concentrations at 91 cm depth of 100%CR non-amended layer and Potential Pyrite Oxidation

c) Sulfates SO4 concentrations at Bottom of 100%CR non-amended layer and Potential Pyrite Oxidation

Figure 70 Comparison of sulfates SO_4 time series with and without tree vegetation bioremediation scenarios at three different amended conditions layers: a) at 61 cm of the amended layer with 10%AC+90%CR. b) at 91 cm of the non-amended layer with 100% and c) at the bottom layer of the non-amended layer with 100%CR. Also, Pyrite Particle Radius is shown as a measure of potential pollution. Time series represent a 100-year simulation.

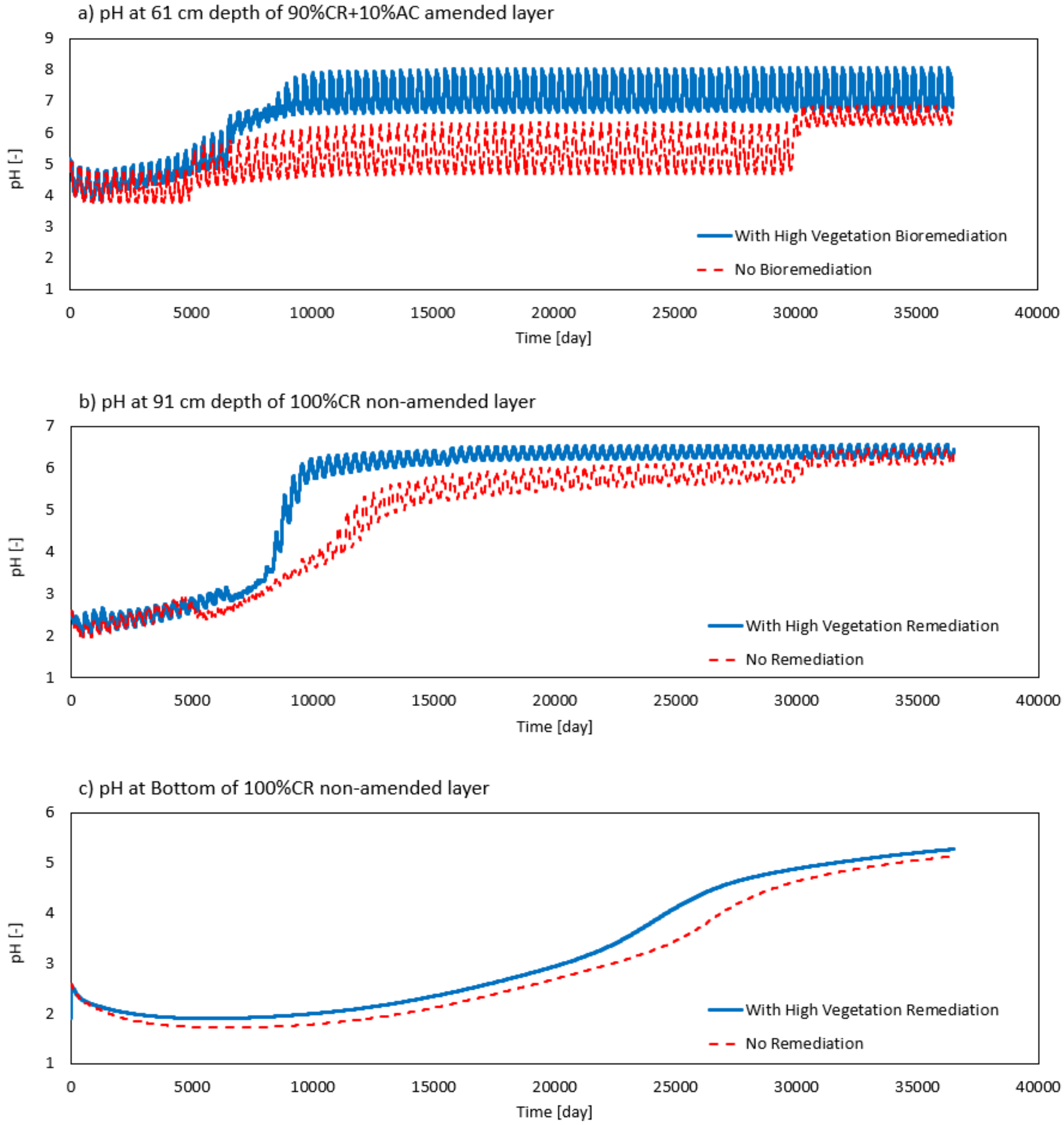

Figure 71 Comparison of pH (as logarithm of Hydrogen ions concentration activity) time series with and without tree vegetation bioremediation scenarios at three different amended conditions layers: a) at 61 cm of the amended layer with 10%AC+90%CR. b) at 91 cm of the non-amended layer with 100% and c) at the bottom layer of the non-amended layer with 100%CR. Time series represent a 100-year simulation.

Figure 71 features coherent results for SO_4 concentrations with tree vegetation, with higher values of pH over time and in all layers. The greater effect of acidic solutes reduction as a result of more plant uptake promotes a greater potential for neutralization of Ca, Si and Al as well as other basic solutes. Despite the production of hydrogen ions by nitrification, the vertical transport is not appreciable enough to be captured by the effect of chemical equilibrium among the solutes.

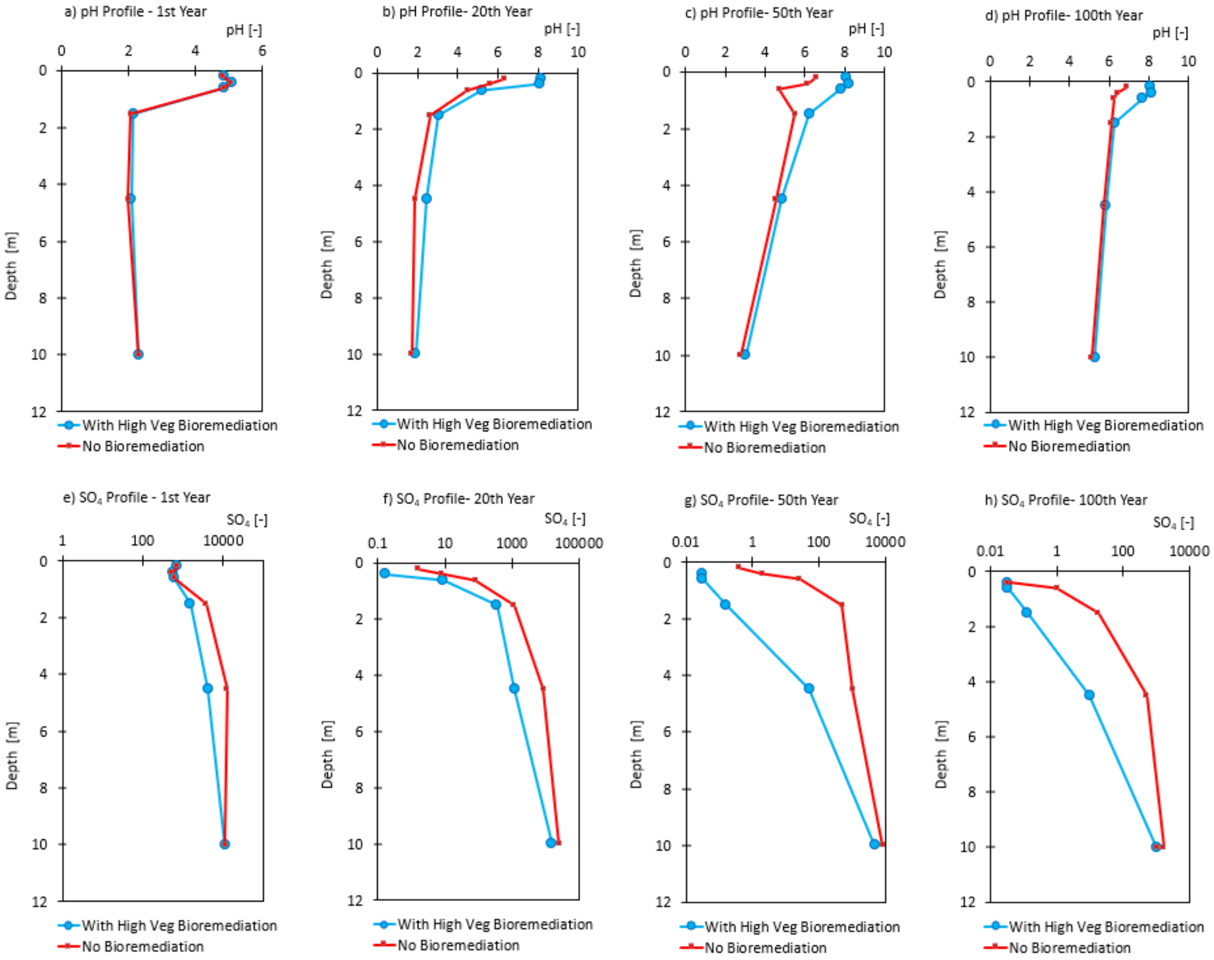

Figure 72 Comparison of Sulfates pH and SO_4 depth distributions with and without tree vegetation bioremediation at four different simulation times: 1st Year, 20th Year, 50th Year and 100th Year.

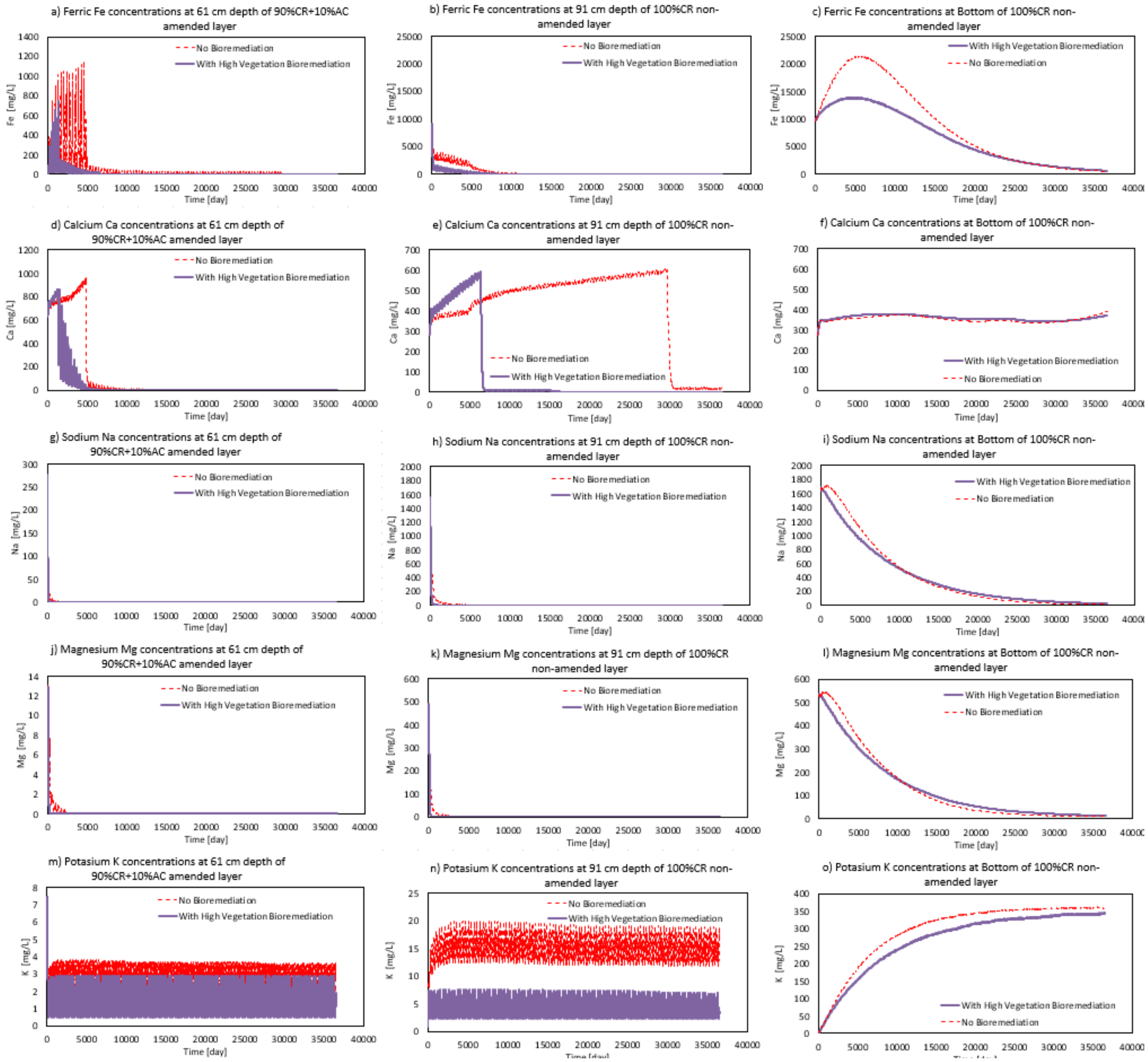

Figure 73 Comparison of Ferric Fe, Calcium Ca, Sodium Na, Magnesium Mg and Potassium K concentrations time series with and without tree vegetation bioremediation scenarios at three different amended conditions layers: a) at 61 cm of the amended layer with 10%AC+90%CR. b) at 91 cm of the non-amended layer with 100% and c) at the bottom layer of the non-amended layer with 100%CR. Time series represent a 100-year simulation.

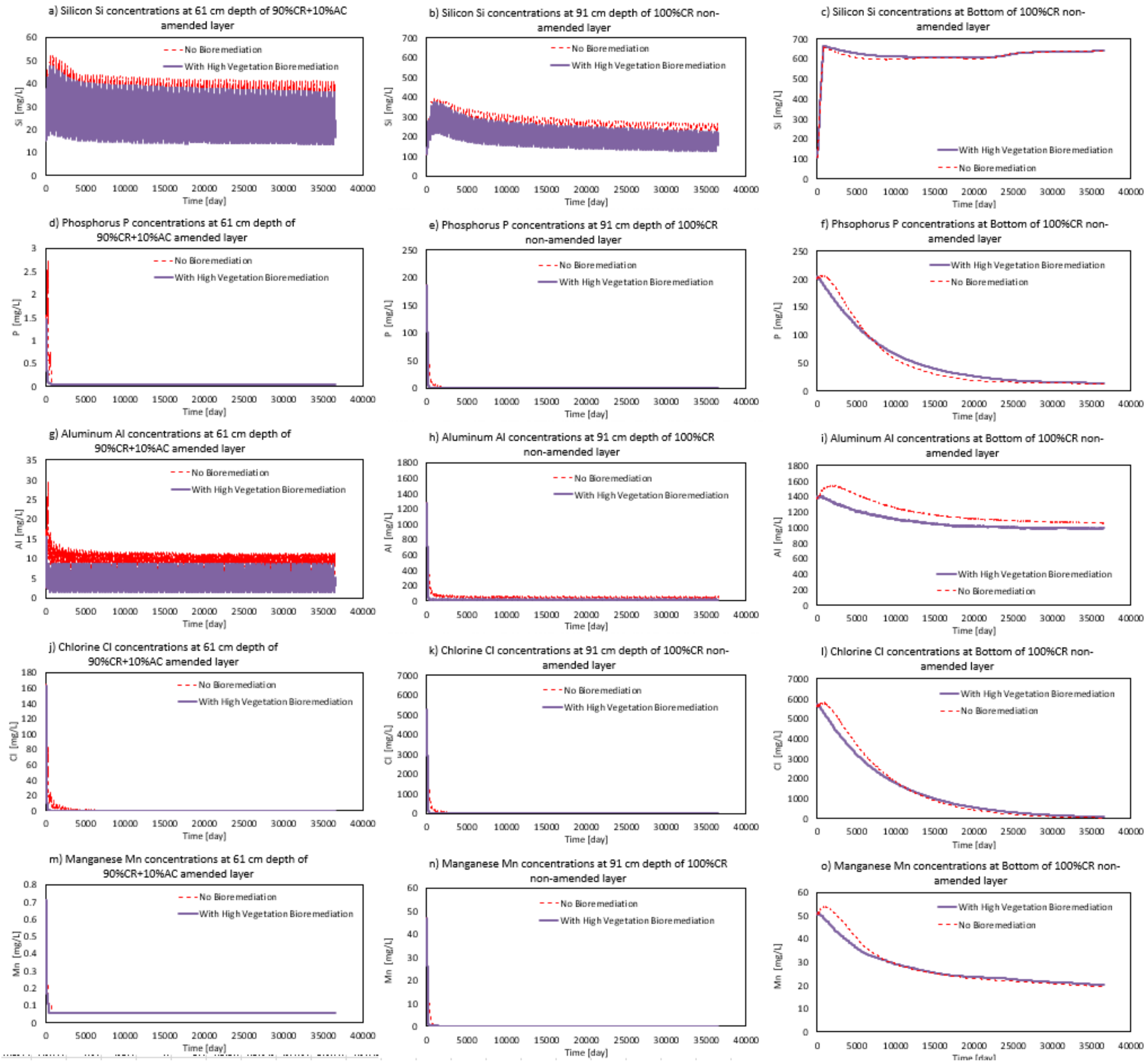

Figure 74 Comparison of Silicon Si, Phosphorus P, Aluminum Al, Chlorine Cl, and Manganese Mn concentrations time series with and without tree vegetation bioremediation scenarios at three different amended conditions layers: a) at 61 cm of the amended layer with 10%AC+90%CR. b) at 91 cm of the non-amended layer with 100% and c) at the bottom layer of the non-amended layer with 100%CR. Time series represent a 100-year simulation.

Figure 72 depicts more appreciable differences between the bioremediation and no remediation conditions in terms of depth distribution of SO_4 concentration and pH. All the snapshots show considerable reduction of pollution, especially over the SO_4 concentrations.

In contrast to the grass vegetation scenario, Figures 73 and 74 show lower concentrations for all solutes at the bottom layer also, again as a consequence of deeper metals plant uptake. Even for basic acidic-neutralizers solutes such as Ca, K, Si and Al the concentrations are lower in both the amended and non-amended layers, with almost similar values at the bottom layers.

In partial conclusion, we can observe based on the long-term simulations that use of tree vegetation as passive remediation has a more relevant environmental impact on the reduction of pollution due to potential plant uptake. Moreover, the capacity of bioaccumulation of metals can be increased using plants a more resilient than grass species. For both cases with grass vegetation and tree vegetation, the expected reduction in SO_4 solutes in the amended layer is around 15 years. According to Plaza (2018) this time can serve as a guide for when to cut off the vegetation to restore the capacity of bioaccumulation.

3.8 Conclusions

The simulations and analyses show that the main interactions between the biogeochemical processes and pyrite oxidation as a main AMD process are driven primarily by the seasonal plant evapotranspiration as a result of the soil moisture variation, where mineral nitrogen processes and organic matter oxidation reduce the pH and the solute plant uptake reduces the level of solute concentrations. Despite the increase in hydrogen ions production caused by nitrification and organic matter oxidation, the final resulting effect scenario with bioremediation decreases the solute concentration values and increases the pH.

The long-term simulation of passive bioremediation with grass vegetation shows this to be environmentally efficient only in the amended layer, where the biogeochemical processes operate. For the deeper non-amended layers, the simulations reveal that solutes concentrations are higher even with bioremediation except for neutralization species such as Ca and Si.

On the other hand, the simulation with tree vegetation shows better performance at reducing solute concentrations and increasing the soil pH. With a larger root zone, the solute capture by trees promotes lower solute concentrations along the depth of soil column. Therefore, the final result of the biogeochemical interactions using tree vegetation with acid mine drainage is more prevalent than in the grass vegetation scenario, which has only influence on the amended layer.

Using the pyrite oxidation equations and the qualitative system dynamics analysis, we can explain the sequence of the AMD process, starting by examining the availability of oxygen throughout the soil matrix, then looking at the shrinking core radius reduction and finally, examining the sulfate, ferric ion and hydrogen ion production. The sequence of the process allows us to clarify the importance of oxygenation of the soil. Whereas it seems that initially it might worsen the general pollution conditions, oxygenation actually seems to accelerate the pyrox process, making it available to be used as a remediation method. This means that we can create and implement devices to increase the oxygenation mechanisms in the soil to prompt the cessation of the pyrite oxidation.

Finally, we can assume the time for the cutoff of planting to be after the cessation of the first layer pyrite oxidation process, when the production of SO4 solutes has completely declined. In both phytoremediation scenarios this time is around 10 years.

4.0 Acid Mine Drainage Pollutant Storage Capacity and Transport on the Watershed Scale

4.1 Introduction

Solute pollution on the watershed scale is still one of the main concerns in engineering and environmental science (Beer and Young 1984; Mortensen et al. 2016). One open research question in watershed contaminant analysis is how we can evaluate the ability of environmental systems to recover from adverse or deteriorated conditions to return to their original or natural cycling states before the pollution disturbance (Li and Lence 2007; Mcintyre et al. 2003). Restoration capacity is often studied using risk-resilience analysis, which can inform best remediation management practices and allow prediction of long term effects of disturbances (Mcintyre et al. 2003; Park et al. 2015). On the other hand, water quality of the streams in the watershed is one of the main indicators of environmental health of natural systems (Beer and Young 1984; Mortensen et al. 2016). Both environmental issues can be addressed by the usage of transport modeling on the watershed scale. Indeed, both pollution risk-resilience analysis and water quality modeling are intrinsically intertwined when explaining watershed pollution transport behavior due to the anthropogenic impacts.

Resilience analysis of water systems can be determined by focusing on three main features (Wang and Blackmore 2009): a) the threshold values for determining system operativity; b) the recovery potential of a natural system; c) the ulterior consequences of disturbances on both ecological and human systems. A probabilistic or uncertainty approach to measure risk and resilience is generally used to operationalize threshold behavior (Mcintyre et al. 2003; Wang and Blackmore 2009). Other approaches based on system response or adaptative capacity have been added in a minor integrated manner in probabilistic resilience analysis. In our transport watershed modeling of AMD effects, we develop a simple conceptual approach to a resilience formulation based on target load and mass storage pollution. Using on this conceptual approach, we explore a measure of the watershed system recovery capacity to overcome AMD pollution, with or without phytoremediation.

On the water quality side of this watershed transport modeling, while most studies have been carried out using geochemical AMD analysis only, we include phytoremediation analysis scenarios. Traditionally, watershed transport modeling in the realm of AMD conditions have focused on 2D or 3D hydrodynamic groundwater coupled with contaminant transport models as shown in Mayer (2019). Other modeling works, such as Galván et al. (2016) may be hydrologically based, using SWAT code to asses AMD areas. One previous transport model, developed by Plaza (2018) is based on using a shrinking core and geochemical model to account for the effects of amended passive remediation of 10% alkaline clay at the watershed outlet at the Mather and Ernest sites, similar to this study. However, there is a tendency to use recent data driven modeling of water and transport quality as Artificial Neural Networks ANN (Ardejani et al. 2013; Bahrami and Doulati Ardejani 2016).

As indicated above, the interrelation between surface water quality and the pollution capacity-resilience analysis is supported by watershed transport computation (Czuba and Foufoula-Georgiou 2014; Gangodagamage et al. 2014). In our approach, we follow the general concept of long-term transport capacity based on cell-links over the watershed as defined in Gangodagamage et al. (2014). These authors establish sediment transport on the watershed scale based on an Incremental Area Function IAF Gangodagamage et al. (2014). Based on the IAF concept, we use the fundamental mass balance idea to estimate the solute transport from each cell to the outlet.

Specifically, we integrate in a novel manner the ADZ modeling (Camacho and Gonzalez 2008) within the DHSVM-HTGCM with the surface solute results computed by the Hydro-Biogeochemical model presented in Chapter 3. We use the cell-link long term solute transport Gangodagamage et al. (2014) to compute the pollution resilience-capacity at the Mather and Ernest watersheds.

In this chapter, we present the results of the Hydro-solute transport model stage of this dissertation. Chapter sections include a description of the model implementation and presentation of a simulation of pollution capacity-resilience analysis and the effects of our two precedent scenarios of phytoremediation on the water quality results.

4.2 Model Implementation

The computation of solute transport developed in this dissertation is an approximation of conventional equations of transport used in this type of analysis. Whereas Advection-Dispersion partial differential equations are commonly used, we use the Advective Dispersive Zone ADZ model (Camacho and Gonzalez 2008). The final implementation of the transport computation uses the original resources of DHSVM developed by Xu (2013) for the computation of concentrations at the watershed outlet, including the 8-direction method for stream network computation. We adapted the representation of the biochemical processes in the vertical column realm to be linked to the watershed stream network in terms of surface and subsurface flows. The next sections explain in detail the implementation of the integration of biogeochemical processes with the solute transport computation in the DHSVM-HTGCM model.

4.2.1 From Column Process to Watershed Scale Modeling

The link between the biogeochemical-pyrox processes and the transport across a watershed is made using surface and subsurface flows. Figure 75 shows how the flows computed by DHSVM-HTGCM are to compute the column mass balance of the main pyrite solutes SO_4, Fe and H^+. Then a solute mass balance is computed in the subsurface zone and the transport of solutes is given by the flows computed previously by the unsaturated module inside DHSVM-HTGCM. The surface transport is computed with a simplified ADZ model using previous flow routing discharges.

The main inputs in this study's configuration are computed using the Hydro-Biogeochemical Model and include: a) the bottom vertical discharge layer from unsaturated module $q_{vert\text{-}in}$, in the Hydro-biogeochemical model and b) the bottom solute concentration C_{in} as computed by the solute transport equation in the Hydro-biogeochemical model.

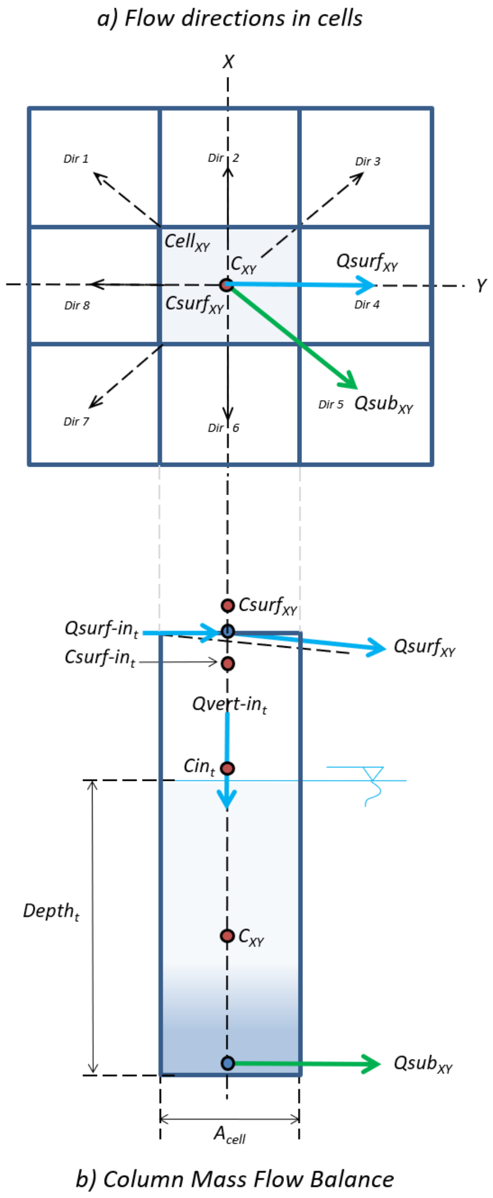

a) Flow directions in cells

b) Column Mass Flow Balance

Figure 75 Scheme linking column pyrite-biogeochemical computation to watershed stream network transport computation. a) The 8-direction flow direction method is used to transport solutes through the watershed. b) The soil unsaturated-saturated column mass balance represents the pollution storage at each cell.

Once the solute mass balance within the column is computed, the 8-direction method is used to compute the transport through the stream network of the watershed. Then, the mass is transported along the stream network to the outlet of the watershed, as shown in Figure 76.

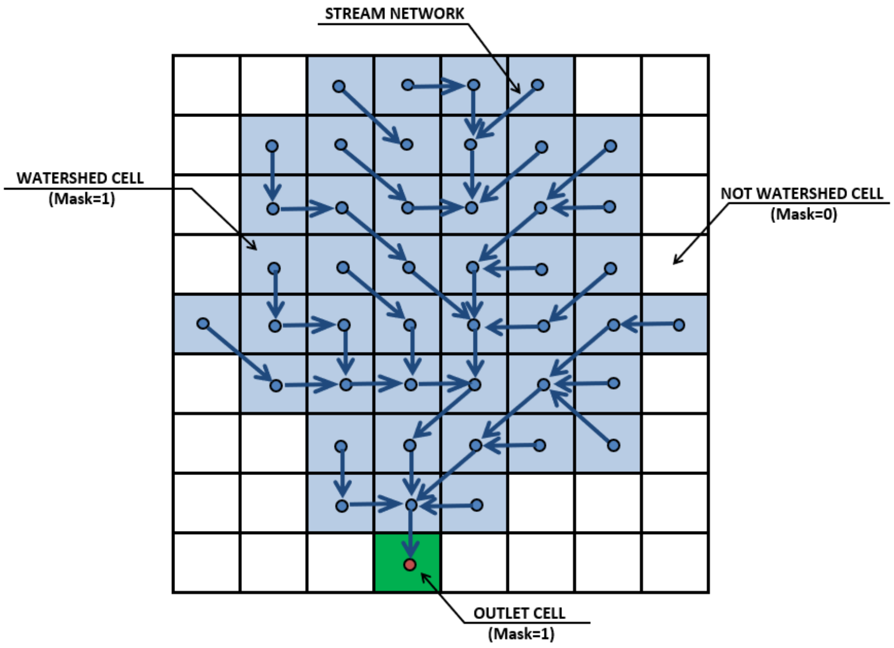

Figure 76 Schematic formulation of stream network based on 8-direction Digital Elevation Model DEM information. This system information for stream network is used to develop the connection between the soil column model in Chapter 3.0 and the subsurface and surface transport models.

Figure 77 presents the DEM configuration for the Mather and Ernest sites and the stream network determined by the 8-direction method suitable for the application of the transport models.

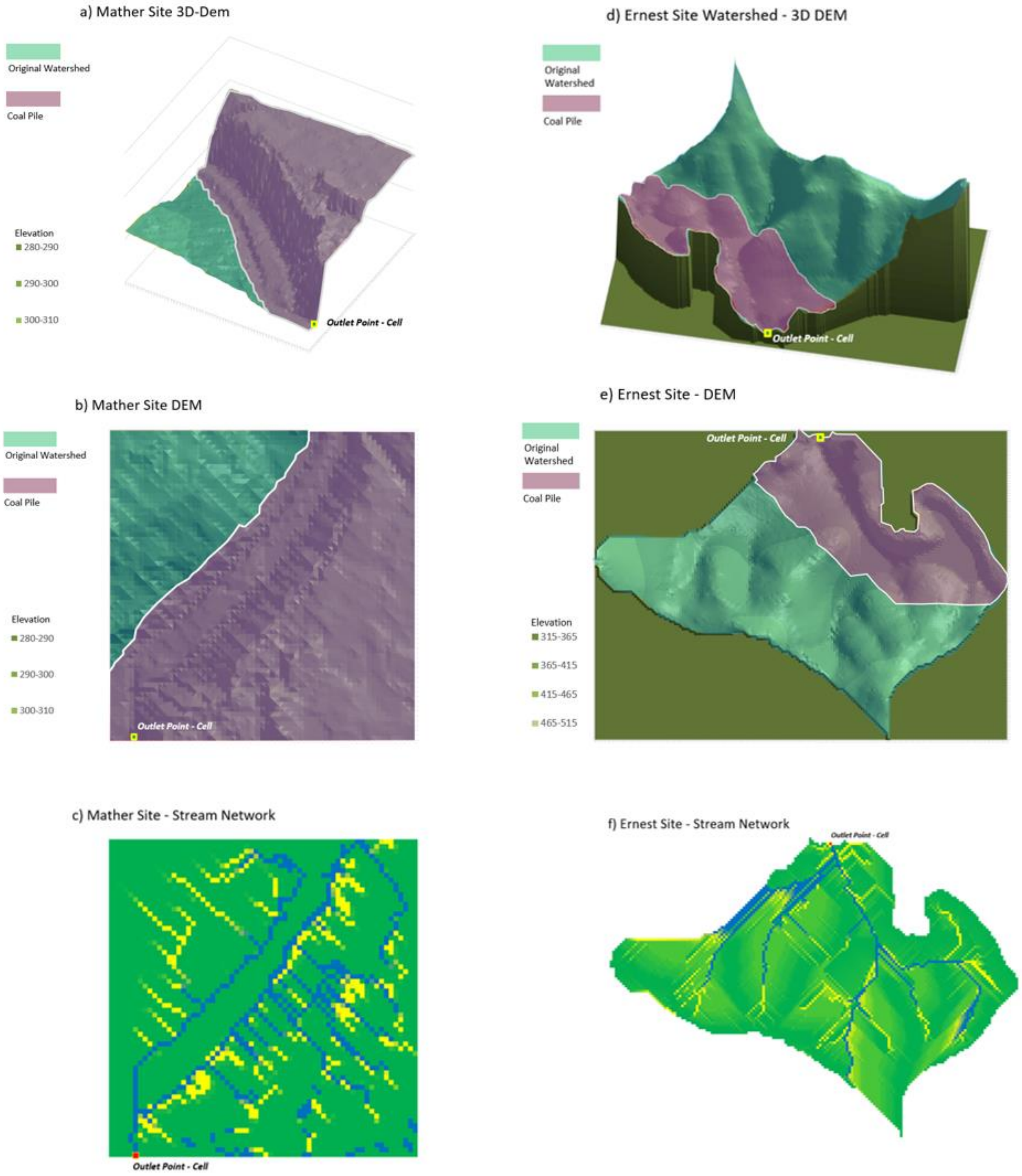

a) Mather Site 3D-Dem

d) Ernest Site Watershed - 3D DEM

b) Mather Site DEM

e) Ernest Site - DEM

c) Mather Site - Stream Network

f) Ernest Site - Stream Network

Figure 77 Digital Elevation Models for Mather and Ernest sites watersheds used for column to watershed transport computations.

4.2.2 Subsurface Acid Mine Drainage Solute Transport on the Watershed Scale

The subsurface solute transport from each column cell to the outlet of the watershed is carried out through a mass balance over all the cells within the watershed, as shown in Equation 4.1 below. The 8-direction method is used to determine the cell balance and the vertical solute mass from the bottom layer of the soil column. Figure 78 illustrates the subsurface mass balance used to estimate the pollution capacity over the watershed.

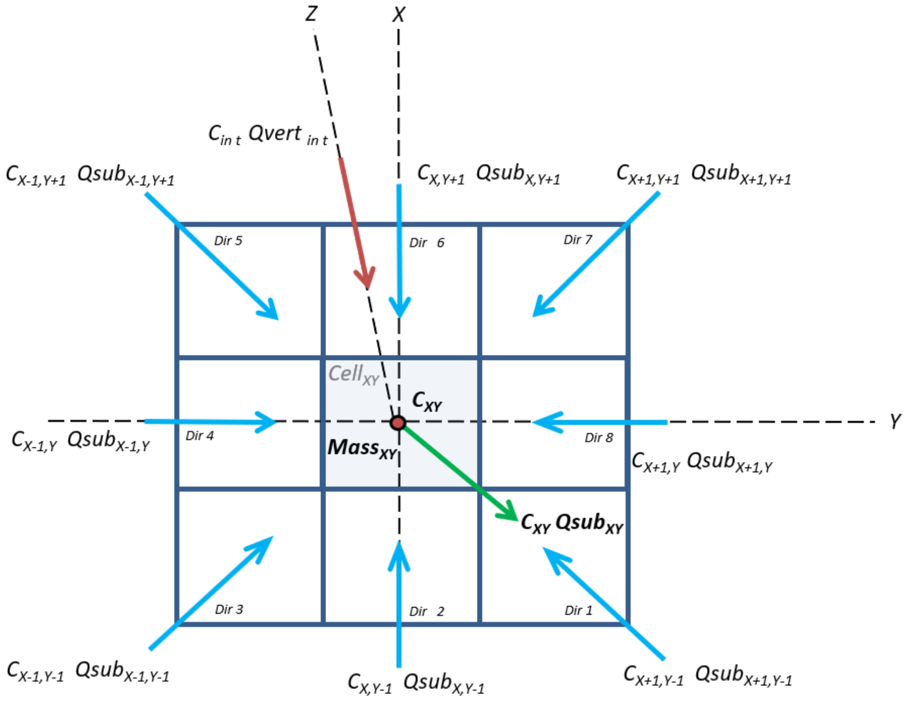

Figure 78 Scheme of subsurface solute balance for each cell according to Equation 4.1, extension of scheme in Figure 75.

$$A_{cell}D\frac{dC_{xy}}{dt} = \left[\sum_{cell}^{8-dir} q_{cell}^{sub}C_{cell} - q_{xy}^{sub}C_{xy}\right] + q_{in}^{vert}C_{in} \qquad [4.1]$$

where C_{xy} [mg/L] is cell *xy* solute pollutant concentration; A_{cell} [m^2] cell *xy* horizontal area; *D* [m] cell *xy* water table depth; C_{cell} [mg/L] 8-direction adjacent cells solute pollutant concentration; q^{sub}_{cell} [m^3/s] 8-direction adjacent cells subsurface discharge; q^{sub}_{xy} [m^3/s] cell xy subsurface discharge; q^{vert}_{in} [m^3/s] cell xy vertical leaching discharge; and C_{in} [mg/L] cell xy leaching solute pollutant concentration.

4.2.3 Surface Acid Mine Drainage Solute Transport on the Watershed Scale

The subsurface transport implementation is similar to that of subsurface. In the subsurface model implementation, each cell input concentration is given by the surface concentration at the surface layer from the hydro-biogeochemical column model. The tracks for the solute routings follow the stream network structure. The discharges used in the model are computed using the routing incorporated within DHSVM-HTGCM by Xu (2013). The ADZ model is used for the solute transport as follows:

$$\frac{dC_{link}}{dt} = \frac{1}{T_{res}}\left[\sum_{link-sn} q_{link-sn} C_{link-sn} + q_{runoff}\,[C_{surf}] - q_{link}\, C_{link}\right] \qquad [4.2]$$

where C_{link} [mg/L] is solute pollutant concentration at the end of the *link*; T_{res} [day] residence-travel time in *link*; $C_{link\text{-}sn}$ [mg/L] solute pollutant concentration at the end of the *link of the inflow stream network*; $q_{link\text{-}sn}$ [m^3/s] *link-stream network* discharge; q_{link} [m^3/s] *link* discharge; [C_{surf}] [mg/L] surface pollutant concentration at cell-link; and q_{runoff} [m^3/s] cell-link runoff discharge.

4.2.4 Conceptual Acid Mine Drainage Capacity and Resilience on the Watershed Scale

We can define Acid Mine Drainage Capacity (AMDC) as the maximum level of pollutant storage mass that the watershed has reached in a long-term dynamic simulation. Based on this simple concept, we can associate the resilience of the watershed to overcome pollution with the ability to transport out as much as pollution as possible. Consequently, the better the resilience, the greater and faster the transport out of AMDC quantity of pollution from the watershed. We use the subsurface transport to estimate the AMDC throughout the long term 100-year simulation because pyrite oxidation has ceased and so the low solutes concentrations cannot be used as a main input of pollution to the watershed. Therefore, as a resilience indicator we can take the time required by the watershed to export as much of the pollution quantity AMDC as possible. Based on the proposed AMDC concept, the following equation can be taken as its representation:

$$AMDC = max\left[M_{pol} = \sum_{y}^{Ny} \sum_{x}^{Nx} A_{cell} D C_{xy} \right] \quad [4.3]$$

where *AMDC* [Ton] is Acid Mine Drainage Capacity as the maximum total mass of pollutant storage in the watershed in the extent of simulation time; C_{xy} [mg/L] cell *xy* solute pollutant concentration computed by subsurface transport model; A_{cell} [m^2] cell *xy* horizontal area; *D* [m] cell *xy* water table depth; and M_{pol} [Ton] Total mass of pollutant within the subsurface realm in the watershed.

The next section explores the capacity and resilience concepts using simulations on the watersheds at both the Mather and the Ernest sites.

4.3 Application Simulations and Analyses

This section presents the application of solute transport of AMD processes on the watershed scale to answer the question about pollution capacity using the following three concepts: a) the AMDC for the Mather and Ernest sites and the interpretation of the subsurface Sulfate SO_4 transport results to understand spatial and temporal distribution of the AMD pollution; b) the autonomous recovery capacity of export Sulfates SO_4 based on the AMDC for the Mather and Ernest sites as a resilience concept in both watersheds; and finally, c) a comparison of main solute pyrox concentrations under the Chapter 3.0 vegetation scenarios.

4.3.1 Capacity and Resilience of AMD Pollutants on the Watershed Scale

Figure 79 depicts how the capacity of pollutant Sulfate SO_4 mass storage reaches a maximum value around the 70th year after of the beginning the pyrite oxidation pollution for Mather site. The AMDC can be estimated to be 485 tons of SO_4. The maximum value of AMDC for SO_4 is reached because the level of inflow of pollution has a maximum value around at 25 years. After these 25 years a sustained decline to lower values explains the maximum AMDC value. The outlet subsurface concentration follows the same behavior as AMDC but with a high dilution value (from average concentration of 15000 mg/L to 600 mg/L) in comparison to the values at bottom layers of non-amended layers.

Figure 80 corroborates the substantial order of magnitude difference between the input and the export of Sulfate SO_4 pollution at the Mather site, presenting this information as a detailed plot of Figure 79. This difference explains the initial increase in AMDC and the maximum value as the input of pollution is almost dissipated at the end of the simulation time. The increase of the total watershed discharge can explain lower value concentrations at the Ernest site than those in Mather, where the area of corresponding total discharge is less. The simulations show behavior of the target load similar to that in Reinds et al. (2009) in terms of the yearly changes.

Figure 81 and Figure 82 present results of the AMDC at the Ernest site and the Mather site, showing their similarity. At the Ernest site, the maximum mass SO_4 storage is encountered at the end of the simulation time. As at the Mather site, the input of sulfates pollution is maximized about 20 years after the initial conditions and falls to almost zero at the end of the simulated 100 years. The computed export is 10 times less in comparison to the order of magnitude at the Mather site.

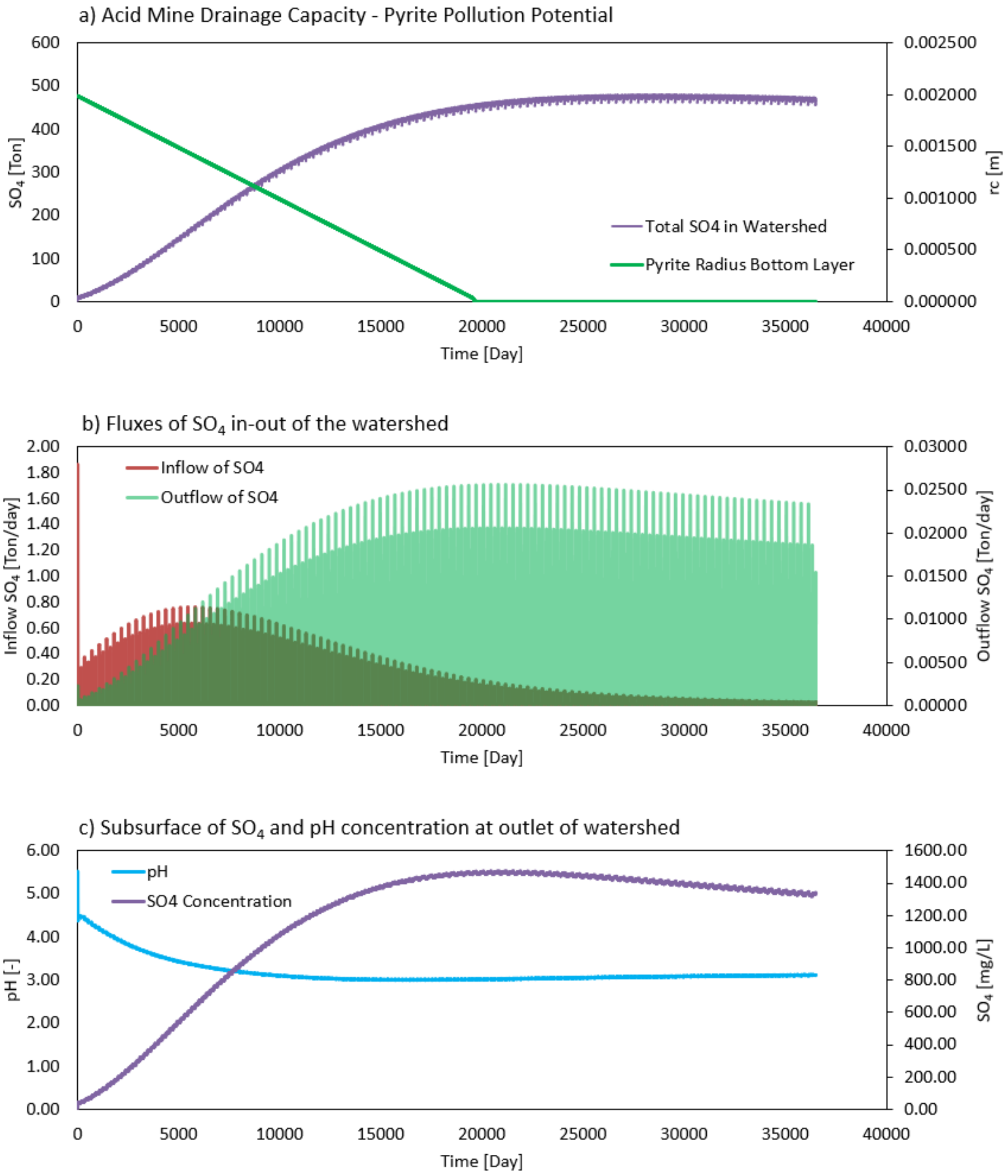

Figure 79 Time series of Acid Mine Capacity as pollution mass storage and fluxes in Mather site portion of coal pile. The outlet pH and SO_4 concentrations are also shown in plot c).

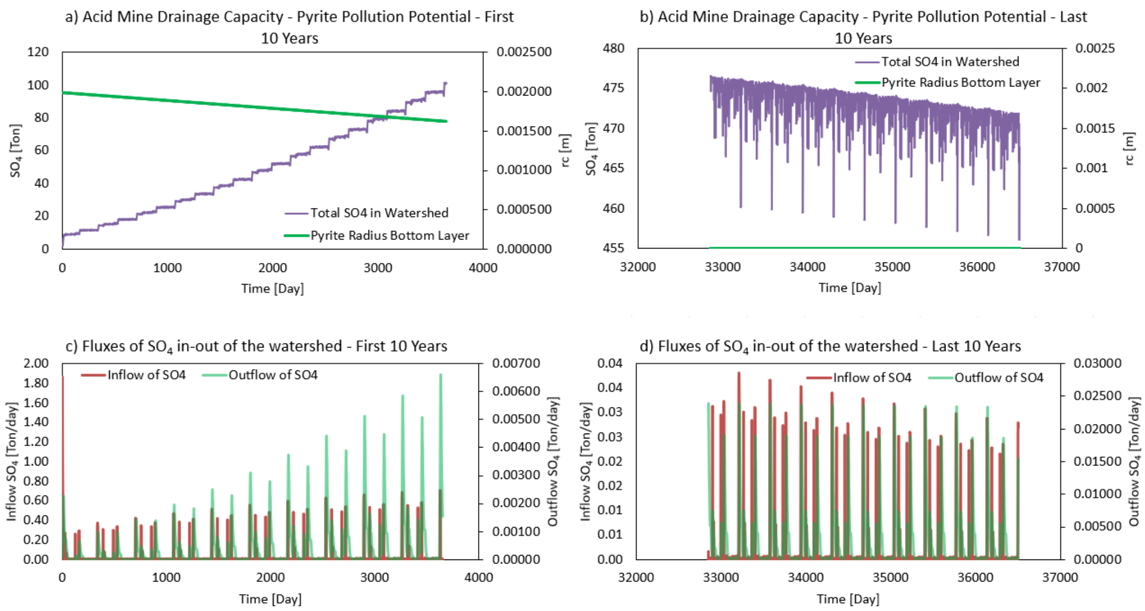

Figure 80 Time series at first and last 10 years of Acid Mine Capacity as pollution mass storage and fluxes in Mather site portion of coal pile. The plots show the details of simulation of mass storage, import and export of SO_4 from data in Figure 79.

The pH outlet subsurface values decay to 4 at the Ernest site, which is higher than at the Mather site in accordance with the export of less SO_4. Figure 80 shows constant annual behavior of mass storage at the end of the year in the first 10 years of simulation, with a variation in mass SO_4 storage over the last 10 years.

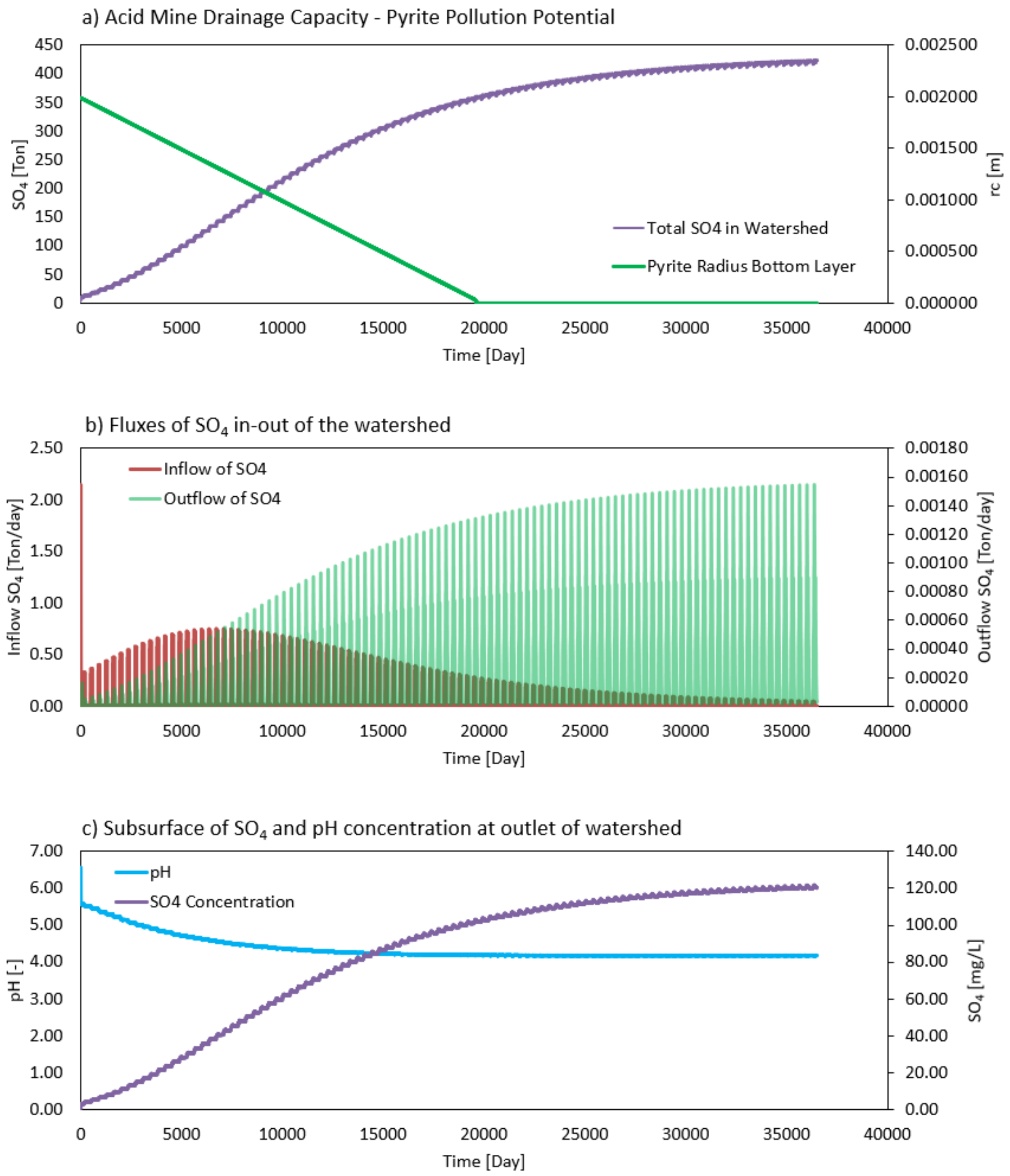

Figure 81 Time series of Acid Mine Capacity as pollution mass storage and fluxes at the Ernest site watershed with coal pile. The outlet pH and SO_4 concentrations are also shown in plot c).

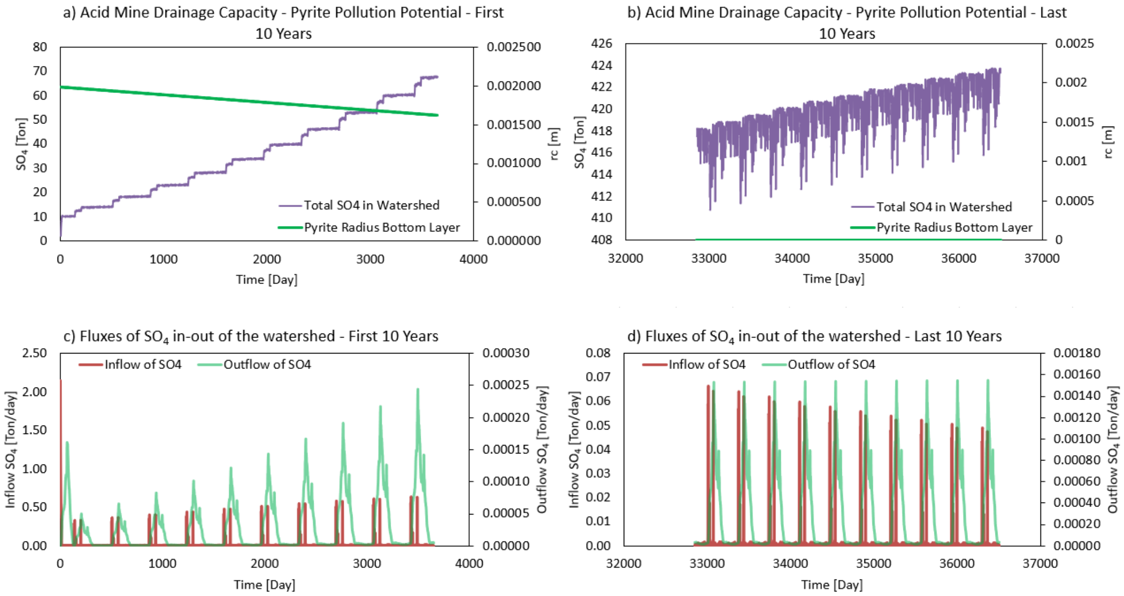

Figure 82 Time series at first and last 10 years of Acid Mine Capacity as pollution mass storage and fluxes at the Ernest site watershed with coal pile. The plots show the details of simulation of mass storage, import and export of SO_4 from data in Figure 81.

One of the important aspects of AMDC is the spatial distribution of mass pollution storage along the simulation time. Figure 83, is intended to show the plots of both sites, Mather and Ernest, on the watershed scale with the internal mass at first year, 25th year, 75th year and 100th year. The plots show increasing AMDC at both sites. At the end of the first year at the Mather site the simulation presents high storage at the outlet and along the main stream. In Ernest, the 1st year plot describes low storage at the outlet and in the stream network with the exception of two boundary branches. At the 25th year the spatial simulations show high storage in the main stream network at both sites. At the 75th year at the Mather site, a higher storage accumulation is computed at the right main branches and lower accumulation at the left main course.

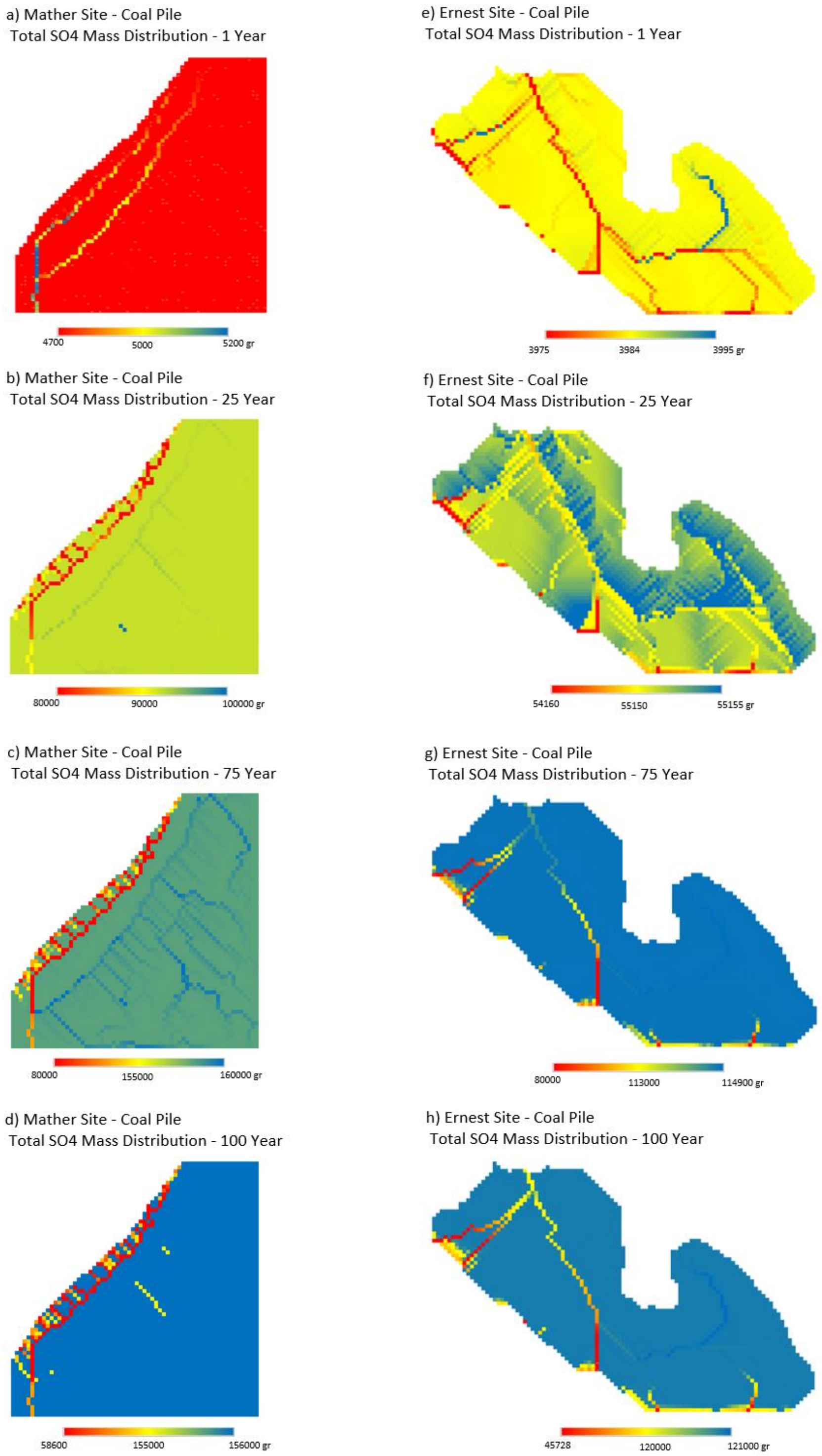

Figure 83 Spatial distribution of SO_4 mass storage or Acid Mine Drainage Capacity at the end of 1st, 25th, 75th and 100th year at the Mather site a), b), c), d) and the Ernest site e), f), g), h).

At the Ernest site, the major extension of the area has high storage and low storage in the head water main branches. Finally, for both sites, the 100th year of the simulation shows the maximum storage accumulation in a majority of areas, with low values at main stream network branches.

Once the AMDC is computed for the watersheds at both the Mather and the Ernest sites, we can proceed to make an estimation of the autonomous pollution recovery using the export of the entire mass storage of Sulfate SO_4 without any input of pollution. Following this simple idea of a simulation, we account the required time to release the majority of the AMDC as an index of the watershed-scale pollution resilience.

Figure 84 helps us to estimate that it would take about 1500 years for the Mather site to recover in a 95% of the Sulphate SO_4 mass storage of AMDC computed from a simulation of over 100 years of pyrite oxidation as a main subsurface input pollution. Both the subsurface SO_4 concentration at the outlet and the total SO_4 mass export decline slowly with time following a kind of exponential decay, which is determined by the system of transport, Equation 4.1, over the stream network. The shape of the decay of the SO_4 export serves to determine some uniformity of the flow among the cells all over the stream network. It means that the transport of the watershed at the Mather site could be simplified more in terms of modeling complexity. Our simulations show consistency with a previous analysis developed by Blodau (2006), where it is mentioned that the initial release of pollution can be from 10 to 40 first years, with an acidity lasting for centuries.

On the other hand, Figure 85 presents a different behavior for the possible recovery on the subsurface SO_4 mass at the Ernest site. Though the simulation conditions are equivalent to those at the Mather site, longer simulation time is needed to get higher values of pollution recovery. For the Ernest site, at 2500 years of simulation (computed on daily basis), it was only possible to get a 23% removal of pollution. Moreover, the computation of outflow of SO_4 shows an important decline of 50% at around 200 years after initiating the hydrological removal process. After this drop event, the export becomes almost constant over time. The difference in order of magnitude of SO_4 exported in comparison to that at the Mather site and the slow decay after 300 years of recovery explain the low capacity of the watershed at the Ernest site to get a significant level of pollution removal. The behavior of the SO_4 exported in the first 300 years serves to infer that the flow structure among the cells or within the stream network is non-homogenous and therefore the model complexity can be preserved.

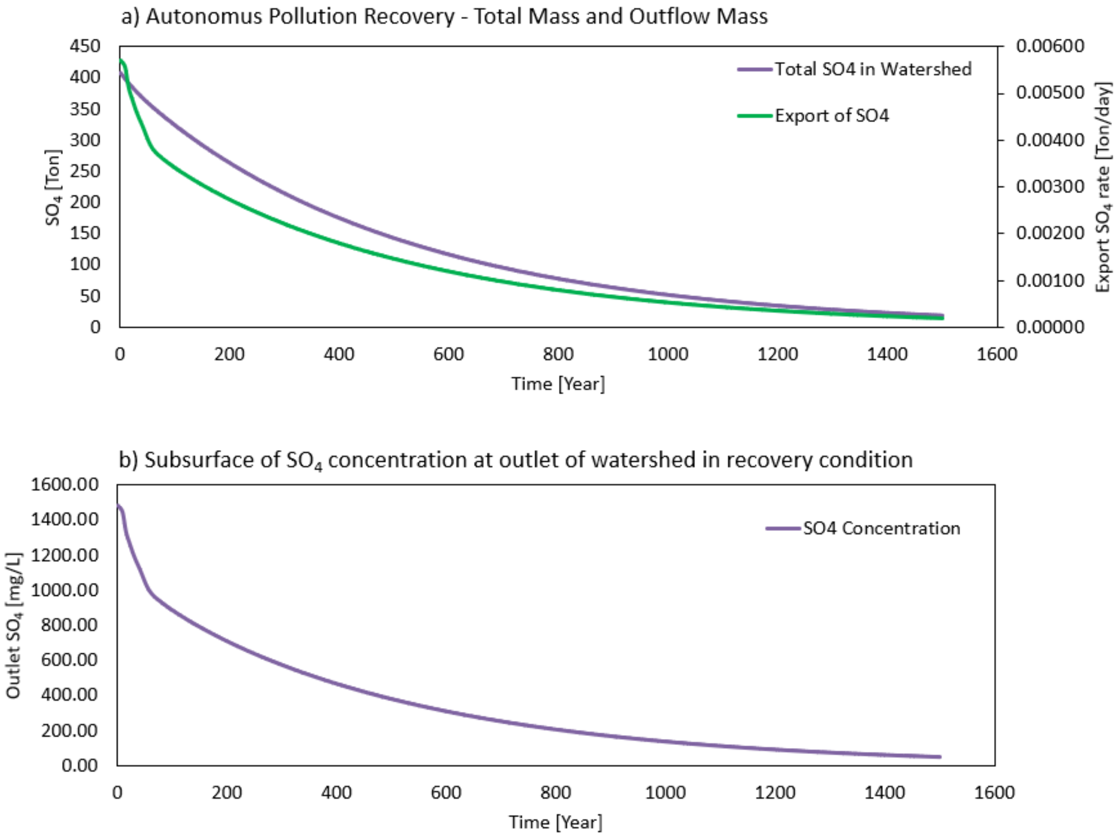

Figure 84 Time series of Total Mass of SO_4, export of SO_4 out of portion of watershed coal pile, and SO_4 concentration at outlet in Mather site coal pile as measurement of pollution recovery capacity or resilience.

In addition, the SO_4 mass exported and hydrological pollution removal computation developed in this study serve not only to discriminate a certain level of resilience of the watershed but also demonstrate the modeling complexity of flows in long term simulations. In our particular cases, the Mather and Ernest sites, we can interpret the results as a measure of possible restauration of the non-polluted natural conditions on abandoned coal mines.

a) Autonomous Pollution Recovery - Total Mass and Outflow Mass

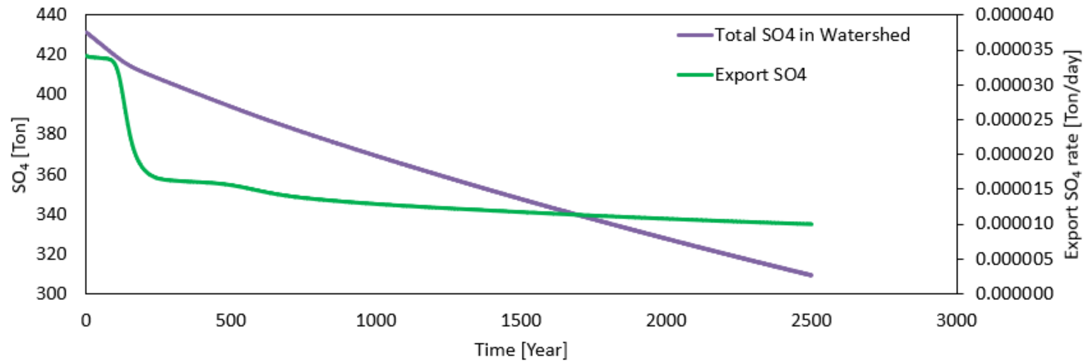

b) Subsurface of SO_4 concentration at outlet of watershed in recovery condition

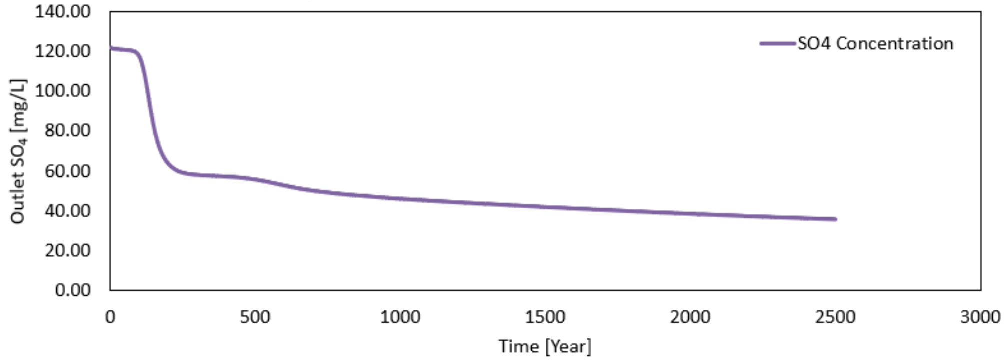

Figure 85 Time series of Total Mass of SO_4, export of SO_4 out of watershed coal pile, and SO_4 concentration at outlet in Ernest site coal pile as measurement of pollution recovery capacity or resilience.

In sum, the AMDC is reached after pyrite oxidation long-term processes are finished. The capacity depends on the stream network flow structure and drainage area. Another factor in AMDC is the large areas that generate more dilution transport then low export capacity. The pollution removal or recovery resilience depends on the complexity of the stream network flow and the dilution effect of natural areas in proportion to coal pile areas.

4.3.2 Transport Scenario with Grass, Alkaline Clay and Coal Refuse

This section explores the general watershed scale transport results under the first bioremediation scenario with grass vegetation for the coal refuse abandoned mine sites at Mather and Ernest. The general idea is to simulate a condition of covering all the coal pile area with grass vegetation and with a subsurface having an amended layer of 90%CR and 10%AC. In this case, we can simulate conditions of AMDC and surface water quality at the outlet for SO_4, Fe, pH and Ca as main AMD indicators with the passive remediation condition. We can establish as a benchmark scenario a no bioremediation condition similar to that in Chapter 3, Section 3.7.1 and Section 3.7.2.

Figure 86 and Figure 87 illustrate that at the Mather and Ernest sites, grass as vegetation passive remediation does not reduce acidic ion SO_4, Fe and H^+ export and mass storage AMDC. Moreover, the Ca mass storage does not change with bioremediation. For example, the simulations report an increased AMDC of 5% with grass at the Mather site and 30% at the Ernest site. The dilution effect explains the difference in the grass case AMDC values between Mather and Ernest, demonstrating that in general cases, more concentrated coal pile locations are more suitable for remediation treatments. In terms of surface water quality, the grass implementation generates a substantial reduction in pollution due to the immobilization effect of vegetation on surface pyrite solutes, which decline monotonically in time.

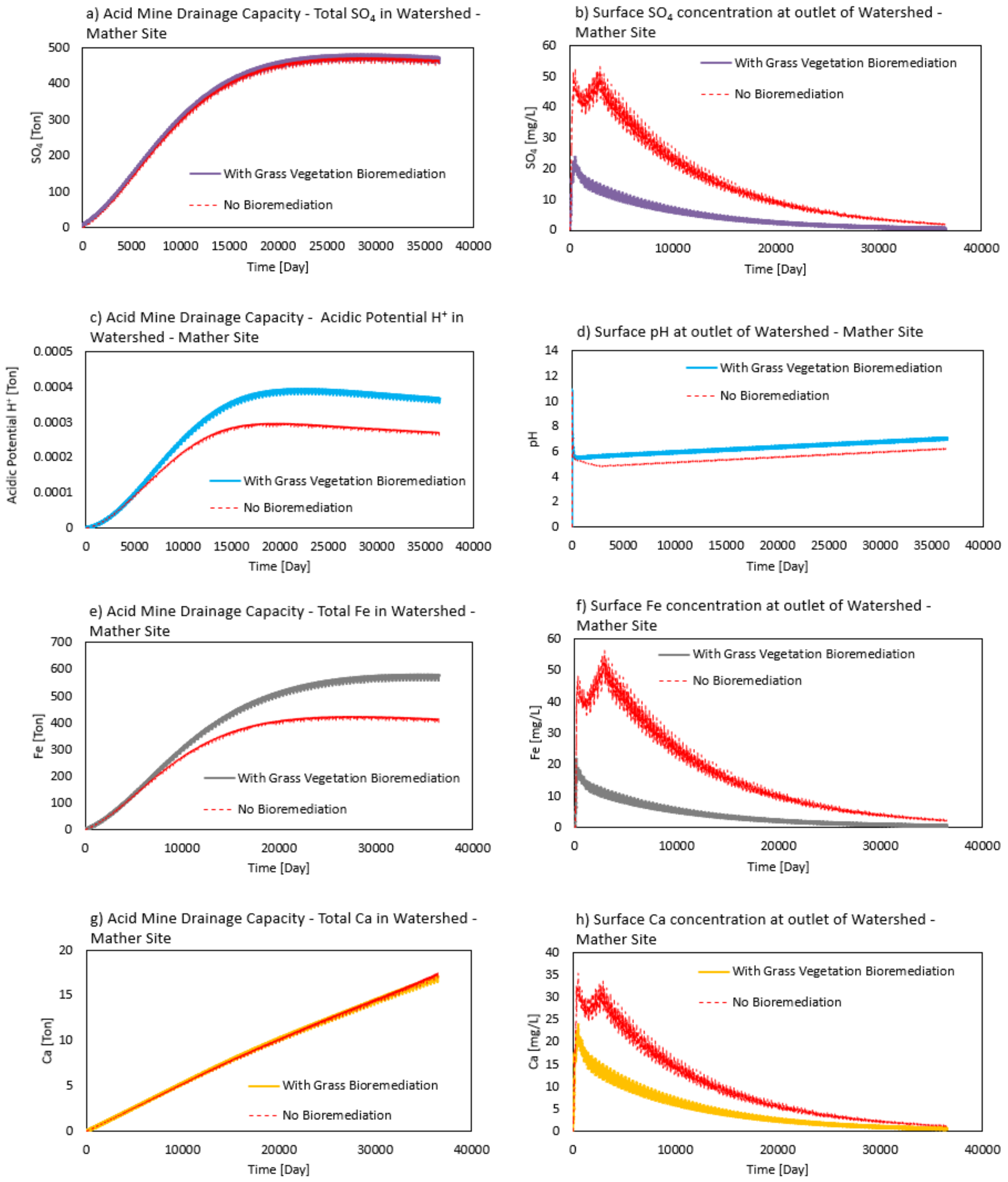

Figure 86 General transport results for SO_4, Fe, Ca and pH with grass bioremediation at the Mather site.

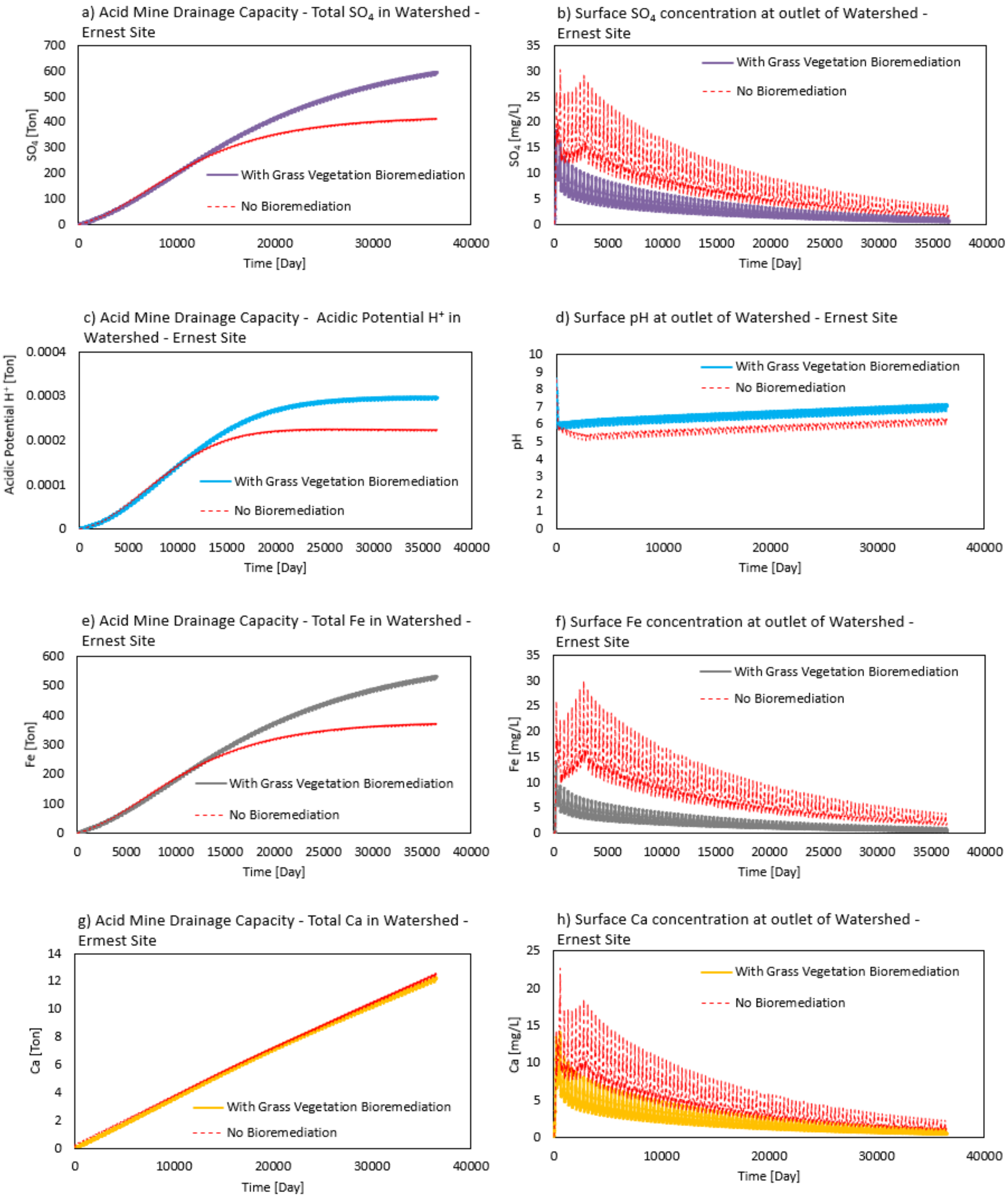

Figure 87 General transport results for SO_4, Fe, Ca and pH with grass bioremediation at the Ernest site.

The water quality computations show that the reduction in Mather is higher than in Ernest, which is mostly explained by more drainage area dilution in Ernest, which produces lesser concentration values at the outlet. In general, based on these simulations results we observe that lower concentrations are related with lower mitigation effects.

We can conclude that bioremediation with grass vegetation is worth it in terms of surface water quality but in terms of AMDC it is expected to have little or no effect.

4.3.3 Transport Scenario with Tree Vegetation and AC-CR

This section is intended to present the general transport results under the use of tree vegetation similar the situation in Section 3.7.2 of the Chapter 3. As with the grass remediation scenario, we use the no bioremediation condition as a benchmark scenario for comparison analysis purposes. The setup of the modeling has values from the soil column simulation computed for the tree vegetation scenario presented in Section 3.7.2.

Figure 88 and Figure 89 depict that tree vegetation offers a substantial reduction in AMDC, between 20% and 25% in the no bioremediation condition. The surface water quality is also improved. However, the reduction in transported solutes is relatively less than that which occurs in the grass remediation scenario. This is due to the redistribution of evapotranspiration values over the larger root zone in the tree vegetation, despite the fact that transpiration rates are higher for tree vegetation.

Finally, we can argue that bioremediation improves surface water quality, whether grass or tree vegetation is used. However, the AMDC is reduced significantly with tree vegetation usage.

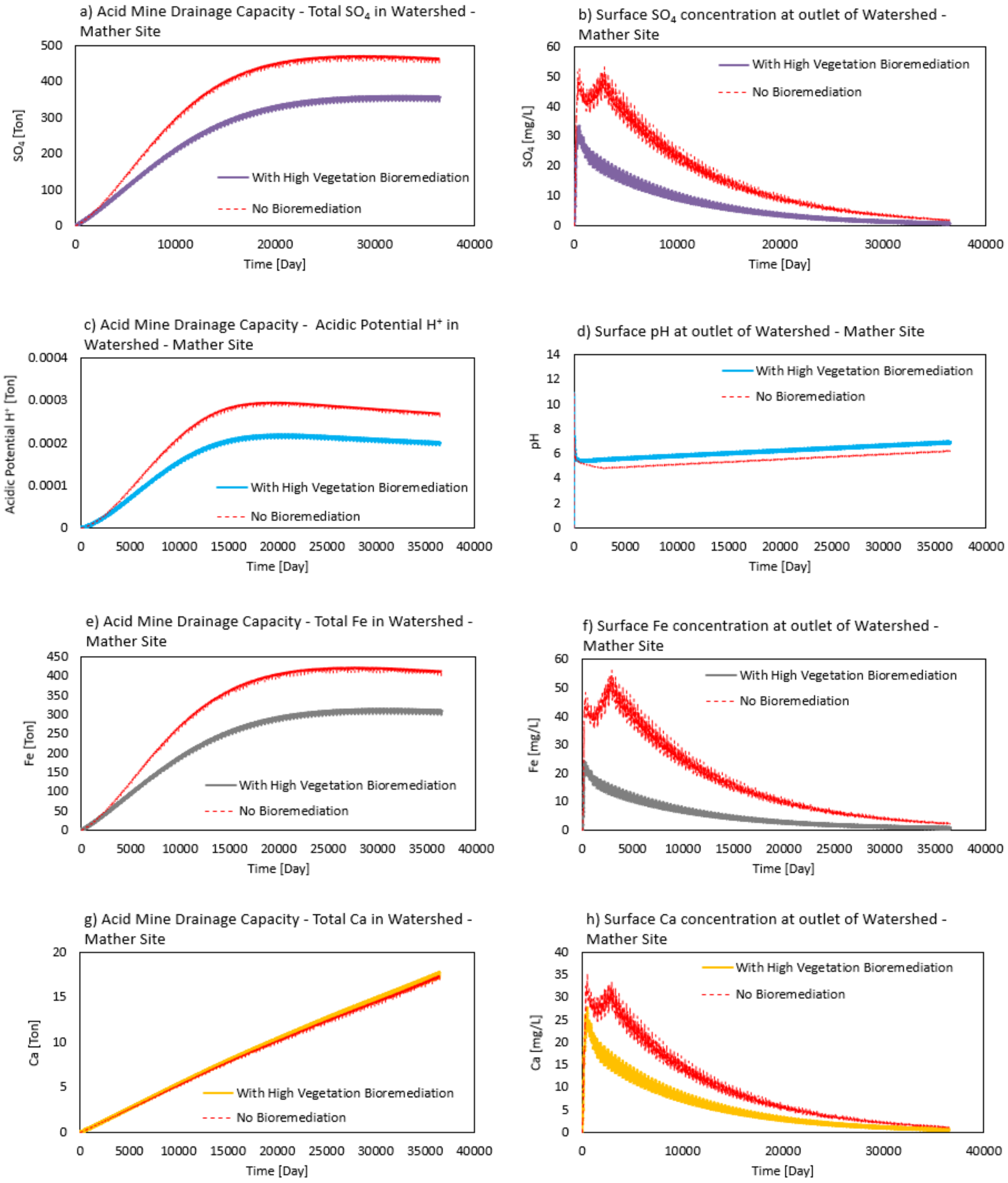

a) Acid Mine Drainage Capacity - Total SO_4 in Watershed - Mather Site

b) Surface SO_4 concentration at outlet of Watershed - Mather Site

c) Acid Mine Drainage Capacity - Acidic Potential H^+ in Watershed - Mather Site

d) Surface pH at outlet of Watershed - Mather Site

e) Acid Mine Drainage Capacity - Total Fe in Watershed - Mather Site

f) Surface Fe concentration at outlet of Watershed - Mather Site

g) Acid Mine Drainage Capacity - Total Ca in Watershed - Mather Site

h) Surface Ca concentration at outlet of Watershed - Mather Site

Figure 88 General transport results for SO_4, Fe, Ca and pH with tree vegetation bioremediation at the Mather site.

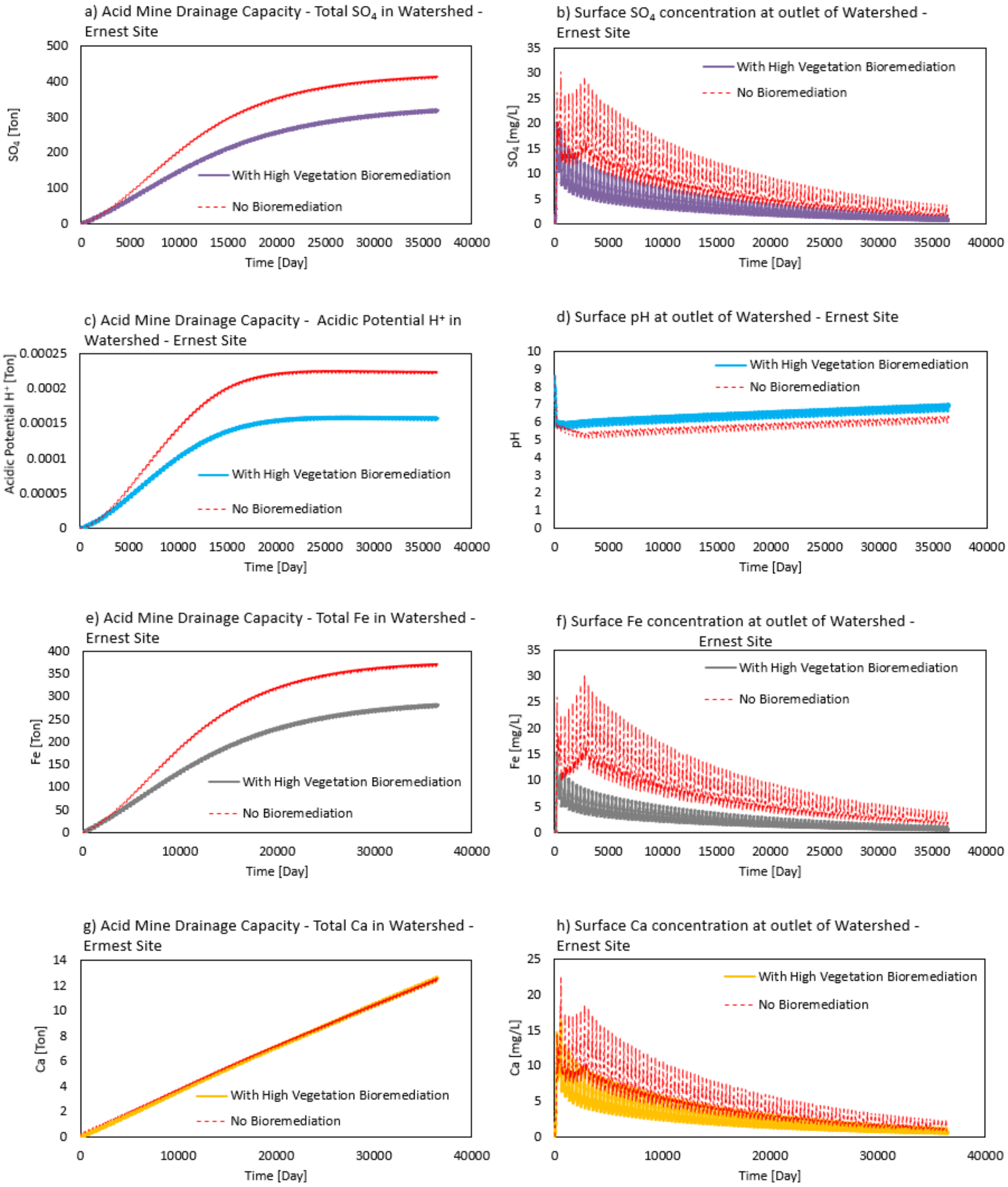

Figure 89 General transport results for SO_4, Fe, Ca and pH with tree vegetation bioremediation at the Ernest site.

4.4 Conclusions

The solute transport simulations allow an approximation to estimate the maximum mass storage of pollution as a measure of Acid Mine Drainage Capacity (AMDC). Using this concept, we can also estimate the autonomous time for pollution recovery on the watershed scales at the Mather and Ernest sites.

The AMDC at both sites in terms of sulfates SO_4 pollution was identified using a maximum value of mass storage within the 100-year simulation and after the pyrite oxidation processes have finished according to the shrinking core radius. The adopted concept as a resilience measure depends on the stream network, the hydrologic regime, and on the ratio of coal pile mine area to undisturbed area because of the dilution effect of discharge of the main stream.

Lastly, the use of vegetation such as grass or trees as passive bioremediation is valuable in terms of improving surface water quality. The impact of using tress as phytoremediation on the adopted concept of AMDC is significant in terms of magnitude and potential recovery in comparison to a condition with no bioremediation. On the other hand, the grass vegetation scenario showed little effect or in some cases the opposite effect on mass storage SO_4 pollution.

5.0 Contributions and Future Work

After the comprehensive exploration of the modeling work of the integrated processes between Acid Mine Drainage and Biogeochemical processes, we have learned that there are feedbacks between both processes which have effects on other related processes. For example, plant physiology can impact the pH chemical equilibrium condition. In addition, the biogeochemical and Acid Mine Drainage processes determine pollution capacity and recovery. The next section presents the concluding remarks on our contributions, and the final section proposes some aspects of the research that can be explored in further work.

5.1 Contributions

5.1.1 From the Hydro-Biological Model Study

We consider the main contribution of the hydro-biological component of our study to be its further support for the hypothesis of needing as many equations as possible to constrain parameters as presented in Luo et al. (2013) and applying a wide variety of approaches on the plant physiology modeling. Therefore, the modeling strategy formulated in this study showed to be useful in reducing parameter calibration issues and a sort of uniqueness modeling description of the soil-plant-atmosphere processes.

The plant physiology approach developed in this dissertation could be considered a more integrated formulation with its body of equations of soil hydrology and atmosphere interactions than other similar plant modeling approaches based on land surface models. In our approach, we derived a general Prentice optimal formulation based on whole equations with minor simplifications. Also, we were able to reduce the apparent mathematical complexity of the optimization problem to a two-variable system of equations, which is comparable to the complexity when using the empirical approach. Based on these developments, we could perform some geometrical and conceptual analyses which allowed us more insights into how the physiology variables work together.

Finally, we found some limitations of the Prentice optimal concept when a more constrained and integrated formulation is used. The increase in stomatal conductance out of the upper bound limits is a result of the integration of plant hydraulics and Penman-Monteith, which enables higher stomatal conductance values when the actual evapotranspiration approaches the potential evapotranspiration.

5.1.2 From the Hydro-Biogeochemical-Pyrox Model Study

The development and simulations of the Hydro-Biogeochemical-Pyrox Model could be considered our main contribution to the understanding of the interactions between biogeochemical and acid mine processes from a holistic perspective, including plant physiology. As a result, we could contribute to make an environmental assessment of the passive remediation of vegetation use on abandoned coal pile mines.

The mathematical model and its methodological implementation are a useful tool that can be replicated at other mine sites. The methodology can also be adjusted to model other types of mining or pollution disturbances.

5.1.3 From the Hydro-Transport Model Application

The implementation of a watershed scale transport modeling extension of the biogeochemical-pyrite oxidation interactions allow us to contribute in two main directions: a) the exploration of a conceptual measure of pollution capacity and resilience on the watershed scale; b) and a detailed discrimination of passive bioremediation effects on water quality when using two different generic types of vegetation.

The first contribution is the long term (100 year) simulations of SO_4 storage mass in the watershed as a measure of pollution capacity linked to a longer-term simulation of hydrologically pollution recovery including the washout capacity of the watersheds.

The second contribution is the assessment of water quality under passive bioremediation scenarios as an engineering solution to the environmental impairment of surface water at the outlets of the watersheds.

5.2 Future Work

The development of this dissertation served to allow more detailed modeling to emerge as well as questions regarding biogeochemical interaction processes. One further research is modeling management features (the use of different soil mixtures, fertilization schedules and species trials) for revegetation and conditions for better plant growth at initial stages when there is some issue regarding the success of phytoremediation. For phytoremediation management analysis, it is necessary to perform field studies on the effects of the different remediation measures to confirm the modeling scenario results. Additionally, the next step in modeling is to involve explicitly the microbial activity within soil organic matter (by using specialized oxidizing bacterial growth models). However, this microbial modeling addition needs a laboratory microbial characterization for the growth rates of the cultures and the kinetic interactions on ferric oxidations. Finally, we foresee the need to develop a modeled assessment of interactions and bioremediation effects under climate change scenarios with special efforts on the carbon soil efflux process linked to root transpiration, for which it is necessary to obtain better biogeochemical characterization of the soil under AMD conditions.

Appendix A Derivation of Equations for the Optimization Problem for Plant Physiology using Prentice Optimality Theory and Complete water-controlled conditions

A compact formulation for the optimization problem for the plant physiology using the Prentice unit cost and the complete water limited conditions is developed. The analytical solution for the optimization is derived using all the required derivates for all the complete equations. As a result, the system of equations for the optimization problem is compared to the system of equations for the empirical approach.

Prior to develop the derivation for the optimality approach, we can show each of the equations which are part of the constraints of the general mathematical formulation. First, we explain the equations for evapotranspiration: a) Penman-Monteith Equations and b) Capacitance-Resistance water transport (Plant Hydraulics). Second, we show the equations for carbon assimilation and carbon diffusion.

After the explanation of the basic equations for evapotranspiration and carbon assimilation, the general and compact formulations of the optimization problem are presented. Then, the derivation of the optimality condition equation is presented.

A.1 Penman-Monteith Equation

The Penman-Monteith Equation (ASCE 2000; Daly et al. 2004; Luo et al. 2013) is an energy balance for the surface. In the adjusted version it has a relationship between actual evapotranspiration and stomatal conductance and Leaf Area Index LAI jointly. The equation is as follows:

$$E = \frac{[S\,R + \rho_a\, C_p\, D\, g_a\,]\, g_s\, LAI}{\rho_w\, \lambda_w\, [g_s\, LAI\, S + \gamma_w\, [g_s\, LAI + g_a]]} \qquad [A1]$$

where E [m/s] is the actual evapotranspiration; S [Pa/^{o}C] slope of vapor pressure-temperature curve; R [W/m^2] solar radiation; ρ_a [Kg/m3] air density; C_p [Pa] pressure constant; D [Pa] vapor pressure deficit; g_a [m/s] aerodynamic conductance; g_s [m/s] stomatal conductance; LAI [m2/m2] Leaf Area Index; ρ_w [Kg/m3] water density; λ_w [Wm^3/Kg] Latent heat of vaporation; γ_w [MJ Kg^{-1} °C^{-1}] psychrometric constant.

The equation A1 can be presented in terms of forcing data constants as follows,

$$E = \frac{C_1\, g_s}{C_2 + C_3\, g_s} \qquad [A2]$$

where $C_1 = [S\,R + \rho_a\, C_p\, g_a\, D]\, LAI$; $C_2 = \rho_w\, \lambda_w\, \gamma_w\, g_a$; and $C_3 = \rho_w\, \lambda_w\, [S + \gamma_w]\, LAI$.

A.2 Water storage and transport model (capacitance model)

A plant hydraulics model representing dynamic water storage and water transpiration from roots to leaves is the Katerji model (Katerji et al. 1986; Luo et al. 2013). The water storage is explained by a capacitance component and the following equations,

$$E = Cp\frac{d\Psi_p}{dt} + \frac{[\,\Psi_s - \Psi_L\,]}{R} \tag{A3}$$

$$Cp\frac{d\Psi_p}{dt} = -\frac{[\,\Psi_p - \Psi_L\,]}{R_p} \tag{A4}$$

where *E* [m/s] is the actual evapotranspiration; *Cp* [Pa/^{o}C] water leaf storage capacity; Ψ_p [MPa] water leaf storage potential; Ψ_L [MPa] water leaf potential; Ψ_S [MPa] water soil potential; *R* [Pa] pressure constant; R_P [m/s] aerodynamic conductance.

In discrete formulation, the water transport hydraulics can be represented below.
First, a discrete aproximation of Katerji model,

$$E = \frac{[\,\Psi_p - \Psi_L]}{R_P} + \frac{[\,\Psi_s - \Psi_L\,]}{R} \tag{A5}$$

Second, the water storage potential via Katerji model,

$$\psi_p = \left[\Psi_p^{t-1}\left[\frac{C_p R_p}{\Delta t}\right] + \Psi_L\right]\left[\frac{1}{1+[C_p R_p/\Delta t]}\right] \tag{A6}$$

And, third, by plugging [A6] into [A5],

$$E = \frac{1}{R}[\psi_s - \psi_L] + \frac{1}{R_p}\left[\left[\psi_p^{t-1}\left[\frac{C_pR_p}{\Delta t}\right] + \psi_L\right]\left[\frac{1}{1+[C_pR_p/\Delta t]}\right] - \psi_L\right] \qquad [A7]$$

The water leaf boundaries are given by the following equations on the discrete formulation of Equation A7.

1-For $\Psi_p<\Psi_L$

$$\psi_s^* = \left[E^* - \frac{1}{R}\psi_s\right] / \left[-\frac{1}{R}\right] \qquad [A8]$$

2- For $\Psi_p>\Psi_L$

$$\psi_s^* = \left[E^* - \left[\frac{1}{R}\psi_s + \frac{1}{R_p}\left[\frac{[C_pR_p/\Delta t]}{1+[C_pR_p/\Delta t]}\right]\psi_p^{t-1}\right]\right] / \left[-\frac{1}{R} + \frac{1}{R_p}\left[\left[\frac{1}{1+[C_pR_p/\Delta t]}\right] - 1\right]\right] \qquad [A9]$$

A.3 Carbon assimilation (Biochemical Farquhar model)

The carbon assimilation equation describes the kinetic rate of photosynthesis reaction at mesophyll cells (Farquhar, 1980). This biochemical model has three components: a) A Rubisco-limited rate. b) A light-limited rate, c) A half-Rubisco component. Collatz, 1996, developed a biquadratic formulation of the three components to avoid the discontinuity of the minimal function among the rates. The components and the biquadratic equation are as follows:

$$A_n = A_F(c_i)f(\Psi_L) \tag{A10}$$

where A_n [mol/m2/s] is net carbon assimilation; A_F [mol/m2/s] is the Farquhar model of biochemical carbon assimilation; c_i [mol/mol] CO_2 in-leaf concentration; Ψ_L [MPa] water leaf potential; $f(\Psi_L)$ [-] water stress factor function on carbon assimilation.

The biquadratic system of equations solves A_F in terms of the carboxylation, ligth-limited and saturation components of biogeochemical Farquhar-Collatz model of carbon assimilation. The biquadratic equations (Equations A11 and A12) and its components (Equations A13, A14 and A15) are show below:

$$\beta_2 A_F^2 - \left(A_p + A_s\right)A_F + A_p A_s = 0 \tag{A11}$$

$$\beta_1 A_p^2 - \left(A_c + A_q\right)A_p + A_c A_q = 0 \tag{A12}$$

$$A_c = V_{cmax}\left[\frac{c_i - \Gamma}{c_i + K_c(1 + o_i/K_o)}\right] \tag{A13}$$

$$A_q = \frac{J}{4}\left[\frac{c_i - \Gamma}{c_i + 2\Gamma}\right] \tag{A14}$$

$$A_s = \frac{V_{cmax}}{2} \tag{A15}$$

$$f(\Psi_L) = \frac{[\Psi_L - \Psi_o]}{[\Psi_M - \Psi_o]} \quad for\ \Psi_M < \Psi_L < \Psi_o;\ \ 0\ otherwise \tag{A16}$$

A.4 Carbon diffusion

Carbon diffusion equation (Equation A17) represents the availability of carbon from the atmosphere to be captured by plants. It is mediated by an equivalent stomatal conductance (Equation A18) that includes the aerodynamic and boundary layer conductance g_{ab}. The equation is as follows:

$$A_n = G_s(\Psi_L)[c_a - c_i] \tag{A17}$$

$$G_s(\Psi_L) = \frac{1}{1/g_s + 1/g_{ab}} \tag{A18}$$

where A_n [mol/m2/s] is net carbon diffusion; G_s [mol/m2/s] is an equivalent total conductance; c_a [mol/mol] CO_2 atmospheric concentration; c_i [mol/mol] CO_2 in-leaf concentration; g_s [mol/m2/s] stomatal conductance; g_{ab} [mol/m2/s] aerodynamic-boundary layer conductance. The stomatal conductance is a function of Ψ_L through the inverse Penman-Monteith equation coordinated to water transport plant hydraulics equation $g_s=E^{-1}(\Psi_L)$.

A.5 General Mathematical Formulation for the Optimization Problem-Prentice and Luo et al (2013) Equations

The optimization problem in this case is composed by the objective function given by the unit physiological unit cost, the equations for evapotranspiration in Penman-Monteith model and Katerji model with a $E'=1.6G_sD$ in the unit cost function, the equation for carbon diffusion and the equation for carbon assimilation with a factor for water limited conditions. The optimization problem is to minimize the two components of the unit cost function; the water use efficiency component and the carboxylation component. The system of equations for the general formulation is therefore:

$$\text{Min} \quad Cost = a\frac{E\prime}{A} + b\frac{V_{cmax}}{A} \qquad \text{Objective Function Unit Cost} \quad [A19]$$

Subject to

$$E' = 1.6\ G_s\ D \qquad \text{Evapotranspiration used by Prentice (2014)} \quad [A20]$$

$$E = g_s \frac{C_1}{C_2 - C_3 g_s} \qquad \text{Actual Evapotranspiration - Penman-Monteith Equation} \quad [A21]$$

$$E = \frac{1}{R}[\psi_s - \psi_L] + \frac{1}{R_p}\left[\psi_p - \psi_L\right] \text{ Actual Evapotranspiration - Ohm's law analogy} \quad [A22]$$

$$A(\psi_L, c_i) = G_s(\psi_L)[c_a - c_i] \text{ Carbon Diffusion Equation used by Luo et al. (2013)} \ [A23]$$

$$A(\psi_L, c_i) = f(\psi_L)\ A_F(c_i) \qquad \text{Carbon Assimilation - Farquhar-Collatz-Water} \quad [A24]$$

$$G_s(\psi_L) = \frac{g_s(\psi_L) g_{ab}}{g_s(\psi_L) + g_{ab}} \qquad \text{Equivalent stomatal conductance and boundary layer} \quad [A25]$$

A.6 Compact Mathematical Formulation of the Optimization Problem- Prentice and Luo et al (2013) Equations.

One way to solve the optimization problem is using the Lagrange method for the objective function, the equations as constraints and two variables c_i and Ψ_L. Another way is to use a compact formulation where there is an objective function and one decision variable that is coupled to the second variable by the constraint. In this case, one can simplify the problem of optimization problem for five variables, A, E, g_s, c_i and Ψ_L, to a problem of one variable c_i and one constraint which relates c_i and Ψ_L. The compact formulation now is given by the following equations.

$$\text{Min} \quad Cost = a\frac{E\prime(\psi_L)}{A(\psi_L,c_i)} + b\frac{V_{cmax}}{A(\psi_L,c_i)} \qquad \text{Objective function unit cost} \quad [A26]$$

$$f(\psi_L)A_F(c_i) = G_s(\psi_L)[c_a - c_i] \quad \text{Equilibrium Constraint Equation (Equation 2.3)} \quad [A27]$$

where G_s is an aggregate function for the total equivalent stomata conductance in terms of g_s and g_{ab}, and the relationship between g_s and E using the inverse Penman-Monteith equation. The decision variables are c_i and Ψ_L, but using the constraint we can solve it using just c_i. Among the equations below,

$$g_s(\psi_L) = \frac{k_1 E(\psi_L)}{k_1 - k_3 E(\psi_L)} \qquad \text{Inverse Penman-Monteith-Ohm's Law equation} \quad [A28]$$

$$E' = 1.6\ g_s(\psi_L)\ D \quad \text{Potential Evapotranspiration - Prentice (2014)} \quad [A29]$$

$$G_s(\psi_L) = \frac{g_s(\psi_L)g_{ab}}{g_s(\psi_L) - g_{ab}} \quad \text{Equivalent Stomata conductance in carbon diffusion Eq.} \quad [A30]$$

A.7 Optimality Condition for the Optimization Problem

To solve the problem given by [A26] and [A27], we can derivate respect to c_i, taking in account the constrain [A27] and the complete equations. The first order condition as optimality conditions is developed as follows,

$$\frac{\partial Cost}{\partial c_i} = \frac{\partial}{\partial c_i}\left[a\frac{E'}{A}\right] + \frac{\partial}{\partial c_i}\left[b\frac{V_{cmax}}{A}\right]$$ First order condition [A31]

$$\frac{\partial}{\partial c_i}\left[a\frac{E'}{A}\right] = a\left[\frac{\partial E'}{\partial c_i}\frac{1}{A} - \frac{E'}{A^2}\frac{\partial A}{\partial c_i}\right]$$ First order condition in water efficiency component [A32]

$$\frac{\partial}{\partial c_i}\left[b\frac{V_{cmax}}{A}\right] = -b\left[\frac{V_{cmax}}{A^2}\frac{\partial A}{\partial c_i}\right]$$ First order condition in carboxylation component [A33]

Hence, the optimality condition for the problem is an equation for ci and ψ_L variables.

$$a\left[\frac{\partial E'}{\partial c_i}\frac{1}{A} - \frac{E'}{A^2}\frac{\partial A}{\partial c_i}\right] - b\left[\frac{V_{cmax}}{A^2}\frac{\partial A}{\partial c_i}\right] = 0$$ General Optimality Condition Equation-Eq.2 [A34]

A.8 Components of the Optimality Condition Equation

The development of the components of the optimality equation are shown below. The first one is the derivate *dE'/dci*, which needs the development of the slope of the constraint. The second component is the derivate *dA/dci* where needs the implicit derivate for the carbon assimilation Farquhar model.

1-Potential transpiration derivate

$$\frac{\partial E'}{\partial c_i} = \frac{\partial E'}{\partial G_s}\frac{\partial G_s}{\partial g_s}\frac{\partial g_s}{\partial E}\frac{\partial E}{\partial \psi_L}\frac{\partial \psi_L}{\partial c_i}$$ Total Derivate Potential transpiration to *ci*. [A35]

$$\frac{\partial E'}{\partial G_s} = 1.6\,D$$ Derivate Potential transpiration to gs – Prentice (2014) [A36]

$$\frac{\partial g_s}{\partial E} = \frac{k_1 k_2}{[k_2 + k_3 E]^2}$$ Derivate Inverse Penman-Monteith-Ohm's law Equation [A37]

$$\frac{\partial E}{\partial \psi_L} = -\frac{1}{R} + \frac{1}{R_p}\left[\frac{1}{[1 + C_p R_p/\Delta t]} - 1\right]$$ Evapotranspiration derivate to ψ_L [A38]

$$\frac{\partial \psi_L}{\partial c_i} = \frac{f(\psi_L)\frac{\partial A_F}{\partial c_i} + G_s(\psi_L)}{\frac{\partial G_s}{\partial g_s}\frac{\partial g_s}{\partial E}\frac{\partial E}{\partial \psi_L}[c_a - c_i] - \frac{\partial f}{\partial \psi_L}A_F(c_i)}$$

Derivate of Slope Equilibrium equation [A39]

$$\frac{\partial G_s}{\partial g_s} = \frac{g_{ab}^2}{[g_{ab} + g_s]^2}$$

Derivate of Equivalent Complete Stomata conductance [A40]

$$\frac{\partial f}{\partial \psi_L} = \frac{1}{[\psi_M - \psi_o]} \quad for\ \psi_M < \psi_L < \psi_o;\ \ 0\ otherwise$$

Derivate of factor for water-controlled condition in carbon assimilation [A41]

2-Derivate for Farquhar-Collatz-Water Controlled Condition Carbon Assimilation Equation

$$\frac{\partial A}{\partial c_i} = \frac{\partial f}{\partial \psi_L}\frac{\partial \psi_L}{\partial c_i}A_F(c_i) + f(\psi_L)\frac{\partial A_F}{\partial c_i}$$

Total Derivate of Farquhar-water controlled condition carbon assimilation [A42]

3-Derivate for Complete Carbon Diffusion Equation

$$\frac{\partial A}{\partial c_i} = \frac{\partial G_s}{\partial g_s}\frac{\partial g_s}{\partial E}\frac{\partial E}{\partial \psi_L}\frac{\partial \psi_L}{\partial c_i}[c_a - c_i] - G_s(\psi_L)$$

Total Derivate of complete carbon diffusion [A43]

A.9 System of Equations for Optimality Approach

Therefore, with all the derivation we can arrange the final system of equations as follows.

$$g_s = \frac{a}{b}\frac{[g_{ab} + g_s]}{g_{ab}[c_a - c_i]}\left[\frac{\partial E'}{\partial c_i} - \frac{E'}{A}\frac{\partial A}{\partial c_i}\right]\frac{A}{V_{cmax}}\frac{A}{\partial A/\partial c_i}$$

Optimality condition equation-Equation 2.3 [A44]

$$f(\psi_L)A_F(c_i) = G_s(\psi_L)[c_a - c_i]$$

Equilibrium constraint equation-Equation 2.4 [A45]

Appendix B Vegetation species and Empirical Parameter Adjustment and Estimation

According to the optimality formulation in this study, the maximum empirical parameter *a'* is used to constrain the model simulations. This Appendix develops the exercise to compute the maximum *a'* value based on different empirical values reported on literature (Leuning 1995; Medlyn et al. 2011; Miner et al. 2017). The first step is to recognize the vegetation species used in the pilot plots: alfalfa, white clover, red clover and tall fescue grass.

Then according to the database presented in Miner et al. (2017) Table 1, we realized that the maximum possible value for grass vegetation can be assumed as *a'*=23.8 under the grassland, Forb steppe species.

However, the *a'* parameter values correspond to BB initial formulation equation which is different to BBL equation. Then, we need a first transfer function from *a'* (BB) to *a'*(BBL). We used the table data from Leuning (1995) and Medlyn et al. (2011) to compute the first transfer function.

Table 4 Empirical Values Reported by Literature for different species

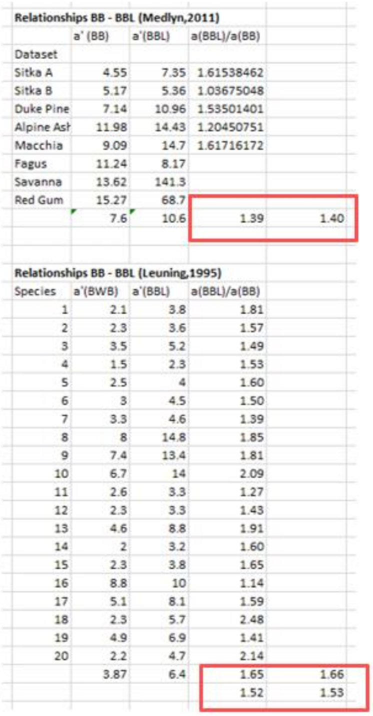

Relationships BB - BBL (Medlyn,2011)

	a' (BB)	a'(BBL)	a(BBL)/a(BB)	
Dataset				
Sitka A	4.55	7.35	1.61538462	
Sitka B	5.17	5.36	1.03675048	
Duke Pine	7.14	10.96	1.53501401	
Alpine Ash	11.98	14.43	1.20450751	
Macchia	9.09	14.7	1.61716172	
Fagus	11.24	8.17		
Savanna	13.62	141.3		
Red Gum	15.27	68.7		
	7.6	10.6	1.39	1.40

Relationships BB - BBL (Leuning,1995)

Species	a'(BWB)	a'(BBL)	a(BBL)/a(BB)	
1	2.1	3.8	1.81	
2	2.3	3.6	1.57	
3	3.5	5.2	1.49	
4	1.5	2.3	1.53	
5	2.5	4	1.60	
6	3	4.5	1.50	
7	3.3	4.6	1.39	
8	8	14.8	1.85	
9	7.4	13.4	1.81	
10	6.7	14	2.09	
11	2.6	3.3	1.27	
12	2.3	3.3	1.43	
13	4.6	8.8	1.91	
14	2	3.2	1.60	
15	2.3	3.8	1.65	
16	8.8	10	1.14	
17	5.1	8.1	1.59	
18	2.3	5.7	2.48	
19	4.9	6.9	1.41	
20	2.2	4.7	2.14	
	3.87	6.4	1.65	1.66
			1.52	1.53

From the table species values for *a'* in BB and BBL equations we derived average values that can allow us to compute a proportion relationship between the two version of equation parameters.

The fist transfer function for the two equations parameters is:

$$a'(\mathrm{BBL}) = 1.53\, a'(\mathrm{BB}) \qquad [B1]$$

The second transfer function enable us to convert a' parameter from original BBL to BBL (Luo 2013; Tuzet et al. 2003) formulation in the use of $f_v(\Psi_L)$ the function that connects evapotranspiration to water leaf potential similar to *f(D)* but in this case dependent on vapor pressure deficit. To get the equivalent proportion between BBL parameters values and Tuzet-Luo parameter formulation we use a linear regression between both simulated values to get the slope that relates both similar equations.

With this relationship we can compute the maximum values for *a'* for Mather and Oensingen sites to be used in the optimal-empirical coupled approach. It is assumed Do = 1000 for the similarity of species to low size species in Leuning (1995). In Figure 90, shows the *a'* (BBL original) and *a'*(BBL-Luo) linear regression which is used to get the second transfer function as follows,

$$a' \text{ (Xiangyu)} = a'\text{(BBL)}/2.21 \qquad \text{[B2]}$$

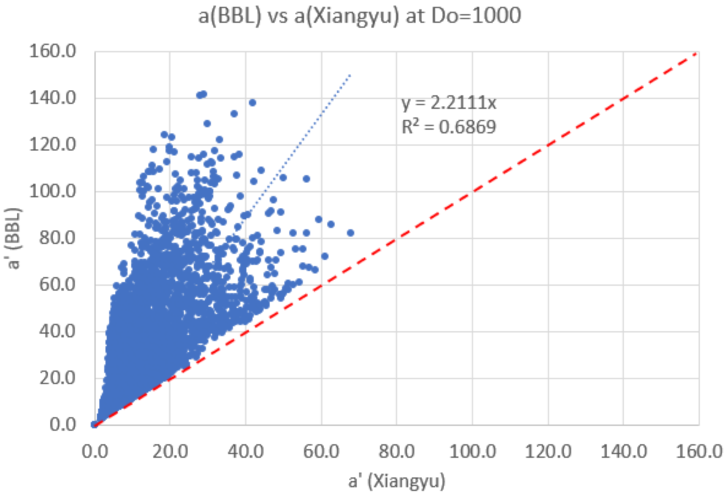

Figure 90 Comparison empirical *a'* (BBL) and *a'*(BBL-Luo) parameters to get second transfer Function in Mather site.

In the case of Oensingen site, the results show the following transfer function based on the comparative linear regression in Figure 91,

$$a' \text{ (Xiangyu)} = a' \text{ (BBL)}/1.52 \qquad \text{[B3]}$$

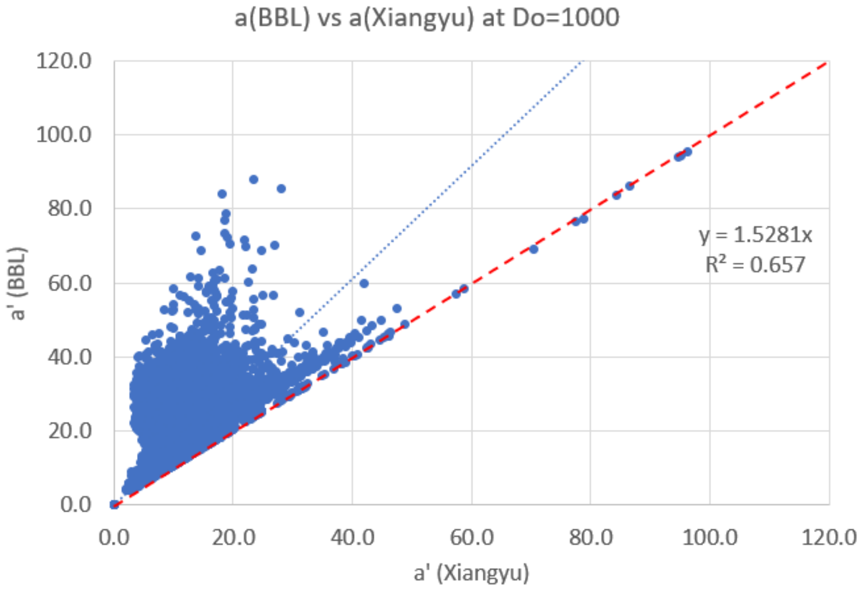

Figure 91 Comparison empirical *a'* (BBL) and *a'*(BBL-Luo) parameters to get second transfer Function in Ernest site.

Finally, we can get the final maximum *a'* parameter suitable for the BBL-Luo equation by using the two sequential transfer functions. The final results are shown as follows.

Table 5 Final Averaging of Empirical Values according to Literature and species

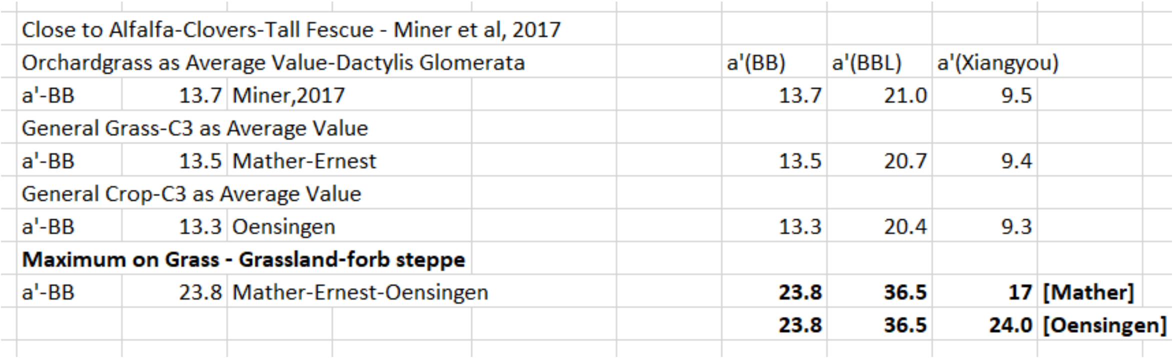

Close to Alfalfa-Clovers-Tall Fescue - Miner et al, 2017						
Orchardgrass as Average Value-Dactylis Glomerata			a'(BB)	a'(BBL)	a'(Xiangyou)	
a'-BB	13.7	Miner,2017	13.7	21.0	9.5	
General Grass-C3 as Average Value						
a'-BB	13.5	Mather-Ernest	13.5	20.7	9.4	
General Crop-C3 as Average Value						
a'-BB	13.3	Oensingen	13.3	20.4	9.3	
Maximum on Grass - Grassland-forb steppe						
a'-BB	23.8	Mather-Ernest-Oensingen	**23.8**	**36.5**	**17**	**[Mather]**
			23.8	**36.5**	**24.0**	**[Oensingen]**

Maximum *a'* - Mather site: *a'*(Xiangyu) = 17

Maximum *a'* - Oensingen site: *a'*(Xiangyu) = 24

Appendix C Solution of Biogeochemical Transport-Reactive Partial Differential Equations

The general partial differential equation for the biogeochemical transport model is given in Equation A1. The system of partial equations of organic matter *OM*, nitrates NO_3, ammonium ions NH_4, ammonia NH_3, carbon dioxide CO_2, bicarbonate HCO_3 and acidic carbon CO_3 uses the Equation C1 in which reaction terms convolutes all the variables:

$$\frac{\partial[\theta C_i]}{dt} = \frac{\partial}{\partial z}\left[D\frac{\partial C_i}{\partial z} + qAC_i\right] + \sum_{j=1}^{nj} R_{ij} + F_i \qquad [C1]$$

Figure 92, illustrates the depth distribution of the discrete method for the computation of the Equation C1. For each cell the solute mass balance is computed with influx and outflux based on vertical discharge transport, dispersion and biochemical reaction among the organic-inorganic species.

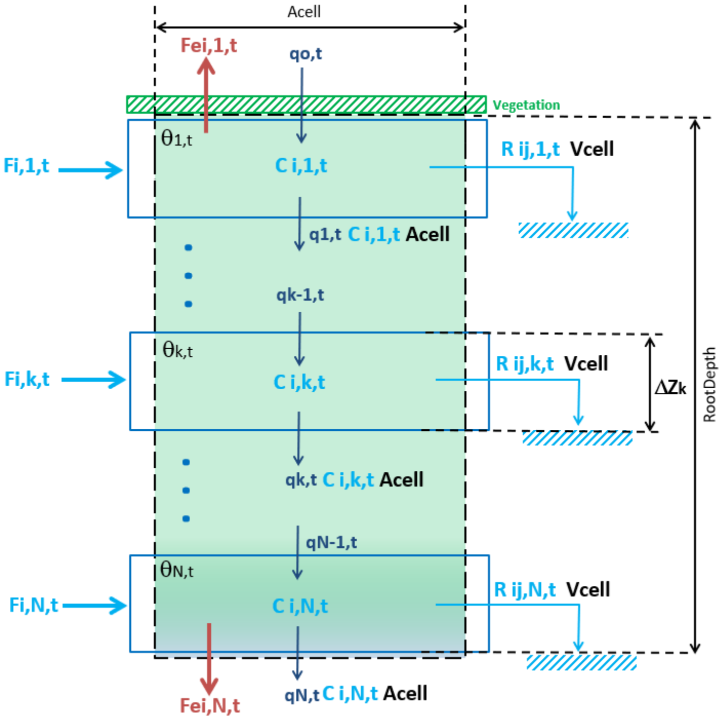

Figure 92 Scheme of the numerical discrete mass balance for the equation C1.

The time derivate component of Equation C1, can be approximated by the discrete explicit difference formulation as follows,

$$\frac{\partial[\theta C_i]}{dt}\,\Delta t \approx \left[\theta_k^{T+\Delta T}\, A_{cell}\, \Delta z_k\, C_{i,k}^{T+\Delta T} - \theta_k^{t}\, A_{cell}\, \Delta z_k\, C_{i,k}^{T}\right] \qquad [C2]$$

The advective and dispersion components of the Equation C1, are represented by the following explicit discrete difference equations:

$$\frac{\partial}{\partial z}[qAC_i]\,\Delta t \approx \left[q_{k-1}^{T}\, A_{cell}\, C_{i,k-1}^{T} - q_k^{T}\, A_{cell}\, C_{i,k}^{T}\right] \qquad [C3]$$

$$\frac{\partial}{\partial z}\left[D\frac{\partial C_i}{\partial z}\right]\Delta t \approx DA_{cell}\left[\frac{C_{i,k-1}^T - C_{i,k}^T}{\Delta z_k}\right] - DA_{cell}\left[\frac{C_{i,k}^T - C_{i,k+1}^T}{\Delta z_k}\right] \quad \text{[C4]}$$

The source and external boundary conditions can be expressed by the following equation,

$$\left[\sum_{j=1}^{nj} R_{ij} + F_i\right]\Delta t \approx \left[\sum_{j=1}^{nj} R_{ij}\ \theta_k^T\ A_{cell}\ \Delta z_k + F_i\ A_{cell}\ \Delta z_k\right]\Delta t \quad \text{[C5]}$$

Finally, the complete numerical equation for the concentration of any substance *i* at any time *t* and dept *k*, $C_{i,k,T}$ is given by the following equation:

$$C_{i,k}^{T+\Delta T} = \left[\theta_k^T\ A_{cell}\ \Delta z_k\ C_{i,k}^T + \left\{\left[q_{k-1}^T\ A_{cell}\ C_{i,k-1}^T - q_k^T\ A_{cell}\ C_{i,k}^T\right] + \left(DA_{cell}\left[\frac{C_{i,k-1}^T - C_{i,k}^T}{\Delta z_k}\right] - DA_{cell}\left[\frac{C_{i,k}^T - C_{i,k+1}^T}{\Delta z_k}\right] + \sum_{j=1}^{nj} R_{ij}\ \theta_k^T\ A_{cell}\ \Delta z_k + F_i\ A_{cell}\ \Delta z_k\right)\right\}\Delta t\right] /\ \theta_k^{T+\Delta T}\ A_{cell}\ \Delta z_k$$

[C6]

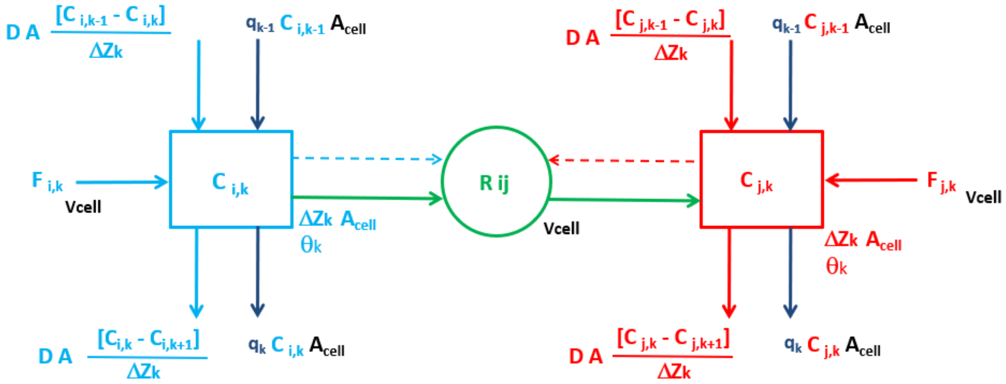

Figure 93 Numerical scheme of the system of partial differential equations based on the interaction between concentration C*i* and concentration C*j* through the jointed reactions *Rij*.

Equation C6 is a difference equation that uses an explicit numerical scheme forward to compute the concentrations. The numerical stability criterion is given by the following constraint for the time step:

$$\Delta T \leq \frac{\Delta z_k}{q^{T}_{k-1} + R^{T}_{i,j,k}\,\Delta z_k} \qquad [C7]$$

The system of equations for the species of organic-inorganic in the soil uses the Equation C6 for each concentration specie which is linked to any other concentration specie as is shown in Figure 91.

Appendix D Solution of The Multiple System of Ordinary and Partial Differential Equations

The solution of the multiple system of equations is carried out in two time-steps: a) an hourly time step for hydrology and plant physiology variables and b) a daily time step for biogeochemical and pyrite oxidation variables. At the end of each day, 24 hourly time steps simulations are done and the hydrology and plant rate variables are accumulated to be used in the daily basis variables.

The hourly time step (*dt*) part is composed of a difference explicit equation for soil moisture $\theta_{t,\ z}$, with initial condition θ(t=0, z) = θ_o, and boundary conditions $d\theta/dz$(t,z=0) = I_o, the infiltration rate and $d\theta/dz$(t,z=D_{max}) = 0, at the maximum depth. The difference equation used is based on the original DHSVM code:

$$d_z\ (\ \theta_z^{t+dt} - \ \theta_z^t) = Q_v(\theta_{z-1}^t) - Q_v(\theta_z^t) - \sum_j f_{jz} E_z \qquad \text{[D1]}$$

After soil moisture is computed, the Clapp and Hornberger, (1963) equations are used to estimate water soil potential Ψ_s. Then, water soil potential is part of the plant physiology system of equations: Equation 2.2 and Equation 2.3 (in Chapter 2) for water leaf potential Ψ_L and CO_2 in-leaf concentration c_i.

Based on Ψ_L and c_i, hourly carbon assimilation A_n, hourly total evapotranspiration E, spatially daily evapotranspiration E_z and GPP are computed to be part of the second part of the multiple system of equations at the end of 24-hourly time steps.

The multiple system of differential equations has three components: 1) carbon and nitrogen cycles component, 2) biogeochemical-transport, and 3) pyrite oxidation component. The numerical solution of the carbon-nitrogen cycles component is based on an explicit simple scheme with a daily time step (ΔT). The following matrix representations of the numerical solution correspond to plant pools, litter pools and soil pool, respectively:

$$\begin{bmatrix} C^{T+\Delta T}_{Plant\ i} \\ N^{T+\Delta T}_{Plant\ i} \end{bmatrix} = \begin{bmatrix} 1 - k_{Planti}\,\Delta T & 0 \\ 0 & 1 - k_{Planti}\,\Delta T\,F_{NP-L\ i} \end{bmatrix} \begin{bmatrix} C^{T}_{Plant\ i} \\ N^{T}_{Plant\ i} \end{bmatrix} + \begin{bmatrix} F_{AlloC\ i}\,GPP\,\Delta T \\ F_{AlloN\ i}\,E\,N_{min}\Delta T \end{bmatrix}$$

[D2]

where $C^{T+\Delta T}_{Planti}$ and $N^{T+\Delta T}_{Planti}$ are the plant carbon and plant nitrogen variables for time step $T+\Delta T$. The initial condition for plant carbon leaf pool is derived from the observed LAI values. The other initial conditions are defined by calibration:

$$\begin{bmatrix} C^{T+\Delta T}_{Litter\ j} \\ N^{T+\Delta T}_{Litter\ j} \end{bmatrix} = \begin{bmatrix} 1 - k_{Litter\ j}\,\Delta T & 0 \\ 0 & 1 - k_{Litter\ j}\,\Delta T \end{bmatrix} \begin{bmatrix} C^{T}_{Litter\ j} \\ N^{T}_{Litter\ j} \end{bmatrix} +$$

$$\begin{bmatrix} FluxC_{PtoL\ j}\,k_{Planti}\,C^{T}_{Plant\ i}\Delta T \\ FluxC_{PtoL\ j}\,k_{Planti}\,C^{T}_{Plant\ i}\Delta T + FluxN_{PtoL\ j}\,k_{Planti}\,N^{T}_{Plant\ i}\Delta T \end{bmatrix}$$

[D3]

where $C^{T+\Delta T}_{Litter\,j}$ and $N^{T+\Delta T}_{Litter\,j}$ are the litter carbon and litter nitrogen pool variables for time step $T+\Delta T$. The initial condition for the litter variables is also defined by calibration:

$$\begin{bmatrix} C^{T+\Delta T}_{Soil\,k} \\ N^{T+\Delta T}_{Soil\,k} \end{bmatrix} = \begin{bmatrix} 1 - k_{Soil\,k}\,\Delta T + Flux_{kk}k_{soil\,k}\Delta T & 0 \\ Flux_{kk}k_{soil\,k}\,Ratio_{NCk}\,\Delta T & 1 - k_{Soil\,k}\,\Delta T \end{bmatrix} \begin{bmatrix} C^{T}_{Soil\,k} \\ N^{T}_{Soil\,k} \end{bmatrix} + \begin{bmatrix} Flux_{LtoS\,j}\,k_{Litter\,j}\,C^{T}_{Litter\,j}\Delta T \\ Flux_{LtoS\,j}\,k_{Litter\,j}\,C^{T}_{Litter\,j}Ratio_{NCk}\Delta T \end{bmatrix} \quad \text{[D4]}$$

where $C^{T+\Delta T}_{Soil\,k}$ and $N^{T+\Delta T}_{Soil\,k}$ are the soil carbon and soil nitrogen pool variables for time step $T+\Delta T$. The soil carbon microbial pool is computed directly from the biogeochemical-transport component as explained in Chapter 3. The initial condition for the soil variables also is defined by calibration.

The matrix representation of the numerical solution explained in Appendix C is shown as follows,

$$\begin{bmatrix} C^{T+\Delta T}_{i\,1} \\ \vdots \\ C^{T+\Delta T}_{i\,k} \\ \vdots \\ C^{T+\Delta T}_{i\,N} \end{bmatrix} = \begin{bmatrix} A_1 & \dots & 0 & \dots & 0 \\ \vdots & \ddots & 0 & 0 & \vdots \\ 0 & A_{k-1} & A_k & A_{k+1} & 0 \\ \vdots & 0 & 0 & \ddots & \vdots \\ 0 & 0 & 0 & A_{N-1} & A_N \end{bmatrix} \begin{bmatrix} C^{T}_{i\,1} \\ \vdots \\ C^{T}_{i\,k} \\ \vdots \\ C^{T}_{i\,N} \end{bmatrix} + \begin{bmatrix} \Phi_1 \\ \vdots \\ \Phi_k \\ \vdots \\ \Phi_N \end{bmatrix} \quad \text{[D5]}$$

where $C^{T+\Delta T}_{i\,k}$ are the concentration of the biogeochemical variables $i = \{C_{OM}, C_{NO3}, C_{NH3}, C_{NH4}, C_{CO2}, C_{HCO3}, C_{CO3}\}$, for each space distribution $k = \{1, 2, ..., N\}$ at time step time step $T+\Delta T$. The initial conditions are given by calibration and the boundary conditions are defined in the $[\Phi]$ vector in equation D5, according to definitions in Chapter 3 and the terms A_1 and A_N. $A_1 = [\theta^{T}_{1} / \theta^{T+\Delta T}_{1} - q^{T}_{1}\, \Delta T/\theta^{T+\Delta T}_{1}\, \Delta z_1$ -D $\Delta T/\theta^{T+\Delta T}_{1}\, \Delta z^{2}_{1}]$, $A_{k-1} = [q^{T}_{k-1}\, \Delta T/\theta^{T+\Delta T}_{k}\, \Delta z_k$ - D $\Delta T/\theta^{T+\Delta T}_{k}\, \Delta z^{2}_{k}]$, $A_k = [[\theta^{T}_{k} / \theta^{T+\Delta T}_{k} - q^{T}_{k}\, \Delta T/\theta^{T+\Delta T}_{k}\, \Delta z_k - 2$ D $\Delta T/\theta^{T+\Delta T}_{k}\, \Delta z^{2}_{k}]$, $A_{k+1} = [$D $\Delta T/\theta^{T+\Delta T}_{k}\, \Delta z^{2}_{k}]$, and $\Phi_k = [[\theta^{T}_{k} / \theta^{T+\Delta T}_{k}\, R_{ij}\, \Delta T + F_k / \theta^{T+\Delta T}_{k}\, \Delta T]$.

The soil carbon microbial pool is computed directly from the biogeochemical-transport component as explained in Chapter 3. The initial condition for the soil variables also is defined by calibration.

According to the numerical representations above described, we can integrate all the variables into one matrix equation of the numerical solution as follows:

$$\begin{bmatrix} C^{T+\Delta T}_{Plant\,i} \\ N^{T+\Delta T}_{Plant\,i} \\ C^{T+\Delta T}_{Litter\,j} \\ N^{T+\Delta T}_{Litter\,j} \\ C^{T+\Delta T}_{Soil\,k} \\ N^{T+\Delta T}_{Soil\,k} \\ C^{T+\Delta T}_{i\,k-1} \\ C^{T+\Delta T}_{i\,k} \\ C^{T+\Delta T}_{i\,k+1} \end{bmatrix} = \begin{bmatrix} A_{11} & 0 & 0 & 0 & 0 & 0 & 0 & 0 & 0 \\ 0 & A_{22} & 0 & 0 & 0 & 0 & 0 & 0 & 0 \\ A_{31} & 0 & A_{33} & 0 & 0 & 0 & 0 & 0 & 0 \\ A_{41} & A_{42} & 0 & A_{44} & 0 & 0 & 0 & 0 & 0 \\ 0 & 0 & A_{53} & 0 & A_{55} & 0 & 0 & 0 & 0 \\ 0 & 0 & A_{63} & 0 & A_{65} & A_{66} & 0 & 0 & 0 \\ 0 & 0 & 0 & 0 & 0 & A_{76} & A_{77} & A_{78} & 0 \\ 0 & 0 & 0 & 0 & 0 & 0 & A_{87} & A_{88} & A_{89} \\ 0 & 0 & 0 & 0 & 0 & 0 & 0 & A_{98} & A_{99} \end{bmatrix} \begin{bmatrix} C^{T+\Delta T}_{Plant\,i} \\ N^{T+\Delta T}_{Plant\,i} \\ C^{T+\Delta T}_{Litter\,j} \\ N^{T+\Delta T}_{Litter\,j} \\ C^{T+\Delta T}_{Soil\,k} \\ N^{T+\Delta T}_{Soil\,k} \\ C^{T+\Delta T}_{i\,k-1} \\ C^{T+\Delta T}_{i\,k} \\ C^{T+\Delta T}_{i\,k+1} \end{bmatrix} + \begin{bmatrix} F_1 \\ F_2 \\ 0 \\ 0 \\ 0 \\ 0 \\ \Phi_{k-1} \\ \Phi_k \\ \Phi_{k+1} \end{bmatrix}$$

$$[C^{T+\Delta T}] = [A][C^{T}] + [\Phi]$$

[D6]

where $[C^{T+\Delta T}]$ is the vector of all biogeochemical variables at time step, [A] the discrete transition matrix, $[C^{T}]$ the vector of biogeochemical variables at time T, and $[\Phi]$ the vector of external, non-linear terms and boundary conditions. The entries for matrix [A] are: $A_{11} = 1\text{-}k_{Planti}\, \Delta T$, $A_{22} = 1\text{-}k_{Planti}\, \Delta T\, F_{NP\text{-}Li}$, $A_{33} = A_{44} = 1\text{-}k_{Litter\ j}\, \Delta T$, $A_{55} = 1\text{-}k_{Soil\ k}\, \Delta T + Flux_{kk}\, k_{soil\ k}\, \Delta T$, $A_{66} = 1\text{-}k_{Soil\ k}\, \Delta T$, $A_{77} = A_{88} = A_{99} = A_k$, $A_{31} = A_{41} = A_{42} = Flux_{PLj}\, k_{Plant\ i}\, \Delta T$, $A_{53} = Flux_{LSkj}\, k_{Litter\ i}\, \Delta T$, $A_{63} = Flux_{LSkj}\, k_{Litter\ i}\, \Delta T\, Ratio_{NCk}\, \Delta T$, $A_{65} = Flux_{SSkk}\, k_{Soil\ k}\, \Delta T\, Ratio_{NCk}$, $A_{76} = A_{87} = A_{87} = A_{k\text{-}1}$, $A_{78} = A_{89} = A_{k+1}$. The entries for vector [Φ] are: $F_1 = F_{AlloCi}\, GPP\, \Delta T$, $F_2 = F_{AlloNi}\, E\, N_{min}\, \Delta T$, and Φ_k as defined in equation D5.

The numerical solution of the pyrite oxidation computations and the other solutes transport calculations are given by the adaptation of the original numerical schemes by Xu, (2013) to include the interaction with biogeochemical processes.

Bibliography

Abdelnour, Alex et al. 2013. “Effects of Harvest on Carbon and Nitrogen Dynamics in a Pacific Northwest Forest Catchment.” *Water Resources Research* 49(3): 1292–1313.

Aber, John D, and Anthony Federer. 1992. “A Generalized, Lumped-Parameter Model of Photosynthesis, Evapotranspiration and Net Primary Production in Temperate and Boreal Forest Ecosystems.” *Oecologia* (92): 463–74.

Ardejani, Faramarz Doulati et al. 2013. “Prediction of the Groundwater Rebound Process in a Backfilled Open Cut Mine Using an Artificial Neural Network.” *Mine Water and the Environment* (32): 251–57.

ASCE. 2000. “ASCE’s Standardized Reference Evapotranspiration Equation Authors: ASCE Standardization of Reference Evapotranspiration Task Committee.” *American Society of Civil Engineering*: 1–11.

Ash, S H, E W Felegy, D O Kennedy, and P S Miller. 1951. *Acid-Mine-Drainage Problems-Anthracite Region of Pennsylvania-Bulletin 508-Bureau of Mines*.

Bahrami, Saeed, and Faramarz Doulati Ardejani. 2016. “Prediction of Pyrite Oxidation in a Coal Washing Waste Pile Using a Hybrid Method, Coupling Artificial Neural Networks and Simulated Annealing (ANN/SA).” *Journal of Cleaner Production* 137: 1129–37. http://dx.doi.org/10.1016/j.jclepro.2016.08.005.

Beer, By Tom, and Peter C Young. 1984. “Longitudinal Dispersion in Natural Streams.” *Journal of Environmental Engineering* 109(5): 1049–67.

Berlin, M, G Suresh Kumar, and Indumathi M Nambi. 2014. “Numerical Modelling on Transport of Nitrogen from Wastewater and Fertilizer Applied on Paddy Fields.” *Ecological Modelling* 278: 85–99. http://dx.doi.org/10.1016/j.ecolmodel.2014.02.008.

Berlin, M, M Vasudevan, G Suresh Kumar, and Indumathi M Nambi. 2015. “Numerical Modelling on Fate and Transport of Petroleum Hydrocarbons in an Unsaturated Subsurface System.” *Journal of Earth System Science* 124(3): 655–74.

Beven, Keith. 2006. “A Manifesto for the Equifinality Thesis.” *Journal of Hydrology* 320: 18–36.

Beven, Keith, and Andrew Binley. 1992. “The Future of Distributed Models: Model Calibration and Uncertainty Prediction.” *Hydrological Processes* 6: 279–98.

Blodau, Christian. 2006. “A Review of Acidity Generation and Consumption in Acidic Coal Mine Lakes and Their Watersheds.” *Science of the Total Environment* 369: 307–32.

Bloomfield, Keith J et al. 2019. “The Validity of Optimal Leaf Traits Modelled on Environmental Conditions.” *New Phytologist* (221): 1409–23.

Bonan, G B, M Williams, R A Fisher, and K W Oleson. 2014. “Modeling Stomatal Conductance in the Earth System : Linking Leaf Water-Use Efficiency and Water Transport along the Soil – Plant – Atmosphere Continuum.” : 2193–2222.

Bonten, Luc T C, Gert Jan, and Maximilian Posch. 2016. “Environmental Modelling & Software A Model to Calculate Effects of Atmospheric Deposition on Soil Acidi Fi Cation , Eutrophication and Carbon Sequestration.” *Environmental Modelling and Software* 79: 75–84. http://dx.doi.org/10.1016/j.envsoft.2016.01.009.

Brunsell, N. A., S. J. Schymanski, and A. Kleidon. 2011. “Quantifying the Thermodynamic Entropy Budget of the Land Surface: Is This Useful?” *Earth System Dynamics* 2(1): 87–103.

Camacho, Luis A., and Ricardo A. Gonzalez. 2008. “Calibration and Predictive Ability Analysis of Longitudinal Solute Transport Models in Mountain Streams.” *Environmental Fluid Mechanics* 8(5–6): 597–604.

Cardoso, João, De Souza Junior, Roberta Corrêa, and Francisco Antonio. 2019. “Ecotoxicology and Environmental Safety Nitrate and Ammonium Proportion Plays a Key Role in Copper Phytoextraction , Improving the Antioxidant Defense in Tanzania Guinea Grass.” *Ecotoxicology and Environmental Safety* 171(September 2018): 823–32. https://doi.org/10.1016/j.ecoenv.2019.01.013.

Clapp, Roger, and George M. Hornberger. 1978. “Empirical Equations for Some Soil Hydraulic Properties.” *Water Resources Research* 14(23): 1559–67.

Clark, Martyn et al. 2016. “Improving the Theoretical Underpinnings of Process-Based Hydrologic Models.” *Water Resources Research* (52): 2350–65.

Collatz, G. James, J. Timothy Ball, Cyril Grivet, and Joseph A. Berry. 1991. “Physiological and Environmental Regulation of Stomatal Conductance , Photosynthesis and Transpiration : A Model That Includes a Laminar Boundary Layer *.” *Agricultural and Forest Meteorology* 54(1074): 107–36.

Cosby, B J, R C Ferrier, A Jenkins, and R F Wright. 2001. “Modelling the Effects of Acid Deposition : Refinements , Adjustments and Inclusion of Nitrogen Dynamics in the MAGIC Model.” *Hydrology and Earth System Sciences* 5(3): 499–518.

Cowan, By I R, G D Farquhar, By I R Cowan, and G D Farquhar. 1977. “Stomatal Function in Relationship to Environment and Metabolism.” *Integration of Activity in the Higher Plant* (I): 471–505.

Crafton, Elizabeth et al. 2019. “Dynamics of Mn Removal in an Acid Mine Drainage Treatment System over 13 Years after Installation.” *Environmental Earth Sciences* 78(1): 1–9. http://dx.doi.org/10.1007/s12665-018-8008-z.

Czuba, Joathan A, and Efi Foufoula-Georgiou. 2014. “A Network-Based Framework for Identifying Potential Synchronizations and Amplifications of Sediment Delivery in River Basins.” *Water Resources Research* 50: 3826–51.

Daly, Edoardo, Amilcare Porporato, and Ignacio Rodriguez-Iturbe. 2004. “Coupled Dynamics of Photosynthesis, Transpiration, and Soil Water Balance. Part I: Upscaling from Hourly to Daily Level.” *Journal of Hydrometeorology* 5(3): 546–58.

Dekker, Stefan C., Jasper A. Vrugt, and Rebecca J. Elkington. 2012. “Significant Variation in Vegetation Characteristics and Dynamics from Ecohydrological Optimality of Net Carbon Profit.” *Ecohydrology* 5(1): 1–18. http://doi.wiley.com/10.1002/eco.177%5Cnhttp://www3.interscience.wiley.com/journal/122653919/abstract.

Dewar, R C. 2010. “Maximum Entropy Production and Plant Optimization Theories.” *Philosophical Transactions of the Royal Society A: Mathematical, Physical and Engineering Sciences* 365: 1429–35.

Dewar, Roderick, Aleksanteri Mauranen, and M Annikki. 2018. “New Insights into the Covariation of Stomatal , Mesophyll and Hydraulic Conductances from Optimization Models Incorporating Nonstomatal Limitations to Photosynthesis.” *New Phytologist* 217: 571–85.

Doulati Ardejani, Faramarz et al. 2013. “Prediction of the Groundwater Rebound Process in a Backfilled Open Cut Mine Using an Artificial Neural Network.” *Mine Water and the Environment* 32(4): 251–57. http://link.springer.com/10.1007/s10230-013-0243-7.

Duursma, Remko A, Christopher J Blackman, and Rosana Lop. 2019. “Tansley Review On the Minimum Leaf Conductance : Its Role in Models of Plant Water Use , and Ecological and Environmental Controls.” *New Phytologist* 221: 693–705.

Eagleson, Peter. 1982. “Ecological Optimality in Water-Limited Natural Soil-Vegetation Systems 1. Theory and Hypothesis.” *Water Resources Research* 18(2): 325–40.

Eagleson, Peter. 2001. 1 Cambridge University Press *Ecohydrology Darwinian Expression of Vegetation Form and Function*. Boston-Massachusetts.

Eller, Cleiton B et al. 2018. “Modelling Tropical Forest Responses to ˜ o with a Stomatal Drought and El Nin Optimization Model Based on Xylem Hydraulics.” *Philosophical Transactions of the Royal Society A: Mathematical, Physical and Engineering Sciences* 373: 12.

Escobar, C et al. 2016. “Selection of Reactive Mixture for Biochemical Passive Treatment of Acid Mine Drainage.” *Environmental Earth Sciences* 75(576): 11.

Farquhar, G. D., S. von Caemmerer, and J. A. Berry. 1980. “A Biochemical Model of Photosynthetic CO2 Assimilation in Leaves of C3 Species.” *Planta* 149(1): 78–90.

Farquhar, Graham D. 1973. “PhD Thesis On the Stomata Conductance and Its Response to the Enviroment.” The Australian National University.

Farquhar, Graham D, Thomas N Buckley, Jeffrey M Miller, and J M Optimal. 2002. “Optimal Stomatal Control in Relation to Leaf Area and Nitrogen Content.” *Silva Fennica* 36(3): 625–37.

Farquhar, Graham D, and Thomas D Sharkey. 1982. “Stomatal Conductance and Photosynthesis.” *Annual Review Plant Physiology* 33: 317–45.

Fatichi, Simone et al. 2016. “An Overview of Current Applications , Challenges , and Future Trends in Distributed Process-Based Models in Hydrology.” *Journal of Hydrology* 537: 45–60. http://dx.doi.org/10.1016/j.jhydrol.2016.03.026.

Franks, Peter J et al. 2018. “Comparing Optimal and Empirical Stomatal Conductance Models for Application in Earth System Models.” *Global Change Biology* (August): 5708–23.

Fung, I. et al. 1997. “Carbon 13 Exchanges between the Atmosphere and Biosphere.” *Global Biogeochemical Cycles* 11(4): 507.

Galván, L et al. 2016. “Hydrological Modeling of a Watershed Affected by Acid Mine Drainage (Odiel River , SW Spain). Assessment of the Pollutant Contributing Areas.” *Journal of Hydrology* 540: 196–206.

Gangodagamage, Chandana, Efi Foufoula-Georgiou, and Patrick Belmont. 2014. “River Basin Organization around the Main Stem: Scale Invariance in Tributary Branching and the Incremental Area Function.” *Journal of Geophysical Research: Earth Surface* 119: 2174–93.

Gerke, Horst H, John W Molson, and Emil O Frind. 1998. “Modelling the Effect of Chemical Heterogeneity on Acidification and Solute Leaching in Overburden Mine Spoils.” *Journal of Hydrology* 209: 166–85.

Gilhespy, Sarah L. et al. 2014. “First 20 Years of DNDC (DeNitrification DeComposition): Model Evolution.” *Ecological Modelling* 292: 51–62. http://dx.doi.org/10.1016/j.ecolmodel.2014.09.004.

Gustafsson, Jon Petter, Salim Belyazid, Eric Mcgivney, and Stefan Löfgren. 2018. “Aluminium and Base Cation Chemistry in Dynamic Acidification Models – Need for a Reappraisal ?” *Soil* 4: 237–50.

Hartman, Melannie D. 2009. “DayCent-Chem Simulations of Ecological and Biogeochemical Processes of Eight Mountain Ecosystems in the United States Scientific Investigations Report 2009 – 5150.” *US Geological Survey Scientific Report 2009-5150* 5150: 29.

Hatton, T J, G D Salvucci, and H I Wu. 1997. “Eagleson ’ s Optimality Theory of an Ecohydrological Equilibrium : Quo Vadis ?” *Functional Ecology* 11(1945): 665–74.

Hernández, Felipe. 2019. “PhD Thesis Integrated High-Resolution Modeling for Operational Hydrologic Forecasting.” University of Pittsburgh.

Héroult, Arnaud et al. 2013. “Optimal Stomatal Conductance in Relation to Photosynthesis in Climatically Contrasting Eucalyptus.” *Plant, Cell & Environment* (36): 262–74.

Hofmann, Andreas F. 2009. Geologica Ultraiectina - Thesis “Quantifying the Influences of Biogeochemical Processes on PH of Natural Waters.” Universiteit Utrecht. http://igitur-archive.library.uu.nl/dissertations/2009-0513-200343/UUindex.html.

Hofmann, Andreas F, F J R Meysman, K Soetaert, and J J Middelburg. 2008. “A Step-by-Step Procedure for PH Model Construction in Aquatic Systems.” *Biogeosciences* 5: 227–51.

Holmberg, Maria et al. 2018. “Science of the Total Environment Modelling Study of Soil C , N and PH Response to Air Pollution and Climate Change Using European LTER Site Observations.” *Science of the Total Environment* 640–641(April): 387–99. https://doi.org/10.1016/j.scitotenv.2018.05.299.

Istanbulluoglu, Erkan, Tiejun Wang, and David A Wedin. 2012. “Evaluation of Ecohydrologic Model Parsimony at Local and Regional Scales in a Semiarid Grassland Ecosystem.” *Ecohydrology* 142(March 2011): 121–42.

Ivanov, Valeriy Y., Rafael L. Bras, and Enrique R. Vivoni. 2008. “Vegetation-Hydrology Dynamics in Complex Terrain of Semiarid Areas: 1. A Mechanistic Approach to Modeling Dynamic Feedbacks.” *Water Resources Research* 44(3): 1–34.

Jassal, R S et al. 2004. “A Model of the Production and Transport of CO 2 in Soil : Predicting Soil CO 2 Concentrations and CO 2 Efflux from a Forest Floor.” *Agricultural and Forest Meteorology* 124: 219–36.

Jesus, Manuel del, Romano Foti, Andrea Rinaldo, and Ignacio Rodriguez-Iturbe. 2012. “Maximum Entropy Production, Carbon Assimilation, and the Spatial Organization of Vegetation in River Basins.” *Proceedings of the National Academy of Sciences* 109(51): 20837–41. http://www.pnas.org/content/109/51/20837%5Cnhttp://www.pnas.org/content/109/51/20837.full.pdf.

Jodeiri, Behshad, Shokri Faramarz, Doulati Ardejani, and Hamidreza Ramazi. 2016. “A Model of Long-Term Oxidation and Leaching Processes in Pyritic Coal Cleaning Wastes.” *Environmental Earth Sciences* 75(9): 1–16.

Johnson, D B, and K B Hallberg. 2005. “Acid Mine Drainage Remediation Options: A Review.” *Science of the Total Environment* 338(1-2 SPEC. ISS.): 3–14.

Johnson, M O, M Gloor, M J Kirkby, and J Lloyd. 2014. “Insights into Biogeochemical Cycling from a Soil Evolution Model and Long-Term Chronosequences.” *Biogeosciences* 2(11): 6873–94.

Karaca, Oznur, Claudio Cameselle, and Krishna Reddy. 2018. “Mine Tailing Disposal Sites : Contamination Problems , Remedial Options and Phytocaps for Sustainable Remediation.” *Reviews in Environmental Science and Bio/Technology* 17(1): 205–28.

Katerji, N, Marc Hallaire, and Yvette Menoux-boyer. 1986. “Modelling Diurnal Patterns of Leaf Water Potential in Field Conditions.” *Ecological Modelling* 33(1986): 185–203.

Katul, Gabriel, Stefano Manzoni, Sari Palmroth, and Ram Oren. 2010. “A Stomatal Optimization Theory to Describe the Effects of Atmospheric CO2 on Leaf Photosynthesis and Transpiration.” *Annals of botany* 105(3): 431–42.

De Kauwe, M. G. et al. 2015. “Do Land Surface Models Need to Include Differential Plant Species Responses to Drought? Examining Model Predictions across a Mesic-Xeric Gradient in Europe.” *Biogeosciences* 12(24): 7503–18.

Kauwe, M et al. 2015. “A Test of an Optimal Stomatal Conductance Scheme within the CABLE Land Surface Model.” *Geoscientific Model Development* 8: 431–52.

Kleidon, A., E. Zehe, U. Ehret, and U. Scherer. 2013. “Thermodynamics, Maximum Power, and the Dynamics of Preferential River Flow Structures at the Continental Scale.” *Hydrology and Earth System Sciences* 17(1): 225–51.

Kleidon, A. 1997. “Simulating Root Carbon Storage With a Coupled Carbon - Water Cycle Root Model.” *Phys. Chem. Earth* 21(5): 499–502.

Laio, F., A. Porporato, L. Ridolfi, and I. Rodriguez-Iturbe. 2001. “Plants in Water-Controlled Ecosystems: Active Role in Hydrologie Processes and Responce to Water Stress II. Probabilistic Soil Moisture Dynamics.” *Advances in Water Resources* 24(7): 707–23.

Laio, F, A Porporato, C.P Fernandez-Illescas, and I Rodriguez-Iturbe. 2001. “Plants in Water-Controlled Ecosystems: Active Role in Hydrologic Processes and Response to Water Stress II. Probabilistic Soil Moisture Dynamics.” *Advances in Water Resources* 24(7): 745–62.

Leuning, R. 1995. “A Critical Appraisal of a Combined Stomatal-Photosynthesis Model for C3 Plants.” *Plant, Cell & Environment* 18(4): 339–55. http://dx.doi.org/10.1111/j.1365-3040.1995.tb00370.x.

Leuning, R, F M Kelliher, and D G G D E Pury. 1995. “Leaf Nitrogen , Photosynthesis , Conductance and Transpiration : Scaling from Leaves to Canopies.” *Plant, Cell and Environment* 18: 1183–1200.

Li, Changsheng et al. 2000. “A Process-Oriented Model of N2O and NO Emissions from Forest Soils: 1. Model Development.” *Journal of Geophysical Research: Atmospheres* 105(D4): 4369–84. http://dx.doi.org/10.1029/1999JD900949.

Li, Changsheng, Steve Frolking, and Tod A. Frolking. 1992. “A Model of Nitrous Oxide Evolution From Soil Driven by Rainfall Events: 1. Model Structure and Sensitivity.” *Journal of Geophysical Research* 97(D9): 9759–76.

Li, Yi, and Barbara J. Lence. 2007. “Estimating Resilience for Water Resources Systems.” *Water Resources Research* 43(7): 1–11.

Liu, Hui-Hai. 2014. “A Thermodynamic Hypothesis Regarding Optimality Principles for Flow Processes in Geosystems.” *Chinese Science Bulletin* 59(16): 1880–84. http://dx.doi.org/10.1007/s11434-014-0302-x.

Liu, L, L Li, W Song, and M Guo. 2018. “Science of the Total Environment Remediation Techniques for Heavy Metal-Contaminated Soils : Principles and Applicability.” *Science of the Total Environment* 633: 206–19. https://doi.org/10.1016/j.scitotenv.2018.03.161.

Luo, Xiangyu. 2013. “PhD Thesis An Investigation of Interactions between Plants and Water, Energy and Carbon Budgets in the Soil-Plant-Atmosphere Continumm.” Unviersity of Pittsburgh.

Luo, Xiangyu, Xu Liang, and Jeen-Shang Lin. 2016. “Plant Transpiration and Groundwater Dynamics in Water-Limited Climates: Impacts of Hydraulic Redistribution.” *Water Resources Research* 52: 4416–37.

Luo, Xiangyu, Xu Liang, and Heather R. McCarthy. 2013. “VIC+ for Water-Limited Conditions: A Study of Biological and Hydrological Processes and Their Interactions in Soil-Plant-Atmosphere Continuum.” *Water Resources Research* 49(11): 7711–32.

Luo, Xiangyu, Xu Liang, and Heather R Mccarthy. 2013. “VIC 1 for Water-Limited Conditions : A Study of Biological and Hydrological Processes and Their Interactions in Soil-Plant-Atmosphere Continuum.” 49: 7711–32.

Manzoni, Stefano et al. 2011. “Optimizing Stomatal Conductance for Maximum Carbon Gain under Water Stress : A Meta-Analysis across Plant Functional Types and Climates.” *Functional Ecology* 25(C): 456–67.

Manzoni, Stefano et al. 2014. “Optimal Plant Water-Use Strategies under Stochastic Rainfall.” *Water Resources Management* 50: 5379–94.

Manzoni, Stefano, Gabriel Katul, and Amilcare Porporato. 2014. “A Dynamical System Perspective on Plant Hydraulic Failure.” *Water Resources Research* 50: 5170–83.

Marsland, Robert, and Jeremy England. 2015. “Far-from-Equilibrium Distribution from near-Steady-State Work Fluctuations.” *Physical Review E - Statistical, Nonlinear, and Soft Matter Physics* 92(5): 1–15.

Martyushev, Leonid M. 2010. “The Maximum Entropy Production Principle : Two Basic Questions.” *Philosophical transactions of the Royal Society of London. Series B, Biological sciences* 365: 1333–34.

Mayer, Ulrich. 2019. “Reactive Transport Modeling.” In *Geochemical Modeling Mine Site Characterization and Remediation*, Society for Mining Metalurgy and Exploration, 73–87.

McDonnell, Jeffrey J., and Tadashi Tanaka. 2001. “On the Future of Forest Hydrology and Biogeochemistry.” *Hydrological Processes* 15(10): 2053–55. http://doi.wiley.com/10.1002/hyp.493.

Mcguire, Kevin J. et al. 2014. “Merging Perspectives in the Catchment Sciences: The US-Japan Joint Seminar on Catchment Hydrology and Forest Biogeochemistry.” *Hydrological Processes* 28(5): 2878–80.

Mcintyre, Neil R, Thorsten Wagener, Howard S Wheater, and Zeng Si Yu. 2003. “Uncertainty and Risk in Water Quality Modelling and Management.” *of Hydroinformatics* (05.4): 259–74.

Medlyn, Belinda E. et al. 2011. “Reconciling the Optimal and Empirical Approaches to Modelling Stomatal Conductance.” *Global Change Biology* 17(6): 2134–44.

Mencuccini, Maurizio, and Bradley Christoffersen. 2019. “Tansley Review Modelling Water Fluxes in Plants : From Tissues to Biosphere.” *New Phytologist* (1991): 16.

Meysman, Filip J R, and Stijn Bruers. 2010. “Ecosystem Functioning and Maximum Entropy Production : A Quantitative Test of Hypotheses.” *Philosophical Transactions of the Royal Society A: Mathematical, Physical and Engineering Sciences* 365: 1405–16.

Miner, Grace L, William L Bauerle, and Dennis D Baldocchi. 2017. “Estimating the Sensitivity of Stomatal Conductance to Photosynthesis : A Review.” *Plant, Cell and Environment* 40: 1214–38.

Molina-Herrera, Saúl et al. 2016. “A Modeling Study on Mitigation of N 2 O Emissions and NO 3 Leaching at Different Agricultural Sites across Europe Using LandscapeDNDC.” *Science of the Total Environment* 553(3): 128–40.

Mortensen, Jacob G et al. 2016. “Advancing the Food-Energy-Water Nexus: Closing Nutrients Loops in Arid River Corridors.” *Environmental Science and Technology*: 1–42.

Myers, Tom. 2016. “Acid Mine Drainage Risks – A Modeling Approach to Siting Mine Facilities in Northern Minnesota USA.” *Journal of Hydrology* 533: 277–90. http://dx.doi.org/10.1016/j.jhydrol.2015.12.020.

Neitsch, S.L, J.G Arnold, J.R Kiniry, and J.R Williams. 2011. “Soil & Water Assessment Tool Theoretical Documentation Version 2009.” *Texas Water Resources Institute, TR-406*: 1–647.

Nordstrom, D. Kirk. 2011. “Hydrogeochemical Processes Governing the Origin, Transport and Fate of Major and Trace Elements from Mine Wastes and Mineralized Rock to Surface Waters.” *Applied Geochemistry* 26(11): 1777–91. http://dx.doi.org/10.1016/j.apgeochem.2011.06.002.

Nordstrom, D Kirk. 2019a. “Geochemical Modeling and Environmental Systems.” In *Geochemical Modeling Mine Site Characterization and Remediation*, Society for Mining Metalurgy and Exploration, 7–26.

Nordstrom, D Kirk. 2019b. “Geochemical Modelling for Mine Site Characterization and Remediation.” *E3S Web of Conferences* 05013(98): 4–8.

Nordstrom, D Kirk. 2019c. “Recap : What Models Can and Cannot Do.” In *Geochemical Modeling Mine Site Characterization and Remediation*, Society for Mining Metalurgy and Exploration, 127–29.

Park, Sang-min, Jong-chan Yoo, and Sang-woo Ji. 2015. “Selective Recovery of Dissolved Fe , Al , Cu , and Zn in Acid Mine Drainage Based on Modeling to Predict Precipitation PH.” *Environmental Science and Pollution Research* 22: 3013–22.

Perunov, Nikolai, Robert Marsland, and Jeremy L. England. 2014. “Statistical Physics of Adaptation.” *arXiv preprint* 021036: 1–24. http://arxiv.org/abs/1412.1875v1.

Perunov, Nikolay, and Jeremy L. England. 2014. “Quantitative Theory of Hydrophobic Effect as a Driving Force of Protein Structure.” *Protein Science* 23(4): 387–99.

Plaza, Fernando et al. 2017. “Acid Rock Drainage Passive Remediation : Potential Use of Alkaline Clay , Optimal Mixing Ratio and Long-Term Impacts.” *Science of the Total Environment* 576: 572–85.

Plaza, Fernando J. 2018. “Environmental Impacts of Acid Rock Drainage Passive Remediation in Coal Waste Pile Using Alkaline Clay: An Experimental and Hydro-Geochemical Modeling Approach. Civil and Environmental Engineering; Ph.D. Dissertation; University of Pittsburgh.”

Plaza, Fernando, Yipei Wen, and Xu Liang. 2018. “Acid Rock Drainage Passive Remediation Using Alkaline Clay : Hydro-Geochemical Study and Impacts of Vegetation and Sand on Remediation.” *Science of the Total Environment* 637–638: 1262–78. https://doi.org/10.1016/j.scitotenv.2018.05.014.

Porporato, Amilcare, and Ignacio Rodriguez-iturbe. 2013. “Ecohydrology Bearings — Invited Commentary From Random Variability to Ordered Structures : A Search for General Synthesis in Ecohydrology.” *Ecohydrology* 342: 333–42.

Posch, Maximiilan, and Gert Jan Reinds. 2009. “Environmental Modelling & Software A Very Simple Dynamic Soil Acidification Model for Scenario Analyses and Target Load Calculations.” *Environmental Modelling and Software* 24(3): 329–40. http://dx.doi.org/10.1016/j.envsoft.2008.09.007.

Potter, C. S. Cs, and Jt Randerson. 1993. “Terrestrial Ecosystem Production: A Process Model Based on Global Satellite and Surface Data.” *Global Biogeochemical Cycles* 7(4): 811–41. http://www.scopus.com/inward/record.url?eid=2-s2.0-0027836106&partnerID=tZOtx3y1%5Cnhttp://onlinelibrary.wiley.com/doi/10.1029/93GB02725/full.

Prentice, I. Colin et al. 2014. “Balancing the Costs of Carbon Gain and Water Transport: Testing a New Theoretical Framework for Plant Functional Ecology.” *Ecology Letters* 17(1): 82–91. http://doi.wiley.com/10.1111/ele.12211.

Quijano, Juan C et al. 2012. “Competitive and Mutualistic Dependencies in Multispecies Vegetation Dynamics Enabled by Hydraulic Redistribution.” *Water Resources Research* 48(W05518): 1–22.

Reinds, Gert Jan, Maximilian Posch, and Rik Leemans. 2009. “Science of the Total Environment Modelling Recovery from Soil Acidi Fi Cation in European Forests under Climate Change.” *Science of the Total Environment, The* 407(21): 5663–73. http://dx.doi.org/10.1016/j.scitotenv.2009.07.013.

Rodriguez-Iturbe, Ignacio, and Amilcare Porporato. 2004. 1 Cambridge University Press *Ecohydrology of Water-Controlled Ecosystems*.

Rodríguez, Mónica et al. 2019. “Remediation of Acid Mine Drainage.” *Environmental Chemistry Letters* (0123456789). https://doi.org/10.1007/s10311-019-00894-w.

Sas, L, Z Rengel, and C Tang. 2001. “Excess Cation Uptake , and Extrusion of Protons and Organic Acid Anions by Lupinus Albus under Phosphorus Deficiency.” *Plant Science* 160: 1191–98.

Schaefer, Kevin et al. 2008. “Combined Simple Biosphere/Carnegie-Ames-Stanford Approach Terrestrial Carbon Cycle Model.” *Journal of Geophysical Research: Biogeosciences* 113(3): 1–13.

Schroedinger, Erwin. 1944. *What Is Life?* Dublin. http://books.google.com/books?hl=en&lr=&id=VwsRNzrcCf4C&oi=fnd&pg=PR7&dq=What+Is+Life?&ots=5HABBa0tNY&sig=9ZP7tNSDLTPRTojov_VQxV2evxs.

Schymanski, J. et al. 2007. “A Test of the Optimality Approach to Modelling Canopy Properties and CO 2 Uptake by Natural Vegetation.” *Plant, Cell & Environment* 30(12): 1586–98. http://doi.wiley.com/10.1111/j.1365-3040.2007.01728.x.

Schymanski, S J et al. 2008. “An Optimality-Based Model of the Coupled Soil Moisture and Root Dynamics.” *Hydrology and Earth System Sciences* 12: 913–32.

Schymanski, Stanislaus J, Axel Kleidon, Marc Stieglitz, and Jatin Narula. 2010a. “Maximum Entropy Production Allows a Simple Representation of Heterogeneity in Semiarid Ecosystems.” *Philosophical transactions of the Royal Society of London. Series B, Biological sciences* 365(1545): 1449–55.

Skousen, Jeff et al. 2017. “Review of Passive Systems for Acid Mine Drainage Treatment.” *Mine Water and the Environment* 36(1): 133–53. http://dx.doi.org/10.1007/s10230-016-0417-1.

Smith, Nicholas G et al. 2019. “Global Photosynthetic Capacity Is Optimized to the Environment.” *Ecology Letters* 22: 506–17.

Sperry, John S et al. 2017. “Predicting Stomatal Responses to the Environment from the Optimization of Photosynthetic Gain and Hydraulic Cost.” *Plant, Cell and Environment* 40: 816–30.

Strogatz S H. 1995. *Nonlinear Dynamics and Chaos: With Applications to Physics, Biology, Chemistry, and Engineering*. Addison-Wesley.

Tague, C. L., and L. E. Band. 2004. “RHESSys: Regional Hydro-Ecologic Simulation System—An Object-Oriented Approach to Spatially Distributed Modeling of Carbon, Water, and Nutrient Cycling.” *Earth Interactions* 8(19): 1–42.

Tuzet, a, a Perrier, and R Leuning. 2003. “A Coupled Model of Stomatal Conductance , Photosynthesis.” *Plant, Cell and Environment* 26: 1097–1116.

Vitousek, Peter M, Harold A Mooney, Jane Lubchenco, and Jerry M Melillo. 1997. “Human Domination of Earth’ s Ecosystems.” *Science* 277(5325): 494–99.

Volk, Tyler, and Olivier Pauluis. 2010. “It Is Not the Entropy You Produce , Rather , How You Produce It.” *Philosophical Transactions of the Royal Society A: Mathematical, Physical and Engineering Sciences* 365: 1317–22.

Vrugt, Jasper A, and Keith J Beven. 2018. “Embracing Equifinality with Efficiency : Limits of Acceptability Sampling Using the DREAM (LOA) Algorithm.” *Journal of Hydrology* 559: 954–71. https://doi.org/10.1016/j.jhydrol.2018.02.026.

Wang, Chi-hsiang, and Jane M. Blackmore. 2009. “Resilience Concepts for Water Resource Systems.” *Journal of Water Resources Planning and Management* 135(6): 528–36.

Wang, H., I. C. Prentice, and T. W. Davis. 2014. “Biophsyical Constraints on Gross Primary Production by the Terrestrial Biosphere.” *Biogeosciences* 11(20): 5987–6001.

Wang, Han et al. 2017. “Towards a Universal Model for Carbon Dioxide Uptake by Plants.” *Nature Plants* 3(September). http://dx.doi.org/10.1038/s41477-017-0006-8.

Wang, Jingfeng, and R. L. Bras. 2011. “A Model of Evapotranspiration Based on the Theory of Maximum Entropy Production.” *Water Resources Research* 47(3): 1–10.

Wang, Weile et al. 2009. “A Hierarchical Analysis of Terrestrial Ecosystem Model Biome-BGC: Equilibrium Analysis and Model Calibration.” *Ecological Modelling* 220(17): 2009–23.

Wang, Y. P., R. M. Law, and B. Pak. 2010. “A Global Model of Carbon, Nitrogen and Phosphorus Cycles for the Terrestrial Biosphere.” *Biogeosciences* 7(7): 2261–82.

Wang, Y, B Z Houlton, and C B Field. 2007. “A Model of Biogeochemical Cycles of Carbon , Nitrogen , and Phosphorus Including Symbiotic Nitrogen Fixation and Phosphatase Production.” *Global and Planetary Change* 21(December 2006): 1–15.

Wang, Ying Ping, B. Z. Houlton, and C. B. Field. 2007. “A Model of Biogeochemical Cycles of Carbon, Nitrogen, and Phosphorus Including Symbiotic Nitrogen Fixation and Phosphatase Production.” *Global Biogeochemical Cycles* 21(1): 1–15.

Westhoff, M. C., and E. Zehe. 2013. “Maximum Entropy Production: Can It Be Used to Constrain Conceptual Hydrological Models?” *Hydrology and Earth System Sciences* 17(8): 3141–57. http://www.hydrol-earth-syst-sci.net/17/3141/2013/.

Wigmosta, Mark S., Lance W. Vail, and Dennis P. Lettenmaier. 1994. “A Distributed Hydrology-Vegetation Model for Complex Terrain.” *Water Resources Research* 30(6): 1665–79.

Wigmosta, Ms, Bart Nijssen, and Pascal Storck. 2002. “The Distributed Hydrology Soil Vegetation Model.” *Mathematical Models of Small Watershed Hydrology and Applications*: 7–42. http://www.cabdirect.org/abstracts/20033121322.html.

Wissmeier, L., and D. A. Barry. 2010. “Implementation of Variably Saturated Flow into PHREEQC for the Simulation of Biogeochemical Reactions in the Vadose Zone.” *Environmental Modelling and Software* 25(4): 526–38. http://dx.doi.org/10.1016/j.envsoft.2009.10.001.

Wright, Ian J, Peter B Reich, and Mark Westoby. 2003. “Least-Cost Input Mixtures of Water and Nitrogen for Photosynthesis.” *The American naturalist* 161(1): 98–111.

Wright, R F et al. 2006. “Modelling the Effect of Climate Change on Recovery of Acidified Freshwaters : Relative Sensitivity of Individual Processes in the MAGIC Model.” *Science of the Total Environment* 365: 154–66.

Wunderly, M D, D W Blowes, E O Frind, and C J Ptacek. 1996. “Sulfide Mineral Oxidation and Subsequqnt Reactive Transport of Oxidation Products in Mine Tailings Impoundments: A Numerical Model.” *Water Resoures Research* 32(10): 3173–87.

Xu, Yi. 2013. Ph.D. Dissertation Thesis Unviersity of Pittsburgh “Investigation of Environmental Impacts of Beneficial Reuse of Bauxite Residue in Coal-Refuse Area Based on a Hydro-Thermal-Geochemical Model.”

Xu, Yi et al. 2020. “A Hydro-Thermal-Geochemical Modeling Framework to Simulate Reactive Transport in a Waste Coal Area under Amended and Non-Amended Conditions.” *Helyon* 6(August 2019).

Yao, Zhitong, Jinhui Li, Henghua Xie, and Conghai Yu. 2012. “Review on Remediation Technologies of Soil Contaminated by Heavy Metals.” *Procedia Environmental Sciences* 16: 722–29. http://dx.doi.org/10.1016/j.proenv.2012.10.099.

Zehe, E et al. 2011. “HESS Opinions: Hydrologic Predictions in a Changing Environment: Behavioral Modeling.” *Hydrology and Earth System Sciences* 15(2): 635–46. http://www.hydrol-earth-syst-sci.net/15/635/2011/.

Zeng, Mufan et al. 2017. “Model-Based Analysis of the Long-Term Effects of Fertilization Management on Cropland Soil Acidification.” *Environmental Science and Technology* 51: 3843–51.

Zhou, Haoran et al. 2018. “C 4 Photosynthesis and Climate through the Lens of Optimality.” *Proceedings of the National Academy of Sciences* 115(47): 1–6.